Structural Studies on Actin : Gelsolin Segment 1 Complexes

by

Walter Manfred Morton

Doctor of Philosophy

(Ph.D.)

The University of Edinburgh

1999

I declare to have composed and written this thesis myself and to have personally done the work described.

28/05/99

I dedicate this thesis to my beloved fiancée Andrea, my parents, and my sister.

Acknowledgements

I want to thank my supervisor, Dr. Paul McLaughlin, for instructing me in the tools and techniques necessary to embark on this project, and for all the guidance and advice he has provided me with, showing great patience and understanding throughout the course of my work for this thesis.

I am also indebted to Dr. Sutherland Maciver for sharing his considerable experience in the field of protein chemistry and the actin cytoskeleton, and his advice on procedures and techniques in the biochemical laboratory.

I am further indebted to Dr. Dimitri Alexeev who gave very helpful advice on theory and techniques concerning the experimental and the computational side of X-ray diffraction analysis.

I want to extend my gratitude to Prof. Malcolm Walkinshaw for all the support I received in the Structural Biochemistry Group, and to Prof. John Phillips, the Faculty of Medicine, and the Austrian Ministry for Science for the financial support.

Also I wish to thank all the members of the Department of Biochemistry and the Institute of Cell and Molecular Biology for their help, friendship, and supporting me during the work for my thesis.

Special thanks go to my parents, my fiancée and her family for the love and support they have always shown me, especially during the time I worked for this thesis in Britain.

Abstract

The regulation of the dynamic assembly and disassembly of actin filaments in eukaryotic cells is vital to the cell's ability to reshape, migrate and differentiate. An important part is played by the actin-binding protein gelsolin, which can bind to two actin monomers. Activated by calcium it is capable of severing actin filaments and capping them at the fast growing end. Alternatively it can act as a nucleus for the growth of a new filament. The tight binding of the first segment of gelsolin to an actin monomer (K_d ~ 5pM) is an example of a lock and key fit between two proteins. When calcium is removed gelsolin retains the actin monomer tightly bound to segment 1, preventing exchange of the actin-associated ATP. Prevention of actin polymerisation is lethal to cells. Latrunculin A, a toxic metabolite of Red Sea sponges, binds tightly to actin monomers (K_d ~ 0.2μM) and prevents those monomers participating in actin filament formation, disrupting the actin cytoskeleton. This thesis investigates the structural consequences of gelsolin segment 1 binding to actin isoforms, as well as the structural control gelsolin segment 1 exerts on actin preventing nucleotide exchange. To this end the crystal structures of gelsolin segment 1 on its own and in complex with β-actin and α-actin were solved at 100 Kelvin to a resolution of 2.2Å, 2.3Å, and 2.3Å respectively. Furthermore the marine toxin latrunculin A was successfully soaked into crystals of α-actin : gelsolin segment 1 and the structure determined at 100 Kelvin and to a resolution of 2.0Å. The refined structures were compared with each other and with previously published crystal structures of gelsolin segment 1 and actin. The investigations revealed conformational differences between the structures of gelsolin segment 1 crystallised on its own, in its complex with actin, and in the published horse gelsolin crystal structure. The structure determination of α- and β-actin complexed to gelsolin segment 1 resulted in actin displaying a different conformation than that found in the complex with profilin, particularly in respect to the actin subdomain 2. The binding of latrunculin A just above the actin ATP-binding site induces changes along the protein chain of the actin subdomain 4. Other changes to the actin structure are located in subdomain 2.

Abbreviations used

σ	Standard deviation
α_{hkl}	Relative phase angle of F_{hkl}
<I(hkl)> or <I>	Mean of all intensity measurements at hkl or in given range
$\|F_{hkl}\|$	Structure factor amplitude of reflection hkl
ADP	Adenosine-5'-diphosphate
ASU	Asymmetric unit
ATP	Adenosine-5'-triphosphate
BCA	Bicinchoninic acid
CapG-1	Segment 1 of CapG
CCD	Charge-coupled device
DMF	Dimethylformamide
DMSO	Dimethylsulphoxide
DTT	Dithiothreitol
EDTA	Ethylenediaminetetraacetic acid
EGTA	Ethylene glycol-bis-[β-aminoethyl ether]-N,N,N',N'-tetraacetic acid
F-actin	Filamentous actin
F_{hkl}	$= \|F_{hkl}\|e^{i\alpha_{hkl}}$, Structure factor of reflection hkl
G-actin	Monomeric actin
G1	Gelsolin segment 1
G1C	N57C mutant of gelsolin segment 1
I	Intensity
i	$(-1)^{1/2}$
$I_j(hkl)$	jth measurement of the intensity at hkl
IP	X-ray storage-phosphor imaging plate
IPTG	Isopropyl-β-D-thiogalactopyranoside
latA	Latrunculin A
MAD	Multi-wavelength anomalous dispersion
MES	2-[N-morpholino]-ethanesulfonic acid
MIR	Multiple isomorphous replacement
MR	Molecular replacement
NCS	Non-crystallographic symmetry
PEG	Polyethylene glycol
Pi	Phosphate ion (HPO_4^{2-} or $H_2PO_4^-$)
PIP_2	Phosphatidylinositol-4,5-bisphosphate
PIPES	1,4-Piperazine-diethanesulfonic acid
PMSF	Phenylmethylsulfonyl fluoride
R_{cryst}	$= \Sigma_{hkl} \mid w_{hkl}\|Fo(hkl)\| - k\|Fc(hkl)\| \mid / \Sigma_{hkl}\|Fo(hkl)\|$
R_{free}	R_{cryst} for 5% of the data excluded from the refinement
R_{sym}	$= \Sigma_{hkl}\Sigma_j\|I_j(hkl) - <I(hkl)>\| / \Sigma_{hkl}\Sigma_j I_j(hkl)$
RT	Room temperature
SDS-PAGE	Sodium dodecylsulphate - polyacrylamide gel electrophoresis
Tris	2-Amino-2-(hydroxymethyl)-1,3-propanediol

Table of Contents

1. Introduction 1-1

1.1 Actin and the actin binding protein gelsolin 1-1

1.1.1 Biological characteristics of actin 1-1

1.1.2 Relationships within the actin family 1-5

1.1.3 Actin polymerisation 1-5

1.1.4 The structure of G- and F-actin 1-7

1.1.5 Gelsolin 1-10

1.1.6 Binding of gelsolin segment 1 to actin 1-12

1.2 Protein X-ray crystallography 1-12

1.2.1 The usefulness of X-ray diffraction analysis for structure determinations 1-13

1.2.2 Crystallisation of proteins 1-13

1.2.3 Crystal structure 1-15

1.2.4 X-ray diffraction 1-19

1.2.5 Analysis of X-ray diffraction data 1-21

1.2.6 Solving the phase problem 1-24

1.2.6.1 Multiple isomorphous replacement 1-24

1.2.6.2 Multi-wavelength anomalous diffraction 1-25

1.2.6.3 Molecular replacement 1-26

1.2.7 Refinement of the model for a protein crystal structure 1-27

1.3 The flexibility of the actin structure 1-29

1.3.1 Previous considerations 1-29

1.3.2 The binding of gelsolin segment 1 to actin 1-31

1.3.3 Drug molecules binding to actin 1-33

1.3.4 The investigations of this thesis 1-34

2. Methods 2-1

2.1 Biochemical procedures 2-1

2.1.1 Acetone powder preparation of rabbit skeletal muscle tissue 2-1

2.1.2 Purification of α-actin from rabbit muscle acetone powder 2-2
2.1.3 Purification of human platelet β-actin 2-3
2.1.4 Transformation of *E.coli* strains BL21(DE3) and JM109 with vectors containing gene for G1, G1C, or CapG-1 2-5
2.1.5 Plasmid amplification in *E.coli* strain JM109 2-6
2.1.6 Expression and purification of gelsolin segment 1 2-7
2.1.7 Expression and purification of CapG segment 1 2-8
2.1.8 Actin ATP-ADP exchange and complex formation with G1C 2-11
2.1.9 Purification of actin : gelsolin segment 1 2-11
2.1.10 Crystallisation in hanging drops 2-12
2.1.11 Soaking of α-actin:G1C crystals 2-13
2.2 X-ray diffraction data collection 2-15
2.2.1 Preparation for X-ray data collection at room temperature 2-15
2.2.2 Preparation for X-ray data collection at 100K 2-15
2.2.3 Recording X-ray diffraction data 2-17
2.2.3.1 X-ray sources and detectors 2-17
2.2.3.2 Collecting X-ray diffraction data 2-20
2.2.4 Evaluation of X-ray diffraction data 2-21
2.3 Computer software used 2-22
2.3.1 Programs of the CCP4 suite 2-22
2.3.2 Other programs used 2-24

3. Structural studies of α- and β-actin : gelsolin segment 1 3-1
3.1 Introduction 3-1
3.2 The structure of α-actin:G1C at 100K 3-3
3.2.1 Complex formation and crystallisation 3-3
3.2.1.1 Preparing α-actin from rabbit muscle acetone powder 3-3
3.2.1.2 Expression and purification of N57C gelsolin segment 1 (G1C): 3-3
3.2.1.3 Formation of the complex: 3-4
3.2.1.4 Crystallisation: 3-5
3.2.2 X-ray diffraction analysis 3-6

3.2.3 Molecular replacement 3-7
3.2.4 Comparison of α-actin:G1C structures at room temperature and at 100K 3-13
3.3 The structure of β-actin : gelsolin segment 1 3-16
3.3.1 Complex formation and crystallisation 3-16
3.3.1.1 Preparing β-actin from platelet acetone powder: *3-16*
3.3.1.2 Formation of the complex: *3-17*
3.3.1.3 Crystallisation: *3-17*
3.3.2 X-ray diffraction analysis 3-17
3.3.3 Molecular replacement 3-18
3.3.4 Conformational changes during refinement 3-24
3.3.5 Comparison of actin structures 3-25
3.3.6 Comparison of β-actin:G1C and α-actin:G1C 3-26
3.3.7 Comparison of β-actin:G1C with tight-state β-actin:profilin 3-28
3.4 Conclusion 3-31

4. Structural studies on gelsolin segment 1 4-1
4.1 Introduction 4-1
4.2 Structure determination of gelsolin segment 1 4-3
4.2.1 Purification and crystallisation 4-3
4.2.2 X-ray diffraction analysis 4-5
4.2.3 Molecular replacement 4-6
4.2.4 Discussion of the structure of gelsolin segment 1 4-11
4.2.4.1 Secondary, tertiary, and quaternary structure in the asymmetric unit *4-11*
4.2.4.2 Contacts between the NCS related molecules *4-14*
4.2.4.3 Calcium ion binding *4-16*
4.3 Gelsolin segment 1 and 4 in the equine gelsolin structure 4-18
4.3.1 Comparison of conformation 4-18
4.3.2 Protein interactions 4-20
4.4 Segment 1 of human CapG (CapG-1) 4-24

4.4.1 Crystallisation 4-24
4.4.2 X-ray diffraction 4-26
4.5 Conclusion 4-26

5. Binding of latrunculin A to α-actin : gelsolin segment 1 5-1
5.1 Introduction 5-1
5.2 Structure determination of the latrunculin A containing α-actin :G1C complex 5-4
5.2.1 Soaking of latrunculin A into α-actin:G1C crystals 5-4
5.2.1.1 Preparation of α-actin:G1C crystals 5-4
5.2.1.2 Soaking 5-5
5.2.2 X-ray diffraction analysis 5-6
5.2.3 Molecular replacement 5-7
5.2.3.1 Refinement with XPLOR 5-7
5.2.3.2 Refinement with REFMAC 5-9
5.3 Discussion of latrunculin A binding to actin 5-14
5.3.1 The binding site of latrunculin A on actin 5-14
5.3.2 Changes in thermal displacement and disorder: 5-15
5.3.3 Changes to the main chain: 5-16
5.3.4 Changes to individual residues: 5-18
5.3.5 Residues involved in conferring resistance to latrunculin A: 5-22
5.4 Cytochalasin D 5-26
5.4.1 Attempt to soak cytochalasin D into the α-actin:G1C complex 5-26
5.4.2 The crystal structure of cytochalasin D 5-27
5.5 Conclusion 5-29

6. Discussion 6-1
6.1 Previous considerations of the flexibility of actin 6-1
6.2 The conformations of α- and β-actin complexed to G1 6-2
6.3 Structures of gelsolin segment 1 6-3

6.4 Probing the α-actin:G1 structure with latrunculin A 6-5
6.5 Actin flexibility and its interfaces with G1 and other actin molecules 6-7
6.6 Conclusions drawn in this thesis 6-8
6.7 Future studies 6-10

7. References 7-1

Table of Figures

Figure 1.1: The actin monomer 1-1

Figure 1.2: Schematic representation of the actin filament 1-2

Figure 1.3: Actin crystal structures. 1-8

Figure 1.4: Cartoon of the domains of gelsolin. 1-10

Figure 1.5: A schematic view of a unit cell 1-16

Figure 1.6: Examples of cubic and rhombohedral crystal systems. 1-18

Figure 1.7: The Ewald sphere and the reciprocal lattice 1-20

Figure 1.8: Average B-factors of α-actin 1-29

Figure 1.9: Superposition of α-actin and open-state β-actin 1-30

Figure 1.10: Actin binding drugs 1-34

Figure 2.1: Crystal setup in glass capillary for X-ray exposure. 2-15

Figure 2.2: Storage of flash frozen crystal in cryo-vial. 2-17

Figure 2.3: Setup of X-ray diffraction experiment. 2-20

Figure 3.1: Plot of α-actin:G1C S200 column run 3-4

Figure 3.2: SDS-PAGE of samples after S200 gel-filtration 3-5

Figure 3.3: Actin : gelsolin segment 1 (N57C) crystals 3-6

Figure 3.4: RMS distances (room temperature versus 100K model). 3-9

Figure 3.5: SA-OMIT Fo-Fc map (ATP omitted). 3-10

Figure 3.6: SA-OMIT Fo-Fc map (Phe200 to Glu207 omitted). 3-10

Figure 3.7: SA-OMIT Fo-Fc map (Lys115 of G1C omitted) 3-11

Figure 3.8: Ramachandran plot of α-actin:G1C (100K) 3-12

Figure 3.9: LSQ fit of α-actin:G1C at room temperature and 100K. 3-13

Figure 3.10: Average B-factors versus residues (α-actin at 100K and RT). 3-15

Figure 3.11: Difference electron density for G1C. 3-20

Figure 3.12: Electron density for residue 162 of actin 3-22

Figure 3.13: Ramachandran plot of β-actin:G1C. 3-24

Figure 3.14: The large domain core of actin (Page et al. 1998)..... 3-26
Figure 3.15: RMS deviations (β-actin:G1C versus α-actin:G1C)..... 3-27
Figure 3.16: RMS deviations (refined β-actin versus tight-state β-actin) 3-29
Figure 3.17: Superposition of β-actin:G1C and tight-state β-actin:profilin 3-30

Figure 4.1: Gel-filtration of gelsolin segment 1 4-3
Figure 4.2: SDS-PAGE (samples from G1 gel-filtration) 4-4
Figure 4.3: Crystals of gelsolin segment 1..... 4-4
Figure 4.4: Patterson correlation coefficients 4-7
Figure 4.5: G1 intramolecular calcium ion sites..... 4-8
Figure 4.6: Ramachandran plot of the refined model. 4-10
Figure 4.7: The contents of the asymmetric unit 4-12
Figure 4.8: Topology of gelsolin segment 1 4-12
Figure 4.9: Cα traces of G1B and G1A superimposed over G1B.. 4-13
Figure 4.10: N-terminal association of molecule A and B. 4-15
Figure 4.11: Contacts between molecule A and B..... 4-16
Figure 4.12: Superposition of G1A, G1B, G1C, equine G1 and G4. 4-19
Figure 4.13: N57C mutant of gelsolin segment 1 and α-actin..... 4-21
Figure 4.14: Equine G1-G4. 4-22
Figure 4.15: CapG-S1 crystal fragments 4-25
Figure 4.16: Diffraction pattern of CapG-S1..... 4-26

Figure 5.1: Representatives of the cytochalasin family 5-1
Figure 5.2: Latrunculin A. 5-2
Figure 5.3: Cα trace of the actin model after initial refinement. 5-8
Figure 5.4: Positive difference electron density for latA..... 5-10
Figure 5.5: Ramachandran plot..... 5-12
Figure 5.6: SA-OMIT Fo-Fc map (latA omitted).. 5-13
Figure 5.7: Latrunculin A bound to actin. 5-14
Figure 5.8: Plot of main-chain B-factors 5-15
Figure 5.9: RMS distances (refined model versus native model)..... 5-16

Figure 5.10: Distance between subdomain 2 and 4. 5-17
Figure 5.11: Salt bridge between Arg206 and Asp187..... 5-20
Figure 5.12: Schematic view of the latA binding site of actin. 5-21
Figure 5.13: Residues involved in conferring resistance to latA..... 5-23
Figure 5.14: LatA binding-site on actin..... 5-25
Figure 5.15: Needles of crystallised cytochalasin D..... 5-27
Figure 5.16: Asymmetric unit of crystallised cytochalasin D..... 5-29

Figure 6.1: The contents of the asymmetric unit of the G1 crystal structure..... 6-3
Figure 6.2: Latrunculin A bound to actin.. 6-6

1. Introduction

1.1 Actin and the actin binding protein gelsolin

1.1.1 Biological characteristics of actin

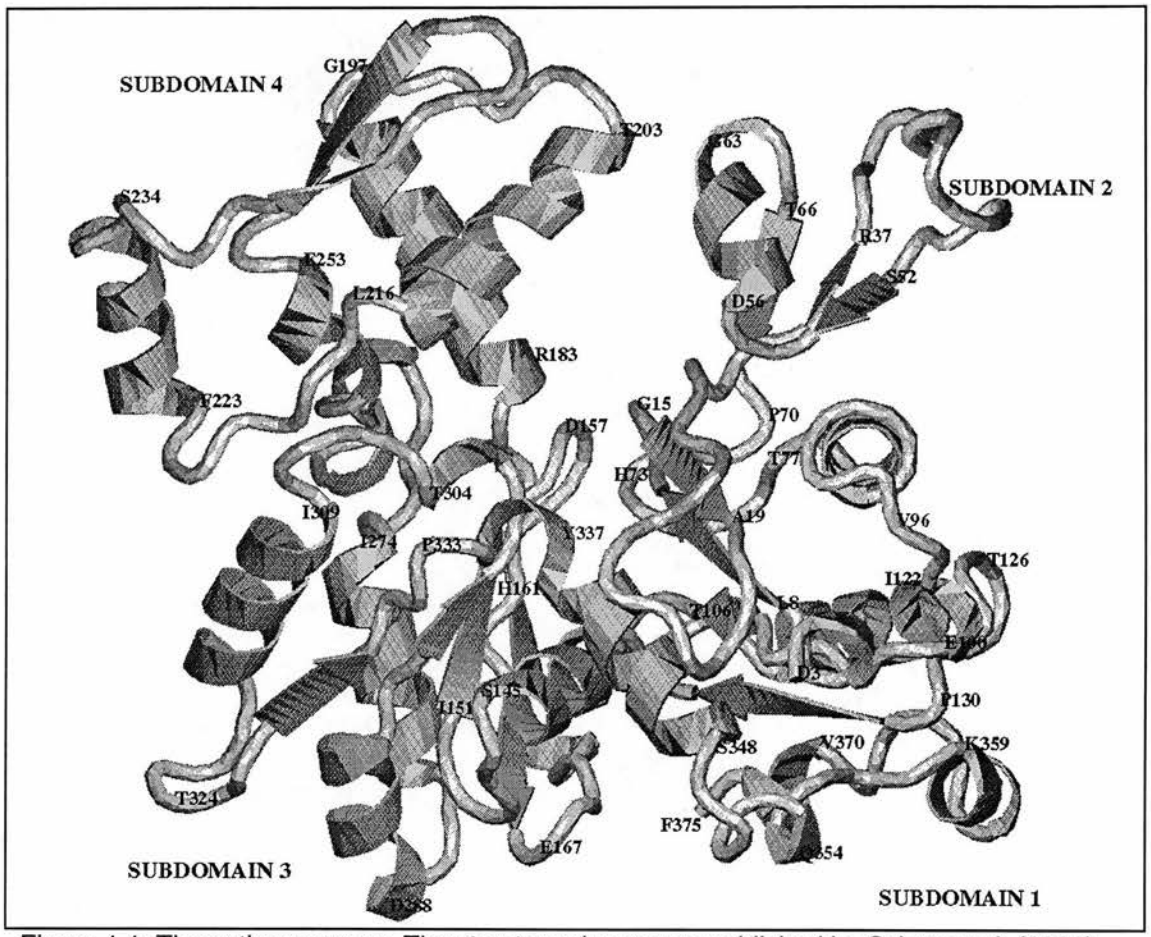

Figure 1.1: The actin monomer. The structure shown was published by Schutt et al. (1993). Amino acids labelled are identical in both α- and β-actin sequence. The tightly bound nucleotide binds at the bottom of the cleft between subdomain 2 and 4.

Actin is a soluble protein with a calculated molecular weight of 42,051 Dalton and is one of the most abundant proteins in many eukaryotic cells with a high degree of sequence conservation (Elzinga et al. 1973, Elzinga et al. 1976, Nakajima-Iijima et al. 1985). In the best studied cases, actin and all of its associated proteins constitute more than 25% of protein in non-muscle cells and over 60% in muscle cells

(reviewed by Vandekerckhove 1993). Characteristics of actin are binding of ADP and ATP (Straub and Feuer 1950) and self-assembly of the globular monomer (G-actin) into long filaments (Figure 1.2), which induces the hydrolysis of bound ATP to ADP (Cooke 1975, Brenner and Korn 1983). Filamentous actin (F-actin) exhibits polarity as can be seen by decoration with myosin fragments and visualisation with an electron microscope. The picture of a filament thus displayed resembles a multi-barbed arrow with a "pointed" and a "barbed" end (Woodrum et al 1975). The literature on this subject is extensive and has been comprehensively reviewed (Carlier 1991, Janmey 1993, Sheterline and Sparrow 1994).

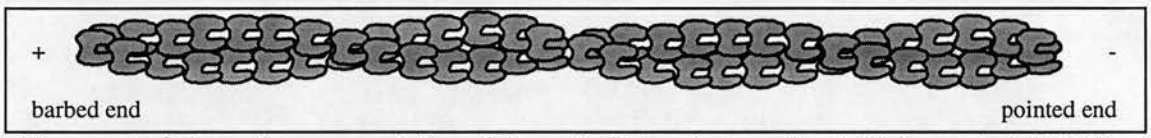

Figure 1.2: Schematic representation of the actin filament according to Holmes et al. (1990). Monomers are drawn with the nucleotide binding cleft between subdomains 2 and 4 pointing to the right (the pointed end).

The actin isoforms in vertebrates display slightly different filament assembly characteristics and their expression is tissue dependent (Otey et al. 1987). The α-actin in vertebrate muscle has been the most extensively studied. It forms stable actin filaments, which are arranged in parallel together with myosin filaments and other proteins to form the contractile unit of the muscle, the sarcomer. These in turn, sequentially arranged, form the myofibrils, which run along the length of muscle cells and bundle together to form muscle fibres. This has been reviewed by Schutt and Lindberg (1992).

Muscle cells have evolved specialising on generating large forces in a single direction by the interaction of static actin filament structures with myosin filaments and other proteins. In non-muscle cells the contractile structures are less obviously organised. These F-actin structures often exhibit dynamic assembly and disassembly in response to different physiological situations, and the direction of force generation is not as strictly defined as in muscle cells. Non-muscle cells appear to have retained the means to exert both spatial and temporal control over the dynamical forming of

three-dimensional contractile actin networks (reviewed by Pollard in 1986(a) and Stossel 1993).

Unpolymerised non-muscle cytosolic actin is mostly associated with actin binding proteins (reviewed by Vandekerckhove 1990, Pollard et al. 1994, McLaughlin and Weeds 1995), e.g. Actin Depolymerising Factor ADF (Hayden et al. 1993), thymosin β_4 (Yu et al. 1993), or profilin (Goldschmidt-Clermont et al. 1991, Korenbaum et al. 1998), and contains a tightly bound adenosine nucleotide (Kuehl and Gergely 1969) with one Ca^{2+} or Mg^{2+} (Selden et al. 1987, Kinosian et al. 1993, Rosenblatt et al. 1995). Removal of the nucleotide results in rapid denaturation of actin although high concentrations of sucrose or glycerol can prevent irreversible denaturation and even stabilise nucleotide-free actin (De La Cruz and Pollard 1995)

The location, extent, polarity, and timing of filament assembly is regulated by a large number of actin binding proteins (Schafer and Cooper 1995, Barkalow et al. 1996, Moldovan et al. 1997). Assembled filaments are organised into different three-dimensional structures by a further group of actin binding proteins, that can cross-link, cap and bundle filaments and also attach actin filaments to membranes, often via transmembrane solute transporters, adhesion- or signal-receptors (Yang and Fuchs 1996, Rybakova et al. 1996, Rivero et al. 1996). Most actin structures are highly dynamic in non-muscle and the rates and patterns of actin subunit incorporation differ in different regions of the cytoplasm (Okabe and Hirokawa 1989).

In general there are at least three characteristic levels of organisation of actin filaments. Firstly, actin filaments are arranged in anti-parallel arrays as in muscle myofibrils and in stress fibres of substrate adherent cells in tissue cultures (Trotter et al. 1978). Secondly, uniform parallel arrays form dynamic protrusive structures at the cell surface, e.g. microspikes and filopodia (Albrecht-Buehler and Lancaster 1976). Thirdly, isotropic arrays of actin filaments are found underlying the plasma

membrane of most eukaryotic cells, attached via actin binding proteins to transmembrane proteins in the bilayer (Clarke et al. 1975, Lauweryns et al. 1975).

Actin structures appear to contribute to two aspects of motility characteristic of eukaryotic cells. The first requires actin filaments to be arranged to form tracks along which myosin molecules can generate force in an appropriate direction. This is determined by the polarity of the actin filament, since the myosins move from the pointed to the barbed end. Examples are the contractile action in muscle tissue and the movement of membranes relative to the actin filaments (Stossel and Hartwig 1976, Kuznetsov et al. 1992). The latter presumably contributes to the movement of cellular organelles along actin filaments and of the leading lamellipodium of monocellular organisms over substrates. Also the contraction of the collar that forms between daughter cells during cytokinesis and the morphogenic movements during development and clot reaction by platelets are performed by myosin based motility (Sanger and Sanger 1980).

The second form of motility together with changes of cell shape is generated by induced changes in the structure of cross-linked actin filament gels and by polymerisation against a surface (Wang 1977, Yin and Stossel 1979). Swelling and shrinkage of actin gels can be induced by selective breakage or formation of crosslinks, thereby releasing or storing osmotic energy. On the other hand, polymerisation may progressively consolidate space under a membrane formed as a result of random thermal movement or by pumping of ions to induce local influx of water. Ruffling of leading lamellipodia , phagocytosis and shape changes of cells may include such mechanisms of motility. The complex process of cell locomotion clearly involves aspects of both polymerisation driven protrusion and myosin based motility (reviewed by Stossel 1993).

Apart from its involvement in cellular motility the actin cytoskeleton serves as matrix, where cytoplasmic proteins can be immobilised, e.g. certain glycolytic enzymes (Westrin and Backman 1983) and ribosomes (Hesketh 1991), and which

interacts with other polymer systems of the cytoskeleton, e.g. microtubules (Griffith and Pollard 1982) and intermediate filaments (Yang and Fuchs 1996).

1.1.2 Relationships within the actin family

The protein sequences of the eukaryotic actin family are highly conserved. Over 160 actin sequences from sources as diverse as yeasts, plants, Drosophila, Tetrahymena, and sea urchin have been described (Vandekerckhove 1993). Mammals and birds express six distinct isoforms solely in a tissue specific manner and independently of the species. Two striated muscle actins (skeletal and cardiac), two smooth muscle actins (vascular and visceral), and two co-expressed non-muscle actins have been identified (Vandekerckhove and Weber 1979). Isoelectric focusing separated these isoforms into three isoelectric variants, referred to as α-, β-, and γ-actin (Whalen et al. 1976).

The general high conservation of actin sequences means that, unlike the situation in many other protein families, it is difficult to identify important sites on the protein by simply seeking those regions with the most conserved sequences. Conversely, regions of sequence variation may identify sequences which either have no specific function and only serve as linker regions or which are important for the functions of specific isoforms.

1.1.3 Actin polymerisation

F-actin is a non-covalent polymer that assembles spontaneously *in vitro* under ionic conditions similar those believed to exist in cells, i. e. 50-100mM KCl, pH 7, and 1mM free Mg^{2+}. Under these conditions actin will polymerise, if its concentration is

0.1μM or higher. This threshold concentration is often termed "critical concentration" (Wegner and Engel 1975). In cells spontaneous polymerisation is inhibited by monomer-sequestering proteins bound to G-actin (McLeod et al. 1989). *In vitro* the critical concentration can be increased, if the ionic strength of the buffer is lowered or Mg^{2+} is substituted with Ca^{2+}. Addition and release of monomers occurs on both ends of the growing filament, but due to the kinetics of actin polymerisation (Pollard 1986 (b)), filament growth is essentially unidirectional and overall elongation occurs at the barbed end (Kondo and Ishiwata 1976).

Actin polymerisation is accompanied by conformational changes (Frieden and Patane 1985, Holmes et al. 1990, Shu et al. 1992, Orlova and Egelman 1992) and the stoichiometric hydrolysis of bound ATP (reviewed by Carlier 1990). Under physiological conditions each actin monomer binds one molecule of Mg^{2+}-ATP at a high affinity site between the major domains. The hydrolysis step takes place after the monomer has added to the filament, since G-actin does not exhibit ATPase activity. Comparison between the rate of addition of subunits and the rate of ATP hydrolysis in a population of rapidly assembling filaments, shows that the ATP hydrolysis lags behind filament growth (Pollard and Weeds 1984). The immediate product is necessarily an actin unit carrying ADP and Pi in the filament. The release of phosphate is slower than ATP hydrolysis. Thus a filament, which started from ATP-G-actin, will first be composed of ATP-actin towards the barbed end and ADP-Pi-actin towards the pointed end. As the filament elongates, the fraction of ADP-actin at the pointed end will increase, whereas the fraction of ATP-actin at the barbed end will rapidly decrease and the fraction of ADP-Pi-actin will slowly decrease (reviewed by Carlier 1991).

At steady state, where the rate of monomer addition equals the rate of monomer dissociation, the filament will be composed of ADP-actin, with ADP-Pi-actin units towards the barbed end and a small cap of ATP-actin at the barbed end (reviewed by Carlier, 1991). There will be net loss of monomers at the pointed and net gain at the barbed end. Effectively, monomers are therefore shuttled across the filament from the

barbed to the pointed end. This process is called "treadmilling" and its overall rate is determined by the slowest step in the process, which is the release of ADP-actin at the pointed end (Kirschner 1980).

ATP hydrolysis is not essential for polymerisation but the critical concentration is higher and the rate and extent of polymerisation is lower when only ADP-actin is used *in vitro* (Lal et al. 1984, Pollard 1984, Pollard and Schwarz 1992).

1.1.4 The structure of G- and F-actin

The F-actin structure was determined by electron-microscopy and by fitting an atomic model based on the ADP-actin monomer to the X-ray diffraction pattern obtained from an orientated F-actin gel in capillary tubes (Holmes et al. 1990). The diameter of the filament is 9-10nm and it can be described either as a single-start left handed helix with a pitch of 36nm and 13 monomers or a two-start right handed double helix with a half pitch of 36nm. The latter model seems more appropriate, especially since the contacts along the long pitch strand appear stronger than across.

The atomic structure of the actin monomer (Figure 1.1) has been elucidated by X-ray crystallographic analysis. Four complexes of actin with three actin-binding proteins (Figure 1.3) have been crystallised and their structure determined: rabbit skeletal muscle actin:bovine DNaseI (Kabsch et al. 1990), rabbit skeletal muscle actin:gelsolin segment 1 (McLaughlin et al. 1993), bovine β-actin (tight state):bovine profilin (Schutt et al. 1993), and bovine β-actin (open state):bovine profilin (Chik et al. 1996).

From examination of the 3D structure (Figure 1.1) it can be seen that the shape of the actin molecule approximates to a thick slice of a cube 55x55x35Å. The single chain is folded into the major domains I and II (Table 1.1) which are of approximately

equal size and are connected by two strands termed the "hinge". Between the two domains is a cleft where the adenine nucleotide binds. The similarity of the two domains suggests that the gene was formed by duplication. The fold of the whole molecule is remarkably similar to those of the glycolytic enzyme hexokinase and the ATP-binding domain of the heat shock cognate protein HSC-70, thus raising the possibility that all three have a common ancestor, although their sequences are quite different except for the residues contacting the adenine nucleotide in the cleft.

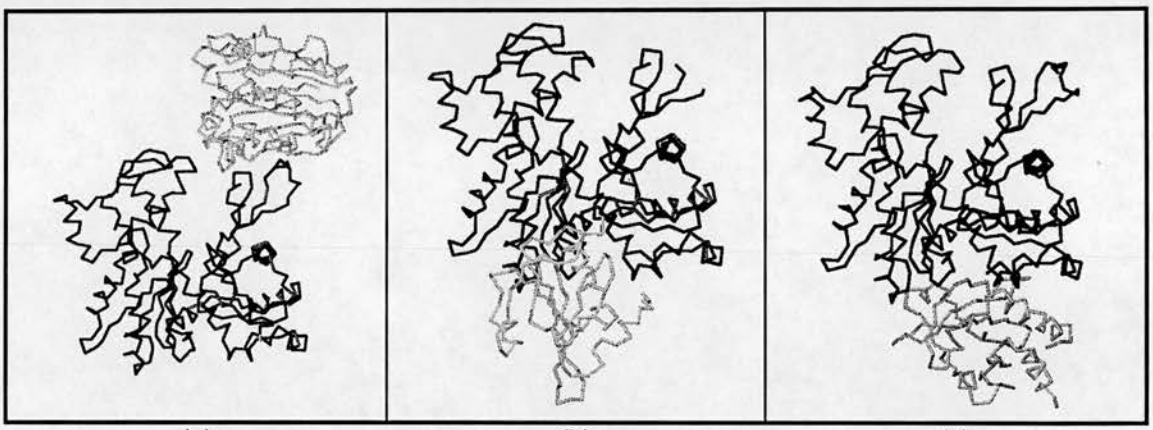

(a) (b) (c)

Figure 1.3: Actin crystal structures. The Cα-trace of actin is drawn in black and the Cα-trace of the respective binding protein in grey. Actin subdomain 1 is at the bottom right and subdomain 4 at the top left. (a) α-actin:DNaseI (Kabsch et al. 1990). (b) α-actin:gelsolin segment 1 (McLaughlin et al. 1993). (c) tight-state β-actin:profilin (Schutt et al. 1993).

Major domain I:	
residue 6-30, 74-137, 336-375	subdomain 1
residue 31-73	subdomain 2
Major domain II:	
residue 138-182, 264-335	subdomain 3
residue 183-263	subdomain 4

Table 1.1: Domains of actin.

Each of the two major domains can be further divided into two subdomains (Table 1.1). The barbed end of the molecule corresponds to the narrow side spanning both major domains below the hinge, the pointed end to the narrow side opposite the barbed end (subdomains 2 and 4).

Both the N- and the C-terminus are located in subdomain 1. Starting from the N-terminus the chain loops through subdomain 1 and then moves on to subdomain 2, which is composed of three anti-parallel β-sheets, a short α-helix, and the DNaseI binding loop. The chain then re-enters subdomain 1, where it forms a helix-strand-helix-strand motif followed by a β-sheet. An α-helix then connects the major domains I and II by running from the "back" of the molecule (Figure 1.1) to the front of subdomain 3. The chain then rises "upwards" to the nucleotide binding site and continues to travel "down" to the "bottom" of subdomain 3 only to immediately rise "upwards" again to form subdomain 4 with four α-helices connected by loops and two short β-sheets. After completing subdomain 4 the chain forms the rest of subdomain 3 with three helices connected by loops and two short β-sheets. It then crosses over to the major domain I, again beneath the nucleotide binding cleft, to the start of an α-helix of subdomain 1. A loop/helix region follows at the "bottom" of subdomain 1 to end in the C-terminus at the "back" of the molecule and at the cleft between subdomain 1 and 3.

The structure of ADP-actin was obtained from DNaseI:ATP-actin crystals, which had aged to a point where the bound ATP had completely auto-hydrolysed (Kabsch et al., 1990). A comparison with the ATP-actin structure gave virtually no differences apart from the missing phosphate. A comparison of the α-actin in complex with DNase1 with β-actin in complex with profilin showed the two halves of the actin molecule in the latter complex to be displaced by 5°. Using the structure of ADP-actin obtained form the complex with DNaseI, fibre X-ray diffraction data, and frozen-hydrated images of actin, the actin filament was convincingly modelled by Holmes et al. (1990).

1.1.5 Gelsolin

The gelsolin family of actin binding proteins occurs widely, from lower eukaryotes to mammals (Weeds and Maciver 1993). They bind to the barbed end of F-actin and are activated by calcium ions. Most of them are also able to sever actin filaments in addition to blocking the barbed end. All consist of three- or six-fold repeats of a segment, which is made up of approximately 150 amino-acids and is highly conserved (Way and Weeds 1988, Matsudaira and Janmey 1988).

Gelsolin was initially characterised as a macrophage cytoplasmic protein, which effects gel-sol transition of the actin cytoskeleton on activation by Ca^{2+} ions (Yin and Stossel 1979, Yin 1988, Grazi et al. 1991). It is expressed in humans as an 80.5kD cytoplasmic form mostly in non-muscle and smooth muscle cells (Hartwig et al. 1989, Dabrowska et al. 1996) and as an 83.0kD secreted blood plasma form with an N-terminal 25 amino acid leader sequence (Yin and Stossel 1979). A mutated form of gelsolin is responsible for familial amyloidosis Finnish type, where a single amino-acid, Asp187, is changed to Asn, resulting in a vulnerability to proteolytic cleavage of gelsolin, and subsequent deposition of fragments in amyloid plaques leading to hyper-elastic skin and facial muscle weakness (Maury 1991, Maury and Nurmiaho-Lassila 1992, Weeds et al. 1993, Maury et al. 1994).

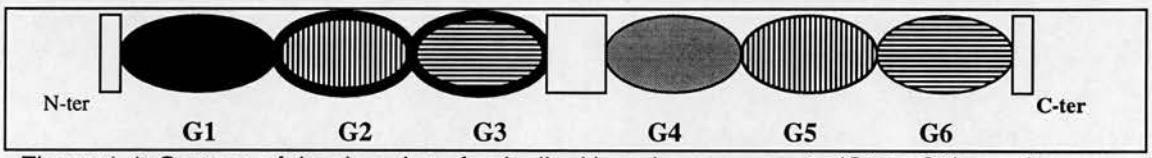

Figure 1.4: Cartoon of the domains of gelsolin. Homologous repeats (G1 to G6) are drawn as ellipses. G1 contains high-affinity monomer binding site, G2 contains filament binding site, and G4-G6 contain weak Ca^{2+}-dependent monomer binding sites. Calcium ion binding sites have been localised to one in G2-G3 and one in G4-G6.

The sequence of gelsolin is a six-fold repeat (Figure 1.4) of a well conserved sequence motif (Way and Weeds 1988). Three actin binding sites (Bryan 1988) and two high-affinity Ca^{2+}-binding sites (Yin and Stossel 1980) have been identified. When activated by calcium, gelsolin binds to two actin molecules at their barbed

ends. Complex formation proceeds more rapidly with ADP-actin than with ATP-actin (Coué and Korn 1986). Removing Ca^{2+} with EGTA dissociates one actin molecule from the ternary complex, leaving one actin molecule bound to gelsolin (Bryan and Kurth 1984). In this binary complex, gelsolin promotes the ATPase activity of bound actin and also inhibits nucleotide exchange (Tellam 1986, Bryan 1988). Phosphatidylinositol-4,5-bisphosphate molecules inhibit the severing activity and dissociate gelsolin from the barbed end of filaments (Hiyoshi et al. 1989, Janmey and Stossel 1989). In addition there is evidence that the type of nucleotide bound to actin affects the binding of actin to gelsolin (Laham et al. 1993).

Segment 1 (G1) binds with high affinity and independently from calcium to an actin monomer (Way et al. 1989). Segment 2 (G2) binds to F-actin independently of calcium, whereas segment 4 binds an actin monomer calcium-dependently and with lower affinity than G1 (Pope et al. 1991). G5 and G6 are implicated in the Ca^{2+}-dependent regulation of actin-binding by gelsolin (Pope et al. 1995). Removal of Ca^{2+} from solution via EGTA causes one actin monomer bound to G4-G6 to dissociate, but only the presence of polyphosphoinositides will release the actin monomer bound to G1 (Bryan and Kurth 1984). The first two segments are the minimum unit required for severing and capping and contain two putative PIP_2 binding sites (Yu et al. 1992). Gelsolin mutants lacking segment 1 decorate actin filaments, but do not sever them, while gelsolin mutants without segment 2 do not bind to F-actin (Way et al. 1989).

Mutagenesis experiments have identified two PIP_2 binding sites, one near the N-terminus of segment 2, the other near the C-terminus of segment 1 (Weeds et al., 1993). The ability of gelsolin to block the barbed end of both ATP- and ADP-F-actin has been used to study kinetic parameters associated with the pointed end of filaments assembled from ADP-G-actin (Coue and Korn 1986). *In vivo* it is likely that the action of gelsolin has to be supported by other actin binding proteins, since high concentrations of macromolecules, as exist in the cytoplasm, reduce gelsolin activity (Grazi et al. 1991).

The crystal structure of inactived Ca^{2+}-free horse plasma gelsolin was determined by Burtnick et al. (1997) confirming the anticipated structural similarity between the individual segments. In its inactivated form gelsolin is packed together in a compact globular structure where actin binding to the site on G1 (McLaughlin et al. 1993) is obstructed by G3.

1.1.6 Binding of gelsolin segment 1 to actin

The structure of segment 1 was determined in complex with G-actin by X-ray crystallography (McLaughlin et al. 1993). It forms a globular domain of 13x26x25Å and comprises residues 25 to 149 of plasma gelsolin. Interestingly, conserved residues present in all members of the gelsolin family contribute to the apolar core of the molecule but do not play a role at the actin binding site. On the other hand, actin amino acids contacting gelsolin segment 1 are well conserved among actin isoforms and even across different species. Conservation of amino acids in the gelsolin family can probably be attributed to the selective evolutionary pressure to maintain the close-packed apolar core of the gelsolin segments.

Gelsolin segment 1 binds actin at a cleft formed by the actin subdomains 1 and 3 at the barbed end. The binding site on both molecules can be described as an apolar patch surrounded by a ring of polar atoms. Two Ca^{2+} ions were found in the complex. The intermolecular Ca^{2+} is complexed by residues from both actin and segment 1, the intramolecular Ca^{2+} is exclusively bound to segment 1.

Knowledge related to the protein structures and the detailed interaction of residues comes from protein crystal X-ray diffraction analysis. This method is a most valuable tool in elucidating mechanisms of protein action and was chosen in this thesis for investigations of protein structure and interaction.

1.2 Protein X-ray crystallography

1.2.1 The usefulness of X-ray diffraction analysis for structure determinations

The geometry of a molecule can be determined in atomic detail by analysing the X-ray diffraction patterns obtained from a crystal of these molecules. The wavelength of X-rays is of the order of the distances between atoms, approximately one Ångström (1Å) or 10^{-10} metres. This is why this particular range of the electro-magnetic spectrum is used. The disadvantage of this method is that, unlike visible light, X-rays cannot be focused by a lens as in an optical microscope. To "visualise" molecules X-rays diffracted by a crystal have to be recorded and diffraction patterns combined by mathematical methods. Every individual molecule diffracts X-rays and the regularly repeating internal structure of a crystal causes reinforcement of the diffraction effect making it readily measurable.

1.2.2 Crystallisation of proteins

For obvious reasons one would ideally wish for crystals to be absolutely perfect in terms of their internal order as described above. In practice crystals, especially of proteins, are of varying quality which limits the information gained by analysing X-ray diffraction patterns.

Crystal growth is dependent on the thermodynamically driven solubility of the compound and the kinetically driven events of nucleation and addition of free compounds to crystals and crystal nuclei. The first stage in crystal formation is nucleation induced by conditions such as precipitation from supersaturated solutions or temperature gradients. Proteins are usually crystallised by slowly increasing the concentration of a precipitating compound (the precipitant), until supersaturation is reached and crystal nuclei form. Protein molecules then condense in an ordered

manner on the nuclei until an equilibrium is reached between the solid protein phase and the protein in solution.

A complete theory on the effects of temperature, buffer composition, pH, and vapour pressure on crystal nucleation, growth, and internal order has not yet been put forward, but the crystallographer can draw from a wealth of practical experience and treatises on certain aspects of crystallisation (Gilman 1963; Strickland-Constable 1968, Feher and Kam 1985, McPherson 1985, DeLucas et al. 1986). A recent survey of the knowledge on macromolecular crystallisation can be found in the publications included in Macromolecular Crystallography, Part A, Methods in Enzymology, Volume 276 (1997).

The most common methods used for protein crystallisation are based on vapour diffusion and dialysis (solvent gradients). The concept behind vapour diffusion techniques, such as crystallisation by hanging drop or by sitting drop, is that a tiny amount (e.g. 1-20µl) of liquid containing the protein is mixed with an equal volume of crystallisation buffer and placed separate from a much larger volume (e.g. 1ml) of crystallisation buffer reservoir in a small sealed environment (e.g. $3cm^3$). The crystallisation buffer has a far greater salt and/or precipitant content than the initial protein containing liquid. The mixed drop containing the protein in the closed environment will have a water content almost double that in the buffer reservoir. Equilibration will occur via water evaporation from the drop and condensation on the reservoir. This leads to a gradual concentration of the precipitant in the drop until equilibrium is reached between drop and reservoir. If the conditions are right, then the protein will have reached supersaturation and will have formed crystal nuclei before the water content is equilibrated. Crystals will grow by protein adding on to the nuclei until a state of equilibrium has been attained between the solid phase and the solution.

When crystallising by dialysis, a solution containing the protein and precipitant at lower concentration is dialysed against a higher concentrated crystallisation buffer

separated by a semi-permeable membrane. Along the concentration gradient nuclei will form and initiate crystallisation growth.

Both the vapour diffusion and the dialysis technique can be used to initialise crystallisation via organic precipitants (e.g. polyethylene glycol), inorganic precipitants (e.g. ammonium sulfate), or pH variation. To employ pH variation with vapour diffusion it is necessary to choose a volatile acid or base to achieve pH equilibrium in the closed system (McPherson 1976).

It is desirable to find the conditions which result in the formation of a minimum number of nuclei. If too many nuclei form too quickly then the result will be a "shower" of tiny crystals, too small for X-ray diffraction analysis. In the worst case the protein will precipitate so quickly that ordered association is not possible. Precipitation in the form of "clouds" of aggregated protein is the result. To little precipitant will obviously lead to neither crystallisation nor precipitation. This borderline between still keeping all of the protein soluble and precipitation can be very fine indeed.

Crystals larger than 0.1 mm are usually of the size desired for X-ray diffraction analysis. But even these crystals might not be sufficient for the purpose. Satellite crystals can grow on the surface of growing crystals, having been nucleated on a surface and growing with their lattice in a different orientation to the parent crystal. Even single crystals do not usually have a crystal lattice of absolute order. Crystals have to be regarded as being composed of tiny *mosaic blocks* whose lattice is orientated slightly differently than the surrounding mosaic blocks. These slight misorientations of the blocks cause the *mosaicity* of a crystal examined in the X-ray beam. At larger values of mosaicity analysis of diffraction spots becomes more difficult or impossible altogether. When the misorientations of the mosaic blocks increases, the reinforcing effect from the repeated lattice on the diffracted X-rays is more and more reduced until no diffraction is observed even though the crystal might appear undamaged.

1.2.3 Crystal structure

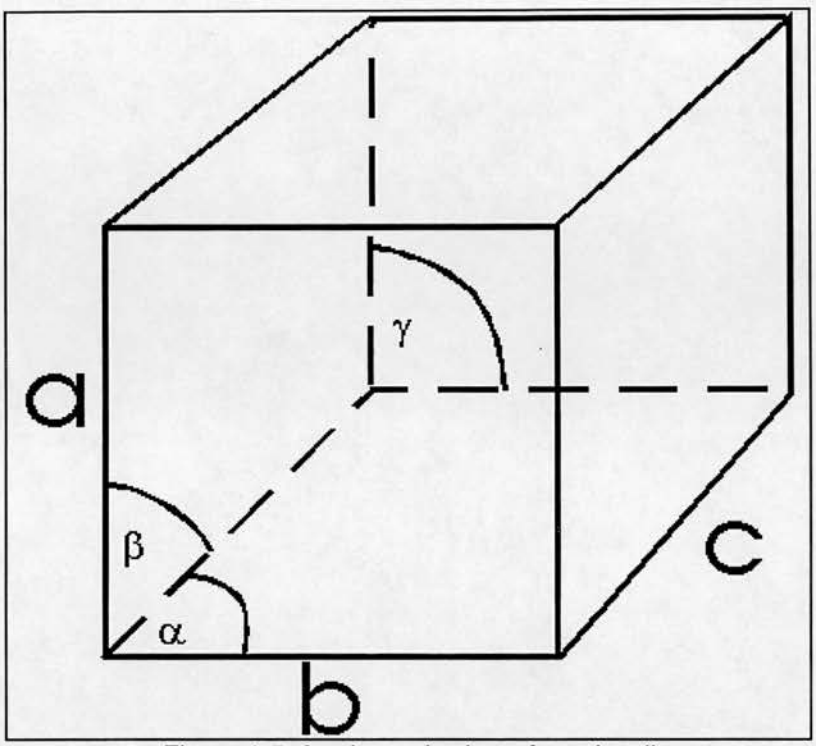

Figure 1.5: A schematic view of a unit cell

Crystals are defined as solids with a regular repeated internal arrangement of atoms contained in a *unit cell* (Figure 1.5). The *unit cell* is a box defined by its axes (width, height and length) and the three interaxial angles. Usually the longest axis is called *c* and the shortest *a*. The angle α is defined as the angle between *b* and *c*, β as the angle between *a* and *c*, and γ as the angle between *a* and *b*.

The *crystal lattice* describes the repeated translations of unit cells in all dimensions to form the crystal. It is described by replacing each unit cell with a lattice point, disregarding the actual atomic content of the unit cell. Another way to consider the crystal lattice is to see it as three intersecting sets of parallel planes. The three sets of planes can simply be defined by the *Miller indices h k l*. The number of times a set of parallel planes intersects unit cell axis *a* is the value of *h*. The value of *k* is the number of times this same set intersects *b*, and *l* is the number of times it intersect *c*.

The three sets of planes describing the crystal lattice are therefore (1 0 0), (0 1 0), and (0 0 1).

The crystal structure can also be described in terms of *symmetry*. The *asymmetric unit* (ASU) is the smallest collection of atoms of a crystal structure from which the complete structure can be derived, first by use of *point group symmetry operations*, then by translational symmetry operations. *Point groups* are sets of *symmetry elements* which leave at least one point of the object, which they are applied to, unmoved. Examples are rotation axis, inversion centres, and mirror planes, which pass through or lie within the object.

It was shown that there are only 32 unique point groups in respect to the symmetry classes of crystals (Hessel 1830). The combinations of translations and point groups, excluding those combinations which result in purely integral lattice translations, are called the *space groups*. For crystal lattices there exist 230 space groups which convert an asymmetric unit into an infinitely extending three-dimensional pattern. A comprehensive list and description is published in the International Tables of Crystallography by the International Union of Crystallography (1987). In the case of protein crystals the number of possible space groups is only 65 because amino acids contain at least one asymmetric centre (the Cα atom) which precludes the use of inversion symmetry operations.

The entire arrangement of atoms in a crystal can be described in terms of unit cell dimensions, the co-ordinates of each atom in the asymmetric unit, and the space group symmetry. Space groups are designated by the Hermann-Mauguin symbols (Bragg et al. 1935) starting with a letter (P, A, B, C, F, I, or R) indicating the type of lattice symmetry (Figure 1.6, Table 1.2). Then follows a set of characters describing the various symmetry elements. Rotation axis are symbolised by number which is the number of rotations needed to bring the object back to the original position, e.g. 3 for 3-fold rotation axis. Screw axis are represented by their rotation number and the number of times the object is translated along a unit cell edge to be taken to the

equivalent starting position in the following unit cell, e.g. 2_1 for a two-fold screw axis. A very common space group for protein crystals is $P2_12_12_1$. It creates a primitive lattice symmetry and defines the unit cell shape as orthorhombic with all angles (α, β, γ) at 90° but without constraining the length of the unit cell edges *a, b,* and *c*.

Lattice symmetry	Description
P	primitive
A	face-centred on (100) planes
B	face-centred on (010) planes
C	face-centred on (001) planes
F	all face-centred
I	body (inner) centred
R	primitive trigonal crystal system

Table 1.2: Description of lattice symmetry symbols. (xxx) defines a set of planes according to their Miller indices.

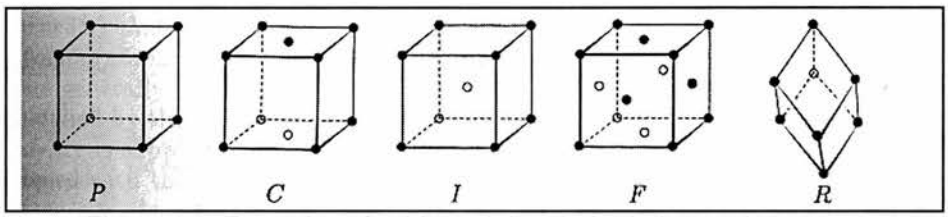

Figure 1.6: Examples of cubic and rhombohedral crystal systems.

The symmetry operators of each space group can be found in the International Tables of Crystallography. They describe how to create an infinite crystal lattice starting with the knowledge of the co-ordinates of the asymmetric unit and of the space group. Usually these symmetry operators are represented as a triplet of operations, one for each of the x, y, and z co-ordinates for each atom.

For example applying the symmetry operator 1/2-x,-y,1/2+z to the orthogonal co-ordinates of the atoms in the asymmetric unit results in the following new orthogonal atom co-ordinates:

new x co-ordinate = (unit cell length of a) * 0.5 - (original x co-ordinate)

new y co-ordinate = (original y co-ordinate) * -1

new z co-ordinate = (unit cell length of c) * 0.5 + (original z co-ordinate).

Obviously these calculations are more conveniently performed using fractional co-ordinates based on the unit cell axis lengths.

1.2.4 X-ray diffraction

X-ray diffraction is akin to visible light being diffracted by small holes and slits. It is an interference effect between X-ray beams coherently scattered by the electrons surrounding atomic nuclei. This interference effect causes reinforcement to the point of observability of the diffracted X-rays if their path length difference is an integral multiple of their wavelength (Friedrich et al. 1912). A difference in path length occurs when X-rays are diffracted by parallel planes of the crystal lattice. This is equivalent to visual light reflected by semi-permeable mirrors stacked in parallel one after the other. To achieve maximum reinforcement of X-rays scattered by parallel planes, the plane separation, scattering angle of the scattered X-ray beams, and wavelength must be related as described by Bragg's Law (Bragg 1913):

$$n\lambda = 2d_{hkl}\sin\theta_{hkl}$$

n ..... integer number

λ ..... wavelength

d_{hkl} ..... separation of planes (hkl)

θ_{hkl} ..... scattering angle

A geometrical description (Figure 1.7) of relationships formulated by M. Laue and W.H. Bragg was composed by P.P. Ewald (1921). An X-ray diffraction pattern from a crystal recorded on a flat detector surface appears as a pattern of dots. Each dot records the impact of an X-ray which was diffracted by the set of all parallel planes of a specific orientation in the crystal and causes diffraction at angle 2θ from the main incident beam. In a diffraction experiment the undiffracted beam is usually prevented from reaching the detector because it is much more intense than diffracted beams.

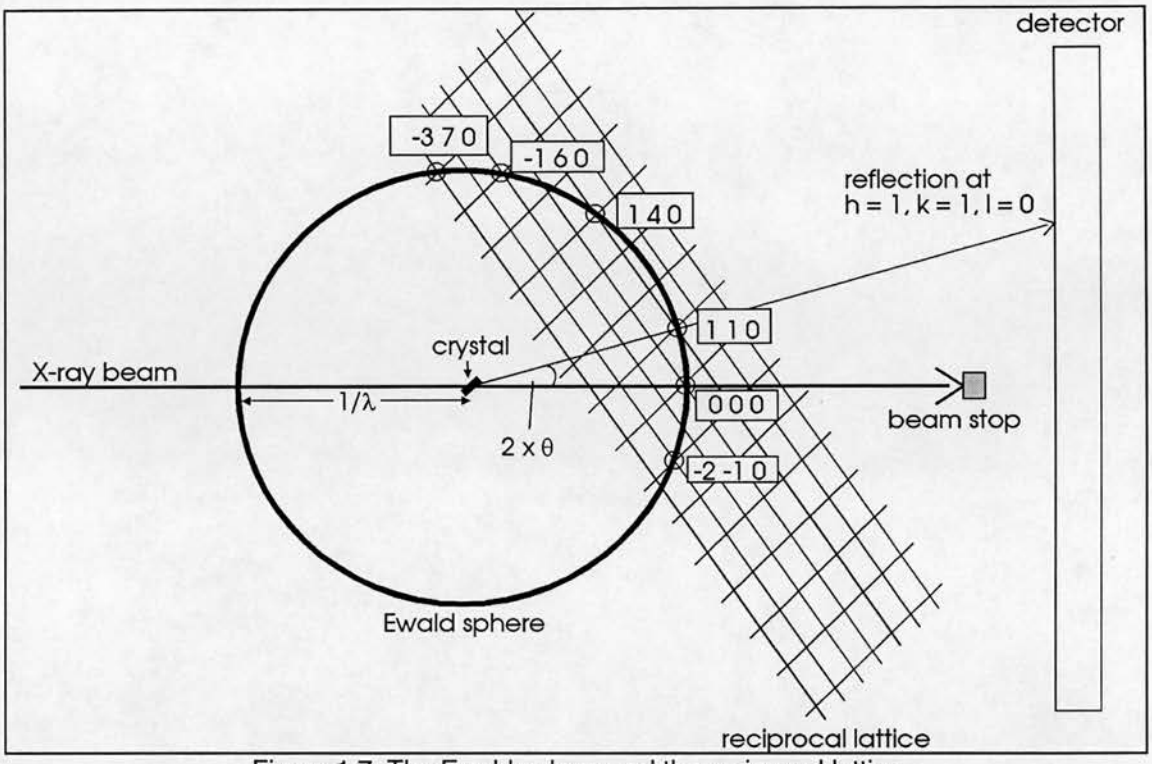

Figure 1.7: The Ewald sphere and the reciprocal lattice

In terms of P.P. Ewald's geometric description, the detector will only record those X-rays which were diffracted by a set of planes (hkl) whose representation as a lattice point in the *reciprocal lattice* falls on the circumference of the Ewald sphere with the origin (h=0, k=0, l=0) of the *reciprocal lattice* set on the intersection of the undiffracted beam with the circumference of the Ewald sphere. Rotating the crystal in the X-ray beam around an axis perpendicular to the X-ray beam causes the reciprocal lattice to rotate around its origin and allows other reciprocal lattice points to fall on the circumference of the Ewald sphere thus making the diffraction by other sets of parallel planes recordable.

The reciprocal lattice is solely influenced by the dimensions of the unit cell and the space group. The distances between spots on the same gridline are inversely proportional to the length of the respective unit cell axis. Conventionally h is associated with *a*, k with *b*, and l with *c*. In the case of an orthorhombic unit cell,

where all axis are at right angles to each other, the diffraction spots will also lie on a grid with all axis at right angles. If the distance between crystal and detector is many times longer than the spot separation, the separation between two spots along one of the grid lines can be related to the unit cell axis by:

$$x = 1/d_{hkl} = \lambda * L / R$$

x .....one of the unit cell axis a, b, or c.

d_{hkl}.....separation of parallel planes (in this particular case the planes defining the crystal lattice)

λ.....wavelength

L.....distance between crystal and detector

R.....separation of two adjacent spots on the same gridline measured on the detector

The space group of the crystal structure can cause *systematic absences* to occur in the diffraction pattern. The translational component of the symmetry elements causes selective and predictable destructive interference which leads to the "extinction" of certain reflections. An analysis of these extinctions will reveal the spacegroup involved, although sometimes two or more spacegroups fit the analysis giving rise to *spacegroup ambiguity.*

The initial analysis of the X-ray diffraction pattern of a crystal will therefore reveal information on the unit cell parameters and the spacegroup. To obtain information on the content of the asymmetric unit, an analysis of the intensity distribution of as many unique reflections as possible is required.

1.2.5 Analysis of X-ray diffraction data

A.B. Porter (1906) showed that the diffracting action of a grid on visual light can be interpreted as a Fourier analysis. An optical lens can recombine the diffracted beams to form an image which is equivalent to performing a Fourier synthesis of the diffracted visual light beams passing through the lens.

The wavelengths of visual light are not short enough to resolve distances at atomic level and lens systems cannot bend diffracted X-ray beams to practically reform the image of the electron density around the atoms in the crystal which caused the X-ray diffraction. But the crystal lattice is a three-dimensional diffraction grid like those used to cause diffraction of visual light, only at much smaller level. In analogy the studies of Porter show how the spots caused by the X-ray diffraction of a crystal can give the amplitude components of a Fourier series representing the electron density ρ:

$$\rho\,(xyz) = 1/V * \Sigma_h \Sigma_k \Sigma_l [\, |F(hkl)| e^{i\alpha_{hkl}} e^{-2\pi i(hx + ky + lz)} \,]$$

V ..... unit cell volume

x,y,z ..... real space co-ordinates

h,k,l ..... reciprocal space co-ordinates of the Bragg reflection at h,k,l

|F(hkl)|..... *structure factor amplitude*, i.e. amplitude of the scattered X-ray beam causing reflection at h,k,l

α_{hkl} ..... relative phase angle of the scattered X-ray beam causing reflection at h,k,l, if an imaginary wave scattered from a corner of the unit cell has a phase angle of 0.

If the positions of all atoms in the unit cell are known, e.g. from a model structure and the asymmetric unit content and spacegroup is known, then the structure factor amplitudes |Fc(hkl)| and the corresponding phase angle α_{hkl} can be calculated:

$$|Fc(hkl)| = ((\Sigma_j[f_j * \cos 2\pi(hx_j+ky_j+lz_j)])^2 + (\Sigma_j[f_j * \sin 2\pi(hx_j+ky_j+lz_j)])^2)^{-1/2}$$

$$\alpha_{hkl} = \tan^{-1}[\Sigma_j[f_j * \sin 2\pi(hx_j+ky_j+lz_j)] / \Sigma_j[f_j * \cos 2\pi(hx_j+ky_j+lz_j)]]$$

f_j is the atomic scattering factor which gives the scattering power of an atom of an element j relative to the scattering power of a single electron modified by a factor describing the disorder or vibration the atom experiences in the crystal structure.

$$f_j = f_{j0} * e^{-B_j(\sin^2\theta/\lambda)}$$

f_{j0} ..... atomic scattering factor for a stationary atom j

λ ..... wavelength

θ ..... scattering angle

$B_j = 8\pi^2\langle u^2\rangle$ ..... the displacement paramenter (B-factor)

$\langle u^2\rangle$ ..... isotropic mean square amplitude of atomic vibration

In analogy to the way the amplitude of an electro-magnetic wave is described, the amplitude (*structure factor*) F_{hkl} of a diffracted X-ray can be described as:

$$F_{hkl} = |F(hkl)| * e^{i\alpha_{hkl}} , i = (-1)^{1/2}$$

Once as many reflections as possible of the three-dimensional reciprocal lattice have been measured, e.g. using the rotation method (see Chapter 2: Methods), and their hkl-indices determined, an average for symmetry related reflections and a standard deviation σ including an estimation for the instrument uncertainty is calculated. The quality of the data set is often assessed using R_{sym}:

$$R_{sym} = \Sigma_{hkl}\Sigma_j|I_j(hkl) - \langle I(hkl)\rangle| / \Sigma_{hkl}\Sigma_j I_j(hkl)$$

$I_j(hkl)$ ..... jth symmetry related intensity of hkl

$\langle I(hkl)\rangle$ ..... mean of all symmetry related intensities at hkl

To convert the averaged intensities to structure factor amplitudes, they have to be corrected for X-ray background intensity, beam polarisation, time spent by the reciprocal lattice point in diffracting position resulting in a correction by applying the *Lorentz* factor, absorption effects, and radiation damage to the crystal. These corrections can be applied as a constant multiplier k to the intensities since the relation between intensities and structure factor amplitudes can be expressed as:

$$I(hkl) = k * |F(hkl)|^2$$

After scaling all $|F(hkl)|^2$ in respect to the scattering structure factor amplitude of a single electron, the results of the X-ray diffraction experiment can be presented as a table with columns h, k, l, $|F_{hkl}|$ or $|F_{hkl}|^2$, and $\sigma(|F_{hkl}|)$ or $\sigma(|F_{hkl}|^2)$.

The relative phase angle α_{hkl} cannot be directly obtained from the X-ray diffraction experiment but its important contribution to calculating the electron density function $\rho(x,y,z)$ requires that its value be estimated as accurately as possible. In protein crystallography the commonly used methods to estimate α_{hkl} *are multiple isomorphous replacement* (MIR), *multiwavelength anomalous diffraction* (MAD), and *molecular replacement* (MR).

1.2.6 Solving the phase problem

1.2.6.1 Multiple isomorphous replacement

In MIR heavy-atom derivatives are prepared by soaking the native crystals in a buffer containing a heavy-metal compound or by co-crystallising a protein with a heavy-metal compound. If binding of the heavy atom does not change the conformation of the protein, the native structure and the derivative structure are considered to be

isomorphous. The structure factors of the heavy-atom derivative (F_{PH}), of the native protein (F_P), and of the heavy-atom (F_H) are related by:

$$F_P = F_{PH} - F_H$$

The magnitudes of $|F_{PH}|$ and $|F_P|$ are obtained experimentally. Information on $|F_H|$ and α_H can be obtained due to the strong diffracting power of the heavy atom. To estimate F_H, a Patterson map P of the heavy-atom derivative is calculated:

$$P(uvw) = 1/V * \Sigma_h \Sigma_k \Sigma_l [\, ||F_{PH}| - |F_P||^2 * \cos 2\pi(hu + kv + lw) \,]$$

Since the calculation of this map does not include the phase angle, vectors drawn from the origin of the co-ordinate system (u, v, w) to peaks in the map represent distances between atoms within the unit cell. Vectors involving the heavy atom will dominate the map and enable an estimation of F_H. With $|F_{PH}|$, $|F_P|$, and F_H known, two solutions of the relative phase angle α_{hkl} can be obtained. The correct solution can be identified by using a second derivative with a heavy atom at a different position than in the first derivative.

Using the refined value of α_{hkl} together with $|F_P|$ an electron density map can be calculated and a protein chain fitted to the density. Further refinement allows the identification of amino acid side-chains in electron density if the resolution of the X-ray diffraction is sufficient.

1.2.6.2 Multi-wavelength anomalous diffraction

Friedel's Law (Friedel 1913) states that the intensity distribution in the diffraction pattern is centrosymmetric, even for non-centrosymmetric crystal structures. This holds true for atoms usually encountered in biological macromolecules, i.e. phosphorus and lighter atoms. Heavier atoms in non-centrosymmetric crystal

structures can cause observable *anomalous scattering* due to their interaction with X-rays. At energies of the X-rays just above an absorption edge of the heavy atom which would lead to excitement of an outer shell electron, the scattering of the X-ray becomes wavelength dependent. The effect on the diffraction pattern is that centro-symmetrically related Bragg reflections (*Friedel pairs*) display different intensities. Measurement of X-ray diffraction of heavy atom containing protein crystals at two or more different wavelengths near the absorption edge and knowledge of the position of the anomalous scatterer in the crystal structure allow estimation and refinement of the relative phase angle α_{hkl} and subsequently the calculation of electron density maps.

1.2.6.3 Molecular replacement

Sometimes a model of the majority of the protein atoms can be constructed which is sufficiently close to the structure under investigation for MR purposes. Examples for the application of MR are soaking of protein crystals with compounds expected to diffuse through the crystal to a binding site on the protein, or crystals of proteins with high sequence homology to structures previously determined.

The interatomic vectors which can be identified in the Patterson map

$$P(uvw) = 1/V * \Sigma_h \Sigma_k \Sigma_l [\, |F_{hkl}|^2 * \cos 2\pi(hu + kv + lw) \,]$$

do not allow a localisation of atoms in the unit cell but the shorter intramolecular vectors can be used to find all orientations of the model structure in the unit cell. When the spacegroup of the crystal is taken into account, the results of the *rotation search* can be narrowed down to the orientations to be found in the asymmetric unit.

Using only the longer interatomic vectors of the Patterson map the positions of the model in the unit cell can be identified in a *translation search*. The model atom co-ordinates thus obtained can then be used to calculate an electron density (Fo) map:

$$\rho^{Fo}(x,y,z) = 1/V * \Sigma_h \Sigma_k \Sigma_l [\ |Fo(hkl)|\ e^{i\alpha^c_{hkl}} e^{-2\pi i(hx + ky + lz)}\ ]$$

$|Fo(hkl)|$ ..... structure factor amplitudes calculated from the observed diffraction intensities

$\alpha^c_{hkl} = \tan^{-1}[\ \Sigma_j[f_j * \sin 2\pi(hx_j+ky_j+lz_j)] / \Sigma_j[f_j * \cos 2\pi(hx_j+ky_j+lz_j)]\ ]$

x_j,y_j,z_j ..... co-ordinates of model atom j

f_j ..... atomic scattering factor of model atom j

1.2.7 Refinement of the model for a protein crystal structure

This is the process of improving α^c_{hkl} and the parameters of a trial structure until the best fit of calculated structure factor amplitudes to those observed is obtained. The parameters refined are usually the atomic co-ordinates and the B-factors of the individual atoms. Because of the usually low observations-to-parameters ratio in protein X-ray diffraction analysis, appropriate terms have to be included in the refinement to prevent the refinement procedure from changing the models bond lengths, bond angles, dihedral angles, and atom distances to inappropriate values. These pre-defined restraints are derived from previous knowledge gained from small molecule structure analysis. The target function D, to be minimised in the commonly used *least-squares refinement*, is defined as:

$$D = \Sigma_j[w_{hkl}(\ |Fo(hkl)| - |Fc(hkl)|\ )^2] + D'$$

$|Fo(hkl)|$ ..... observed structure factor amplitude

$|Fc(hkl)|$ ..... calculated structure factor amplitude

$w_{hkl} = (\ \sigma^2(|Fo(hkl)|) + k|Fo(hkl)|^2\ )^{-1}$ ..... weight of a measurement

k ..... measure for the instrumental error

D' ..... an additional term based on the geometry of the model (distances, bonds, angles) with its individual components weighted according to restraints.

The measure most commonly used to monitor the progress of the refinement is the R_{cryst} which decreases as the fit of the model to the data improves. Refined final protein structures should display an R_{cryst} of 0.25 or less.

$$R_{cryst} = \Sigma_{hkl} \mid w_{hkl}|Fo(hkl)| - k|Fc(hkl)| \mid / \Sigma_{hkl}|Fo(hkl)|$$

w_{hkl} ..... weight

k..... scale factor

The R_{cryst} alone cannot indicate overfitting of a model to the diffraction data. To avoid overdetermination of the structure the cross-validation method of R_{free} (Brünger 1992) is commonly used. Usually 5-10% of the data are excluded from the refinement and a separate R factor (R_{free}) is calculated only for these data, the value of R_{free} being usually higher than the value for R_{cryst}. An increasing value for R_{free} despite a decreasing value for R_{cryst} during refinement is an indication of overfitting where parameters become linearly correlated.

During the refinement and at the end the model has to be visually compared to electron density maps because in some cases the refinement procedure will not optimally position atoms of the model due to entrapment in local minima or stringent restraints on the ability of the refinement procedure to move atoms. Electron density maps can be calculated as sigmaA weighted (Read 1986) difference maps:

$$\rho(xyz) = 1/V * \Sigma_h\Sigma_k\Sigma_l[(n*m|Fo(hkl)| - D|Fc(hkl)|) * e^{i\alpha c_{hkl}} e^{-2\pi i(hx + ky + lz)}]$$

n .....integer multiplier, value is 2 for 2Fo-Fc and 1 for Fo-Fc map

m.....figure of merit for the phase-probability distribution

D .....estimation for the co-ordinate error

SigmaA-weighting helps to remove the bias introduced into map calculations due to using phases calculated from a model. Fo-Fc maps are used to identify incorrect placements of model atoms and 2Fo-Fc maps are used to check the overall fit of the model.

1.3 The flexibility of the actin structure

1.3.1 Previous considerations

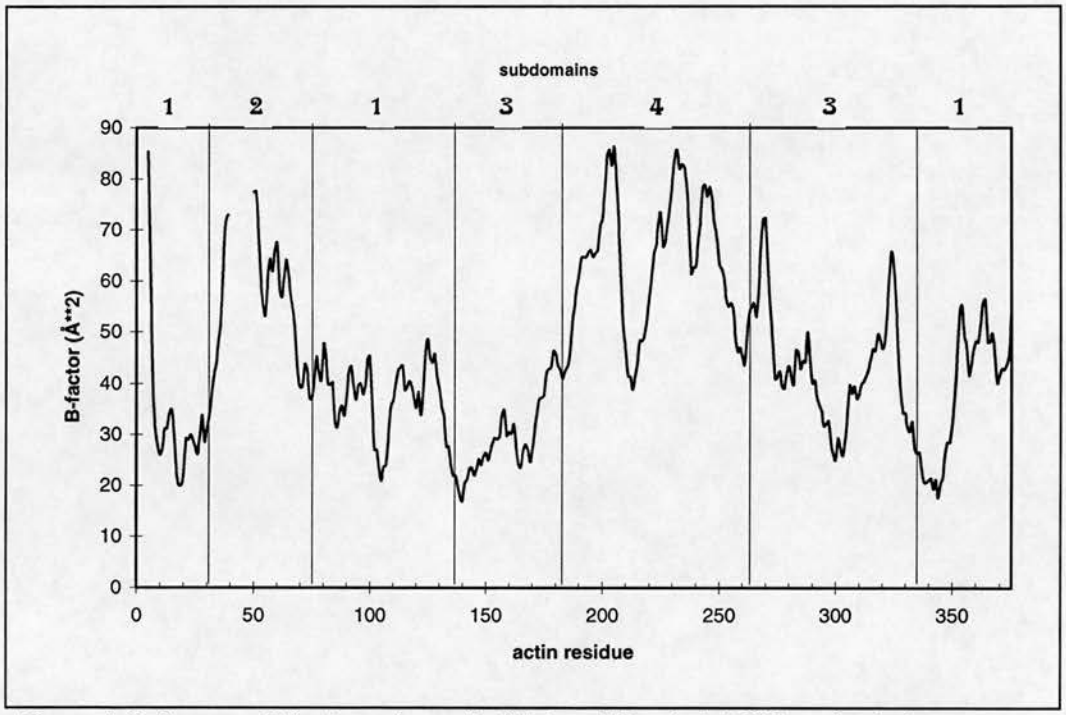

Figure 1.8: Average B-factors of α-actin (McLaughlin et al. 1993) main chain versus residue number. The distribution of residues over actin subdomains is indicated by vertical lines and the subdomain number. The picture was generated with MS EXCEL.

The conformations of the four available actin crystal structures show marked flexibility in defined regions of the main chain, which is evident from structural comparisons and the distribution of B-factors (Figure 1.8), and in the orientations of

subdomains to each other. The most flexible of the four actin subdomains are subdomains 2 and 4 (Page et al. 1998). β-Actin in complex with profilin experiences enough structural freedom to open the orientation between the actin major domains by approximately 10° under variation of the crystallisation conditions (Chik et al. 1996, Figure 1.9).

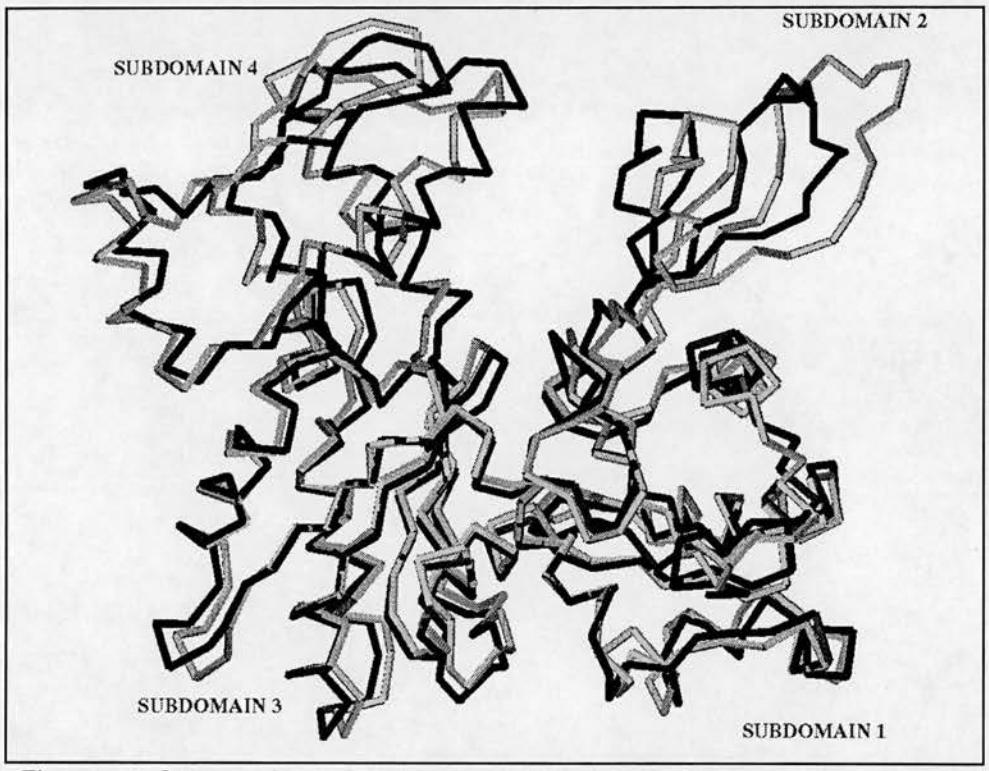

Figure 1.9: Superposition of α-actin from the complex with DNaseI (black Cα trace) and open-state β-actin from the complex with profilin (grey Cα trace). The picture was generated with Oplot, SNAPSHOT, and XV.

The amino acid sequence of mammalian α- and β-actin is 95% identical, but despite this high identity, the crystal structures of α-actins are more similar to each other than to the β-actin structures. Although the different crystallisation conditions also have to be taken into account, one cannot rule out an influence of the sequence difference on the actin conformation, which could lead to structural differences if the two isoforms were crystallised under the same conditions.

It also is not clear whether any of the crystal structures represents the conformation of F-actin. For example, the actin:profilin complex cannot cap the barbed end of F-actin and profilin can increase the rate of ATP-hydrolysis of the actin bound to it, although the profilin:actin complex can add on to the barbed end of an actin filament (Pring et al. 1992). The role and activity of profilin therefore appears to be rather complex. To explain observed data it had been proposed that profilin dissociates from the actin monomer it is bound to after the complex adds on to the barbed end of a filament and ATP-hydrolysis has taken place (Korenbaum et al. 1998).

The F-actin structure had been modelled by refinement of the ADP-α-actin crystal structure (Kabsch et al. 1990) against X-ray fibre diffraction data (Holmes et al. 1990, Lorentz et al. 1993, Tirion et al. 1995). The result indicated changes in the conformation of subdomains and secondary structure elements, mainly in subdomain 2 and 4 of actin, when switching between the G- and the F-state. A different model for the interaction of actin monomers in the filament has been proposed by Schutt et al. (1993) and some changes to the secondary structure in subdomains 1 and 3, predicted by Tirion et al. (1995), were found to be at odds with the analysis of the structural flexibility of actin by Page et al. (1998). Yet, the approach of Holmes et al. appears to be the closest one can get to the conformation of actin in the filament with the experimental data available at present.

1.3.2 The binding of gelsolin segment 1 to actin

Of the two actin monomers bound to gelsolin in the presence of calcium ions, only the one tightly bound to G1 appears to be retained when calcium ions are removed with EGTA. The structure of gelsolin in complex with actin has not been determined yet but the structure of α-actin:G1 (McLaughlin et al. 1993) has given substantial insight as to how G1 binds actin. Extrapolation of the knowledge gathered from that complex and the crystal structure of gelsolin (Burtnick et al. 1997) to the association

of gelsolin and actin is hampered by the fact that gelsolin was crystallised in its inactive Ca^{2+}-free form where G3 is placed in a position which obstructs the actin binding site on G1.

The conformation of G1 in equine gelsolin and in the α-actin:G1C complex are very similar, demonstrating the stability of this important segment. An important difference is that the C-terminal valine of G1, whose trans-carbonyl oxygen interacts with Ca^{2+} in the α-actin:G1 complex, is in cis conformation in the Ca^{2+} -free equine gelsolin structure and points in the opposite direction. Gelsolin can bind two Ca^{2+} ions and biochemical experiments showed that gelsolin binding to actin creates a third high affinity Ca^{2+} binding site on gelsolin (Way et al. 1989).

The work of Weeds et al. (1995) suggests that the third site could be where the G1C-intramolecular Ca^{2+} is bound in the α-actin:G1C complex (McLaughlin et al. 1993) and that a fourth low affinity actin - G1 intermolecular Ca^{2+} binding site is created at pH6.6. Contrary to this, previous biochemical studies could not detect Ca^{2+} binding to G1 in the absence of actin (Way et al. 1990).

It would be of interest to see what effect the calcium ion has on the structure of G1 relieved from constraints imposed by being part of gelsolin or complexed to actin. Solving the crystal structure of G1 on its own could be very revealing and also show how much the stable fold of G1 is influenced by constraints imposed in the previously solved crystal structures. It would allow to compare the structure of this biologically important protein domain taken out of the context of the whole protein, in complex with actin, and integrated into the gelsolin structure.

CapG, also known as Macrophage Capping Protein (Young et al. 1990, Dabiri et al. 1992), Mbh1 (Prendergast et al. 1991) or gCap39 (Yu et al. 1991, Onoda et al. 1993), is another member of the gelsolin family of actin binding proteins and is predominantly expressed in macrophages (Mishra et al. 1994). It can cap the barbed end of F-actin in a Ca^{2+} dependent manner and is de-activated by

phosphatidylinositol-4,5-bisphosphate. It consists of only three homologous repeats (Mishra et al. 1994) and, unlike gelsolin segments 1-3, it cannot sever actin filaments and can be dissociated from actin by lowering the Ca^{2+} concentration (Young et al. 1994). Because of CapG's weaker affinity to actin and inability to sever actin filaments, a structural comparison between the first segment of CapG and gelsolin would be very interesting as it might allow further insight into the mechanism of gelsolin segment 1's specificity for actin.

1.3.3 Drug molecules binding to actin

Natural drugs that act by inhibiting actin polymerisation have previously been used for studies of the dynamic actin cytoskeleton (Tellam and Frieden 1982, Cribbs et al. 1982, Lees et al. 1984, Carlier et al 1986, Goddette and Frieden 1986, Spector et al. 1989, Friederich et al. 1993). These tools can also be used to probe the actin conformation in the crystal structure. Only two suitable families of related drugs, which disrupt the dynamic actin cytoskeleton by binding to actin, have been found to date. The cytochalasins (Sheterline and Sparrow 1994) are a group of metabolites produced by certain fungi of the subclasses *Ascomycotina* and *Deuteromycotina*, whereas latrunculins (Spector et al. 1983) are produced by the Red Sea sponges, e.g. *Latrunculia magnifica* (Kashman et al. 1980), and Pacific Ocean sponges, e.g. *Spongia mycofijiensis* (Quiñoà et al. 1988) and *Fasciospongia rimosa* (Jefford et al. 1996). The representatives of these two families chosen for the structural studies were latrunculin A (Figure 1.10), binding an actin monomer with a K_d of 0.2μM (Coue et al. 1987), and cytochalasin D (Figure 1.10) with K_d = 18μM for the complex with one actin monomer and K_d = 2.6μM for a complex with two actin monomers (Goddette and Frieden 1985).

The exact site of action on actin for these compounds has not been pinpointed yet. The cytochalasins are expected to interact with the barbed end of actin filaments

(Suzuki and Mihashi 1991) and with a site between subdomains 1 and 3 of actin, near the hinge region between the large and small domain (Ohmori et al. 1992). The binding site of latA on actin could be close to the nucleotide binding cleft between the large and small actin domain where several amino acids involved in conferring resistance are located (Ayscough et al. 1997). Considering the effects these drugs have on actin it would be of great interest to elucidate the structural changes which occur when the respective drug binds to an actin monomer. The introduction of these toxins into actin:G1C crystals would also test the degree of structural restriction gelsolin segment 1 imposes on actin, if the overall conformation of the complex is not mainly dictated by the crystallisation conditions.

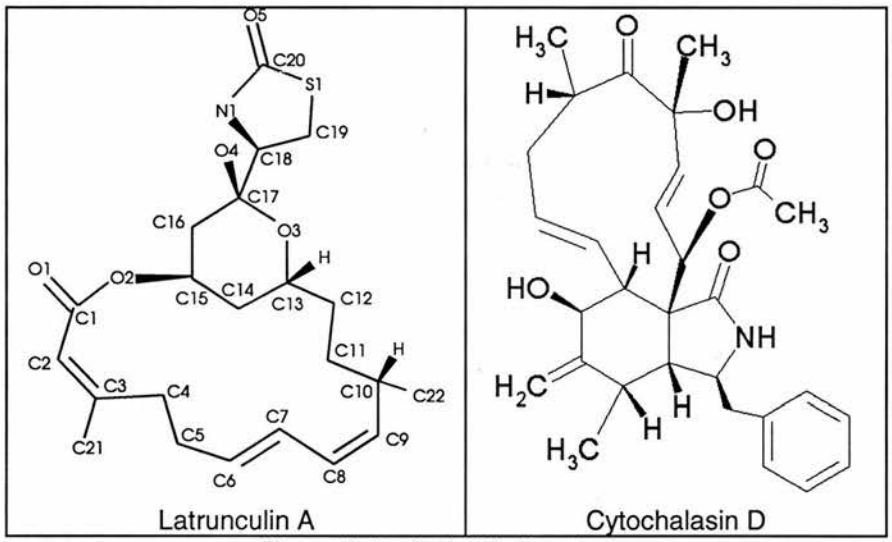

Figure 1.10: Actin binding drugs

1.3.4 The investigations of this thesis

We decided to determine all structures at 100K, because X-ray diffraction of protein crystals at 100K yields better quality diffraction to higher resolution than at room temperature and at the same time considerably reduces the adverse effects of radiation damage (Hope 1990, Rodgers 1997).

Determination of the structures of α-actin:G1C at 100K promises to provide additional detailed information on the α-actin:G1C complex due to the expected higher structural order of mobile loops at 100K. This structure will also be a very good basis to allow comparative studies with the 100K crystal structure of β-actin:G1C. This will establish the influence of the sequence difference of the two isoforms on their conformation and answer the question whether the conformational difference between α-actin:G1C (McLaughlin et al. 1993) and tight-state β-actin:profilin (Schutt et al. 1993) is due to the different isoform used or the crystallisation conditions and the binding protein.

The influence of bound G1 on the conformation of actin will be investigated by determining the structure of the α-actin:G1C complex containing latrunculin A. The drug is expected to bind at a different site than G1 and the extent of induced conformational changes in the actin structure will be an indication of the tightness of control G1 exerts on the actin conformation. This should allow conclusions as to whether actin complexed to G1 is restrained in its conformation or is allowed a degree of flexibility. This could lead to further conclusions whether the actin conformation in the complex with G1 is similar to F-actin or has the flexibility to adopt F-conformation, possibly explaining the ability of actin complexed to gelsolin to cap the barbed end of filaments.

The crystal structure of G1 on its own will allow comparisons to its structure determined in the context of Ca^{2+}-free whole gelsolin (Burtnick et al 1997) and in complex with α-actin. Crystallisation in the presence of calcium ions will also reveal the intrinsic calcium binding sites of the G1 domain, determining the ability of G1 to adopt the right conformation for binding the intramolecular calcium ion found in the α-actin:G1C structure. Additionally, comparisons with the structure of segment 1 of CapG could reveal the reason for the weaker affinity of CapG to actin and possibly determine the role Ca^{2+} plays in activating these actin binding proteins.

2. Methods

2.1 Biochemical procedures

2.1.1 Acetone powder preparation of rabbit skeletal muscle tissue

The extraction of actin from rabbit muscle was performed as described by Spudich and Watt (1971) and is based on the first part of the procedure for myosin preparation (Perry S.V. 1955).

Guba-Straub buffer:	0.3M NaCl 0.1M NaH_2PO_4 0.05M Na_2HPO_4 1.0 mM NaN_3 0.05mM PMSF 1mM $MgCl_2$ 1mM $Na_4P_2O_7$ H_2O pH 6.5
10x Buffer I:	500mM $NaHCO_3$ 1mM $CaCl_2$
Buffer II:	10mM $NaHCO_3$ 10mM Na_2CO_3 0.1mM $CaCl_2$

Table 2.1: Buffers for acetone powder preparation

Muscle from upper legs and the back of one or two rabbits were excised quickly with scalpels and immediately wrapped in cling film and placed on ice in a styro-foam box to preserve endogenous ATP.

All following steps were carried out at 4°C, whenever possible, in a cold room, and all buffers were pre-cooled to 4°C. Fat and connective tissue were removed and the muscle tissue ground through a hand mincer. Ground meat was extracted in 4l of Guba-Straub buffer while stirring for 10-15 minutes. The suspension was centrifuged at 2550xg for 20 min. The muscle residue was suspended in 10 volumes of buffer I, stirred at for 15 minutes, and the suspension filtered through a cheese cloth to remove salt and adjust pH to about 9. The residue was suspended in 1l buffer II, stirred for 10 minutes and filtered through cheese cloth. The residue was diluted into 5l of H_2O and

quickly squeezed through cheese cloth. The residue was suspended in 2.5l acetone and left standing for approximately 15minutes. Then the suspension was filtered through cheese cloth. The acetone washing and filtering was repeated until supernatant became clear (3-4 times). The residue was spread out on filter paper to dry in a fume hood at room temperature overnight.

Muscle tissue of roughly 1kg yielded 43g of dried filter residue (acetone powder).

2.1.2 Purification of α-actin from rabbit muscle acetone powder

G-buffer:	2.5mM Tris-HCl pH 8.0 0.1mM ATP 1mM NaN_3 0.1mM $CaCl_2$ 0.5mM DTT
G1MT buffer:	1M Tris-HCl pH 8.0 0.1mM ATP 1mM NaN_3 0.5mM DTT 0.1mM $CaCl_2$

Table 2.2: Buffers for actin extraction from acetone powder

The following procedure is based on the work reported by Spudich and Watt (1971). Depolymerisation of F-actin with G1MT buffer is based on the work of Pinder and Gratzer (1995)

To each gram of acetone powder 40ml of G-buffer, pre-cooled to 4°C, was added. Actin was extracted in monomeric (G) form by stirring the suspension for two hours at 4°C, then filtering through No 54 paper filter on a water pump, cooling all solutions with ice, and again filtering through 8μm and then through 0.22μm Millipore filters. KCl was added to 0.8M and $MgCl_2$ to 2mM and the solution was stirred for one hour on ice. The solution was clarified at 4°C and 158,000xg for 2 hours, pelleting the polymerised actin. The F-actin pellet was homogenised in

G1MT-buffer and left at 4°C overnight. The remaining polymerised actin was removed from the solution by centrifugation at 150,000xg and 4°C for two hours. Actin was then purified by another cycle of polymerisation, depolymerisation and clarification.

The purity of actin was assayed by sodium dodecylsulphate polyacrylamide gel electrophoresis. The concentration of purified actin was determined spectroscopically using a cell pathlength of 1cm:

actin concentration (mg/ml) = A_{290} / 0.63 (Houk et al. 1974)

The actin yield over five extractions was 1.5±0.4% (w/w) of the acetone powder used.

2.1.3 Purification of human platelet β-actin

Human blood platelets in 1.5l plasma were obtained from the Blood Transfusion Unit of the Edinburgh Royal Infirmary. After extraction from a human donor the platelets had been stored by the Blood Transfusion Unit at room temperature for 5 days. On receipt, the platelets were then stored at 4°C for one week before beginning the extraction.

The protocol is based on that reported by Winder et al. (1995). Depolymerisation of F-actin with G1MT buffer is based on the work of Pinder and Gratzer (1995)

The platelets were pelleted at 2550xg and 4°C for 35 minutes. The pellet (ca. 10ml) was pooled with platelets (ca. 60ml) supplied by Dr. Steve Winder (ICMB of The University of Edinburgh). The pooled platelets were suspended in acetone, pre-cooled to 4°C, and stirred at 4°C for 15 minutes. The acetone was removed by filtration through a no.54 paper filter with a water pump in the cold room at 4°C. The

platelets were washed three more times with cold acetone and left to dry at room temperature in a fume hood overnight.

The total yield was 7g of platelet acetone powder.

The 7g platelet acetone powder were suspended in 200ml G buffer and stirred at 4°C for one hour. The suspension was clarified at 160,000xg and 4°C for 2 hours and the supernatant filtered through a 8µm filter. To polymerise actin, $MgCl_2$ was added to 2mM, KCl to 0.8M, and the solution left at 4°C for one hour. F-actin was pelleted at 160,000xg and 4°C for two hours. The F-actin pellet was homogenised in 40ml G1MT buffer and left at 4°C over two nights to depolymerise (homogenate 1).

The supernatant from pelleting F-actin, which was kept for one night at 4°C, was spun at 160,000xg and 4°C for two hours. The F-actin pellet was homogenised in G1MT buffer and left at 4°C overnight (homogenate 2).

Homogenate 1 and 2 were clarified at 160,000xg and 4°C for two hours, pooled, concentrated to 10ml and gel-filtered over a 550ml S200 column at 1ml/min overnight. Fractions containing actin were identified by their absorbance at 290nm and an SDS-PAGE, and pooled.

Actin was polymerised by adding to this pool $MgCl_2$ to 2mM, ATP to an additional 0.1mM, EGTA to 1mM, and KCl to 0.8M, and incubating at 4°C overnight, then clarified at 10,000xg and 4°C for 25min and the F-actin pelleted at 160,000xg and 4°C for two hours. The pellet was homogenised in 16ml G1MT buffer and left to depolymerise at 4°C overnight. The homogenate was clarified at 160,000xg and 4°C for two hours. This polymerisation-depolymerisation purification step was repeated a second time. The G-actin solution was concentrated to 10ml and passed over a Sephacryl S200 column at 0.5ml/min with G-buffer as running buffer overnight. Fractions containing purified actin were identified by their absorbance at 290nm and SDS-PAGE, and pooled.

The initial amount of 7g platelet acetone powder (70ml packed platelets) yielded 4.3mg platelet actin.

2.1.4 Transformation of *E.coli* strains BL21(DE3) and JM109 with vectors containing genes for G1, G1C, or CapG-1

The procedure is based on a protocol published by Sambrook and Maniatis (1989).

2xTY medium:	1.6%(w/v) tryptone 1%(w/v) yeast extract 5%(w/v) NaCl
AMP-2xTY-agar plates:	1.5%(w/v) agar 100µg/ml ampicillin 1.6%(w/v) tryptone 1%(w/v) yeast extract 5%(w/v) NaCl

Table 2.3: Culture media.

Pre-cultures of *E.coli* BL21(DE3) (strain for expressing gelsolin segment 1) or JM109 (high copy strain for plasmid amplification) in 5ml 2xTY medium were incubated while shaking at 37°C overnight.

100ml of 2xTY were inoculated with 1ml of pre-culture and incubated at 37°C until A_{600} reached 0.6 (at least 3h for BL21 and 4h for JM109). The culture was incubated on ice for 10minutes and cells pelleted at 4°C and 2550xg for 20minutes. The supernatant was removed and the pellet gently suspended in 10ml ice cold 100mM $CaCl_2$ and incubated on ice for 30minutes. The suspension was spun at 2550xg and 4°C for 20minutes. The supernatant was removed and the pellet gently suspended in 2ml ice cold 100mM $CaCl_2$.

Plasmids carrying the genes for G1 (plasma gelsolin residues 25-149) and G1C (as G1 but containing the N57C point mutation) were obtained from P. McLaughlin and

M.Way (MRC Laboratory of Molecular Biology, Cambridge, UK) and plasmids containing the genes for CapG-1 (Cap-G residues 1-131) from F.S. Southwick (Division of Infectious Diseases, Department of Medicine, University of Florida, USA). These plasmids had been constructed using the pMW172 vector which contained genes for an IPTG activated promotor and for ampicillin resistance. Into this vector the genes for either G1, G1C, or CapG-1 had been subcloned.

Of a plasmid DNA stock solution (see 2.1.5) 3-5µl were added to 2ml of calcium competent cells and the cells incubated on ice for 1h. The cell suspension was heat shocked at 42°C for three minutes, then incubated on ice for 5 minutes. 1ml of 2xTY was added and the cell suspension incubated at 37°C for 20 minutes. 200µl of cell suspension were each plated on AMP-2xTY-agar plates with a glass spreader. The plates were left for 10 minutes in an upright position to soak the agar and then were incubated upside down at 37°C overnight.

2.1.5 Plasmid amplification in *E.coli* strain JM109

The procedure is based on a protocol published by Sambrook and Maniatis (1989).

GTE buffer:	1%(w/v) glucose 25mM Tris-HCl pH8 10mM EDTA
stock buffer:	10mM Tris-HCl pH8, 20ng/ml RNase

Table 2.4: Buffers used in plasmid amplification

The cells of a 2ml pre-culture of JM109, incubated overnight at 37°C, were pelleted at 13,000xg and room temperature for 1 minute and re-suspended in 200µl GTE buffer and 400µl 0.2M NaOH, 1% SDS. The suspension was left on ice for 5 minutes. 300µl 3M potassium acetate pH 4.8 were added and the suspension mixed by inversion, and left on ice for 5 minutes. Cell debris was pelleted at 13,000xg and

room temperature for 5 minutes and the supernatant mixed with 525µl isopropanol and left for 20 minutes at room temperature. Plasmid DNA was pelleted at 13,000xg and room temperature for 5 minutes, washed with 70%(v/v) ethanol, and air-dried. The dry pellet was dissolved in 30µl stock buffer and incubated at 37°C for 10 minutes. This plasmid stock solution was stored at -20°C.

2.1.6 Expression and purification of gelsolin segment 1

The procedure is based on a protocol obtained from P. McLaughlin (ICMB, The University of Edinburgh, UK).

2xTY-AMP:	100µg/ml ampicillin 1.6%(w/v) tryptone 1%(w/v) yeast extract 5%(w/v) NaCl
lysis buffer	50mM Tris-HCl pH 8.0 1 mM EDTA 25%(w/v) sucrose 0.05mM PMSF
DE8 buffer	25mM Tris-HCl pH 8.0 1mM DTT 1mM NaN_3 1mM EGTA

Table 2.5: Buffers for expression and purification of G1

1ml of an overnight pre-culture of *E.coli* BL21(DE3) transformed with the plasmid coding for G1 or G1C was used to inoculate 1l of 2xTY-AMP medium. The culture was incubated at 37°C until absorbance at 600nm reached 0.6. 1ml IPTG (600mM) was added per litre of culture, which was then incubated at 37°C for 4h. The culture was spun at 2,550xg and 4°C for 20 minutes. The supernatant was removed and the pelleted cells flash-frozen with liquid N_2. The frozen cells were thawed and suspended in a minimal volume of lysis buffer. 5mg lysozyme was added and the

suspension left stirring at room temperature for about 60 minutes. $MgCl_2$ and $MnCl_2$ were added to 1mM, 0.25mg DN-EP grade DNase was added, and the suspension was left stirring at room temperature for 60 minutes. The suspension was spun at 40,900xg and 20°C for 20 minutes. The supernatant was dialysed with several changes overnight against DE8 buffer with 0.05mM PMSF. The dialysed cell extract was spun at 25,000xg and 4°C for 20 minutes to clarify and loaded onto a 200ml DE52 cellulose column at 0.5ml/min. The column was washed with 200ml DE8 buffer at 1ml/min. A sodium chloride gradient from 0 to 300mM was applied over 500ml at 1ml/min. Fractions were analysed by SDS-PAGE and measuring the absorbance at 280nm. The fractions with the highest G1/G1C concentration were pooled and concentrated in an AMICON ultrafiltration cell with a PM10 membrane to 5ml. The concentrated protein solution was gel-filtered over a Sephacryl S200 column at 1.3ml/min with DE8 buffer as running buffer. The fractions were analysed by SDS-PAGE and those containing purified G1/G1C were pooled and the protein concentration determined using the Bicinchoninic Acid (BCA) Protein Assay Reagent obtained from Pierce Chemical Company.

From two expression and purification runs of G1, 9mg and 24mg respectively were recovered from 1l BL21(DE3) culture. Three runs of G1C yielded 9mg, 25mg, and 40mg G1C per litre BL21(DE3) culture respectively.

2.1.7 Expression and purification of CapG segment 1

The procedure is based on a protocol published by Dabiri et al. (1992). 1ml of an overnight pre-culture of *E.coli* BL21(DE3) transformed with the plasmid coding for CapG-1 was used to inoculate 1l of 2xTY-AMP medium. The culture was incubated at 37°C until absorbance at 600nm reached 0.6. 1ml IPTG (600mM) was added per litre of culture, which was then incubated at 37°C for 4h. The culture was spun at

2,550xg and 4°C for 20 minutes. The supernatant was removed and the pelleted cells flash-frozen with liquid N_2.

2xTY-AMP:	100µg/ml ampicillin 1.6%(w/v) tryptone 1%(w/v) yeast extract 5%(w/v) NaCl
lysis buffer:	50mM Tris-HCl pH 8.0 1 mM EDTA 25%(w/v) sucrose 0.05mM PMSF
DE8 buffer:	25mM Tris-HCl pH 8.0 1mM DTT 1mM NaN_3 1mM EGTA
CM6.5 buffer:	25mM PIPES pH6.5 1mM DTT 1mM NaN_3 1mM EGTA
DE8.5 buffer:	as DE8 buffer except: 50mM Tris-HCl pH 8.5

Table 2.6: Buffers used for expression and purification of CapG-1

The frozen cells were thawed and suspended in a minimal volume of lysis buffer. 5mg lysozyme were added per original litre of culture and the suspension left stirring at room temperature for about 60 minutes. $MgCl_2$ and $MnCl_2$ were added to 1mM, DN-EP grade Dnase (Sigma Chemical Co.) was added to 0.25mg per litre of original culture, and the suspension was left stirring at room temperature for 60 minutes. The suspension was spun at 40,900xg and 20°C for 20 minutes. The supernatant was dialysed with several changes overnight against DE8 buffer with 0.05mM PMSF.

The dialysed cell extract was spun at 25,000xg and 4°C for 20 minutes to clarify and loaded onto a 160ml DE52 cellulose column at 0.3ml/min. The column was washed with 200ml DE8 buffer at 1ml/min. A potassium chloride gradient from 0 to 200mM was applied over 400ml at 0.3ml/min. Fractions were analysed by SDS-PAGE and measuring the absorbance at 280nm. The fractions with the highest CapG-1 concentration were pooled and concentrated in an AMICON ultrafiltration cell with a

PM10 membrane to 10ml. The concentrated protein solution was dialysed overnight against DE8 buffer. A second DE52 run followed.

The fractions with the highest CapG-1 concentration were pooled and concentrated in an AMICON ultrafiltration cell with a PM10 membrane to 5ml. The concentrated protein solution was gel-filtered twice over a sephacryl S200 column at 1.0ml/min with DE8 buffer as running buffer. The fractions were analysed by SDS-PAGE and those containing CapG-1 were pooled.

To remove the remaining contaminating protein the pooled fractions were concentrated to 9ml and dialysed against CM6.5 buffer overnight. The dialysed protein solution was loaded on a CM52 cellulose column at 0.5ml/min. CapG-1 and the contaminating protein eluted unretarded on washing the column with CM6.5 buffer. The CapG-1 containing fractions were pooled and concentrated to 10ml and dialysed overnight into DE8 buffer.

The protein concentration was determined using the Bicinchoninic Acid (BCA) Protein Assay Reagent obtained from Pierce Chemical Company. Despite a contaminating protein band 3mg of protein (BCA assay) were used at this point for crystallisation.

The remaining 60mg of protein were dialysed against DE8.5 buffer overnight. The dialysed protein was loaded on a DE52 cellulose column at 0.5ml/min. The column was washed with 200ml DE8.5 buffer and CapG-1 eluted with a 400ml gradient from 0 to 130mM NaCl. The fractions containing purified CapG-1 were pooled, dialysed overnight against DE8 buffer, and the protein concentration determined using the BCA assay. The final amount of purified CapG-1 was 15mg per initial litre of BL21(DE3) culture.

2.1.8 Actin ATP-ADP exchange and complex formation with G1C

Dowex 1 beads (Sigma Chemical Co.) were washed in 2mM Tris-HCl (pH8) and hexokinase-agarose beads (Sigma Chemical Co.) in 2mM Tris-HCl (pH8) and 0.5mM DTT by suspending in buffer, spinning down at 13,000xg and room temperature for 1 minute and resuspending. ATP-G-actin solution was gently stirred with Dowex 1 beads (30µl per mg actin) at 4°C for 5 minutes. The beads were removed by a centrifugation at 13,000xg and 4°C for 1 minute. To the supernatant ADP was added to 1mM, $MgCl_2$ to 0.08mM, EGTA to 0.2mM, glucose to 1mM and hexokinase-agarose beads to 2 U/ml. The solution was gently stirred at 4°C for 4 hours. The beads were pelleted and the actin solution immediately used for complex formation with G1C.

2.1.9 Purification of actin : gelsolin segment 1

G1C and actin (ATP-α-actin, "ADP"-α-actin, or ATP-β-actin) were added at a molar ratio of 1:1. This solution was gel filtered over a Sephacryl S200 column with G-buffer as running buffer (ADP-G-buffer if following the ATP-ADP exchange procedure). The fractions containing purified complex were pooled and the protein concentration determined with the BCA assay.

Four purification runs of freshly formed complex between ATP-α-actin and G1C resulted in a recovery of 10%, 49%, 67%, and 99% of the maximum theoretical yield for the α-actin:G1C complex.

Six ATP-ADP exchange trials with α-actin, complex formation with G1C and purification yielded 12±10% of the maximum theoretical yield (in respect to the amount of actin before the ATP-ADP exchange procedure).

Purification after complex formation of platelet β-actin and G1C resulted in 61% of the maximum theoretical yield.

2.1.10 Crystallisation in hanging drops

Protein	α-actin:G1C	β-actin:G1C	Gelsolin segment 1
Crystallisation conditions	10mM DTT 150mM NaCl 0.1mM ATP 0.1mM $CaCl_2$ 0.1mM $MgCl_2$ 1mM NaN_3 50mM MES pH6.6 5-9%(w/v) PEG 6000	10mM DTT 150mM NaCl 0.1mM ATP 0.1mM $CaCl_2$ 0.1mM $MgCl_2$ 1mM NaN_3 50mM MES pH6.0, pH6.6, pH7.0, pH7.3 3-12%(w/v) PEG 6000	1mM $CaCl_2$ 10mM DTT 1mM NaN_3 50mM Tris-HCl 1.5 to 2.0M ammonium sulphate at pH7.9, or 1.0 to 1.4M ammonium sulphate at pH8.5
Conditions under which crystals grew	All	5-6% PEG and pH6.0, 6-8% PEG and pH6.6.	1.5-2.0M ammonium sulphate and pH7.6-7.9.
Time until crystal growth was no longer observed	Two weeks	Two weeks	One week
Size of largest crystals	1.0 x 1/4 x 1/40mm	1.0 x 1/4 x 1/40mm	1/40x1/40x1/2mm

Table 2.7: Conditions and results of crystallisation trials.

Glass cover slips were washed by dipping into 5%(v/v) DECON 90 (Decon Laboratories Lmtd.), then deionised H_2O, then acetone. Dried cover slips were dipped into 2% dichloro-dimethylsilane (1,1,1-trichloroethane solution) and left to dry for half an hour in the fume hood. Then the cover slips were dipped into methanol and again left to dry in the fume hood. The wells of a Linbro® (ICN Biomedicals) culture tray were filled with 1ml of the crystallisation buffer. The rim of the wells was smeared with silicon grease. On a siliconised glass cover slip a drop (5-15µl) of crystallisation buffer was placed and mixed with an equally sized drop of protein solution (about 10mg/ml). The cover slip was quickly turned around with the 10-30µl drop, now at half protein and half crystallisation buffer concentration, hanging downwards and the slip was positioned over a well. Sufficient pressure was

applied, so that the silicon smear sealed the chamber airtight. The trays were left in a temperature controlled room at 18°C. Crystallisation was induced by the equilibration process between the drop and the well solution.

Attempts to increase crystal size:

α-Actin:G1C: Crystallisation trials including β-octyl glucoside (McPherson et al., 1986) at 0.75% (w/v) and glycerol at 2% (v/v) in the crystallisation buffer yielded no substantial increase in crystal size. At 0.5 and 0.75% (w/v) β-octyl glucoside crystal size decreased significantly.

Gelsolin segment 1: Microseeding was performed by crushing a needle in crystallisation buffer with 2.0M ammonium sulphate and pH7.9. Dilutions (1/10, 1/100, 1/1000) were made and brush hairs dipped into each of the dilutions were drawn through mixed drops on glass cover slip during a second hanging drop crystallisation setup. The size of crystals that grew did not differ from the initial trial. Macroseeding was performed by transferring one small needle (less than 1/4mm in length) each into mixed drops on glass cover slip during a second hanging drop crystallisation setup. The size of crystals that grew did not differ from the initial trial.

2.1.11 Soaking of α-actin:G1C crystals

α-Actin:G1C crystals were soaked in a soaking buffer comprising crystallisation buffer, and organic solvent in varying concentrations, and the ligand (either latrunculin A or cytochalasin D). 1ml of soaking buffer without ligand was placed in

each well of a Linbro® culture tray. Micro-Bridges® from Oxford Crystal Microsystems were placed in the wells. Into the cavity of the Micro-Bridge® 20µl of soaking buffer with ligand were placed. A protein crystal was quickly transferred into the soaking buffer in the cavity using a Cryoloop from Hampton Research that had been glued to a metal pin that in turn had been glued to a Hampton Research Microcap. To improve the handling a 1ml Gilson pipette tip had been wedged into the back of the Microcap. Grease was applied to the rims of the wells and the wells sealed airtight with a glass cover slip. The trays were left to incubate for different lengths of time at 18°C or 4°C.

Latrunculin A was obtained courtesy of Dr. K. Ayscough (Dept. of Biochemistry, University of Dundee, Dundee, U.K.) and a 50mM latA stock solution was prepared with DMSO. Cytochalasin D was obtained from Sigma Chemical Co. and a 40mM stock solution prepared with DMSO.

Soaking buffer: 10mM DTT
150mM NaCl
0.1mM ATP
0.2mM EGTA
0.1mM $MgCl_2$
1mM NaN_3
50mM MES pH6.6
10% (w/v) PEG 6000
25%(v/v) glycerol
5-30%(v/v) ethanol
10%(v/v) DMSO
4mM cytochalasin D or 5mM latrunculin A

To avoid damaging the crystal due to the transfer into a different buffer, protein crystals were transferred first into soaking buffers with 5%(v/v) ethanol, then 10%, 20%, and finally 30% at 4°C.

Stability of the protein crystals in soaking buffers with and without ligand and at varying ethanol concentrations was tested by observing the behaviour of the crystals in the soaking buffer and obtaining X-ray diffraction patterns with the departmental X-ray generator.

2.2 X-ray diffraction data collection

2.2.1 Preparation for X-ray data collection at room temperature

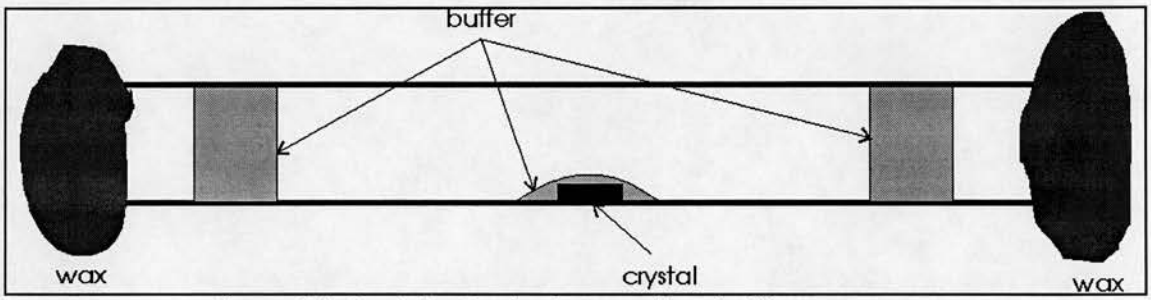

Figure 2.1: Crystal setup in glass capillary for X-ray exposure.

These techniques have been published by (McRee 1993). A protein crystal was sucked into an X-ray penetrable glass capillary of 0.5 to 1.5mm diameter depending on the crystal size. Buffer around the crystal was removed with a very fine glass capillary until the crystal was surrounded by a minimal amount of liquid clinging to only one side of the capillary. A small amount of buffer was injected into the capillary from both ends keeping the liquid away from the crystal in the middle of the capillary. The ends were sealed with wax using a strip of wet filter paper to protect the crystal and buffer from the heat of the wax when first applied (Figure 2.1).

One end of the capillary was attached to the free end of a goniometer head with a piece of plasticene and the goniometer head attached to a mounting arm rotatable around its long axis perpendicular to the incident X-ray beam.

2.2.2 Preparation for X-ray data collection at 100K

The cryo-protectant used during this work was glycerol. Glycerol concentrations of 20-25%(v/v) were sufficient to prevent icing of buffers when flash-frozen. Protein crystals were first flash-frozen in liquid nitrogen contained in a small dewar. Immersed in liquid nitrogen the crystal was taken to the mounting device in front of the detector and mounted on the goniometer head keeping the crystal in a stream of gaseous nitrogen cooled to 100K by the Cryostream cooler 600 (Oxford Cryosystems).

To flash-freeze a crystal, a Micro-Bridge® (Oxford Crystal Microsystems) was placed in a well of a Linbro® culture tray. Into the cavity of the Micro-Bridge® 20µl of buffer containing 20-25%(v/v) glycerol were placed. A protein crystal was quickly transferred into the buffer using a Cryoloop (Hampton Research) mounted as described in 2.1.11. An open cryo-vial from the Microcaps set from Hampton Research was wedged onto a metal cane in a way that the opening of the vial was easily accessible. The vial was then immersed in liquid N_2 in a small dewar. After having been incubated in the cryoprotected buffer for approximately 10s, the crystal was fished out of the Micro-Bridge® and the Microcap quickly screwed onto the vial filled with liquid nitrogen, thereby flash-freezing the crystal. The closed cryo-vial (Figure 2.2), containing the Cryoloop and the frozen crystal immersed in liquid nitrogen, was kept immersed in liquid nitrogen in the dewar until the dewar was brought close to the crystal mounting device of the detector system.

With an equivalent Cryoloop and Microcap the goniometer head on the mounting device was adjusted to hold the loop in the right position for the X-ray beam and the cryo-stream. The closed cryo-vial was removed from the metal cane and the metal disk of the Microcap brought into contact with the magnet on the goniometer head. The cryo-vial was screwed off the Microcap under the continuous stream of gaseous nitrogen cooled to 100K.

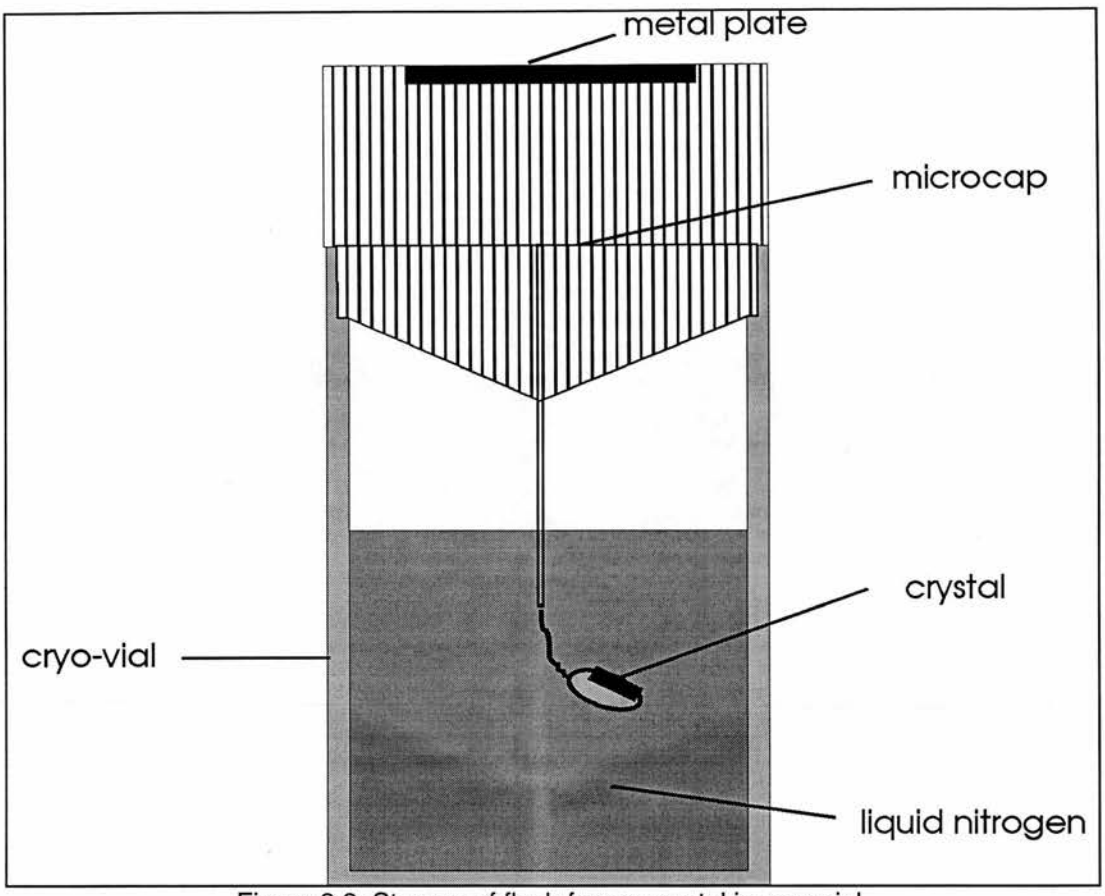

Figure 2.2: Storage of flash frozen crystal in cryo-vial.

2.2.3 Recording X-ray diffraction data

2.2.3.1 X-ray sources and detectors

An overview can be found in "Crystal structure analysis for chemists and biologists" by J.P. Glusker et al., published by VCH Publishers Inc. 1994, and in Methods of Enzymology volume 276 (1997).

a) Rotating anode generator

X-rays for diffraction analysis are typically produced either by a generator bombarding an anode with electrons from the cathode or by a synchrotron.

The rotating anode generator is a widely used example of the first type of X-ray source. When in an evacuated chamber electrons travelling at high speeds from the cathode hit the outer edge of an fast rotating anode, a continuum of radiation (white radiation) is emitted due to collison of the electrons with the target. Anodes are made of metal and an incoming electron can ionise metal atoms of the anode by smashing through the outer electron shell and expelling an inner shell electron. When an electron from the outer shell moves to the inner shell to fill the gap, a "characteristic" radiation is emitted, depending on the initial and the final energy state of the electron. This radiation is anode material specific and presents itself as a few intense peaks in the emission spectrum at the wavelengths equivalent to the energy state difference between which the electron moved. To obtain a monochromatic beam all wavelengths save one of the characteristic wavelengths are removed by one or more monochromator crystals and the beam is focused by mirrors. If a copper anode is used, the wavelength usually chosen is the copper K-α radiation at 1.54Å.

b) Synchrotron radiation

For X-ray diffraction experiments synchrotron radiation is far superior to the radiation generated by a rotating anode generator. Synchrotron radiation is far more intense, has a high degree of polarisation, and a wide range of wavelengths can be selected. It is emitted when very high-energy electrons travelling in an electron storage ring are accelerated. X-rays are emitted tangentially to the ring as nanosecond pulses with very high intensity and a continuous spectral distribution. The desired wavelength can be selected with similar tools as for the rotating anode radiation.

c) Image plate area detector

The X-ray storage-phosphor imaging plate (IP) detector is a flexible plastic plate with a uniform coating of clusters of tiny crystals (~5μm) of a photo-stimulable phosphor mixed with an organic binder. The photo-stimulable phosphor is capable of storing a fraction of the absorbed X-ray energy. When later stimulated by visible light (λ=633nm) it emits photostimulated luminescence (PTL) at approximately 390nm with an intensity proportional to the absorbed X-ray intensity. The PTL is collected with a conventional high quantum efficiency photomultiplier tube, amplified and converted to a digital image which can be processed by a computer. The residual image on the IP is then erased by irradiation with visible light to allow repeated use.

d) Charge-coupled device (CCD) based area detectors

CCDs make use of the photoelectric effect caused by X-rays hitting a semi-conductor surface and are composed of arrays of electrodes called *gates* . Three gates arranged in a column compose a pixel. The middle gate is biased at a positive potential to attract and accumulate electrons freed during X-ray exposure. The other two gates are biased at a negative potential to prevent charge movement across to other pixel rows. Columns of pixels are electrically isolated from each other by a narrow channel-stop strip. In addition to photo-electrons, free electrons are also generated spontanuously in the CCD due to the thermal energy distribution of the electrons. This accumulated "thermal" charge is called the *dark image*, which is considered to be constant and is subtracted from the total charge accumulated during the X-ray exposure.

After the X-ray exposure is completed, charges created are quantitatively registered by electronic micro-chips and converted to a digital computer file. Read-out of data and reinitialising for the next exposure is faster than for the IP plate detector. The physical size of CCDs is limited (typically 20x20mm). To construct CCD area

detectors of sufficient size, a tapered fibre-optic system has to be placed in front of the CCD surface to demagnify the optical image. Again it is not practical to do this in a single stage, if the required area is of the order of 10,000mm^2 or greater. A tiled mosaic of 2x2 or 3x3 fibre-optic CCD elements is usually used for detectors in protein X-ray crystallography.

2.2.3.2 Collecting X-ray diffraction data

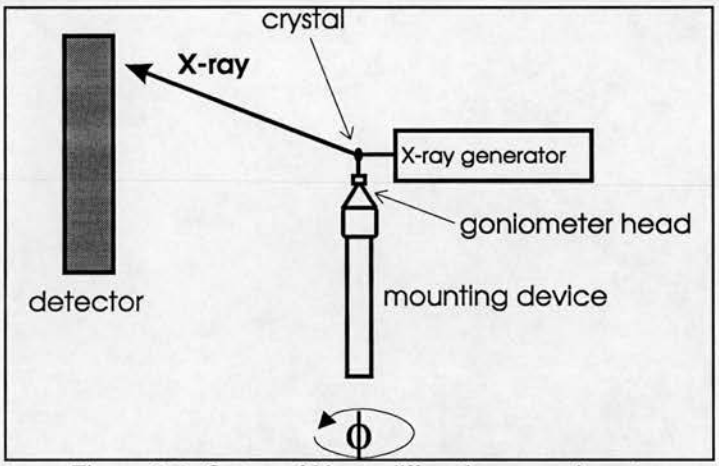

Figure 2.3: Setup of X-ray diffraction experiment.

X-ray diffraction data were generated either with the rotating copper anode X-ray generator FR571 (Enraf Nonius) of the Department of Biochemistry (The University of Edinburgh) or with the X-ray beam provided by the synchrotron generated radiation at the SRS Daresbury (UK) or DESY Hamburg (D).

These data were generally recorded on a MAR image plate (radius: 150mm, pixel size: 150x150µm), but on two occasions data were recorded with a temporarily installed CCD detector (2x2 CCD tiles, total detection area: 188x188mm, pixel size: µm) at the SRS Daresbury. X-ray diffraction patterns were stored as digital files on computer disk containing the information on each image pixel position and intensity.

Individual X-ray exposures lasted between 30minutes (home source) to 5minutes (SRS Daresbury). Crystals were rotated by 0.5° to 1.0° around the ϕ-axis (axis along the length of the mounting arm perpendicular to the incident X-ray beam) during this exposure. Rotation angle depended on how close and how long a crystallographic axis was parallel to the incident X-ray beam.

Initial exposures, 90° apart in ϕ, were taken to determine the unit cell and the crystal orientation using MOSFLM to evaluate the diffraction data images. Data collection was then initiated at a crystal orientation with a major zone close to the centre of the detector, i.e. a crystallographic axis was almost parallel to the X-ray beam. With MOSFLM an estimation of the rotation range necessary for maximum completeness was calculated and the data collection was planned accordingly. This procedure proved particularly useful if the total rotation range obtainable due to time constrictions was less than 90°. This is the total rotation range for maximum data completeness if the spacegroup of the crystal is $P2_12_12_1$, as was the case for all crystals examined during this work.

2.2.4 Evaluation of X-ray diffraction data

The images of the rotation diffraction patterns were used to refine unit cell and crystal orientation parameters with MOSFLM which was also employed to integrate intensities and correct for background intensity, crystal decay, absorption effects, and Lorentz and polarisation factors. Using the program SCALA multiple observations of reflections were scaled together, and multiple observations merged into an average intensity and the standard deviations calculated. Intensities (I) were converted to structure factor amplitudes ($|F_{hkl}|$) using the CCP4 program TRUNCATE. The amplitudes were put on an absolute scale using the scale factor taken from a Wilson plot. A best estimate of the structure factor amplitudes from I, sd(I), and the distribution of intensities in resolution shells was calculated with TRUNCATE. A

single file was obtained containing h,k,l and the respective structure factor amplitudes with respective standard deviations .

2.3 Computer software used

2.3.1 Programs of the CCP4 suite

(Collaborative Computational Project, Number 4 1994)

ACT .....analyse co-ordinates

ARP/wARP.....automated refinement procedure for refining protein structures and identifying density from water molecules

BAVERAGE.....averages B-factors over main and side chain atoms

COMPAR .....comparison of co-ordinates

CONTACT .....computes various types of contacts in protein structures

DISTANG.....distances and angles calculation

FFT .....fast Fourier transform

FREERFLAG.....tags each reflection in an MTZ file with a flag for cross-validation

IPDISP .....displays images from a variety of (crystallographic) sources

LSQKAB .....apply various transformations to co-ordinate files

MAKEDICT .....converts PDB file to TNT or PROTIN dictionaries and PROTIN to PDB

MAPMASK.....map/mask extend program

MATTHEWS_COEF ..calculate Matthews coefficient

MTZ2VARIOUS .....produces reflection file for MULTAN, SHELX, TNT, X-PLOR/CNS, CIF or other ASCII format

MTZDUMP .....dump data from an MTZ reflection data file

MTZUTILS.....reflection data files utility program

PDBSET .....various useful manipulations on co-ordinate files

PEAKMAX.....search for peaks in the electron density map

POLARRFN .....fast rotation function which works in polar angles

PROCHECK.....programs to check the Stereochemical Quality of Protein Structures

PROTIN.....prepare restraints file for REFMAC

REBATCH.....alter batch numbers in an unmerged MTZ file

REFMAC.....This macromolecular refinement program was used for structure refinement against the observed data by maximum likelihood (Pannu et al. 1996, Bricogne et al. 1996, Murshudov et al. 1997). Using this method the model was refined by maximising the likelihood of making the experimental observations with the given model. In practice the negative logarithm of the likelihood function, called LLK_h, was minimised.

$$LLK_h = \frac{|F_o|^2+D^2|F_c|^2}{2\sigma_e^2+\sum} - \log I_o\left(\frac{2|F_o|D|F_c|}{2\sigma_e^2+\sum}\right) + \log(2\sigma_e^2+\sum) \quad \text{for acentric reflections}$$

$$= \frac{|F_o|^2+D^2|F_c|^2}{2\sigma_e^2+\sum} - \log\ \cosh\left(\frac{|F_o|D|F_c|}{\sigma_e^2+\sum}\right) + \frac{1}{2}\log(\sigma_e^2+\sum) \quad \text{for centric reflections}$$

$\Sigma = \varepsilon\ (\ \Sigma_c(1 - D^2) + \Sigma_q\ )$

Σ_c.....sum of the squared atomic scattering factors of all atoms used in the present model.

Σ_q.....sum of the squared atomic scattering factors of all atoms not included in the present model.

ε.....multiplicity of the scattering plane

$D = < \cos(\Delta r * s) >$

Δr.....average co-ordinate error

s.....vector of position of reciprocal space point $|s| = 2\sin(\theta/\lambda)$

F_o.....observed structure factor

F_c.....calculated structure factor

σ_e.....experimental uncertainties of structure factor amplitudes.

RSTATS .....scale together two sets of F's

SCALA .....scale together multiple observations of reflections

SCALEIT.....derivative to native scaling

SFALL .....structure factor calculation and X-ray refinement using forward and reverse FFT

SIGMAA.....improved Fourier coefficients using calculated phases

SORTMTZ.....sort a MTZ reflection data file

SURFACE .....surface accessibility program and for preparing input file to program volume

TRUNCATE.....obtain structure factor amplitudes using Truncate procedure

UNIQUEIFY.....generate a unique list of reflections

XLOGGRAPH.....viewer of specially formatted `log' files

XPLOT84DRIVER.....viewer for Plot84 meta files

2.3.2 Other programs used

LSQMAN ..... (Kleywegt 1996) for superimposing and analysing of multiple models and/or molecules

MAPMAN .... (Kleywegt and Jones 1996) for manipulating of electron density maps

MOSFLM ..... (Leslie 1990) for determining the crystal orientation, cell parameters, and space group, generating the reflection lists and integrating the images.

O ..... (Jones et al. 1991) graphical display program for model building and displaying macromolecules, small molecules, atoms, and electron density maps

Oplot ..... Program of the O software package to convert a set of commands in O graphic descriptor language into postscript commands.

SHELX ..... (Sheldrick and Schneider 1997) The programs of the SHELX package used for structure refinement were SHELXPRO, SHELXL, and SHELXWAT.

SHELXPRO was used to create instruction files for SHELXL and SHELXWAT, to create electron density maps, and convert SHELX output files into other formats.

SHELXL was the program employed to refine a model against the observed data by the conjugated gradient minimisation published by Hendrickson and Konnert (1980). The general term minimised was:

$D = \Sigma_{hkl} (w_{hkl}[|F_o^{hkl}|^2 - |F_c^{hkl}|^2)^2)$

w_{hkl} ..... weight for the reflection at (h,k,l)

$|F_o^{hkl}|^2$ ... square of the observed structure factor (= intensity) at hkl

$|F_c^{hkl}|^2$ .... square of the calculated structure factor at hkl

Structure factors (F_c) of the model were calculated by conventional structure factor summation and only isotropic B-factors were refined. Cross-validation (Brünger 1992) was performed with 5% of the data. SHELXWAT is a program which uses SHELXL to identify positive peaks in the difference electron density as possible water oxygen atoms, adding them to the structure and refining the extended model. Usually several consecutive cycles of peak searching and refinement are carried out.

SNAPSHOT.. UNIX utility program to convert part of the screen display into an RGB image file.

SSS_ALIGN . (Sturrock 1997) for comparisons of protein residue sequences

X-PLOR..... The program, first published by Brünger et al. (1987), was used for molecular replacement to determine the protein crystal structure by combining empirical, geometric and effective energy terms describing the experimental data. The combined energy function was minimised by gradient descents, simulated annealing, or conformational search procedures. 5% of the data were used for free R-factor cross-validation (Brünger 1992).

The *rotation function search* was performed by maximising the function: $RF = < P_{obs} * P_{model}(\Omega) >$

P_{obs} ..... Patterson vectors calculated from the observed data

P_{model} .... Patterson vectors calculated from the model structure at orientation Ω

The model orientations with highest solutions for RF were used for a Patterson correlation refinement by minimising the function:

$E_{total}(\Omega,\Omega_i,t_i) = (1 - PC(\Omega,\Omega_i,t_i))$ where

$PC(\Omega,\Omega_i,t_i) = < |E_{obs}|^2 |E_m(\Omega,\Omega_i,t_i)|^2 - < |E_{obs}|^2 > < |E_m(\Omega,\Omega_i,t_i)|^2 > > *$

$* (< |E_{obs}|^4 - <|E_{obs}|^2>^2 > < |E_m(\Omega,\Omega_i,t_i)|^4 - <|E_m(\Omega,\Omega_i,t_i)|^2>^2 >)^{-1/2}$

Ω..... overall orientation

Ω_i ..... individual orientations

t_i ..... individual translations

E_{obs}..... normalised observed structure factors

$E_m(\Omega,\Omega_i,t_i)$.. normalised structure factors of the search model placed in a triclinic unit cell identical in geometry to that of the crystal

The angle brackets denote an averaging over the set of observed reflections expanded to spacegroup P1.

In the *translation function search* the function minimised was the correlation function of $E_{obs}(hkl)$ and $E_c(hkl)$:

$$T = < E_{obs}(hkl)^2 * E_c(hkl)^2 - < E_{obs}(hkl)^2 > < E_c(hkl)^2 > > *$$

$$* (< E_{obs}(hkl)^2 - < E_{obs}(hkl)^2 >^2 > < E_c(hkl)^2 - < E_c(hkl)^2 >^2 >)^{-1/2}$$

E_{obs}...normalised observed structure factors

E_c .....normalised structure factor calculated with the model

The normalised structure factors E(hkl) are computed from the structure factors F(hkl) by averaging F(hkl) in equal reciprocal volume shells within the specified resolution limits.

Angle brackets denote a weighted averaging over all selected Miller indices.

During *rigid body refinement* the six rotational and translational degrees of freedom for each specified group of atoms of the model were minimised, i.e. the groups of atoms are treated as rigid bodies. The rotational parameters were the three Eulerian angles for a rotation around the geometric centre of the rigid group and the three translational parameters were x,y,z. The function minimised was:

$$E_{XREF.} = W_A/N_A * \Sigma(w_{hkl}[|F_{obs}(hkl)|^2-|F_c(hkl)|^2])$$

W_A ..... overall weight

N_A ..... normalisation factor

w_{hkl} ..... individual weights for the reflections

$F_{obs}(hkl)$.... observed structure factors

$F_c(hkl)$ ..... calculated structure factors

Positional refinement was carried out by conjugate gradient minimisation (Powell 1977) of :

$E_{total} = \Sigma(w_{bond}E_{bond} + w_{angle}E_{angle} + w_{impr}E_{impr} + w_{VDW}E_{VDW} +$

$+ w_{dihe}E_{dihe} + w_{PWDV}E_{PWDV}) + E_{XREF}$

w.....weight for individual pairs of atoms

E_{bond}.....covalent bond energy

E_{angle} .....bond angle energy

E_{dihe} .....dihedral angle energy

E_{impr}.....improper dihedral angle energy

E_{VDW}.....intramolecular van der Waals energy

E_{PWDV} ...symmetry-related van der Waals energy

During isotropic *B-factor refinement* the refined function was E_{XREF}. Anisotropic B-factor refinement was not attempted.

The *simulated annealing* process used is described by Brünger et al. (1990). The T coupling method was used to enforce temperature control during the molecular dynamics simulation to solve for $r_i(t)$ in:

$m_i\partial^2 r_i / \partial t^2 = - \nabla_i E_{total} - m_i\gamma_i\upsilon_i(1 - T/T_{curr})$ with

$E_{total} = \Sigma(w_{bond}E_{bond} + w_{angle}E_{angle} + w_{impr}E_{impr} + w_{VDW}E_{VDW} +$

$+ w_{dihe}E_{dihe} + w_{PWDV}E_{PWDV}) + E_{XREF}$

m_i.....mass of atom i

r_i .....co-ordinates of atom i

t .....time

E_{pot}.....potential energy

γ_i .....friction coefficient of atom i

υ_i .....velocity of atom i

T .....target temperature

T_{curr}.....current temperature

The temperature at the start was set to 3000K and sequentially dropped by 25K after calculating co-ordinates by molecular dynamics simulation. The final temperature was set to 300K followed by

conjugate gradient minimisation (Powell 1977) of the co-ordinates of the model.

XV..... Image display and modifying program used under UNIX X-WINDOWS. Copyright held by John Bradley (1994).

3. Structural studies of α- and β-actin : gelsolin segment 1

3.1 Introduction

The structure of actin has previously been determined in complex with three different actin binding proteins (Table 3.1).

α-actin :DNaseI	Kabsch et al. 1990
α-actin : gelsolin segment 1	McLaughlin et al. 1993
β-actin (tight state) : profilin	Schutt et al. 1993
β-actin (open state) : profilin	Chik et al. 1996

Table 3.1

The orientation of the major domains of actin (see chapter 1) opens up by almost 10° when β-actin changes from the tight to the open state. The orientation in the α-actin structures is in between the two for β-actin and differs by 5° when comparing tight-state β-actin to both α-actin structures. This shows that the actin structure has scope for flexibility, and can adopt different conformations when bound to different proteins and crystallised under different conditions. Segment 1 of gelsolin (G1) binds close to the profilin binding site on actin, between subdomains 1 and 3 (see chapter 1). DNaseI binds opposite the G1 binding site on top of subdomain 2 and contacting subdomain 4 (see chapter 1). A detailed summary and analysis of conformational changes between those actin complexes was published by Page et al. (1998).

If the conformational difference between α-actin and β-actin (tight state) is not due to the sequence difference between α- and β-isoform (see chapter 1), then this conformational difference is forced on actin by either the crystallisation conditions, the associated protein (profilin, DNaseI, or G1), or a mixture of influences. Gelsolin segment 1 has a very high affinity (K_D~ 4.5pM in the presence of Ca^{2+}) for actin and on binding inhibits the exchange of the nucleotide bound to actin (Bryan 1988). This is most likely due to the narrowing of the nucleotide binding cleft between the major domains, which would conceivably impede the dissociation of the bound nucleotide.

In order to investigate the influence of G1 binding on the conformation of both actin isoforms, the structure of β-actin:G1C needed to be determined and possible differences between the structures examined. We decided to determine both structures at 100K, because X-ray diffraction of protein crystals at 100K yields better quality diffraction to higher resolution than at room temperature and at the same time considerably reduces the adverse effects of radiation damage (Hope 1990, Rodgers 1997). The previous structure of α-actin:G1 had been determined at room temperature to 2.5Å. Only 52 water oxygen atoms had been located and the co-ordination sphere of the Ca^{2+} ions was incomplete. Several loops were located in regions of weak electron density, particularly the loop in subdomain 2 which makes the majority of contacts between DNaseI and actin.

Determination of the structure of β-actin:G1C at 100K and comparing it to the structure of α-actin:G1C also determined at 100K should give a more detailed picture of the actin complex with G1 and enable comparisons without having to allow for conformational differences due to data collection at 100K instead of room temperature. Also it was hoped that diffraction data at 100K would help localising mobile regions in the structure.

The 100K structure of α-actin:G1C was obtained in the course of trials to determine the structure of α-actin:G1 with bound ADP instead of ATP. The structure resulting from those trials retained the ATP and could serendipitously be used for the comparison with β-actin:G1

3.2 The structure of α-actin:G1C at 100K

3.2.1 Complex formation and crystallisation

The purification and crystallisation procedures used are described in detail in chapter 2. These procedures had been used for unsuccessful trials for obtaining α-actin:G1C crystals containing ADP instead of ATP bound to actin. The structure obtained from those crystals at 100K was of ATP-α-actin and was used for comparisons with ATP-β-actin also determined at 100K.

3.2.1.1 Preparing α-actin from rabbit muscle acetone powder

Rabbit muscle tissue was ground through a hand mincer, washed, and an acetone powder prepared. The yield from roughly 1kg of muscle tissue was 43g of dry acetone powder. Actin was extracted from acetone powder with low ionic strength buffer (G-buffer), filtered, and purified by cycles of polymerisation and depolymerisation followed by gel-filtration over an S200 column. The actin yield over 5 extractions was 1.5±0.4% (w/w) of the acetone powder.

3.2.1.2 Expression and purification of N57C gelsolin segment 1 (G1C):

Ca^{2+} competent *E.coli* of strain BL21(DE3) were transformed with a plasmid encoding genes for an isopropyl-β-D-thiogalactopyranoside (IPTG) activated promotor, for ampicillin resistance, and for G1C (residues 25-149 of human plasma gelsolin, point mutation N57C, M_r = 14048).

G1C differs from native gelsolin segment 1 at residue 57, where Asn 57 had been replaced with Cys. The mutation had been introduced with the aim of facilitating the formation of heavy metal derivatives of the crystals. These derivatives had not been

made because the α-actin model from the complex with DNaseI (Kabsch et al. 1990) could be used to solve the structure of α-actin :G1. Incidentally α-actin:G1C crystals grew to larger sizes than α-actin:G1(native) crystals (McLaughlin et al. 1993). Subsequently G1C was used for crystallisation with actin.

Cells were grown, lysed and G1C extracted by binding to a DEAE-anion exchange column. G1C was further purified by gel filtration over a Sephacryl S200 column (see chapter 2). Between 9mg and 40mg of protein were recovered per initial litre of *E.coli* culture.

3.2.1.3 Formation of the complex:

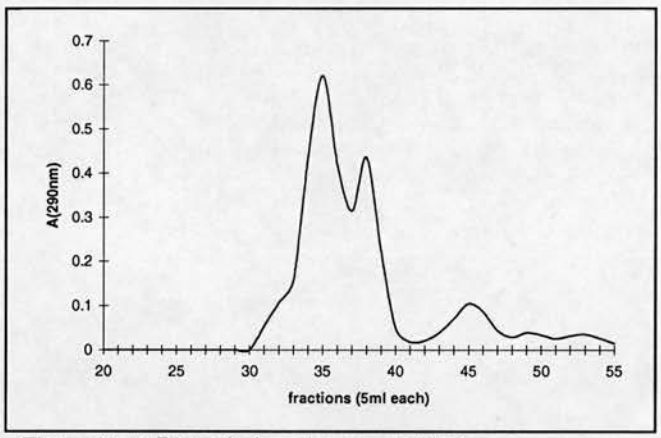

Figure 3.1: Plot of absorbance at 290nm versus fraction number of α-actin:G1C S200 column run. ATP-G-buffer was used as blank during the measurement.

For purposes of converting ATP-actin to ADP-actin (see chapter 2), actin was extracted from rabbit muscle acetone powder and incubated with Dowex-1 beads, ADP, glucose, and hexokinase immobilised on agarose beads. After removal of the beads G1C was immediately added and the complex gel-filtered over a S200 column in the presence of ADP and without any ATP (Figure 3.1 and Figure 3.2). Approximately 12% of the maximum theoretical recovery for α-actin:G1C was pure enough for crystallisation trials.

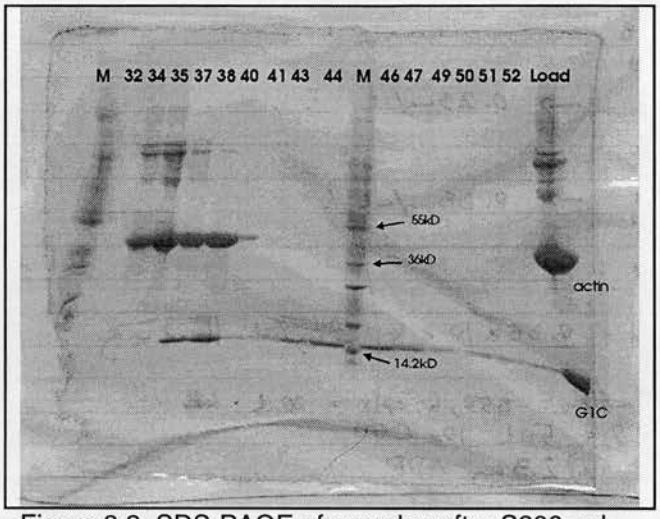

Figure 3.2: SDS-PAGE of samples after S200 gel-filtration of α-actin:G1C complex (Figure 3.1). Numbers indicate the fraction from which the sample was taken. M indicates wide range molecular weight marker, Load is a sample from before the column run. Complexed protein in fractions 37-41 was used for crystallisation. Fractions 43-52 contained uncomplexed G1C.

3.2.1.4 Crystallisation:

The hanging drop crystallisation procedure is described in chapter 2. The crystallisation buffer contained 0.1mM ADP, 0.15M NaCl, 0.1mM $CaCl_2$, 0.1mM $MgCl_2$, 1mM NaN_3, 10mM DTT, 50mM MES pH6.6 and 5-9% (w/v) polyethylene glycol 6000.

Crystals of similar size and shape as ATP-α-actin:G1C resulted from crystallisation trials (Figure 3.3). These plate-shaped clear crystals varied in size with the largest growing to 1 x 0.25 x 0.03 mm (estimated according to the microscope reference grid) . Most crystals had satellite crystals growing on them or were obviously twinned. The influence of β-octyl glucoside (McPherson et al. 1986) to 0.75% (w/v) and glycerol to 2% (v/v) in the crystallisation buffer was also studied. No substantial increase in crystal size could be seen, but at 0.5 and 0.75% (w/v) β-octyl glucoside,

crystal size decreased markedly. Single crystals or fragments with dimensions of at least 0.25 x 0.1 x 0.05 mm were used for X-ray diffraction analysis.

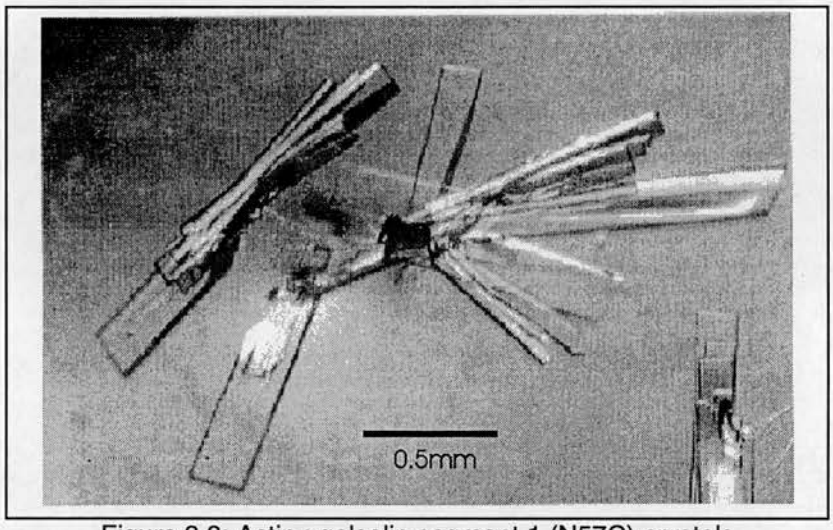

Figure 3.3: Actin : gelsolin segment 1 (N57C) crystals

3.2.2 X-ray diffraction analysis

Crystallographic and refinement data	
Temperature:	100K
Spacegroup:	$P2_12_12_1$
Refined Cell Dimensions:	a = 57.33 Å
	b = 70.88 Å
	c = 183.58 Å
	$\alpha=\beta=\gamma=90.00°$
Resolution range:	2.3 - 15.4Å
Completeness of data:	89.1%
Mean multiplicity:	3.3
Unique reflections:	28998
R_{sym}:	0.092
$\langle I \rangle / \sigma(I)$ (2.33-2.46Å)	3.0
$\langle I \rangle / \sigma(I)$ (all data)	5.7

Table 3.2

The plate-shaped clear crystals (Figure 3.3), obtained as described above, were stable in a crystallisation buffer containing additional 20% (v/v) of glycerol. This solution was used to incubate the crystals before flash-freezing in the nitrogen cryo-stream to achieve a vitreous frozen state of the drop containing the crystal (see chapter 2).

A dataset was collected at DESY Hamburg on beamline X11 using a wavelength of 0.911Å (Table 3.2). The data were autoindexed and processed using MOSFLM (see chapter 2).

3.2.3 Molecular replacement

The co-ordinates of α-actin:G1C solved at room temperature were used as the starting model. Rigid body refinement against the data (4.0 - 8.0Å) was performed with XPLOR (see chapter 2). Positional and grouped B-factor refinement with XPLOR was alternated with displaying the model with O (see chapter 2) and comparing it to "ordinary" OMIT maps (Hodel et al. 1992) calculated with XPLOR. These were sigmaA-weighted 2Fo-Fc maps, which were calculated omitting a region of 30 residues (6% of total residues in model) plus any atoms closer than 5Å to any of the atoms of the selected 30 residues. Only the region omitted for map calculation was compared to its OMIT map. Step by step the chains of α–actin and G1C were compared against the respective OMIT maps. The position of residue side chains was altered when it did not fit the electron density of the OMIT map. After several cycles of refinement the R-factor decreased from an initial 0.414 to 0.316 and R_{free} (for 5% of the data) from 0.406 to 0.379.

For practical reasons water peak identification and addition of water oxygens to the model was performed with SHELX (see chapter 2). Also electron density maps calculated after refinement with SHELX provided better quality electron density maps than with XPLOR. Water oxygen atoms were added in the position of the

highest positive peaks in sigmaA-weighted Fo-Fc maps selecting for peaks which had a height of more than 1.5 x σ and were at a distance between 2.2Å and 4.0Å from any protein oxygen or nitrogen, or peaks with greater difference electron density.

In between cycles of refinement and water addition with SHELX the model was compared to sigmaA-weighted 2Fo-Fc and Fo-Fc maps. The free R-factor (5% of the data) dropped from 0.300 to 0.248 and refinement was continued until R_{cryst} converged to 0.174 and any further refinement caused R-free to increase.

To test the validity of the refined model a simulated-annealed (SA) OMIT map (Hodel et al. 1992) was calculated with XPLOR omitting the ATP, residues 200 to 207 of actin, and Lys115 of G1C. The omitted protein residues were chosen because of their high RMS distances (Figure 3.4) to the starting model after least-squares fitting the main chains of the two complexes over each other with LSQMAN (see chapter 2) and calculating RMS distances with the CCP4 program COMPAR (see chapter 2).

Comparing SA-OMIT maps (Figure 3.5, Figure 3.6, Figure 3.7) with the refined model confirms the presence of the γ-phosphate of ATP and the altered conformation of actin loop 200 to 207. In the case of Lys115 of G1C a sigmaA-weighted Fo-Fc map calculated after the initial rigid body refinement and the SA-OMIT Fo-Fc map calculated starting with the refined structure indicate the change in side chain conformation. The decrease of the average B-factor for Lys115 from 60Å^2 in the room temperature model to 31Å^2 in the 100K model could suggest this to be the more stable side chain conformation, since this decrease is 2.7 times higher than the average B-factor decrease for the protein complex.

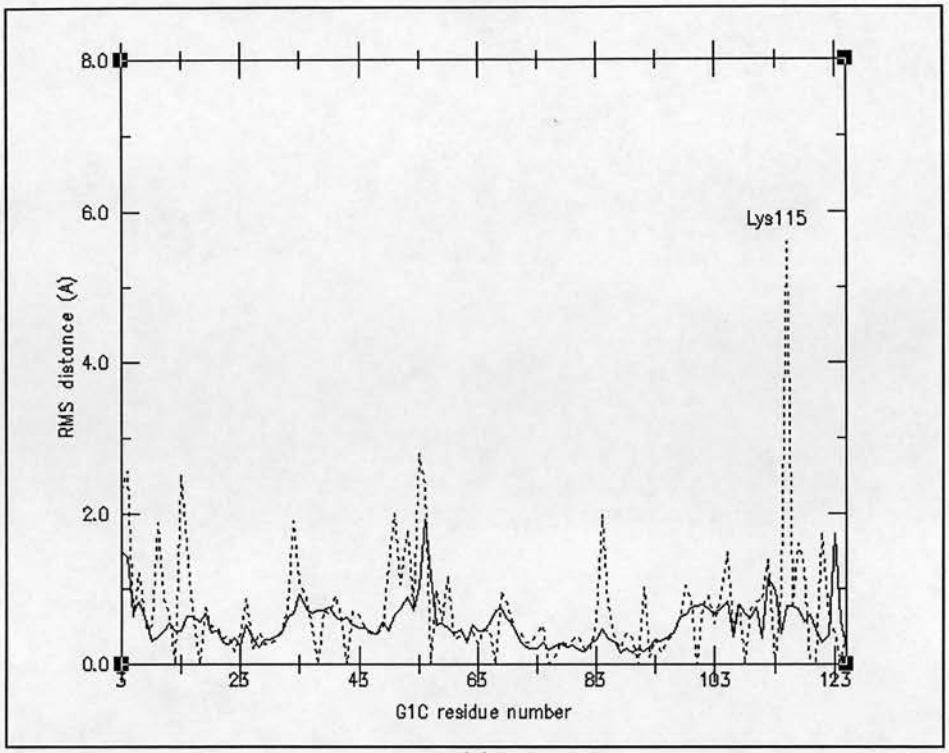

(a)

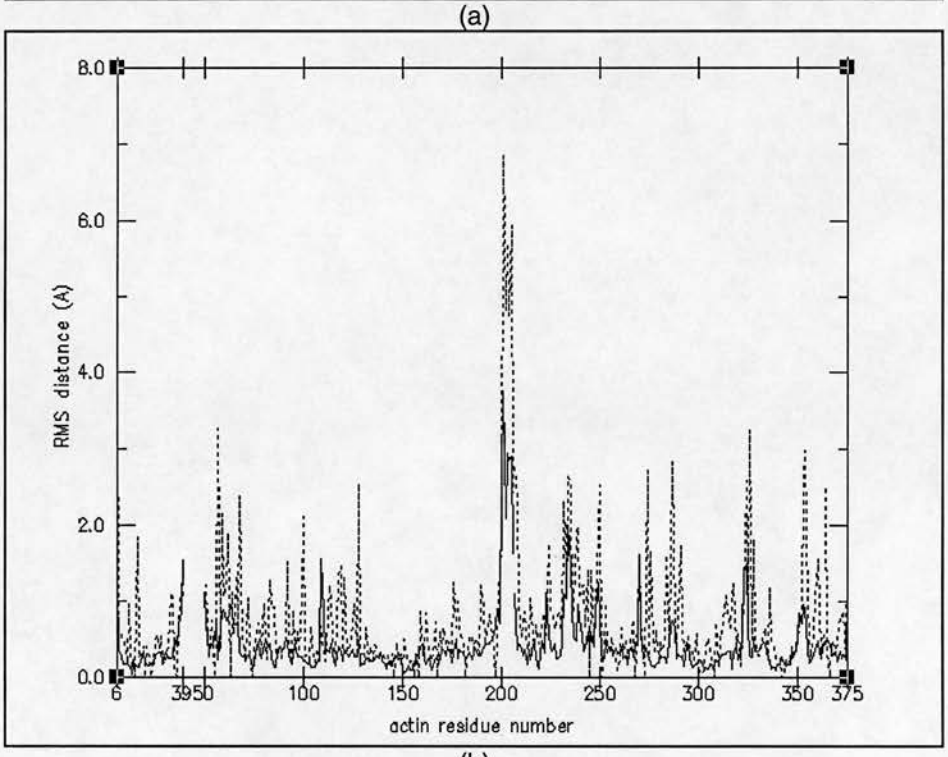

(b)

Figure 3.4: RMS distances between α-actin and G1C of the room temperature and the 100K model. RMS distances calculated for main chain atoms only are shown with a solid line. RMS distances calculated for side chains are shown with a dashed line. (b) RMS distances between α-actin at 100K and RT. The plot was generated using XMgr, SNAPSHOT, and XV.

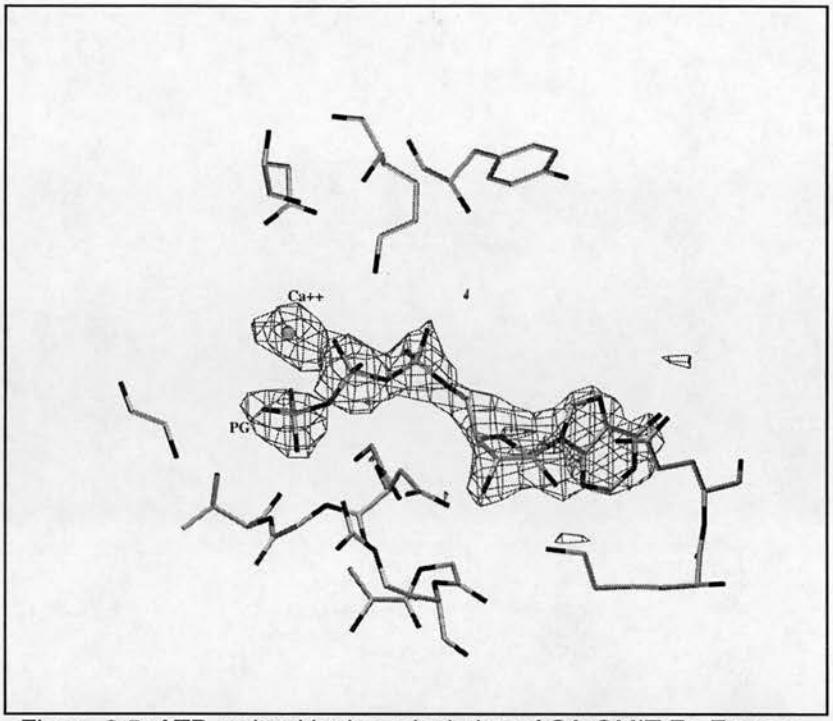

Figure 3.5: ATP omitted in the calculation of SA-OMIT Fo-Fc map. The ATP can be seen in the middle of the picture. The gamma-phosphate is labelled "PG" and the calcium ion "Ca++". The SA-OMIT Fo-Fc map was drawn at a contouring level of 2.2xσ. The picture was generated using Oplot.

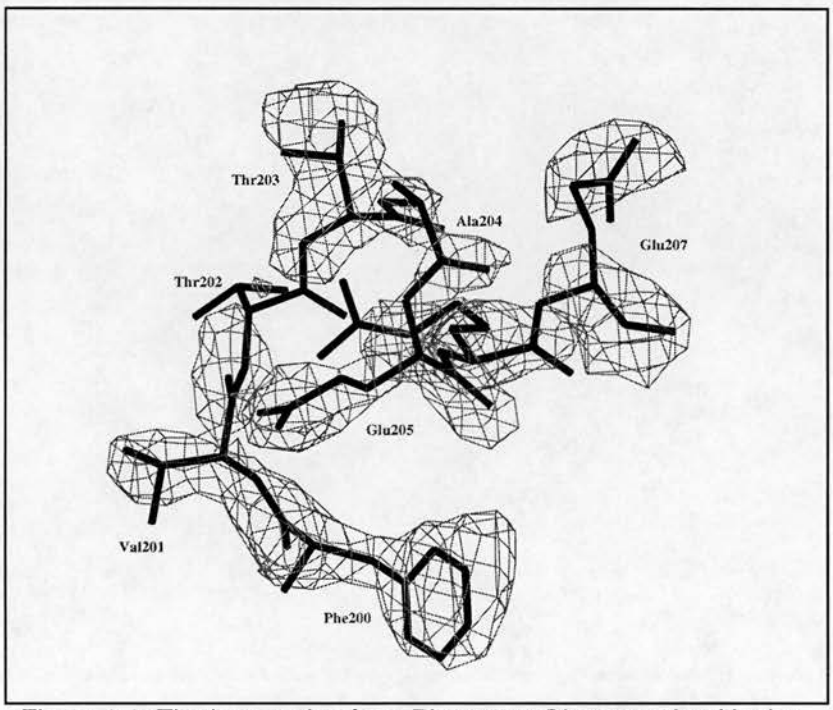

Figure 3.6: The loop region from Phe200 to Glu207 omitted in the calculation of SA-OMIT Fo-Fc map. The map is contoured to 1.5xσ. The pictures were generated using Oplot.

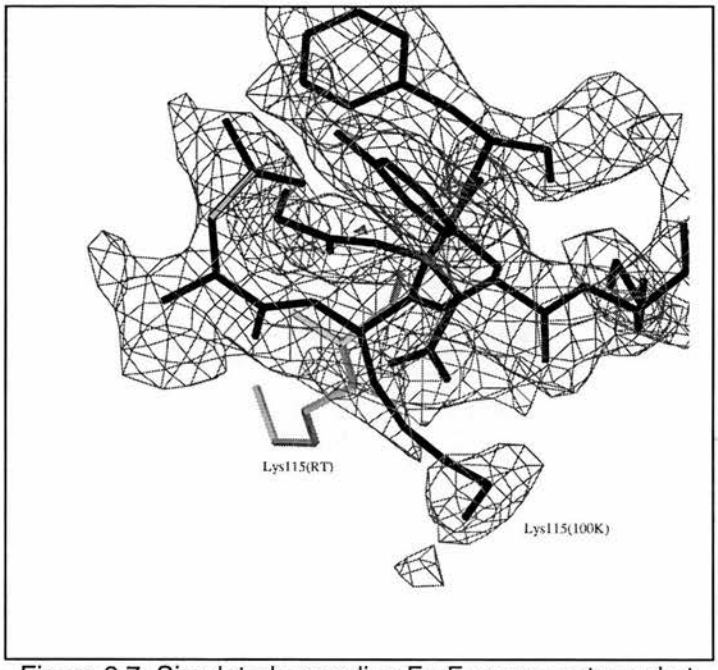

Figure 3.7: Simulated annealing Fo-Fc map contoured at 1.5xσ of the refined structure after omitting Lys115 (G1C) and any residues with an atom at a distance of 5Å or less to any atom of Lys115. Black residues are from the refined structure and Lys115 of G1C (at RT) is shown in grey. The picture was generated using Oplot.

Results of refinement:		
Atoms in asymmetric unit:	2856	atoms of α-actin
	995	atoms of gelsolin segment 1
	31	atoms of ATP
	3	calcium ions
	611	water oxygen atoms
	4496	non-hydrogen atoms
Omitted residues in very weak electron density areas: 1-5 and 40-50 of α-actin		
Average B-factors:	33.9 Å^2...all atoms	
	30.3 Å^2...all main chain atoms	
	34.5 Å^2...all side chain atoms	
	33.6 Å^2...α-actin	
	30.3 Å^2...gelsolin segment 1	
	23.0 Å^2...ATP	
	25.3 Å^2...calcium ions	
	43.8 Å^2...solvent	
RMS deviation from mean B-factor:	10.5 Å^2 for main chain atoms	
	15.9 Å^2 for side chain atoms	
RMS deviations from small molecule data:		
Bonds (1-2 neighbours): 0.007Å		
Angles (1-3 neighbours): 1.54°		
RMS deviation from planarity:		
4.6° for Torsion angle of peptide bonds		
0.00118 Å for planar side chains		
R_{cryst}: 0.174 for all data to 2.3Å		

Table 3.3

Analysis of the refined model is shown in Table 3.3 and the Ramachandran plot shown as Figure 3.8 with appropriate statistics in Table 3.4. Actin residues 232 and 233 are highlighted in the Ramachandran plot as "generously" allowed. These two residues are located at the solvent-exposed C-terminal end of a short α–helix at the side of sub-domain 4 of actin. The electron density is rather weak in this area, which is reflected by the average B-factors of Ser232 and Ser233, 88.5Å^2 and 80.3Å^2 respectively. Since the electron density maps did not suggest a better conformation, the residues were left in their refined positions.

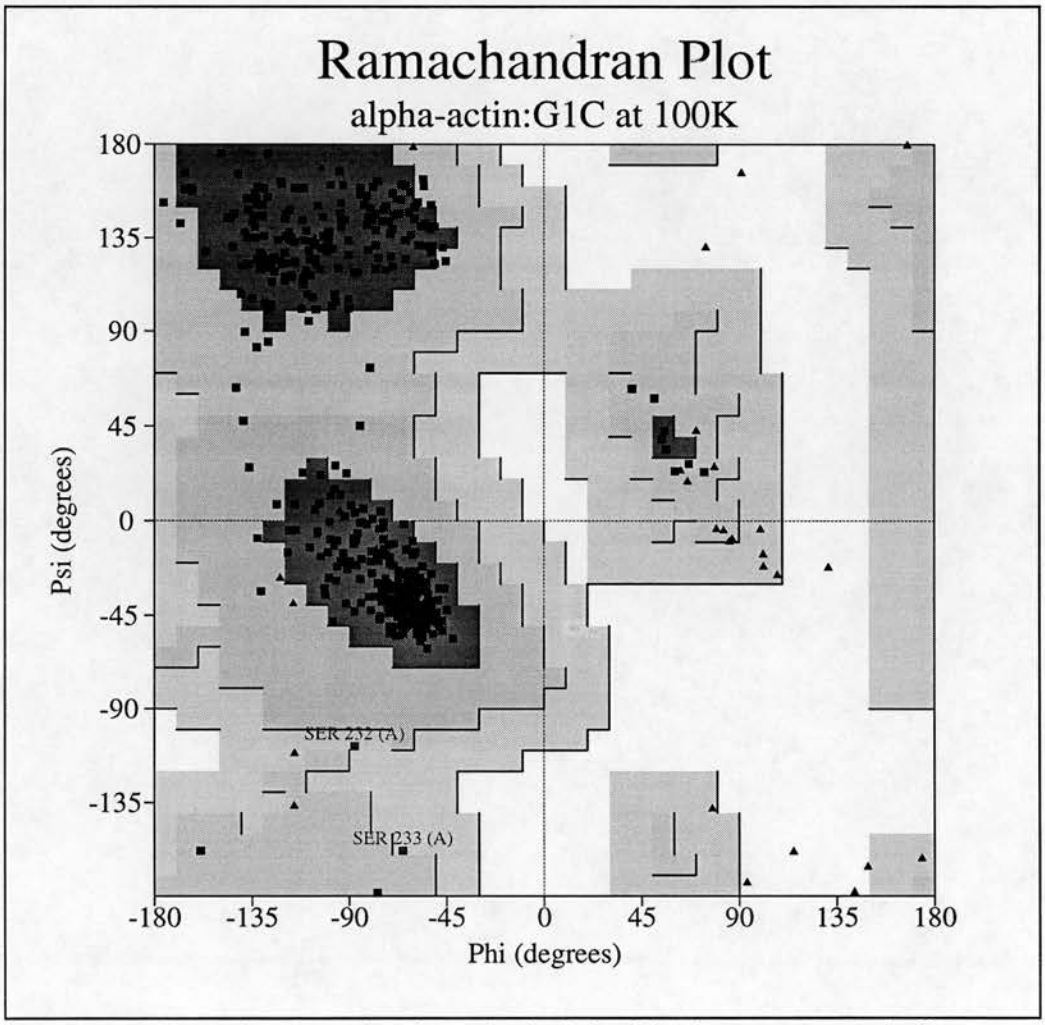

Figure 3.8: Ramachandran plot of α-actin:G1C (100K). Picture generated with PROCHECK. Glycines are represented with black triangles, all other residues with black squares.

Ramachandran plot statistics:		
Residues in most favoured regions (dark grey)	387	92.8%
Residues in additional allowed regions (grey)	28	6.7%
Residues in generously allowed regions (light grey)	2	0.5%
Residues in disallowed regions	0	0.0%
Number of non-glycine and non-proline residues	417	100.0%
Number of end-residues (excl. Gly, Pro, incl. ATP, Ca^{2+})	10	
Number of glycine residues	39	
Number of proline residues	23	
Total number of residues	489	

Table 3.4

3.2.4 Comparison of α-actin:G1C structures at room temperature and at 100K

In the α-actin:G1C structures at both temperatures the residues 40 to 49 of could not be located reliably in electron density maps. In the room temperature model of the complex the first two residues of G1C had not been located but in the 100K model sufficient electron density was visible to locate them.

Figure 3.9: LSQ fitted C-α traces of α-actin:G1C at room temperature (grey) and 100K (black). The picture was generated using Oplot.

Small conformational changes distinguish the structures of the two complexes (Figure 3.9). which is reflected in the low RMS distance of the main chains (0.54 Å) calculated with LSQMAN.

The average B-factor over all atoms of G1C and α–actin measured at room temperature was 44.6 $Å^2$. This value dropped for the complex X-rayed at 100K to 33.9 $Å^2$. The average B-factor for G1C residues decreased by 7.1$Å^2$, less than for α-actin residues where the average B-factor decreased by 12.6$Å^2$. As can be seen in Figure 3.10 the distribution of B-factors over the residues is very similar in both structures with values for the 100K structure being generally lower.

A larger decrease in B-factors can be observed with several loop regions at the surface of the proteins but without significant conformational change of the main chain. The residues involved of G1C are 32-39, 66-68, 99-104, and 112-125, and of actin 186-193 (subdomain 4), 219-225 (subdomain 4), and 306-329 (subdomain 3). The higher degree of order in those regions is presumably a general effect of cooling the crystal to 100K.

In G1C the only region with decreased temperature factors accompanied with significant conformational change is located around Lys115. The side chain moved to avoid contact with the side chain of Lys113 of a symmetry related actin.

As indicated in Figure 3.4 and Figure 3.9 the largest conformational change of the actin main chain occurred in a loop at the top of actin subdomain 4 involving residues 200 to 207. For this actin loop region the averaged B-factor dropped by 31.2$Å^2$ (sd = 8.6$Å^2$). This change in conformation and localisation could be explained by the lower temperature used during data collection which caused a stabilisation of this mobile surface loop.

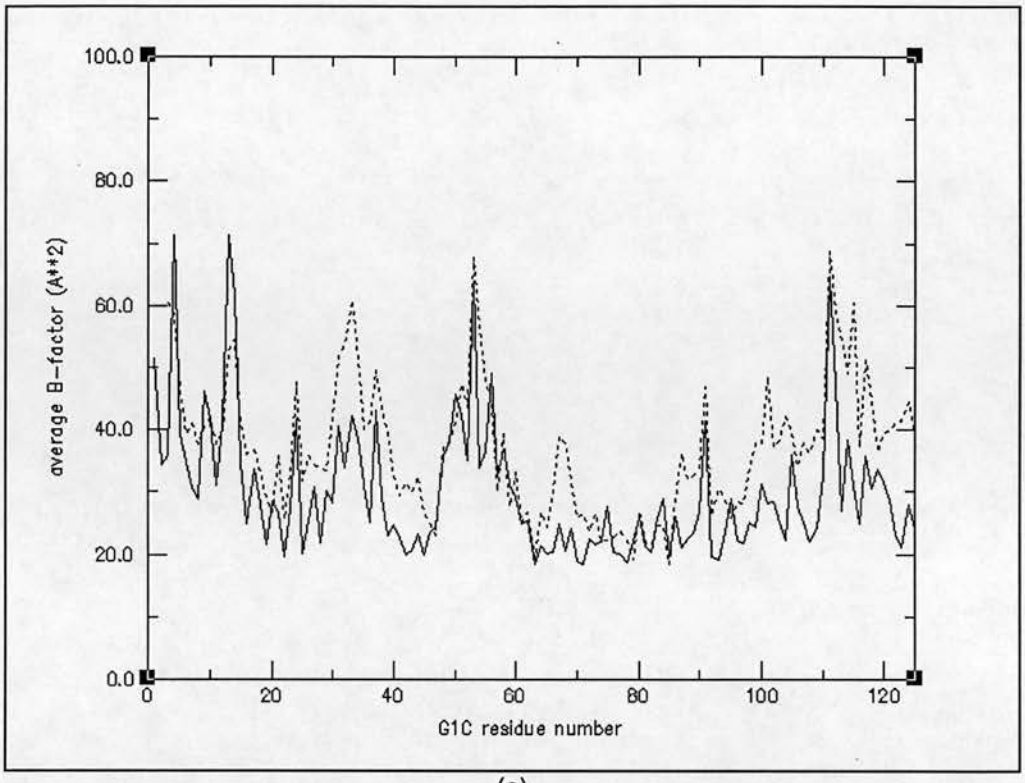

(a)

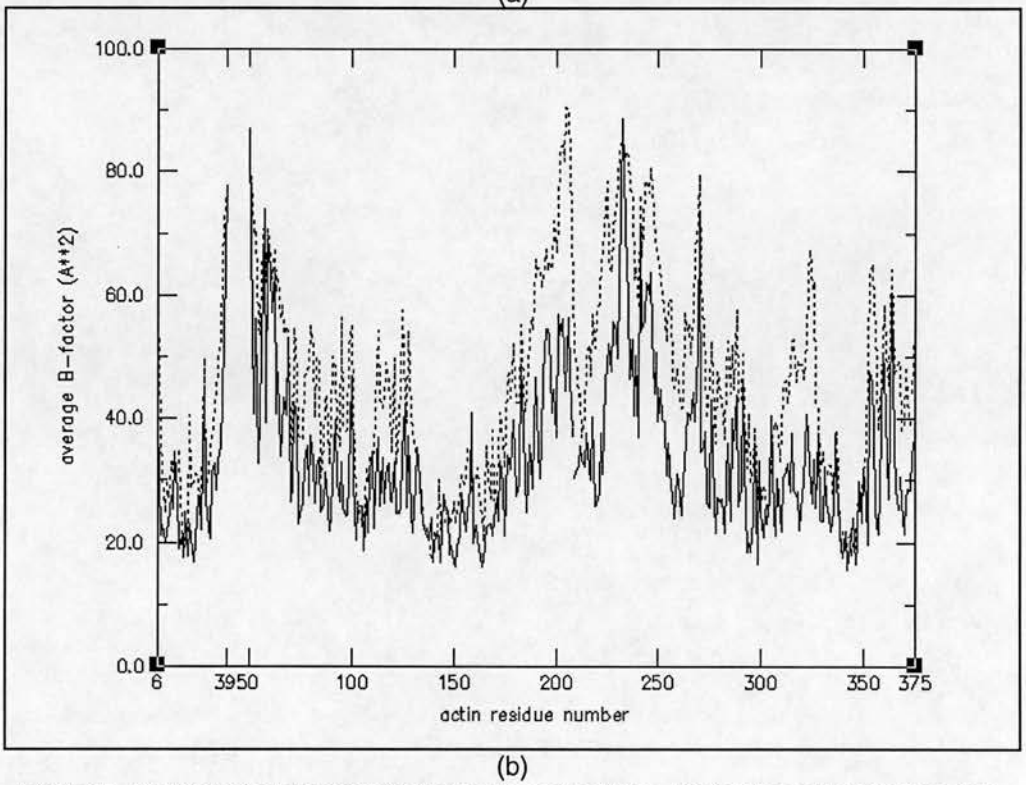

(b)

Figure 3.10: Plot of average B-factors versus residues. Solid lines show values for the 100K model, dashed lines for the room temperature model. The pictures were generated using XMgr, SNAPSHOT, and XV.(a) Comparison of G1C at 100K and at room temperature. (b) Comparison of α-actin at 100K and at room temperature.

In the model for α-actin:G1C at room temperature 52 water oxygens had been localised. At 100K the order of the crystal increased sufficiently to localise 611 water oxygens. Of the water molecules found in addition to the RT water molecules one is co-ordinated to Ca^{2+} in the ATP binding site of actin, three to the intermolecular Ca^{2+} between actin and G1C, and one to the G1C intramolecular Ca^{2+}. All Ca^{2+} ions are therefore sevenfold co-ordinated in the form of a pentagonal bipyramid. Apart from the additional water oxygens no difference was observed in calcium co-ordination between the model at room temperature and at 100K.

3.3 The structure of β-actin : gelsolin segment 1

3.3.1 Complex formation and crystallisation

3.3.1.1 Preparing β-actin from platelet acetone powder:

The purification and crystallisation procedures used are described in detail in chapter 2. Human blood platelets were obtained from the Blood Transfusion Unit of the Edinburgh Royal Infirmary and from Dr. Steve Winder (ICMB). After several washing steps 1.5l of platelets suspended in blood plasma yielded approximately 10ml packed platelets and resulted in roughly 1g of acetone powder. β-Actin was extracted from the acetone powder with a low salt (G) buffer and purified by several cycles of polymerisation, depolymerisation, and gel-filtration. For each gram of platelet acetone powder (70ml packed platelets) 0.6mg platelet actin were recovered.

3.3.1.2 Formation of the complex:

The N57C mutant of gelsolin segment 1 (G1C) was expressed and purified as described in 3.2.1.2. β-Actin extracted from platelet acetone powder was mixed with G1C in a ratio of 1:1 and the complex purified by gel-filtration over Sephacryl S200. Approximately 60% of the theoretical recovery for the complex was obtained pure enough to be used for crystallisation.

3.3.1.3 Crystallisation:

Crystals were obtained in hanging drops as described in chapter 2. The crystallisation buffer contained 0.1mM ATP, 150mM NaCl, 0.1mM $CaCl_2$, 0.1mM $MgCl_2$, 1mM NaN_3, 10mM DTT, 50mM MES pH6.0-pH7.3 and 3-12%(w/v) PEG 6000.

Crystal of similar size and shape as ATP-α-actin:G1C resulted from crystallisation trials with 5-6% PEG at pH6.0 and 6-8% PEG at pH6.6 (Figure 3.3). These plate-shaped clear crystals varied in size with the largest growing to 1 x 0.25 x 0.05 mm. Most crystals had satellite crystals growing on them or were obviously twinned. Smaller single crystals or fragments grown at pH6.6 were used for X-ray diffraction analysis.

3.3.2 X-ray diffraction analysis

The crystals grown at pH6.6 and mounted in a glass capillary diffracted to 3Å at the home source at room temperature. The intensity of the diffraction spots measured on a MAR image plate was poor. There was no change in diffraction quality after immersing the crystal in crystallisation buffer which contained additional 25%(v/v)

glycerol, flash-freezing in liquid nitrogen and X-raying at 100K. Data collection was therefore deferred to synchrotron beam time.

A synchrotron dataset, 77% complete to 2.3Å, for one crystal grown at pH6.6 was collected at the DESY Hamburg beamline BW7A and at 100K using a wavelength of 0.995 Å. Spacegroup and cell parameters obtained from autoindexing and processing of the data matched with those of α-actin:G1C. After data collection the crystal was retrieved and stored in liquid nitrogen. To complete this dataset, a second dataset of the same crystal was collected at the SRS Daresbury on beamline PX7.2 using a wavelength of 1.488 Å (Table 3.5).

Crystallographic and refinement data of merged datasets	
Temperature:	100K
Spacegroup:	$P2_12_12_1$
Refined Cell Dimensions:	a = 57.36 Å
	b = 69.67 Å
	c = 182.18 Å
	$\alpha = \beta = \gamma = 90.0°$
Resolution range:	2.3 - 32.3 Å
Completeness of data:	99.3%
Multiplicity:	3.8
Unique reflections:	37659
R_{sym}:	0.097
$\langle I \rangle / \sigma(I)$ (2.30-2.42Å)	2.8
$\langle I \rangle / \sigma(I)$ (all data)	4.9

Table 3.5

3.3.3 Molecular replacement

The co-ordinates of the α-actin:G1C complex solved at room temperature (McLaughlin et al.,1993) were used as a starting model for the cross-rotation search. The rotation search and the Patterson correlation of the highest 141 results of the rotation search were performed with XPLOR. The orientation with the highest rotation function value (11.2 x σ) was close to the starting model. Orientations with the highest Patterson correlation coefficient were either symmetry related or related

by a rotation of up to 1° to the original orientation. A translation search with the model rotated according to the highest result of the Patterson correlation was performed with XPLOR. The position with the highest translation function value was found to be very close to a symmetry related position of the α-actin:G1C complex, bearing in mind that the unit cells of the two complexes are very similar.

XPLOR rigid body refinement of actin models (McLaughlin, Schutt, and Kabsch), positioned according to the rotation-translation solution, converged in all cases from an initial R_{cryst} of 0.48 to 0.40, with the R_{free} (5% of the data) dropping from 0.48 to 0.45. SigmaA weighted 2Fo-Fc maps were calculated phasing on the rigid body refined actin models. The strongest map was obtained when phasing on the rigid body refined (α-)actin model from Kabsch. The map also followed large parts of the main chain of a G1C model (Figure 3.11). The G1C model had been taken from the α-actin:G1C complex (McLaughlin) after an LSQ fit of the actin main chain over the actin main chain of the rigid body refined model. Electron density for parts of the G1C chain was visible in a sigmaA-weighted 2Fo-Fc map. Calculation of a sigmaA-weighted Fo-Fc map and examination of the highest 64 peaks (4.0xσ cut-off) in the difference map revealed 20 peaks to be in the area where G1C was expected to be according to the LSQ fit described above. This was taken as proof that the position of actin in the β-actin:G1C structure was correct .

Because of the better electron density map quality and also to avoid introducing unnecessary bias from the α–actin:G1C structure solved at room temperature, the structure of α–actin from the complex with DNaseI (Kabsch) was chosen for further refinement against the observed diffraction data.

A new model structure was created by adding the co-ordinates of G1C (McLaughlin), moved as described above for map examination, to the rigid body refined α–actin co-ordinates (Kabsch). This model structure was refined as a rigid body, followed by

cycles of positional and grouped B-factor refinement until the R_{cryst} dropped to 0.35 and R_{free} to 0.40.

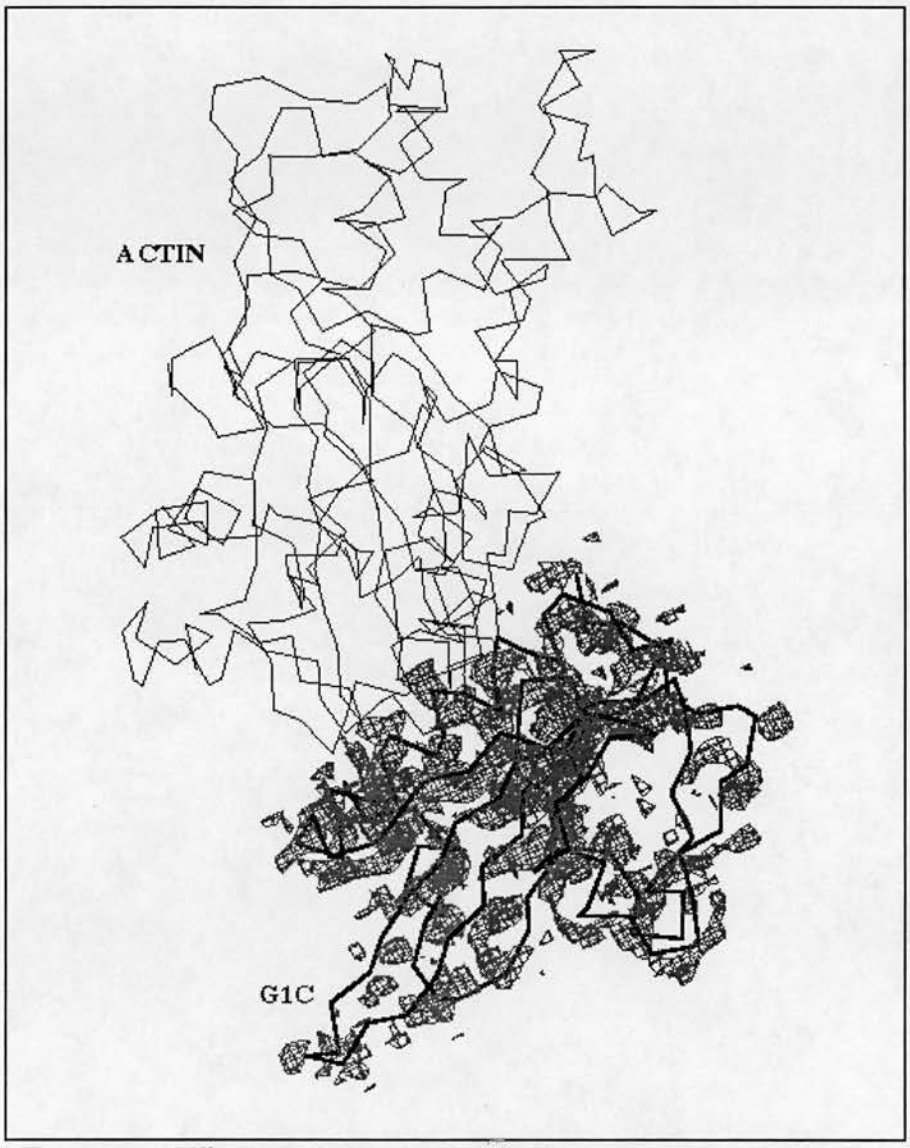

Figure 3.11: Difference electron density for G1C. The picture shows α-actin taken from the complex with DNaseI (Kabsch et al.), superimposed over the main chain of α-actin from the G1C room temperature complex (McLaughlin et al.) and refined as a rigid body against the data for β-actin:G1C. The electron density from the sigmaA-weighted Fo-Fc map is contoured at 1.5xσ The picture was generated with Oplot.

To test the reliability of the refinement a residue side chain was chosen, which had not been moved in respect to the starting model. His161 of actin was moved out of its

refined position followed by positional and grouped B-factor refinement. In the test refined model XPLOR had moved the side chain half-way towards the originally refined position. SigmaA-weighted electron density maps were calculated using the test refined model. The 2Fo-Fc electron density map clearly showed density in the originally refined position and the Fo-Fc map displayed a positive peak in the original position and a negative peak over a part of the test refined His161 side chain. This was evidence that the maps were not over-biased by the chosen starting model.

Further positional and grouped B-factor refinement with XPLOR continued until the R_{cryst} reached 0.26 (R_{free} for 5% of the data was 0.35). The model was compared to sigmaA weighted "ordinary" OMIT maps (Hodel et al. 1992).

```
beta     2 DDDIAALVVDNGSGMCKAGFAGDDAPRAVFPSIVGRPRHQGVMVGMGQKDSYVGDEAQSK 61
           :|:.:||| |||||: ||||||||||||||||||||||||||||||||||||||||||||
alpha    2 EDETTALVCDNGSGLVKAGFAGDDAPRAVFPSIVGRPRHQGVMVGMGQKDSYVGDEAQSK 61

beta    62 RGILTLKYPIEHGIVTNWDDMEKIWHHTFYNELRVAPEEHPVLLTEAPLNPKANREKMTQ 121
           |||||||||||||:|||||||||||||||||||||||.||||||||||||||||||
alpha   62 RGILTLKYPIEHGIITNWDDMEKIWHHTFYNELRVAPEEHPTLLTEAPLNPKANREKMTQ 121

beta   122 IMFETFNTPAMYVAIQAVLSLYASGRTTGIVMDSGDGVTHTVPIYEGYALPHAILRLDLA 181
           |||||||.|||||||||||||||||||:||||||||:|||||||||||||:|||||
alpha  122 IMFETFNVPAMYVAIQAVLSLYASGRTTGIVLDSGDGVTHNVPIYEGYALPHAIMRLDLA 181

beta   182 GRDLTDYLMKILTERGYSFTTTAEREIVRDIKEKLCYVALDFEQEMATAASSSSLEKSYE 241
           ||||||||||||||||||.|||||||||||||||||||||:||||||||||||||||
alpha  182 GRDLTDYLMKILTERGYSFVTTAEREIVRDIKEKLCYVALDFENEMATAASSSSLEKSYE 241

beta   242 LPDGQVITIGNERFRCPEALFQPSFLGMESCGIHETTFNSIMKCDVDIRKDLYANTVLSG 301
           ||||||||||||||||||:|||||||:|||| ||||||:|||||||:|||||||||:|:||
alpha  242 LPDGQVITIGNERFRCPETLFQPSFIGMESAGIHETTYNSIMKCDIDIRKDLYANNVMSG 301

beta   302 GTTMYPGIADRMQKEITALAPSTMKIKIIAPPERKYSVWIGGSILASLSTFQQMWISKQE 361
           |||||||||||||||||||||||||||||||||||||||||||||||||||||||:|||
alpha  302 GTTMYPGIADRMQKEITALAPSTMKIKIIAPPERKYSVWIGGSILASLSTFQQMWITKQE 361

beta   362 YDESGPSIVHRKCF 375
           |||:||||||||||
alpha  362 YDEAGPSIVHRKCF 375
```

Table 3.6: Sequence alignment between mammalian β- and α-actin. Sequence identity 93.58%; Sequence conservation 98.13%; Matches 350; Conservative 17; Mismatches 7

The sequence of β-actin differs at 24 amino acids from the sequence of α-actin, of which 17 are neutral replacements, 7 introduce or eliminate a group capable of hydrogen bonding, none change a full charge, and none differ significantly in size

(Table 3.6). As the model used was α-actin, the sequence had to be changed to β-actin. SigmaA weighted OMIT 2Fo-Fc and Fo-Fc maps were compared to the refined model and the sequence changed to match the β-actin sequence. In most cases the maps were not clear enough to show the difference in sequence. Only in the case of L16M, L153M, N162T (Figure 3.12), I267L, A272C, and Y279F did the maps give a clear indication of the necessary sequence change to the model.

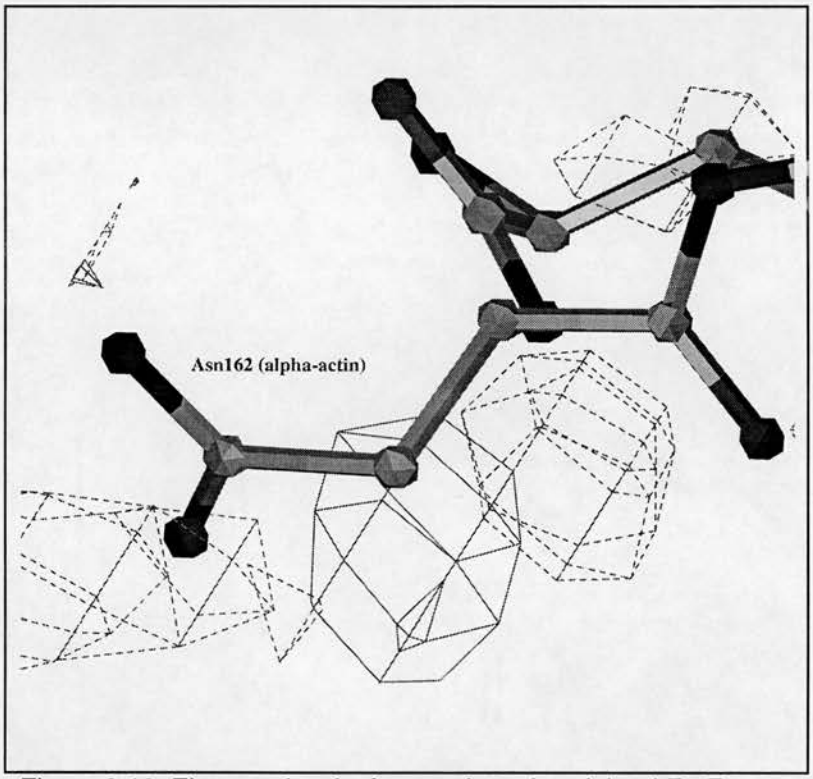

Figure 3.12: Electron density from a sigmaA-weighted Fo-Fc map calculated with the refined model before changing the sequence of actin to the β-isoform. The picture (Oplot) shows residue 162 of actin which is Asn in the α- and Thr in the β-isoform. Positive difference density (solid lines) contoured at 3xσ indicates OG1 of Thr and negative difference density (dashed lines) contoured at 1.5xσ indicates non-existence of OD1 of Asn.

Water oxygen atoms were added to the structure by obtaining the co-ordinates of the positive peaks in a sigmaA weighted Fo-Fc map and selecting for peaks which had a height of more than 1.5 x σ and were at a distance between 2.2Å and 4.0Å from any

protein oxygen or nitrogen, or peak with higher density. For practical reasons water addition and further refinement was done with SHELX (see chapter 2).

Results of the refinement		
Atoms found in asymmetric unit:	995	atoms of gelsolin segment 1
	2799	atoms of β-actin
	31	atoms of ATP
	3	calcium ions
	670	water oxygen atoms
	4498	non-hydrogen atoms
Omitted residues in very weak electron density areas: 1-5 and 40-51 of actin		
Average B-factors:	31.5 Å2...all atoms	
	26.9 Å2...all main chain atoms	
	31.2 Å2...all side chain atoms	
	27.0 Å2...gelsolin segment 1	
	29.7 Å2...β-actin	
	21.1 Å2...ATP	
	20.5 Å2...calcium ions	
	45.5 Å2...water	
RMS deviation from mean B-factor:	8.6 Å2 for main chain atoms	
	13.1 Å2 for side chain atoms	
RMS deviations from small molecule data:		
Bonds (1-2 neighbours): 0.008 Å		
Angles (1-3 neighbours): 1.554°		
RMS deviation from planarity:		
4.5° for Torsion angle of peptide bonds		
0.0015 Å for planar side chains		
R_{cryst}: 0.184 for all data to 2.2Å		

Table 3.7

Ramachandran plot statistics:		
Residues in most favoured regions (dark grey):	385	92.8%
Residues in additional allowed regions (grey):	30	7.2%
Residues in generously allowed regions (light grey):	0	0.0%
Residues in disallowed regions:	0	0.0%
Number of non-glycine and non-proline residues:	415	100.0%
Number of end-residues (excl. Gly, Pro, incl. ATP, Ca^{2+}):	10	
Number of glycine residues:	39	
Number of proline residues:	23	
Total number of residues:	487	

Table 3.8

During the refinement the R_{free} dropped from 0.329 to 0.238. Further refinement resulted in a final R_{cryst} of 0.184. Final analysis of the refined structure is compiled in Table 3.7, Table 3.8, and Figure 3.13.

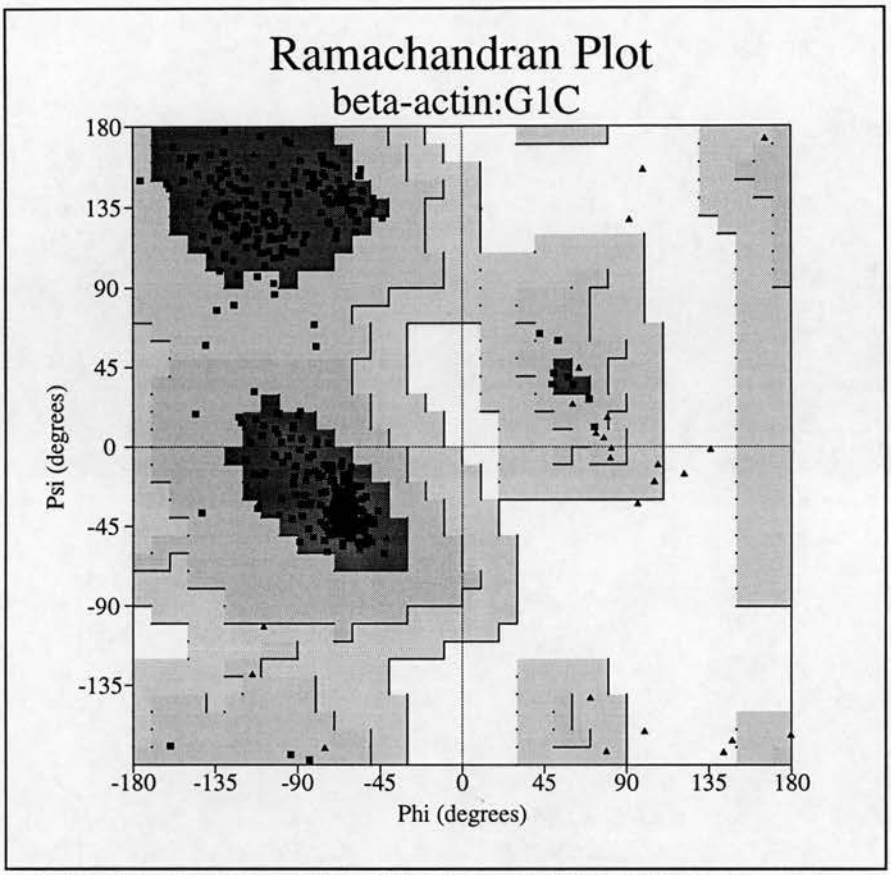

Figure 3.13: Ramachandran plot of β-actin:G1C. Glycines are represented with black triangles, all other residues with black squares.

3.3.4 Conformational changes during refinement

Lys 115 of G1C displayed a large RMS distance (4.3Å) for its side chain between starting model and refined position. Incidentally, the refined position is identical to the one refined for the 100K α-actin:G1C structure.

Actin residues with the largest main chain deviations are 201 to 207, which form a small flexible surface loop on top of subdomain 4 and are, in addition to the DNaseI binding loop, involved in binding to DNaseI. This loop also changed appreciably during the refinement of the model for low temperature α-actin:G1C.

3.3.5 Comparison of actin structures

In order to get an overview of how similar the refined β–actin structure is to other actin structures, previous actin structures were fitted over the refined β-actin using LSQMAN (see chapter 2). The main chain atoms of either most actin residues (11-39,52-370) or of the large domain core of actin (Page et al. 1998) were used for the superpositions.

The large domain core of actin (Figure 3.14) consists of residues 145-161, 164-182, 184-185, 188-192, 211-213, 216-217, 225-228, 254-267, 272-286, 288-290, 292-293, 309-315, and 330-333, and is the most rigid body in the large actin domain when comparing actins (Page et al. 1998) from the complex with DNaseI (Kabsch et al. 1990), with G1C at room temperature (McLaughlin et al. 1993), with profilin in closed (Schutt et al. 1993) and open conformation (Chik et al. 1996). Averaged RMS deviations in Å are given in Table 3.9.

mean RMS dev. of	most residues	LDC residues	most residues
having LSQ fitted over	most residues	LDC residues	LDC residues
α-actin (100K)	0.314	0.284	0.322
α-actin (Kabsch et al.)	0.865	0.347	0.915
α-actin (McLaughlin et al.)	0.553	0.279	0.591
β-actin (Schutt et al.)	1.028	0.418	1.234
β-actin (Chik et al.)	1.569	0.380	2.483

Table 3.9: Mean main chain RMS deviations to the refined β-actin model. Actin structures from the complex with G1C at 100K, with DNaseI (Kabsch et al. 1990), with G1C at room temperature (McLaughlin et al.1993), with profilin in closed (Schutt et al.,1993) and open conformation (Chik et al.,1996) were LSQ fitted over the refined model for β-actin in complex with G1C at 100K. Mean RMS deviations (in Å) were calculated for either most actin residues (11-39,52-370) or only large domain core (LDC) residues.

The average RMS deviation calculated over most actin residues show that the main chain of the refined model for β-actin is most similar to the one of α-actin in complex with G1C and also X-rayed at 100K. Individual fits of main chains of α-actin to β-actin and G1C (α-actin) to G1C (β-actin) resulted in RMS deviations of

0.32Å and 0.35Å respectively. Visualisation of main chain traces of superimposed structures confirms this high degree of structural similarity.

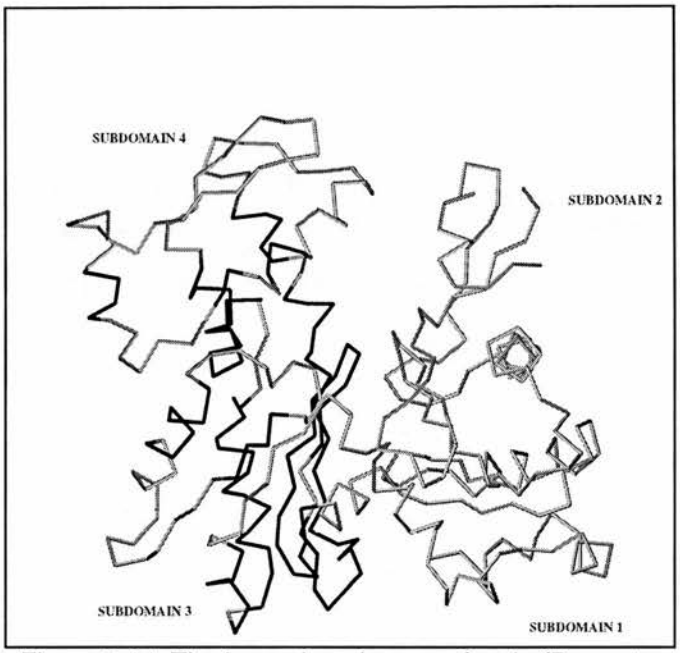

Figure 3.14: The large domain core of actin (Page et al., 1998). The picture shows a Cα trace of β-actin from the complex with G1C. Residues constituting the large domain core are drawn in black. The picture was created with Oplot.

3.3.6 Comparison of β-actin:G1C and α-actin:G1C

Main chain and side chain RMS deviations between the refined model of β-actin and superimposed α-actin taken from the complex with G1C (100K) do not reveal major differences between the two structures (Figure 3.15). No conformational differences are discernible at the ATP binding site and around the three Ca^{2+} ions which have the same ligands in both structures forming a pentagonal bipyramid around each calcium ion.

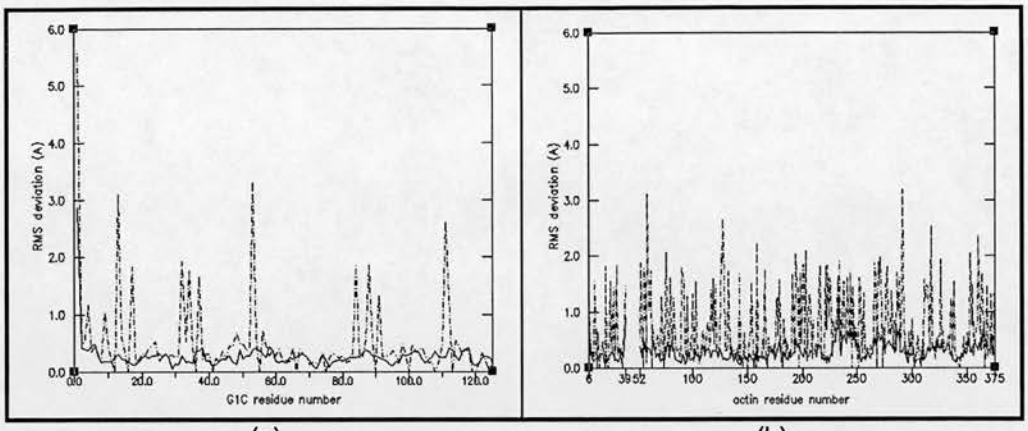

(a) (b)

Figure 3.15: RMS deviations of the refined β-actin:G1C model from the main chain LSQ fitted model of α-actin:G1C. The solid line represents deviations of the main chain, the dashed line deviations of the side chains. (a) RMS deviations for G1C. (b) RMS deviations for the actin isoforms.

The largest change observable in the conformation of the main chain is at Met1 of G1C which also displays the largest RMS distance between side chain atoms (Figure 3.15). The side chain of Met1 previously pointed away from actin residues. In the structure with β-actin it is close (3Å) to the side chain of Lys373, close to the C-terminus of actin. Both conformations seem plausible. Methionine does not have a strongly polar side chain and therefore the side chain would be expected to move to contact a more hydrophobic area of the protein. On the other hand the end of the lysine side chain is positively charged and would try to be solvated. In addition no amino acids different in the sequence of α- and β-actin are close. Therefore no preference for either conformation is immediately obvious.

Other differences in G1C side chain positions are located at Lys13, Arg53, and Lys111. All these residues are located at the surface of the protein and have very flexible side chains protruding out of the protein surface. Differences in conformation are therefore not surprising.

The largest observable differences in side chain position of actin residues are located at Gln59, Asn128, Lys291, and Ile317 (Figure 3.15). In the β-actin structure the Gln59-Arg62 and the Asn128-Lys359 side chain hydrogen bonds are shorter than in

the α-actin structure due to the conformational change of the Gln59 and the Asn128 side chains. Although Asn128 and Lys359 are each adjacent to an amino acid different in the α-actin sequence, this did not appear to have a direct influence on the conformational change.

There is no apparent reason for the conformational change of Ile317. It lies buried in the actin structure but in a less tightly packed region allowing some freedom of rotation around its Cα-Cβ bond. Lys291 protrudes from the protein surface and is not near any symmetry-related molecules allowing for unrestricted movement of the side chain. In both actin complexes Lys291 and Ile317 have average B-factors for their side chains of around 50Å^2 and 25Å^2 respectively. The reason why these side chains do not display a higher degree of disorder due to their freedom of movement is probably the higher degree of order imposed on the crystal due to the low temperature used during X-ray exposure.

Possible implications of the sequence difference between α- and β-actin were examined by LSQ fitting the structure of alpha-actin over beta-actin via the main chain and comparing the amino acids different in sequence. In terms of hydrogen bonds a net loss of three hydrogen bonds was found when switching from α- to β-sequence. It is possible that β-actin compensates for this loss of hydrogen bonds as illustrated by the conformational changes of the side chains of Gln59 and Asn128. No steric clashes could be found if the α-sequence was examined in the context of the β-actin structure. Taken all together the 24 changes in amino acid type appear to have a very subtle influence on the β-actin structure. Their role in the different kinetic properties displayed by α- and β-actin (see chapter 1) is not readily apparent.

3.3.7 Comparison of β-actin:G1C with tight-state β-actin:profilin

Of the two previously solved structures of bovine β–actin the tight state model (Schutt et al.,1993) fits the refined model of human β–actin better, bearing in mind that actin complexes with G1C do not reveal a conformation for actin residues 40 to 51. A plot of main chain and side chain RMS deviations of the superimposed models (Figure 3.16) reveals residues 52 to 66, 194 to 206 and 229 to 249 to be those which are most different in the two structures. Residues 52 to 66 are part of the very flexible subdomain 2. Residues 194 to 206 and 229 to 249 are loops at the top of subdomain 4. Arg37 is the residue with the highest side chain RMS deviation. It lies on the surface of subdomain 2 just before the N-terminal start of the disordered region 40-51.

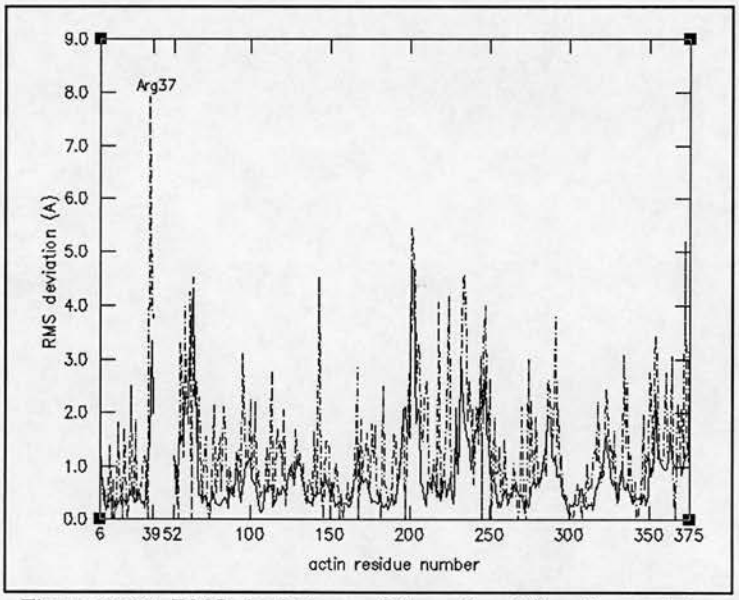

Figure 3.16: RMS deviations of the refined β-actin model from the LSQ fitted model of "tight" state β-actin from the complex with profilin. The solid line represents deviations of the main chain, the dashed line deviations of the side chains.

The superposition of the refined β–actin model and the tight β–actin model taken from the profilin complex (Schutt et al. 1993) results in a higher mean RMS

deviation than with α-actin (McLaughlin et al. 1993) (Table 3.9). When the whole complexes of β-actin:G1C and tight-state β-actin:profilin are superimposed using only the main chain of actin for the LSQ fit, profilin and G1C interpenetrate each other showing that it is most unlikely that they could bind to actin at the same time (Figure 3.17).

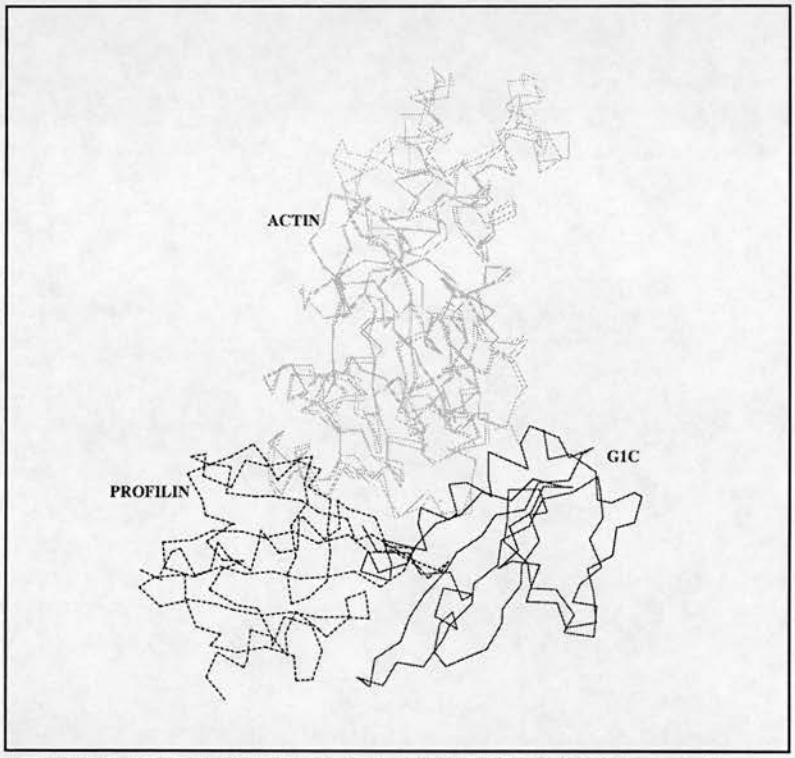

Figure 3.17: Superposition of β-actin:G1C and tight-state β-actin:profilin by LSQ fitting over the main chain of actin. The two actins are orientated with subdomain 1 behind and at the bottom, subdomain 4 at the top and in front. G1C is at the bottom right and profilin (dashed line) at bottom left.

Schutt et al. (1993) found a difference of about 5° between the orientations of the large and the small actin domain to each other in the model for α–actin (Kabsch et al. 1990) and their model for β–actin in complex with profilin. To estimate the equivalent orientational difference between the refined β-actin and tight-state β-actin (Schutt) the refined β–actin model was superimposed over β–actin (Schutt et al.) using in one case the main chain of subdomain 1 for the lsq-fit calculation, in the

other case subdomain 3, which is connected to subdomain 1 by the hinge region. The rotational angle to bring the two LSQ-fitted co-ordinate sets on top of each other is 4.9°. This concurs with the low main chain RMS deviation of the refined β–actin model to α–actin (X-rayed at 100K), α-actin (McLaughlin), and α-actin (Kabsch).

3.4 Conclusion

The comparison of the structures of α-actin:G1C at room temperature (McLaughlin et al.,1993) and at 100K revealed a drop in the overall temperature factor for the model structure by 11Å^2 (25% of the average room temperature B-factor). Small conformational changes, mainly at the surface exposed area of actin subdomain 4 account for a very low RMS main chain deviation (0.54Å) when superimposing the two complexes. As in the room temperature (RT) model the actin residues 40-50 in subdomain 2, which bind to DNaseI in the complex published by Kabsch et al. 1990, are too disordered in the crystal structure to be reliably traced in electron density maps. But the other DNaseI contacting region, residues 200-207 in subdomain 4, is far better localised in the 100K structure than in the RT model. In the 100K model the average B-factor for this loop dropped by 31Å^2 (38%) from 81Å^2 in the RT structure.

Six hundred and eleven water oxygens with an acceptable average B-factor of 44Å^2 have been located in the 100K structure as opposed to 52 in the RT structure. Five of the extra water completed the co-ordination shells around the three Ca^{2+} ions, confirming the seven-fold co-ordination in the form of a pentagonal bipyramid.

The determination of the α-actin:G1C structure at 100K has revealed additional information on the α-actin:G1C complex due to the higher structural order of mobile

loops, particularly of actin subdomain 4. The 100K structure is also a very good basis to allow comparative studies with the 100K structure of β-actin:G1C.

The conformation of the refined β–actin model from the complex with G1C, X-rayed at 100K, is closer to the conformation of α–actin complexed to G1C (100K) than to the conformations of the two previously published structures of β-actin (Schutt et al. 1993, Chik et al. 1996). The major conformational differences to the previously published β-actins are located at the solvent exposed parts of actin subdomain 2 and 4. Also the orientation of the large and the small actin domain to each other differs from the orientation in tight-state β–actin (Schutt et al.,1993) by about 5°, which is very similar to what Schutt et al. found when comparing their structure to Kabsch's α-actin. It appears that either the binding of G1C to β-actin or the chosen crystallisation conditions forced β-actin to adopt an "α-like" conformation.

Noteworthy differences between the structure of α-actin:G1C and β-actin:G1C are the N-terminus of G1C, where Met1 of G1C has adopted a conformation closer to the surface of β-actin. The difference in sequence between α- and β-actin did not cause any steric problems or major rearrangements but resulted in a net loss of three hydrogen bonds for β-actin. It is likely that β-actin can compensate for this, e.g. by the changed side chain conformation of Gln59 and Asn128 to move closer to hydrogen bonding partners. The bound ATP and localised water molecules in the β-actin:G1C structure did not display significant differences to their equivalents in the α-actin:G1C complex.

Since gelsolin can stably cap the barbed end of F-actin, one can assume that G1, which has the highest affinity for actin of all six gelsolin segments, does not change the actin conformation in a way which might lead to dissociation of the ternary gelsolin:actin complex from the barbed end of the actin filament. It could possibly be argued that the same might be true for tight β-actin:profilin complexes (Schutt et al. 1993). This would have to be reconciled with the fact that profilin does not cap the

barbed end of F-actin and is thought to dissociate from its actin as soon as its actin adds on to the barbed end of a filament (Pring et al. 1992).

If G1C is the responsible factor for forcing the same conformation on α- and β-actin, then it might be reasonable to assume, that unless the actin conformation found in complex with G1C is similar to the conformation of actin monomers at the barbed end of an actin filament, sufficient flexibility of the actin molecule should remain to enable it to adopt F-actin conformation, so that gelsolin can cap the barbed end of the filament.

4. Structural studies on gelsolin segment 1

4.1 Introduction

Gelsolin is a calcium-activated actin filament severing, capping, and nucleating protein, acting in eukaryotic non-muscle cells and in a secreted form in the blood stream (see chapter 1). It consists of six highly homologous segments with the first segment (G1) being essential for the severing activity. The structure of G1C (N57C mutant of G1) was determined in complex with α-actin (McLaughlin et al. 1993) and G1 as part of horse plasma gelsolin (Burtnick et al. 1997).

The structural similarity of G1 in the two structures demonstrates the stability of the G1 fold. The major difference between them is the presence of calcium ions in the α-actin:G1C complex. Two calcium ions are bound to G1C in this complex. The intermolecular ion has ligands from both G1C and actin. The G1C intramolecular Ca^{2+} is located near the C-terminus of G1. Equine gelsolin was crystallised without Ca^{2+} and the conformation is therefore that of inactive gelsolin in respect to actin binding.

A small but very significant difference between the two G1 structures is the peptide bond of Val145-Ala146. The peptide bond is in trans-conformation in G1C and the carbonyl oxygen interacts with the intramolecular Ca^{2+}. In the Ca^{2+} -free equine gelsolin structure the bond is in cis-conformation and the carbonyl oxygen and the potential Ca^{2+} binding site are on opposite sides of the peptide bond.

The α-actin:G1C complex was crystallised at pH6.6. Only at this low pH does the complex contain two calcium ions. At pH8.0 only one calcium ion is bound to the complex and the work of Weeds et al. (1995) suggests that this calcium ion is located at the G1-intramolecular site. The physiological role of both binding sites and the detailed activation mechanism of gelsolin by calcium has not yet been elucidated.

In order to investigate the structural influence of actin binding on the conformation of G1, it was considered necessary to obtain the calcium containing structure of G1, free of restraints resulting from association with actin or from being integrated in the gelsolin structure. This would allow the comparison of the structure of this protein domain on its own with its structure in the parent protein and in complex with another protein.

G1 was expressed in *E.coli* and the structure of the purified and crystallised protein determined by X-ray diffraction. For purposes of refinement, residues of expressed G1 had been numbered as in cytoplasmic gelsolin (Met 25 of secreted plasma gelsolin was Met1 in the G1 sequence). In this chapter residues of gelsolin or of gelsolin segments shall be numbered according to the sequence for plasma gelsolin unless specifically stated otherwise.

CapG, also known as Macrophage Capping Protein (Young et al. 1990), Mbh1 (Prendergast et al. 1991) or gCap39 (Yu et al. 1991), is a member of the gelsolin family of actin binding proteins and predominantly expressed in macrophages. It can cap the barbed end of F-actin in a Ca^{2+} dependant manner and dissociates from actin in the presence of phosphatidylinositol-4,5-bisphosphate. Unlike gelsolin it consists of only three homologous repeats (Mishra et al. 1994), cannot sever actin filaments and can be dissociated from the barbed end of F-actin by lowering the Ca^{2+} concentration (Young et al. 1990). This weaker affinity for actin would make a comparison between the structures of the first segment of CapG and gelsolin very interesting as it might allow further insight into the mechanism of gelsolin segment 1's specificity for actin. To enable these comparisons crystallisation trials were set up for the segment 1 of CapG with the intent to determine the structure by X-ray crystallography.

4.2 Structure determination of gelsolin segment 1

4.2.1 Purification and crystallisation

Human gelsolin segment 1 (residues 25-149 of human plasma gelsolin, M_r = 14058) was produced and purified as described in chapter 2. Calcium competent *E.coli* of strain BL21(DE3) were transformed with a plasmid encoding genes for an Isopropyl-β-D-thiogalactopyranoside (IPTG) activated promotor, for ampicillin resistance, and for G1. Cells were grown, lysed and G1 extracted by binding to a DEAE-anion exchange column. G1 was further purified by gel-filtration over a Sephacryl S200 column. The leading protein peak was discarded to avoids contamination with denatured protein and the second peak used for crystallisation (Figure 4.1 and Figure 4.2). The protein yield for crystallisation purposes varied from 8mg to 23mg per initial litre of *E.coli* culture.

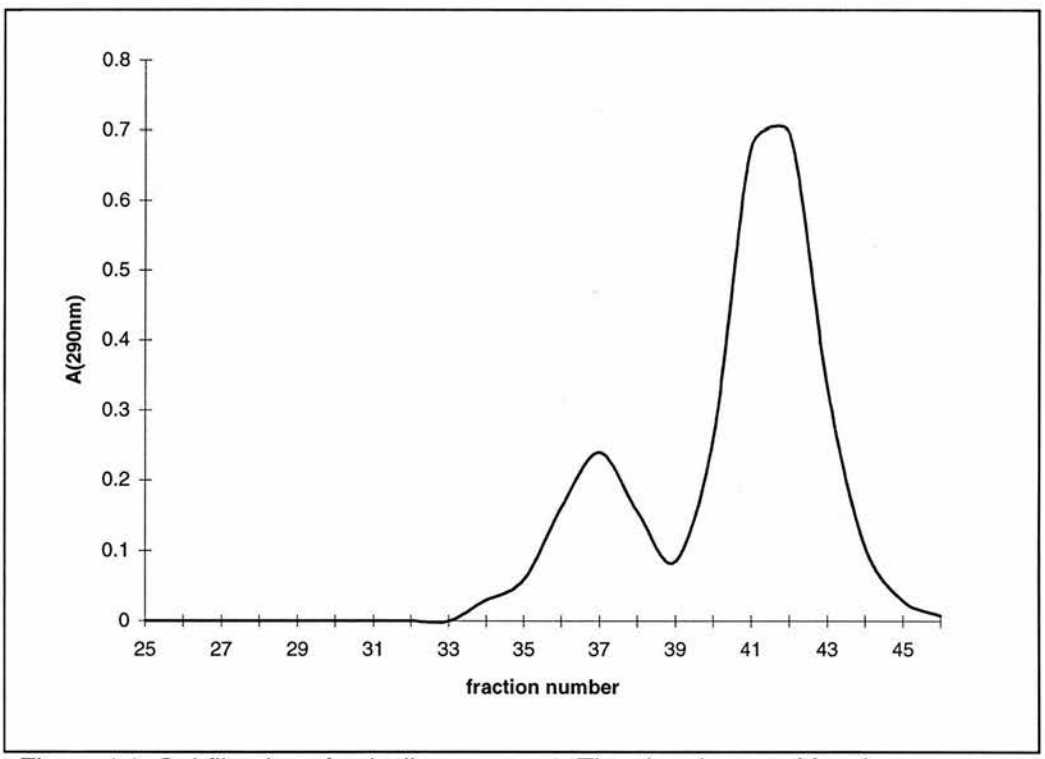

Figure 4.1: Gel-filtration of gelsolin segment 1. The absorbance of fractions at 290nm was measured against running buffer and plotted against fraction numbers. Fractions under the second peak were pooled and used for crystallisation.

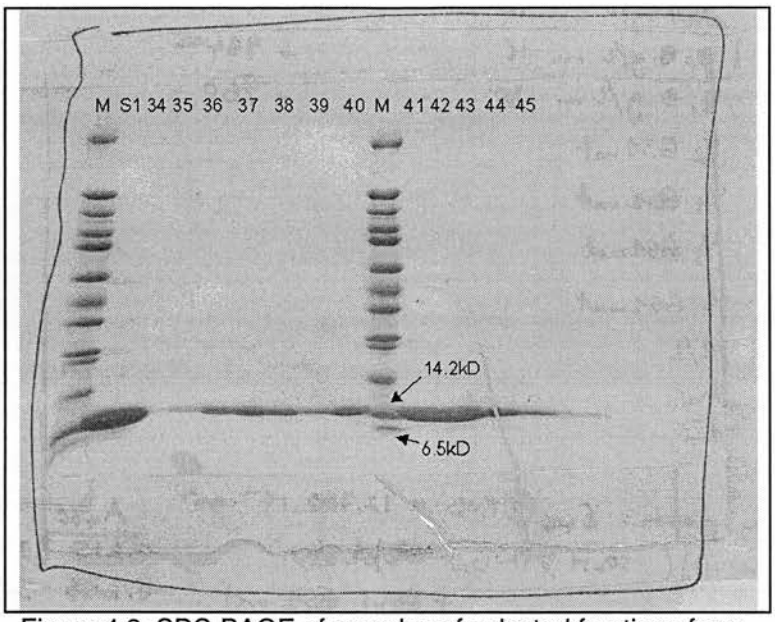

Figure 4.2: SDS-PAGE of samples of selected fractions from the G1 gel-filtration (Figure 4.1). M is a wide range molecular weight marker. S1 is from the concentrated solution before the gel-filtration run.

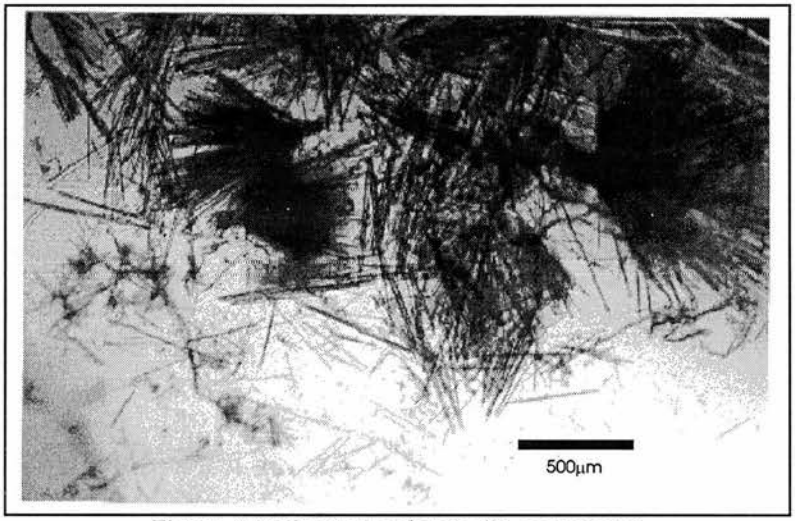

Figure 4.3: Crystals of gelsolin segment 1

To obtain crystallisation conditions, trials were performed using the "hanging drop" method. Initial trials revealed a precipitation border line between 1.5M and 2.0M ammonium sulphate at pH 7.9 and between 1.0M and 1.4M ammonium sulphate at pH 8.5. Trials with polyethylene glycol as precipitant did not prove successful.

Using 1mM $CaCl_2$, 1mM NaN_3, 10mM DTT, 50mM Tris or HEPES and 1.5 - 2.0M ammonium sulphate with the pH adjusted within the range of 7.6 to 7.9, needle-shaped colourless crystals were obtained. The larger crystals grew to dimensions of approximately 25x25x500μm (Figure 4.3). Micro- and macroseeding trials did not result in larger crystals. No crystals could be obtained at pH 8.5.

4.2.2 X-ray diffraction analysis

Diffraction data at room temperature were collected at the SRS Daresbury on beamline PX7.2. A crystal was sealed in a glass capillary and X-rayed at room temperature using a wavelength of 1.488Å. The resulting diffraction pattern was too weak to warrant collection of a full data set. Four images were taken, i.e. two pairs of images consecutive in oscillation angle and the two pairs separated by 90° rotation. The results of autoindexing were $P2_12_12_1$ for the spacegroup and unit cell parameters a=35.73Å, b=82.50Å, c=99.23Å, $\alpha=\beta=\gamma=90.0°$.

Crystallographic data from CCD and MAR datasets:	
Refined Cell Dimensions:	a=35.69 Å
	b=80.96 Å
	c=98.55 Å
	$\alpha = \beta = \gamma = 90.00°$
Resolution range:	2.2 - 31.3 Å
Completeness of data:	96%
Multiplicity:	6.3
Unique reflections:	14481
$\langle I \rangle / \sigma(I)$ (2.20-2.32Å)	10.9
$\langle I \rangle / \sigma(I)$ (all data)	11.3
R_{sym}:	0.046

Table 4.1

To obtain higher resolution and better quality of diffraction, crystals were flash-frozen in liquid nitrogen and X-rayed at 100 Kelvin. Two X-ray diffraction datasets

of the same crystal were collected at 100 Kelvin at the SRS Daresbury beamline PX9.6 using a wavelength of 0.87Å, the first with a temporarily installed CCD detector, the second with the reinstalled MAR image plate one month later. Autoindexing and processing with MOSFLM confirmed spacegroup and cell parameters for G1 crystals (Table 4.1).

4.2.3 Molecular replacement

The obtained values for unit cell and spacegroup together with the known M_r of 14kD for human G1 (blood plasma gelsolin residues 25-149) resulted in a reasonable solvent content of 51%, assuming two molecules per asymmetric unit and a protein density of 1.34g/cm^3 (Matthews 1968). A rather high solvent content of 76% was calculated assuming only one molecule per asymmetric unit, and a rather low solvent content of 27% assuming three molecules per asymmetric unit. Solvent contents for protein crystals usually range between 30% and 75% (Matthews 1968), so one or three molecules per asymmetric unit were considered to be less likely than two molecules per asymmetric unit.

The co-ordinates for the amino acids of G1C from the complex with α-actin at 100K (see chapter 3) were used as the search model. The rotation search, Patterson correlation refinement of the highest solutions of the rotation search differing by at least 10°, and translation searches were calculated with XPLOR (see chapter 2). The 14 highest (at least 1.8xσ higher than mean) solutions from the Patterson correlation refinement (Figure 4.4) were found to be either within 5.4° of the two highest solutions of the rotation search or related by 180°. The rotation parameters of the two highest solutions of the Patterson correlation were used in the translation function calculation to find the position of the two NCS related molecules in the asymmetric unit.

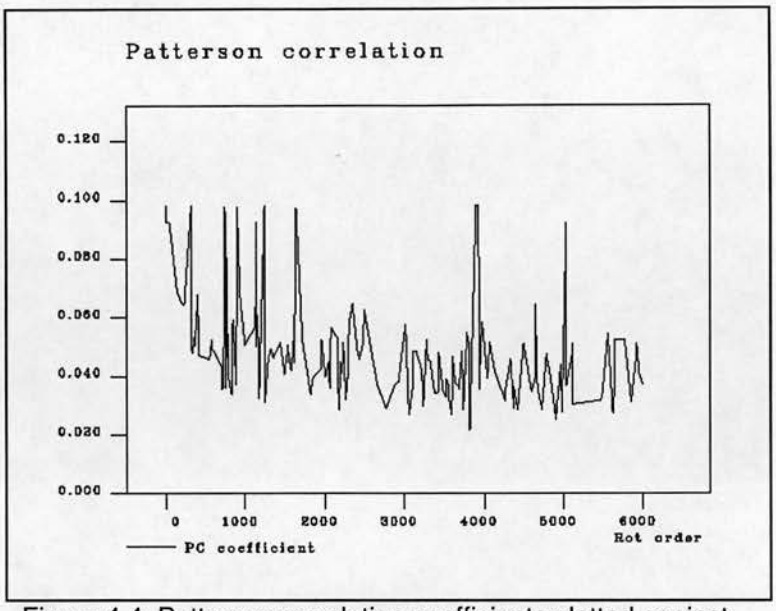

Figure 4.4: Patterson correlation coefficients plotted against their rotation function order. The Patterson correlation coefficient is plotted along the ordinate. The rotation function order is plotted along the abscissa according to the relative height of the rotation function solution with no.1 being the highest.

The two highest solutions of the translation search were investigated using the graphics program O (see chapter 2). No overlaps with each other or symmetry related molecules occurred and two adjacent molecules forming the asymmetric unit were chosen for further refinement against the observed data. The co-ordinates for the amino acids of these two molecules (G1A and G1B) were written into one file and used as input for the program XPLOR.

Rigid body refinement, using 4.0-9.0Å data, and subsequent positional and grouped B-factor refinement, using 2.2-9.0Å data, resulted in a crystallographic R-factor of 0.264 (R_{free} = 0.364 for 5% of the data) starting from 0.576 and 0.537 respectively. SigmaA weighted 2Fo-Fc and Fo-Fc electron density maps (Read 1986) were calculated with XPLOR after simulated annealing of the model (see chapter 2 and Hodel et al. 1992).

The strongest positive difference peak (6.8xσ) was at the same relative position as the Ca^{2+} bound close to the C-terminus of G1C in the actin:G1C complex (also termed the G1C intramolecular calcium ion). Residues involved in contacting the Ca^{2+} in the G1C structure were in the same position as in G1A and G1B and therefore a Ca^{2+} was inserted in this position (Figure 4.5).

In the respective position in molecule B a smaller peak with a height of 3.6xσ could be identified (Figure 4.5). The C-terminus of G1B was in very weak electron density and the last two residues could not be located in electron density. They were therefore omitted. Because of the delocalised C-terminus of molecule B it was not possible to determine with certainty whether the small peak in molecule B should represent a Ca^{2+}.

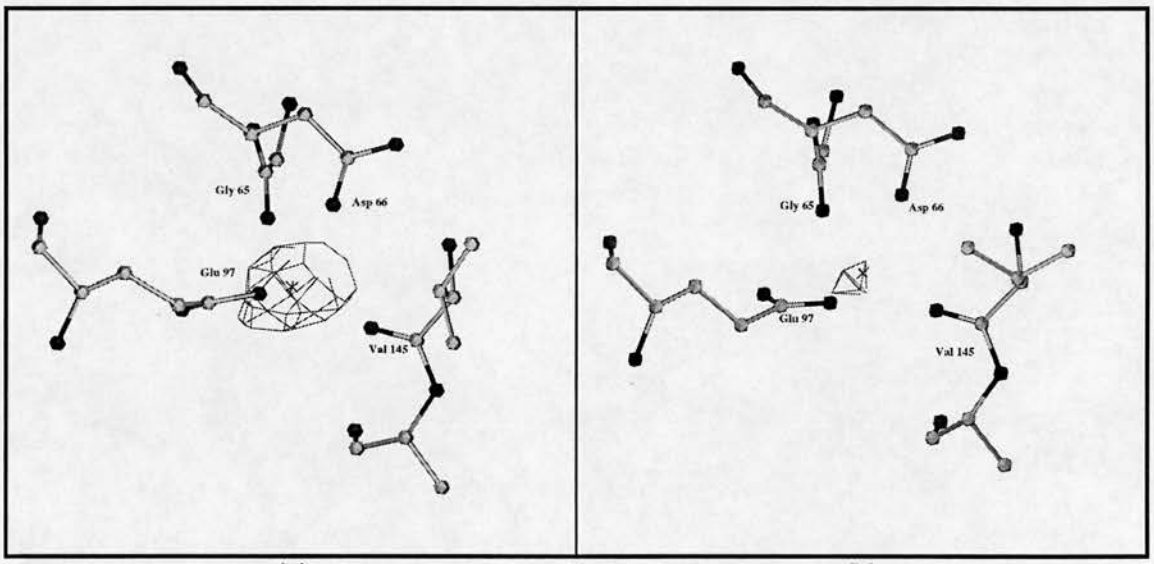

(a) (b)

Figure 4.5: Difference electron density at the G1 intramolecular calcium ion site. The sigmaA-weighted Fo-Fc map after simulated annealing of the model is contoured at 3xσ and the star represents the position of the calcium ion of the G1C model after LSQ fitting over the main chain. (a) Peak in molecule A with a height of 6.8xsigma. (b) Peak in molecule B with a height of 3.6xσ.

Because all potential ligand residues for a Ca^{2+} in G1B were in good electron density and displayed very similar conformations as in molecule A and the structure of G1C, it was decided to continue refinement with a Ca^{2+} inserted at this position in

molecule B. It was also taken into consideration that there was no larger peak closer than 4.2Å to the intramolecular calcium ion position of G1B. Of all peaks larger than 1xσ the closest was 2.9Å away with a height of 2.4xσ. Despite the delocalised C-terminus (G148 and F149) Val145, which co-ordinates to the Ca^{2+} with its main chain oxygen, is located in an area of strong electron density. These observations were taken as an indication for at least partial occupancy by Ca^{2+}.

Results of refinement:	
Atoms in asymmetric unit:	997 atoms of G1A
	973 atoms of G1B
	2 calcium ions
	441 water oxygen atoms
	2413 non-hydrogen atoms
Average B-factors:	22 Å^2...all atoms
	16 Å^2...all main chain atoms
	20 Å^2...all side chain atoms
	17 Å^2...molecule A
	19 Å^2...molecule B
	24 Å^2...calcium ions
	39 Å^2...water
RMS deviation from mean B-factor:	6.8 Å^2 for main chain atoms
	12.8 Å^2 for side chain atoms
RMS deviations from small molecule data:	
Bonds (1-2 neighbours):	0.0065 Å
Angles (1-3 neighbours):	1.563°
RMS deviation from planarity:	
5.2° for Torsion angle of peptide bonds	
0.0018 Å for planar side chains	
Omitted residues in regions of very weak electron density:	
G1A...none	
G1B...Met25, Gly148, Phe149	
R_{cryst}:	0.162 for all data to 2.2Å

Table 4.2

Refinement steps with SHELX (see chapter 2) resulted in better quality electron density maps and, because it implemented the identification and insertion of water oxygens more conveniently, the SHELX software package was used for further refinement. Water oxygen atoms were added in the position of the positive peaks in sigmaA weighted Fo-Fc maps if the peak height was more than 1.5 x sigma and were

at a distance between 2.2Å and 4.0Å from any protein oxygen or nitrogen, or larger difference density peaks than the one under investigation. The R_{cryst} dropped to 0.21 and the R_{free} to 0.33. To check the refinement process the refined model structure was displayed in O and compared to XPLOR generated "ordinary" OMIT maps (Hodel et al. 1992) which had been calculated using the refined model structure omitting stretches of 30 residues plus atoms closer than 5Å to these residues.

The residues omitted in any such OMIT map were compared with the electron density of that OMIT map. This was repeated until all of the model structure had been scrutinised. The protein main chains fit the OMIT maps very well and only very few residue side chains had to be altered manually to better fit the density of the OMIT map.

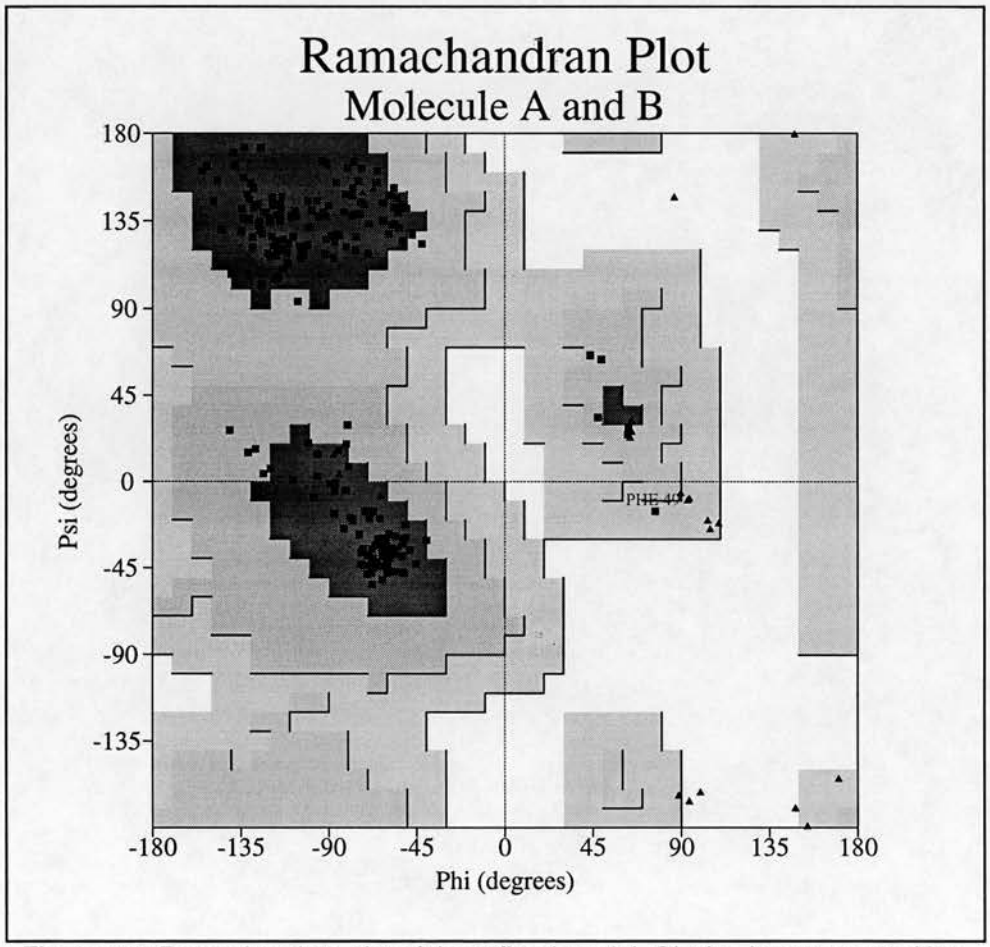

Figure 4.6: Ramachandran plot of the refined model. Glycine is represented by black triangles, other residues by black squares.

The model was subjected to further cycles of water addition and refinement with SHELX and the improved model was compared to OMIT maps. An analysis of the final refined model is presented in Table 4.2, Table 4.3, and Figure 4.6. The B-factors for the two inserted Ca^{2+} refined to 13.4Å^2 for the Ca^{2+} in G1A and 35.3Å^2 for the Ca^{2+} in G1B. No negative electron density peaks were found in difference maps near the Ca^{2+} in G1B and the average B-factor of the co-ordinating residues refined to 18.6Å^2, which is very close to the average B-factor for the residues co-ordinating the Ca^{2+} in G1A (14.8Å^2).

Ramachandran plot statistics for molecules in the asymmetric unit		
Residues in most favoured regions	191	91.8%
Residues in additional allowed regions	16	7.7%
Residues in generously allowed regions	1	0.5%
Residues in disallowed regions	0	0.0%
Number of non-glycine and non-proline residues	208	100.0%
Number of end-residues (excl. Gly and Pro)	4	
Number of glycine residues	27	
Number of proline residues	8	
Number of omitted residues	3	
Total number of residues	250	(two G1 molecules)

Table 4.3

4.2.4 Discussion of the structure of gelsolin segment 1

4.2.4.1 Secondary, tertiary, and quaternary structure in the asymmetric unit

Segment 1 of gelsolin crystallises in the spacegroup $P2_12_12_1$ with two molecules (A and B) per asymmetric unit (Figure 4.7). Both molecules share the same tertiary and secondary structural elements found in the previously published α-actin:G1C complex (McLaughlin et al. 1993) and in the structure of equine plasma gelsolin EGS (Burtnick et al. 1997). Behind the main α-helix lies a β sheet composed of β-strands A,B,C, and D, roughly parallel to the main α-helix. Behind the β-sheet lie the short β-strand C' (parallel to strand A) and the short α-helix, which runs

approximately at right angles to the main α-helix (Table 4.4, Figure 4.8).

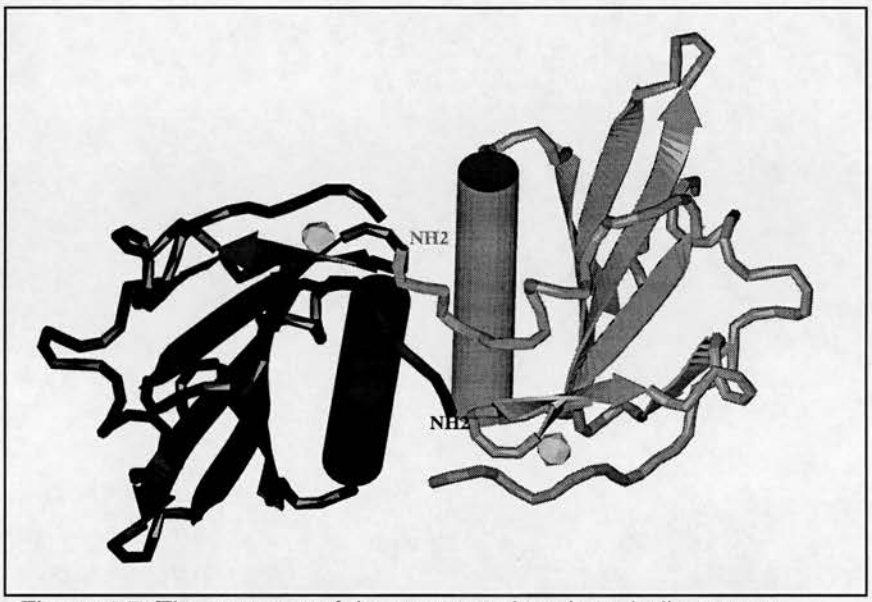

Figure 4.7: The contents of the asymmetric unit excluding water oxygens. G1B is shown in black on the left, G1A in grey on the right. The calcium ions are represented by grey spheres. The N-termini of the proteins are labelled and the main α-helix is drawn as a full cylinder.

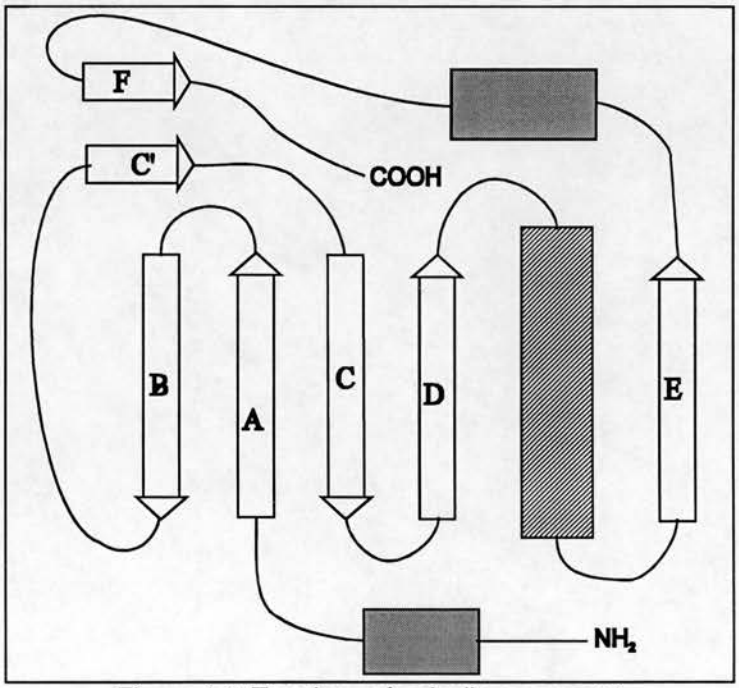

Figure 4.8: Topology of gelsolin segment 1

feature	*(plasma) gelsolin residues*
helix	30-35
β-strand A	40-47
β-strand B	50-54
β-strand C'	60-64
β-strand C	66-76
β-strand D	80-90
main α-helix	94-113
β-strand E	117-123
short α-helix	127-133
β-strand F	138-147

Table 4.4 :Secondary structure of G1

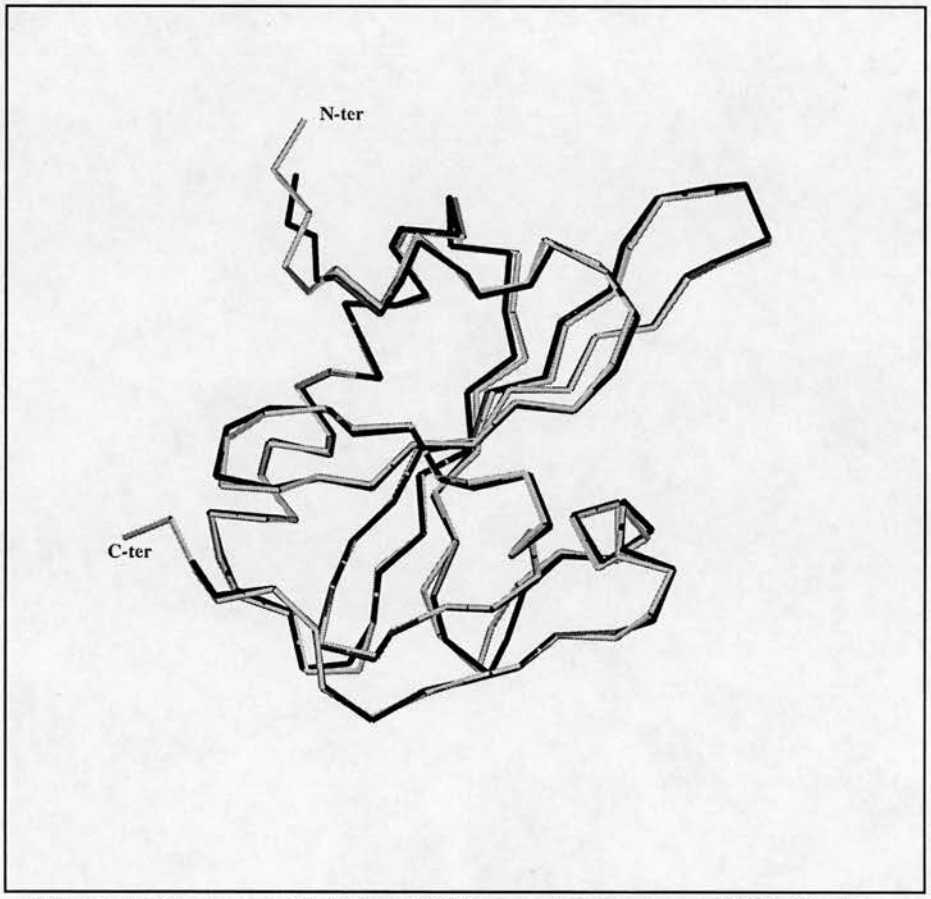

Figure 4.9: Cα traces of G1B and G1A superimposed over G1B. The Cα trace of molecule A is shown in grey, the trace of molecule B in black. The positions of the N- and C-termini are labelled. The picture was generated with Oplot.

The two molecules in the asymmetric unit are oriented such that the main α-helices lie adjacent and almost perpendicular to each other (Figure 4.7). One molecule can be roughly superimposed over the other by turning it by approximately 180° around an axis equidistant to the two helices and tilted roughly 45° in respect to the orientation of the helices.

Least-squares superposition of G1A on G1B (Figure 4.9) over main chain atoms of residues 29-144, excluding carbonyl oxygen, gives an RMS deviation of 0.5Å. The transformation is described by a screw axis rotation of 171° and a translation of 49.4Å.

4.2.4.2 Contacts between the NCS related molecules

The molecules A and B contact each other with the N-termini, their main α-helices, and the loops connecting β-strands A and B. Only a single possibility for a hydrogen bond could be located between the two NCS-related molecules. The main chain oxygen of Glu 28 of molecule A is only 2.9Å away from the main chain nitrogen of Glu 28 of molecule B. No other atom pair capable of forming a hydrogen bond is closer than 3.5Å. On the other hand there are 23 possible hydrogen bonds of molecule A to symmetry related molecules of A and B and 16 possible hydrogen bonds of molecule B to symmetry related molecules of A and B.

The N-termini of the two NCS-related molecules are aligned roughly anti-parallel. They are held together at one end by the main chain - main chain hydrogen bond between the fourth residue of each monomer and at the other by the hydrophobic interaction between Val 26 of molecule A and Pro 30 and Leu 33 of molecule B (Figure 4.10).

Apart from the N-terminal contacts the two molecules associate via various hydrophobic interactions (Figure 4.11). Residues Ala 100(A), Ala 102(A), Ile

103(A), and Val 106(A) of the main α helix of molecule A make hydrophobic contact with a hydrophobic area of G1B comprising residues Phe 49(B), Ile 103(B), and Phe 104(B) from the middle of the main α helix and the loop connecting β-strands A and B.

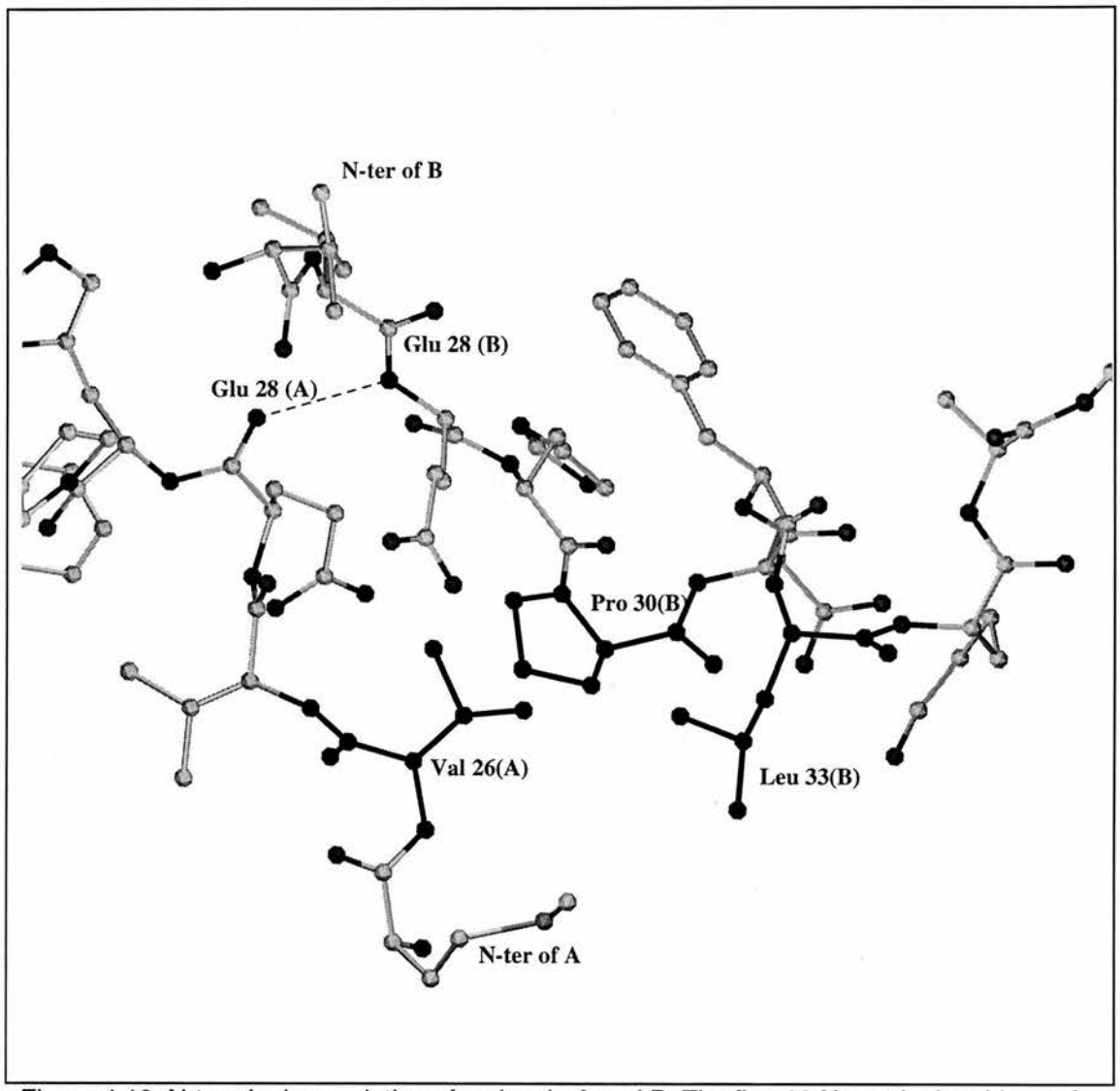

Figure 4.10: N-terminal association of molecule A and B. The first 12 N-terminal residues of each molecule are shown The hydrogen bond is represented with a dashed line and the residues participating in hydrophobic interaction are shown in black. The picture was generated with Oplot.

In addition residues Ala 102(B), Ile 103(B), and Val 106(B) of the main α-helix of

G1B interact with the hydrophobic loop connecting strands A and B of G1A and the C-terminus of G1A. The participating residues of molecule A are Phe 49(A), Ala 100(A), Ile 103(A), and the C-terminal Phe 149(A). Due to the NCS interactions between molecule A and B the C-terminus of molecule B does not lie close to a hydrophobic area as in the case of the C-terminus of G1A. Together with the possible partial occupancy of the Ca^{2+} this may be an additional reason why the G1B C-terminus is located in a region of very weak electron density.

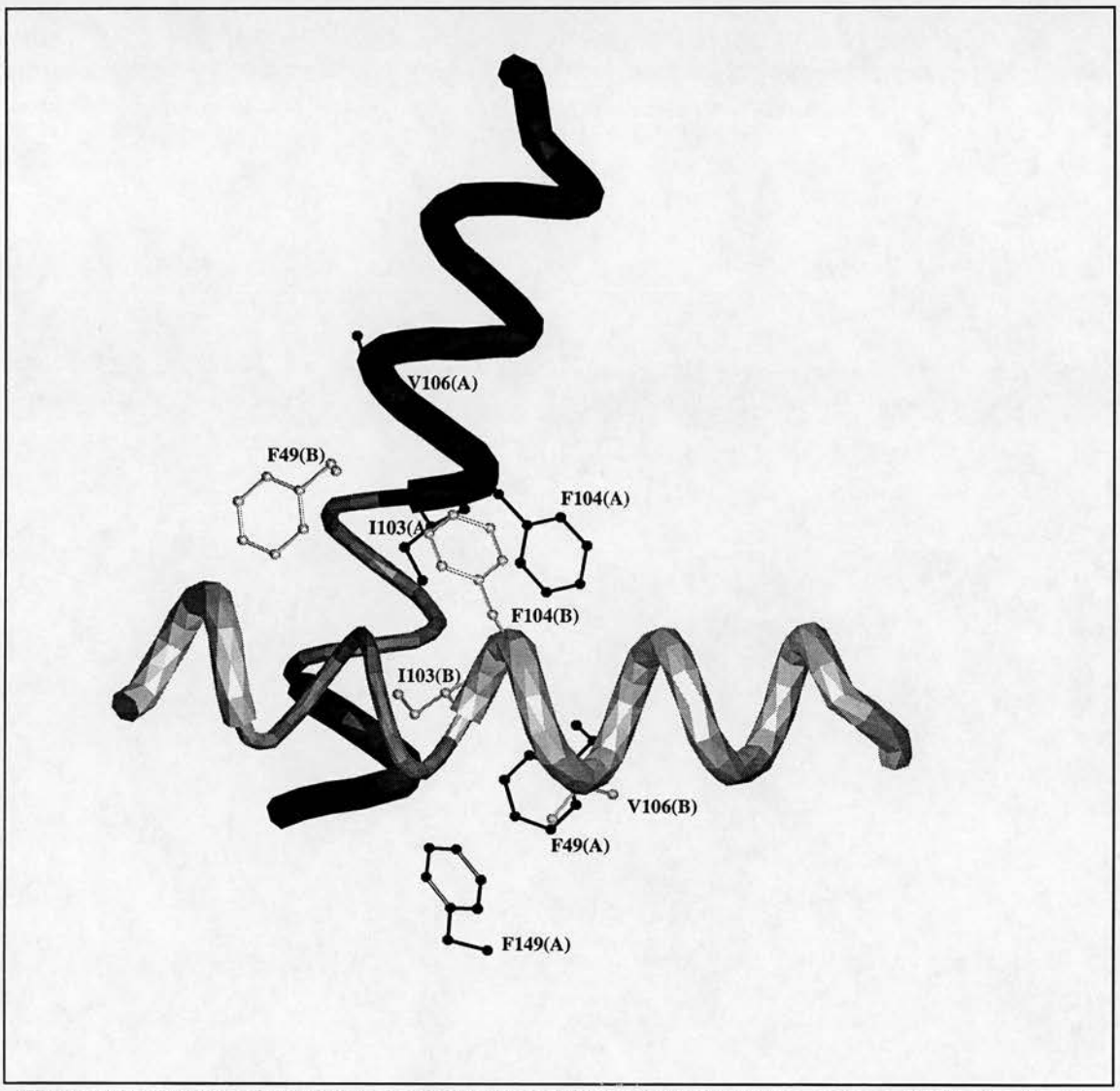

Figure 4.11: Contacts between molecule A and B along their main α-helices. Molecule A and B are shown in black and white respectively, and the helices are represented by tubes following the Cα atoms. The thin tube areas on both helices highlight the positions of glycines and alanines. Other residues involved in hydrophobic interaction are displayed as ball-and-stick models and are labelled with their type, residue number, and in brackets the molecule they belong to. The picture was generated with Oplot.

4.2.4.3 Calcium ion binding

Each molecule in the asymmetric unit binds one seven-fold co-ordinated calcium ion (Figure 4.5). The ligating atoms are main chain oxygens of G65 and V145, the carboxyl oxygens of E97, one carboxyl oxygen of D66, and two water oxygens. The ligands surround the calcium ion in the shape of a pentagonal bipyramid. The position of the calcium ion in this structure confirms the results of Weeds et al.(1995), who showed that of the two calcium ions in the actin : G1C complex at pH6.6 only the one in the position described above (the G1 intramolecular site) can be found in the complex at pH8.

The assumed occupancy of 1.0 for Ca^{2+} in G1A at the start of the refinement is confirmed by electron density maps and the low refined B-factor of 13.4Å^2. In G1B the calcium ion appears to be only partially present, although enough to allow refinement to an acceptable B-factor of 35.3Å^2. This partial occupancy could be a reason, why the C-terminus of G1B lies in a region of very weak electron density. Therefore G1 can be expected to bind Ca^{2+} ions at roughly a 1:1 ratio under the described crystallisation conditions.

No indication was found to suggest a Ca^{2+} bound at the location where the intermolecular calcium ion is found in the actin:G1C complex. The location is accessible to water in the G1 crystal structure and no protein residue from a different G1 molecule is close enough to make contact. Yet the G1 residues involved in binding the intermolecular Ca^{2+} did not adopt a different conformation in the G1 crystal structure.

4.3 Gelsolin segment 1 and 4 in the equine gelsolin structure

4.3.1 Comparison of conformation

The structure of crystallised G1 was compared to the previously published structures of G1C in complex with α-actin (McLaughlin et al. 1993) and eG1 and eG4 in the structure of equine plasma gelsolin EGS (Burtnick et al. 1997). RMS deviations for superimposed structures of gelsolin segment 1 are shown in Table 4.5.

	G1A	*G1B*	*G1C*	*eG1*
G1B	0.5			
G1C	0.7	0.6		
eG1	0.6	0.4	0.6	
eG4	7.3	7.3	7.5	7.5

Table 4.5: RMS distances (Å) between superimposed co-ordinate sets LSQ-fitted over the main chain atoms (excl. carbonyl O) of G1 residues 29-144 or G4 408-523.

Figure 4.12 shows that the conformation of G1 is only influenced to a small extent by its partners. Whether crystallised on its own, in complex with actin, or crystallised as a part of whole gelsolin, it retains its basic fold. The largest conformational differences, particularly between the segments from the equine gelsolin structure and the other G1 structures, can be observed at the N- and C-terminus and in the loop region 74-82

In the structure of G1C complexed to actin the N-terminus of G1C lies close to actin and enables the hydrogen bonds Q354(actin) - E28(G1C) and S350(actin) - H29(G1C) to form via the side chains of the residues involved. The main chains however do not come close enough for main chain - main chain hydrogen bond formation as can be observed in the G1 crystal structure. In the equine gelsolin crystal structure the N-termini of eG1 are not closely associated to any other residues but stretch into the cleft between two symmetry related gelsolin molecules.

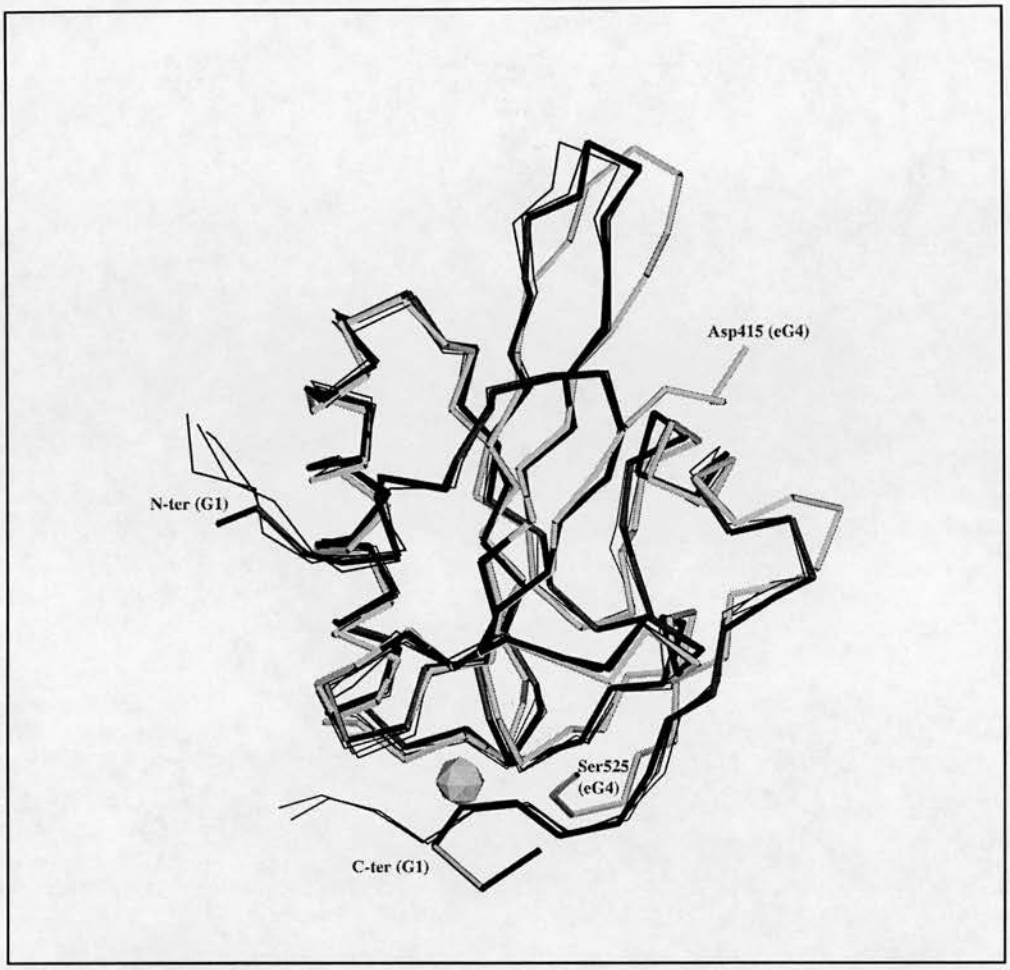

Figure 4.12: Superposition of G1A, G1B, G1C, equine G1 and G4. The Cα traces of G1A, G1B, and G1C are drawn as thin black lines. The Cα trace of equine G1 is represented by a thick black line and the Cα trace of equine G4 by a thick grey line. The N-terminus and the C-terminus for G1A, G1B, and G1C are labelled, as is the N-terminal start (Asp415) and C-terminal end (Ser525) of the displayed equine G4 main chain. The representative position for the Ca^{2+} in the structures of G1A, G1B, and G1C is shown as a grey sphere.

The difference in conformation between the C-terminus of eG1 and the other C-termini is easily explained. Firstly the structure of eG1 has been taken from the structure of equine gelsolin and the C-terminus of eG1 is therefore twisted around to connect to gelsolin segment 2. Secondly whole gelsolin was crystallised without the presence of calcium, whereas the other structures all contain Ca^{2+} tightly bound between the C-terminus and the residues at the N-terminal start of β-strand C.

The residues of G1A, G1B, and G1C comprising the calcium binding site are all in

the same conformation necessary to participate in the formation of the pentagonal-bipyramidal co-ordination of the calcium ion. The equivalent residues in eG1 are in a very similar conformation and it is not immediately obvious how the charge on the side chains of Asp66 and Glu97 is compensated for. One major difference is the conformation of Val145. In the calcium-containing structures of individually expressed G1 the Val145-Ala146 peptide bond is in trans-conformation, enabling the main chain oxygen of Val145 to interact with the calcium ion. In the calcium-free structure of equine gelsolin the Val145 oxygen is in cis-conformation, as reported by Burtnick et al. (1997). When gelsolin is activated by Ca^{2+} and binds to actin via G1, one can expect this peptide bond to experience a flip of 180° creating the third calcium binding site on gelsolin (Way et al. 1989).

4.3.2 Protein interactions

In the crystal structures of G1 (G1A and G1B in the ASU), actin:G1C and equine gelsolin (molecule A and B in the ASU) the segment 1 of gelsolin associates with another protein through its main α-helix which crosses an equivalent α-helix of the other protein. (Table 4.6, Figure 4.7, Figure 4.13, and Figure 4.14).

Complex	*Crossing angle between C-termini of helices*	*Closest distance of helix axis*	*Closest Cα to intersection*
G1A:G1B	78°	8.5Å	Gly99 (G1A) Ala100 (G1B)
actin:G1C	59°	9.3Å	Ala100 (G1C)
eG1-A:eG4-A*	132°	10.8Å	Ala100 (eG1-A) Val476 (eG4-A*)
eG1-B:eG4-B**	132°	10.4Å	Ala101 (eG1-B) Ser479 (eG4-B**)

Table 4.6: Helix contacts

In the G1 crystal structure the central axis of the main α-helices cross each other at

an angle of 78° in respect to the C-terminal ends when viewed along the shortest distance between the central axis. At their closest point they are separated by 8.5Å. The contact normal intersects the helix axes of molecule A at a distance of 2.3Å from Cα of Gly 99 and the helix axes of molecule B 2.2Å away from Cα of Ala 100.

Starting molecule	*Symmetry operator applied to starting molecule*	*Resulting molecule*
A*	1/2-y,1/2+x,z	A
B	1/2-y,1/2+x,z	B**

Table 4.7: Relation ship between gelsolin A, B, A*, and B**:

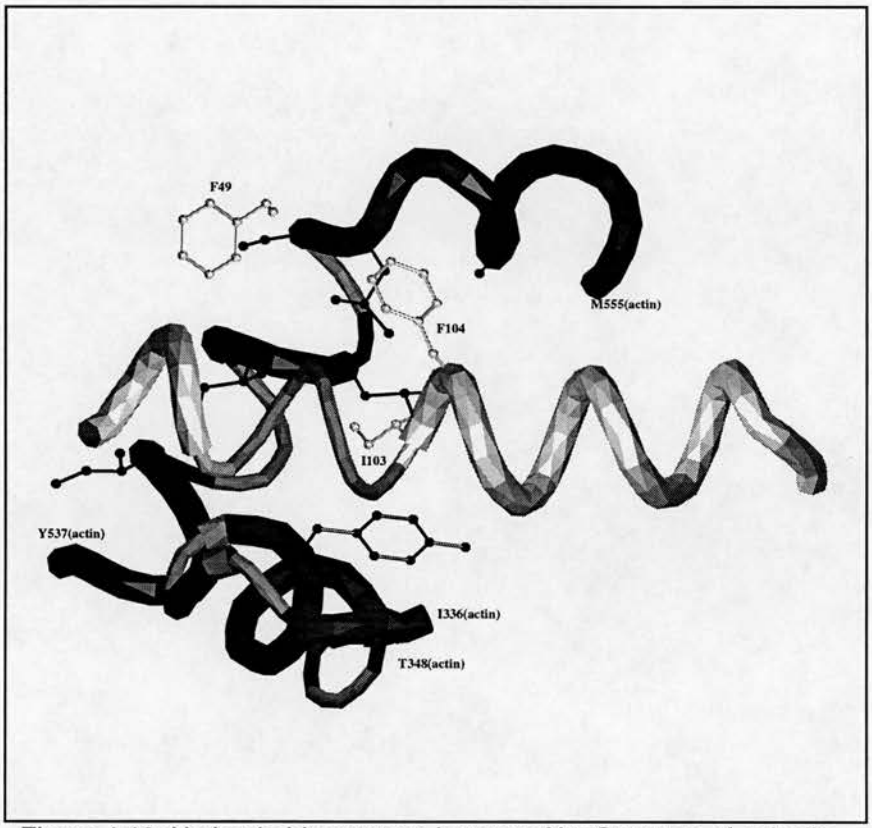

Figure 4.13: Hydrophobic contacts between N57C mutant of gelsolin segment 1 and α-actin. α-Actin and G1 are shown in black and white respectively, and the main-chain traces are represented by tubes following the Cα atoms. The thin tube areas of the helices highlight the positions of glycines and alanines. Other residues involved in hydrophobic interaction are displayed as ball-and-stick models. The picture was generated with Oplot.

In the actin:G1C complex the shorter α-helix of actin at the bottom of Figure 4.13

does not cross the main α-helix of G1 but contacts it at its C-terminal end where an alanine and a glycine are located. The longer α-helix in the background crosses the main α-helix of G1 at an angle of 59° with respect to the C-terminal ends of the helices. The central axes are separated by 9.3Å at their closest and the contact normal intersects the axes of G1 main α-helix 2.3Å away from Cα of Ala100. In the actin:G1 complex this hydrophobic region is surrounded by a ring of hydrogen bonds (McLaughlin et al. 1993), creating the extremely tight association necessary for the actin-filament severing activity of gelsolin. This is also reflected in a larger buried solvent accessible surface area which is 1165Å^2 for each of G1C and actin as opposed to 645Å^2 for each of G1A and G1B.

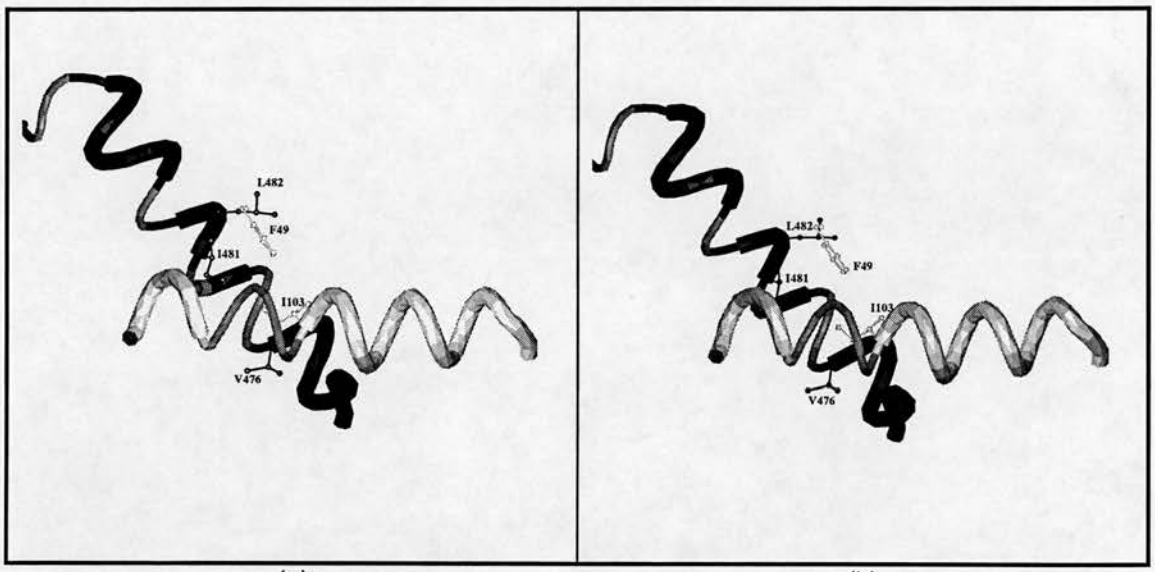

(a) (b)

Figure 4.14: Helix contacts of segment 1 of the two equine gelsolin molecules in the asymmetric unit. The main α-helix of segment 1 is shown in white and the main α helix of segment 4 of the adjacent symmetry related molecule is shown in black. The thin tube areas on both helices highlight the positions of glycines and alanines. Other residues involved in hydrophobic interaction are displayed as ball-and-stick models. (a) Main α-helix of segment 1 of molecule A in contact with the main α-helix of segment 4 of a symmetry-related molecule A*. (b) Main α-helix of segment 1 of molecule B in contact with the main α-helix of segment 4 of a symmetry-related molecule B**. The picture was generated with Oplot.

In contrast the two NCS-related gelsolin segment 1 molecules only share one hydrogen bond at their respective N-termini. Hydrophobic interaction seems to play the major part in the association of these two molecules in the crystal structure. An

association of G1 molecules in solution could be the reason for the leading peak observed during gel-filtration during the purification of the expressed gelsolin segment 1. It can be speculated whether this is due to a dimerisation of G1 molecules, associated to each other as in the asymmetric crystal unit.

The crystal structure of equine gelsolin contains two molecules (A and B) per asymmetric unit in the spacegroup $P42_12$. The main α-helix of segment 1 in molecules A and B lies on the surface of gelsolin and forms a crossed helix association with the main α-helix of segment 4 (eG4) of the respective adjacent symmetry related gelsolin molecule A* and B** (Figure 4.14, Table 4.7).

```
eG1   26 VVEHPEFLKAGKEPGLQIWRVEKFDLVPVPPNLYGDFFTGDAYVILKTVQLRNGILQYDL 85
         ||||||||||||||||||||||||||||||.|||||||||||||||||||||| |||||
hG1   26 VVEHPEFLKAGKEPGLQIWRVEKFDLVPVPTNLYGDFFTGDAYVILKTVQLRNGNLQYDL 85

eG1   86 HYWLGNECSQDESGAAAIFTVQLDDYLNGRAVQHREVQGFESATFLGYFKSGLKYKKGGV 145
         ||||||||||||||||||||||||||||||||||||||||||||||||||||||||||||
hG1   86 HYWLGNECSQDESGAAAIFTVQLDDYLNGRAVQHREVQGFESATFLGYFKSGLKYKKGGV 145

eG1  146 ASGFKHVVP 154
         |||||||||
hG1   146 ASGFKHVVP 154
```

Table 4.8: Sequence alignment of human G1 and equine G1. Residue numbers are according to plasma gelsolin. Residues at intersection of helices (hG1A:hG1B and eG1:eG4**) are printed bold and underlined. Sequence identity: 98.39%, sequence conservation: 98.39%, matches (|): 122, mismatches: 2

```
eG4  419 QKQIWRVEGSNKVPVDPATYGQFYGGDSYIIL--YNYRHGSRQGQIIYNWQGAQSTQDEVAA 478
           ||||||    |||    || |  || | ||     | |  |    | | |    |||  |
hG1   40 GLQIWRVEKFDLVPVPTNLYGDFFTGDAYVILKTVQLRNGNLQYDLHY-WLGNECSQDESGA 100

eG4  479 SAILTAQLDEELGGTPVQSRVVQGKEPAHLMSLFGGKPMIVYKGGT 524
         || | |||  | |  || | ||| | |     |          |
hG1  101 AAIFTVQLDDYLNGRAVQHREVQGFESATFLGYFKSGLKYKKGGVA 146
```

Table 4.9: Sequence alignment for human G1 and equine G4. Residue numbers as for plasma gelsolin. Residues at intersection of helices are printed bold and underlined. Most conserved region: hG1 42-134(92 residues) versus eG4 421-512(91 residues): sequence identity 48.35%, sequence conservation 71.43%, matches (|): 44, mismatches:47, indels (-):3, gaps: 2

For both gelsolin molecules in the asymmetric unit the angle between the central axis of the main α-helices of eG1 and the associated symmetry related eG4 is 132° in

respect to C-termini of the helices. At their closest the central axes of eG1(A*) and eG4(A) are separated by 10.8Å and the axes of eG1(B) and eG4(B**) by 10.4Å. The Cα atoms closest to the intersecting contact normals to the helix axes belong to Ala 100 (eG1-A) and Val 476 (eG4-A*), and Ala 101 (eG1-B) and Ser 479 (eG4-B**). Sequence alignment (Table 4.8 and Table 4.9) shows that Val 476 and Ser 479 of G4 correspond to Ser 98 and Ala 101 of G1 respectively. It appears that this rather hydrophobic region on the main α-helix of G1 and G4 is ideally suited as the closest point for crossed helices due to the number of residues with very short side chains.

4.4 Segment 1 of human CapG (CapG-1)

4.4.1 Crystallisation

CapG-1 (residues 1-131 of human CapG, M_r = 14458) was produced and purified as described in chapter 2. Calcium competent *E.coli* of strain BL21(DE3) were transformed with plasmid pMW172 encoding genes for an Isopropyl-β-D-thiogalactopyranoside (IPTG) activated promotor, for ampicillin resistance, and for CapG-1. Cells were grown, lysed and CapG-1 extracted by binding to a DEAE-anion exchange column and eluting with a NaCl gradient at pH8.0. It was further purified using a Sephacryl S200 gel-filtration column and a CM52 anion-exchange column, eluting with a NaCl gradient at pH6.5. At this stage a contaminant with apparent molecular weight of approximately 30kD on the SDS polyacrylamide gel still accompanied CapG-1.

Already a month had passed since the expression of CapG-1 and it was feared that with increasing age the protein would not crystallise. Therefore 3mg (BCA assay) of protein were used for an initial crystallisation trial. The remaining 60mg of protein (BCA assay) were further purified using a DEAE-anion exchange column, eluting

with a NaCl gradient at the slightly higher pH of 8.5. This yielded about 46mg of purified CapG-1 (ca. 15mg per litre of BL21 culture). This protein was now used for a crystallisation asssay, after storage at 4°C for two months in the interim.

Figure 4.15: CapG-S1 crystal fragments

Crystallisation trials using the "hanging drop" method were set up using a crystallisation buffer with 25 to 50mM Tris or HEPES, 1mM NaN_3, 10mM DTT, and 1.0 - 3.2M ammonium sulphate in a pH range of 7.0 to 8.0.

A single crystal was obtained from the initial trial with impure protein and a buffer containing 25mM Tris pH 7.7, 1.8M ammonium sulfate, 1mM $CaCl_2$, 1mM NaN_3, and 10mM DTT. The colourless crystal was roughly orthorhombic with dimensions of approximately 250x250x200µm. While removing it from attached skin of denatured protein the crystal shattered into fragments (Figure 4.15).

4.4.2 X-ray diffraction

The crystal fragments were exposed to X-rays at the SRS Daresbury on beamline PX9.6 equipped with a CCD detector (see chapter 2). Only one fragment produced observable diffraction (Figure 4.16). Diffraction patterns were recorded to obtain the unit cell parameters. Spots were observed to 2.7Å but it was not possible to obtain unit cell parameters suitable for processing. Therefore no dataset was collected.

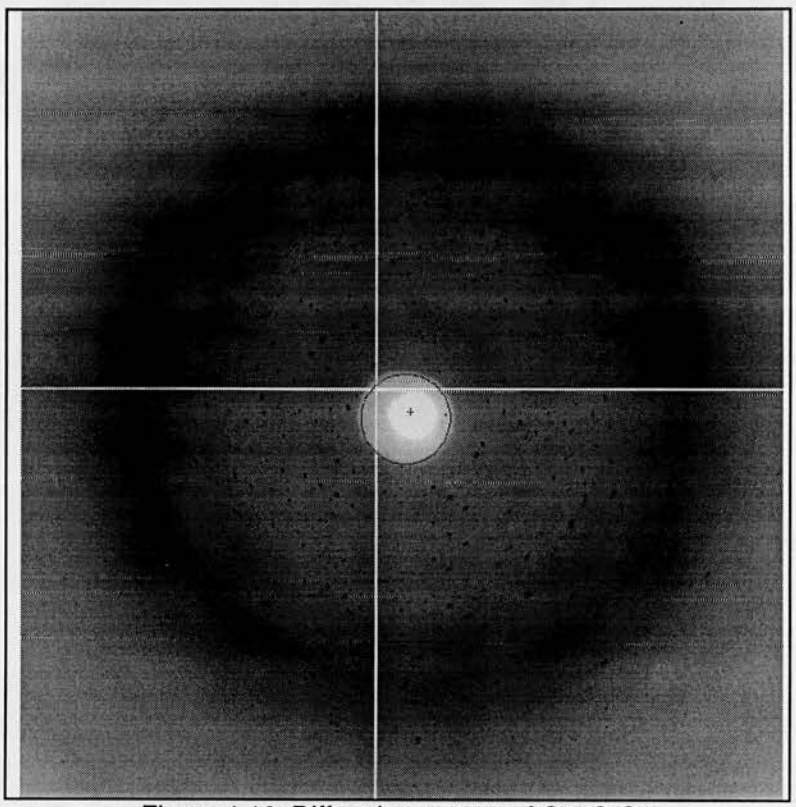

Figure 4.16: Diffraction pattern of CapG-S1

4.5 Conclusion

Apart from conformational changes at the N- and C-termini, gelsolin segment 1 retains its fold regardless of whether incorporated in the whole gelsolin molecule (Burtnick et al. 1997), whether complexed to actin (McLaughlin et al. 1993), or

whether crystallised on its own. The N-terminus of segment 1 is free to adopt the most favourable conformation under the given conditions, but in the presence of calcium ions the C-terminus is held rigidly in the conformation necessary to co-ordinate a Ca^{2+} ion with two carboxyl groups and two main chain carbonyl oxygens.

The position of the calcium ion in this structure confirms the results of Weeds et al. (1995), who showed that of the two calcium ions in the actin : G1C complex at pH6.6 only the one in the position described above (the G1 intramolecular site) can be found in the complex at pH8. The high similarity between the structure of Ca^{2+} containing G1 and G1C in complex with actin in presence of Ca^{2+} demonstrates that G1 is already in the ideal conformation to bind tightly to actin.

Binding to actin and association in a crystal structure with another segment 1 or segment 4 of an adjacent gelsolin molecule, involves hydrophobic interaction of the main α-helix with an α-helix of the binding partner. In the three investigated crystal structures (actin:G1C, equine gelsolin, human G1) the area of closest contact to the other helix involves residues 98 to 101 of gelsolin segment 1 or equivalent residues in segment 4 of the equine gelsolin structure.

The physiological and evolutionary refined role of G1 is to bind tightly to an actin monomer enabling whole gelsolin to not only cap but also sever actin filaments. Its interaction with actin is via a hydrophobic patch centred on G1's main α-helix surrounded by a ring of hydrogen bonds.

When taken out of its context in the gelsolin structure and expressed individually, it is conceivable that G1 should try to reduce the hydrophobic surface presented to the surrounding water. Its overall conformation is stable enough not to denature under these circumstances. It might be possible that the observed association of the G1 molecules in the asymmetric unit is the way G1 overcomes this problem in solution.

5. Binding of latrunculin A to α-actin : gelsolin segment 1

5.1 Introduction

Studies of the actin microfilament system in non-muscle cells are often hampered by the dynamic nature of the actin cytoskeleton. This difficulty is also inherent to other systems, e.g. the microtubular cytoskeleton. In such studies drugs have proven very useful that inhibit polymerisation and filament formation. For studies of the actin cytoskeleton only two suitable families of related drugs have been found to date. The cytochalasins (Sheterline et al. 1994) are a group of metabolites produced by certain fungi of the subclasses *Ascomycotina* and *Deuteromycotina*, whereas latrunculins (Spector et al. 1983) are produced by the Red Sea sponges, e.g. *Latrunculia magnifica* (Kashman et al. 1980), and Pacific Ocean sponges, e.g. *Spongia mycofijiensis* (Quiñoà et al. 1988) and *Fasciospongia rimosa* (Jefford et al. 1996). Molecules from both drug families are toxins produced to increase the chance of survival of the respective species. The latrunculins are particularly effective and enable marine sponges like *Latrunculia magnifica* to grow openly and unmolested by marine life-forms, whereas other sponges need to "hide" in tight crevices and holes (Neeman et al. 1975).

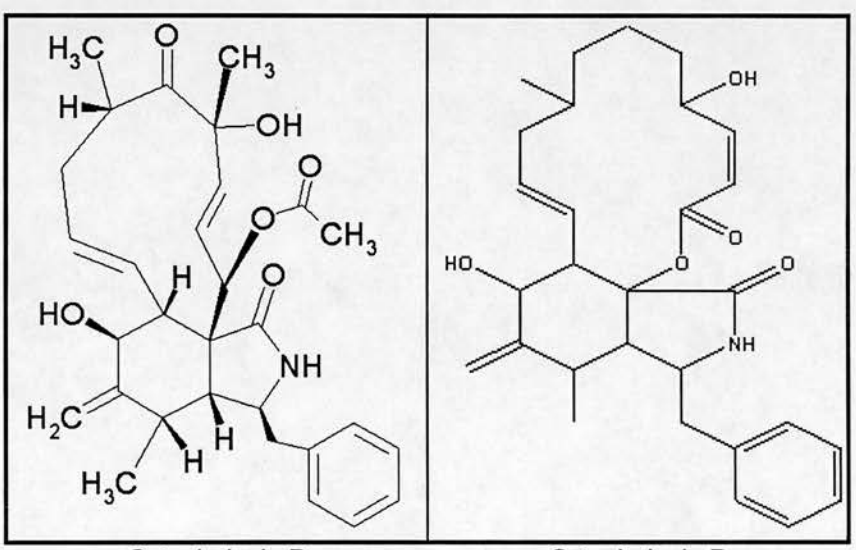

Cytochalasin D Cytochalasin B

Figure 5.1: Representatives of the cytochalasin family

Both the cytochalasins and latrunculins disrupt the dynamic actin cytoskeleton in non-muscle cells. Cytochalasins inhibit monomer addition at the barbed end of F-actin. It has also been found, that cytochalasin D ($C_{30}H_{37}NO_6$, M_r 507, Figure 5.1) induces dimer formation upon binding to G-actin (Goddette and Frieden 1986), accelerates polymerisation, but decreases the extent of polymer formation (Tellam and Frieden 1982), and induces hydrolysis of actin-bound ATP (Brenner and Korn 1980). Cytochalasin D has been used to measure kinetic rate constants for actin at the pointed end of the filament due to its ability to block the barbed end of F-actin (Carlier et al. 1986). Its tight binding to F-actin is demonstrated by a calculated dissociation constant of only 2nM (Brenner and Korn 1979). In contrast its binding to G-actin in the absence of Mg^{2+} ions was reported to result in a K_d of 18μM. In the presence of 250μM Mg^{2+} actin does not yet polymerise but cytochalasin D appears to induce dimer formation. The K_d of this ternary complex was calculated to be 2.6μM (Goddette and Frieden 1985).

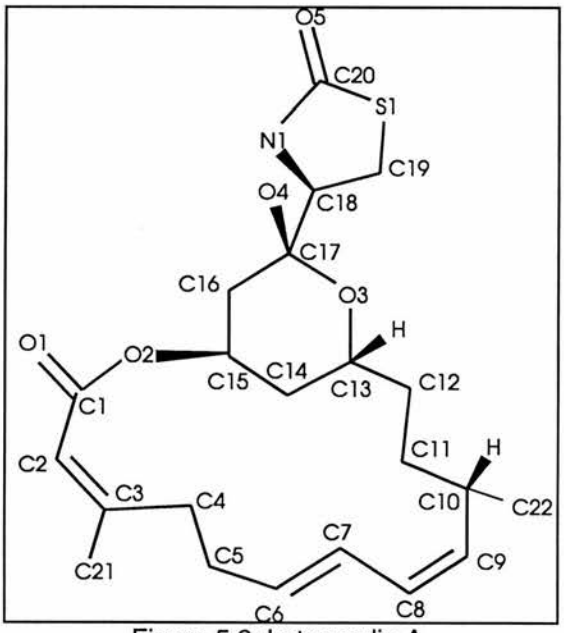

Figure 5.2: Latrunculin A.
Labels are as in PDB file used for refinement

Latrunculin A ($C_{22}H_{31}NO_5S$, $M_r = 421$, Figure 5.2) binds tightly to G-actin at a 1:1 ratio ($K_d = 0.2\mu M$) and has been investigated and used in various studies on the actin cytoskeleton (Coue et al. 1987, Spector et al. 1983 and 1989, Ayscough et al. 1997). Binding of latrunculin A (latA) to G-actin inhibits the actin monomer's ability to participate in filament formation and thereby disrupts the dynamic actin cytoskeleton. It also reportedly impedes nucleotide exchange of actin monomers (Ayscough et al. 1997). The presence of 0.1μM latrunculin A (latA) in the medium is sufficient to cause noticeable effects on the cytoskeleton of cultured cells. Higher concentrations lead to extensive disruption of the thin filament network (Spector et al. 1989).

The exact site of action on actin for these compounds has not been pinpointed yet. The cytochalasins are expected to interact with the barbed end of actin filaments and with a site between subdomains 1 and 3 (see chapter 1) of actin, near the hinge region between the large and small domain (see chapter 1). Two point mutations in the β-actin sequence (V139M, A295D) are known to reduce cytochalasin B ($C_{29}H_{37}NO_5$, Mr 479.62, Figure 5.1) sensitivity (Ohmori et al. 1992), but they are located too far apart that a single cytochalasin molecule could span both.

In contrast several amino acids involved in conferring latrunculin A resistance are clustered in subdomain 4, close to the nucleotide binding cleft between the two major actin domains (Ayscough et al. 1997). Considering the inhibition of nucleotide exchange on binding of latA, this area could indeed be where latA binds to actin.

Considering the effects these drugs have on actin it would be of great interest to elucidate the structural changes which occur when the respective drug binds to an actin monomer. To determine the actin structure containing either bound cytochalasin D or latA, actin crystals were soaked in buffers containing the respective drug. Since crystallising actin for this purpose was done in complex with the N57C mutant of gelsolin segment 1 (G1C, see chapter 3) to avoid spontaneous polymerisation, the introduction of these toxins into the crystal would also test the degree of structural restriction gelsolin segment 1 imposes on actin, if the overall conformation of the

complex is not mainly dictated by the crystallisation conditions.

Although cytochalasin D is expected to bind close to the binding site of gelsolin segment 1 on actin there are indications that both molecules are capable of binding simultaneously to actin. Cytochalasin B, a molecule related to cytochalasin D, does not compete with villin, a member of the gelsolin family of actin-binding proteins, for a binding site at the barbed end of F-actin. This suggests the possibility of simultaneous binding of this toxin with actin-binding proteins of the gelsolin family (Cribbs et al. 1982). Soaking and co-crystallisation trials of α-actin:G1C with cytochalasin D were undertaken with the assumption that the same actin-binding relationship exists between cytochalasin D and gelsolin segment 1 as between cytochalasin B and villin.

5.2 Structure determination of the latrunculin A containing α-actin :G1C complex

5.2.1 Soaking of latrunculin A into α-actin:G1C crystals

5.2.1.1 Preparation of α-actin:G1C crystals

α-Actin:G1C crystals were prepared as detailed by McLaughlin et al.(1993) and described in chapters 2 and 3. Actin was extracted from acetone powder prepared from rabbit muscle using a low salt and ATP containing buffer (G-buffer). Actin was further purified by polymerisation and depolymerisation cycles and was gel-filtered as a final step.

G1C (N57C mutant of gelsolin segment 1, see chapter 3) was purified from an *E.coli* culture, which had been transformed with a plasmid vector engineered to express the

sequence for G1C. After cell lysis G1C was purified by anion-exchange chromatography and gel-filtration.

The protein complex was formed by mixing the actin and G1C in a 1:1 ration and purified by gel-filtration. The complex was crystallised using the "hanging drop" procedure and a crystallisation buffer containing 0.1mM ATP, 0.15M NaCl, 0.1mM $CaCl_2$, 0.1mM $MgCl_2$, 1mM NaN_3, 10mM DTT, 50mM MES pH6.6 and 5-9% (w/v) polyethylene glycol. This resulted in clear plate-shaped crystals of varying size up to 0.7 x 0.3 x 0.03mm as described in chapter 3.

5.2.1.2 Soaking

Latrunculin A was obtained courtesy of Dr. K. Ayscough (Dep. of Biochemistry, University of Dundee, Dundee, U.K.). Dimethylsulfoxide (DMSO) was the solvent for the 50mM latA stock solution. Crystals remained stable in a crystallisation buffer containing 10% (v/v) of the stock solution if an additional 25% (v/v) glycerol was included and the crystals were transferred through buffers with intermediate glycerol concentrations. The final glycerol concentration was also enough to prevent icing of the buffer when flash frozen in liquid nitrogen and during data collection at 100K.

Soaking crystals at 4°C, instead of room temperature, appeared to help the stability of the protein crystals. The quality of diffraction of the soaked crystals was assessed on the X-ray generator of the Department of Biochemistry (see chapter 2). It did not seem to have suffered and diffraction spots were visible to at least 4.5Å as expected.

Unfortunately under these conditions, whether at 4°C or 18°C, latA was not completely soluble and precipitation occurred. At least 30% (v/v) ethanol had to be included in the buffer to keep latA soluble, but under these conditions the diffraction of the crystals deteriorated considerably, whether latA was included or not. Even if, after a quick stepwise transfer, the crystals were exposed to the final solution for only

20 seconds and then flash-frozen in liquid nitrogen, diffraction deterioration occurred.

Some crystals remained stable and without noticeable loss of diffraction quality when soaked in 10% (v/v) DMSO, 5mM latA, 20% (v/v) ethanol, 25% (v/v) glycerol, 0.1mM ATP, 150mM NaCl, 0.1mM $MgCl_2$, 0.1mM EGTA, 1mM NaN_3, 10mM DTT, 50mM MES pH6.6 and 10% (w/v) polyethylene glycol for up to 20 hours.

To maximise the chance of finding a suitably diffracting soaked crystal for data collection at the SRS at Daresbury it was decided to take a variety of flash-frozen soaked crystals to the synchrotron.

Soaks were prepared mostly at 4°C, transferring crystals through buffers with intermediate concentrations to the final solutions, as described above with 10% (v/v) or 20% (v/v) ethanol and partially precipitated latA, at an nominal concentration of 5mM. After various incubation times, ranging from 30s to 20 hours, the soaked crystals were flash-frozen in liquid nitrogen and stored for transport.

5.2.2 X-ray diffraction analysis

Of all flash-frozen crystals one soaked in 5mM latA, 10% (v/v) DMSO, 10% (v/v) ethanol, 25% (v/v) glycerol, 0.1mM ATP, 0.15M NaCl, 0.1mM $MgCl_2$, 0.1mM EGTA, 1mM NaN_3, 10mM DTT, 50mM MES pH6.6 and 10% (w/v) polyethylene glycol for 4 hours gave the best diffraction pattern and was X-rayed at 100K on beamline PX9.6 of the SRS at Daresbury using a wavelength of 0.87Å and a CCD detector. The intensities collected were autoindexed and integrated with MOSFLM. Scaling and structure factor calculation was performed with programs of the CCP4 suite. The results are compiled in Table 5.1.

Results of data processing	
Temperature:	100K
Spacegroup:	$P2_12_12_1$
Cell Dimensions:	a = 56.75Å
	b = 69.25Å
	c = 182.91Å
	$\alpha = \beta = \gamma = 90.0°$
Resolution range:	2.0 - 25.7 Å
Completeness of data:	85.6%
Multiplicity:	2.8
Unique reflections:	42367
R_{sym}:	0.066
$\langle I \rangle / \sigma(I)$ (2.00-2.11Å):	2.2
$\langle I \rangle / \sigma(I)$ (all data):	7.2

Table 5.1

5.2.3 Molecular replacement

5.2.3.1 Refinement with XPLOR

The model of α-actin:G1C at 100K (chapter 3) was the obvious choice as the starting model. The co-ordinates of the structure excluding water oxygens were refined as a rigid body against the data using the program XPLOR (see chapter 2). SigmaA weighted electron density maps were calculated and the positive peaks in the Fo-Fc map analysed. The 9 highest positive difference peaks were very closely associated with atoms of the model structure and could therefore not count as density from a ligand. The tenth highest peak (5.0 x σ) was located above the ATP in the cleft between subdomains 2 and 4. Lowering the display level of the difference map gave only a very sketchy idea of the latA features, the strongest difference density coming from the thiazolidinone group of latA. Incidentally the peak was close to residues, which Ayscough et al. (1997) found to confer latA resistance to cells where groups of two or three residues had been mutated to alanine. These groups of residues are Arg183 and Asp184, Arg210 and Asp211, and Lys213 and Glu214 and Lys215, all located in subdomain 4 and close to the ATP binding site.

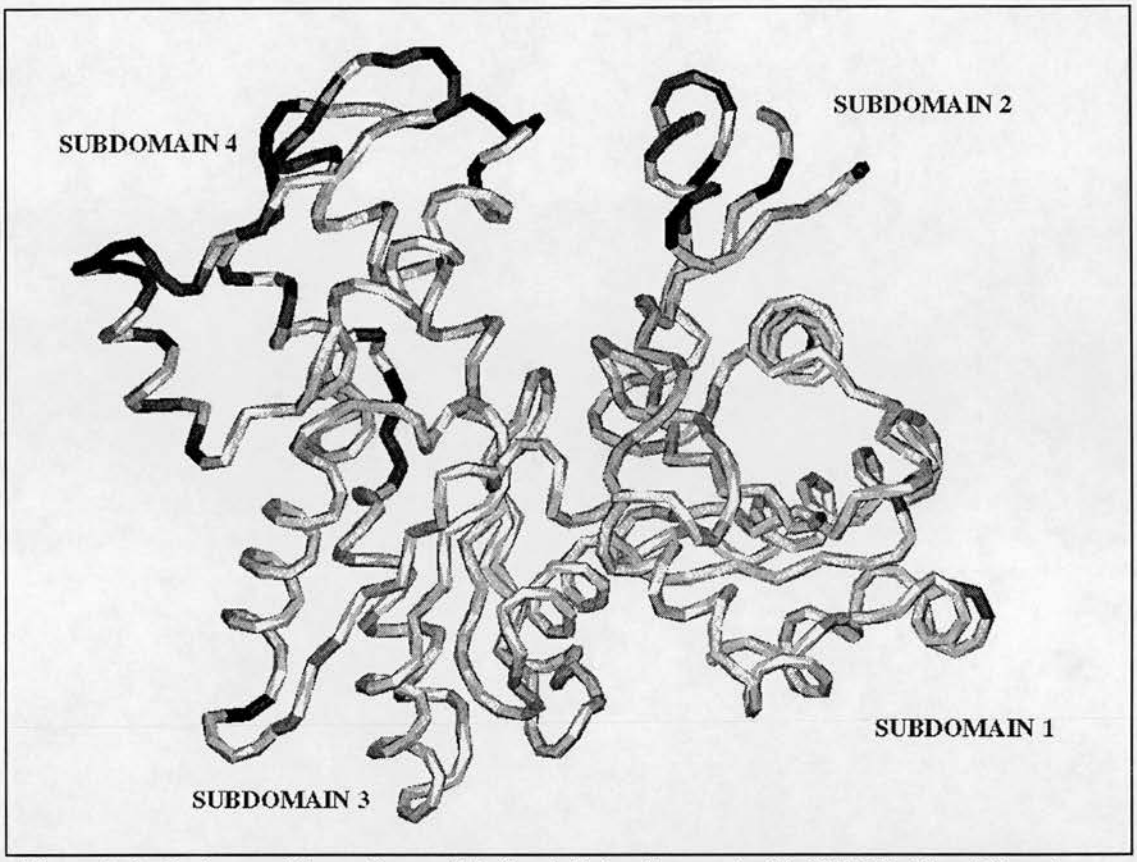

Figure 5.3: Cα trace of the actin model after initial refinement with XPLOR. The DNaseI binding loop in subdomain 2 (40-49) was excluded due to lack of electron density. The protein chain is shown in light grey apart from areas with high B-factors. Dark grey parts of the chain highlight main chain areas with average B-factors between 50Å^2 and 70Å^2, black areas have average main chain B-factors above 70Å^2. The picture was created with Oplot, SNAPSHOT, and XV.

XPLOR least-squares positional and grouped B-factor refinement reduced the R_{cryst} to 0.302 and the R_{free} dropped to 0.334. SigmaA weighted 2Fo-Fc maps showed slightly improved electron density for latA and clear density for most of the models for actin and G1C. As with other actin:G1C complexes (see chapter 3) no significant electron density was found for the DNaseI binding loop of actin (residues 40 to 49 in subdomain 2). Around the residues 50-64, 192-205, 221-255, 267-271, and 323-325 the electron density was very weak and the average B-factor of these residues was as high as 73.0Å^2. The majority of these residues are located at the pointed end of the actin molecule in subdomains 2 and 4 (Figure 5.3). This could be due to the influence of the bound latA.

5.2.3.2 Refinement with REFMAC

The initial α-actin:G1C model was refined again from the start using the CCP4 program REFMAC (see chapter 2) and a maximum-likelihood target for the refinement (Murshudov et al. 1997). Pannu et al. 1996, Bricogne et al. 1996, and Murshudov et al. 1997 had reported on the success of refining by maximising the likelihood (or minimising the negative logarithm of the likelihood) of obtaining the experimental observations with a given model. It was reported to yield better results than least-squares refinement with XPLOR or SHELX (see chapter 2), especially with incomplete models and areas of weak electron density.

After rigid body refinement and 10 cycles of maximum-likelihood residual refinement the R_{cryst} had dropped to 0.277 and the R_{free} to 0.327 (for 5% of the data). Seventy-nine residues of subdomains 2 and 4 in regions of very weak density were deleted and the model refined for 5 cycles. The model was examined in O (see chapter 2) and compared against sigmaA weighted maps calculated with REFMAC. Two to six amino acids were added back into the structure where enough electron density was visible to place them. When only the main chain could be traced, residues apart from glycines and prolines were added as alanines. Then the model was refined for another 5 cycles and again rebuilt in O. This rebuilding procedure was continued until no more residues could be added reliably into electron density. The quality of electron density maps had improved but neither R_{cryst} nor R_{free} had changed appreciably.

Water molecules were added using the CCP4 program ARP/wARP 5.0 (see chapter 2). No more than 50 water oxygens were added in one ARP/wARP run and oxygens added to the binding site were deleted. Five cycles of refinement with REFMAC followed and the model was examined in O. Residue side chains of previously deleted and reinserted amino acids were added into appropriate areas of electron density, replacing water oxygens if necessary. These cycles of rebuilding and refinement were continued until the R_{cryst} converged and R_{free} started to increase.

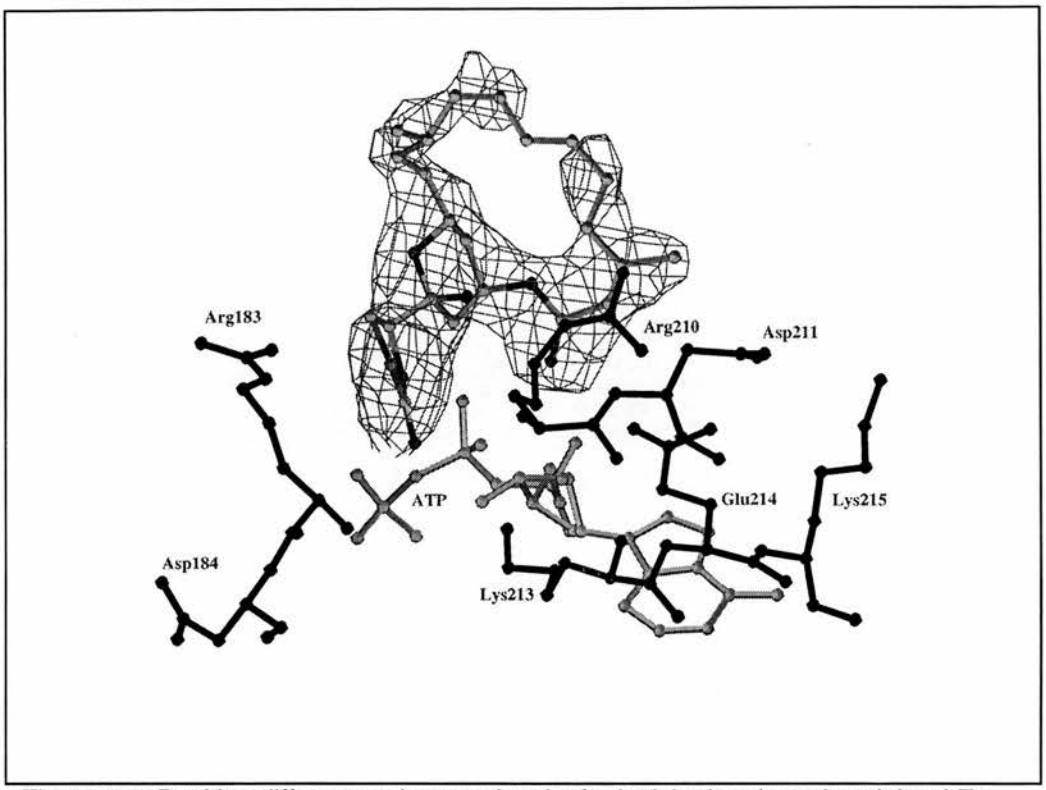

Figure 5.4: Positive difference electron density for latA in the sigmaA weighted Fo-Fc map. The model of α-actin:G1C had been refined with REFMAC with water oxygens added except in the binding site area. The picture shows positive difference density contoured at 2 x σ enveloping the final refined model of latA apart from a small gap over the macrolide ring. The ATP is shown in grey and the amino acids involved in latA binding (Ayscough et al. 1997) in black. The picture was created using O/Oplot.

The refinement converged with an R_{cryst} of 0.227 and an R_{free} of 0.301 with 465 water oxygens added. All previously deleted residues had been added back into the structure but the side chains of 46 residues could not be reliably located in electron density and were therefore added as alanines. The average B-factor for the main chain atoms of residues initially deleted from the model dropped to 52.5Å^2. A sigmaA weighted Fo-Fc map contoured at 2 x σ clearly showed the structure of latA but with a gap in the electron density on the macrolide ring. The gap was closed at a contour level of 1 x σ but did not properly cover the carbon atom located in the gap (Figure 5.4).

Result of the refinement and geometric analysis of the refined model:

Atoms in asymmetric unit:	984	atoms of gelsolin segment 1
	2691	atoms of α-actin
	29	of latA
	31	atoms of ATP
	3	Ca^{2+} ions
	444	water oxygen atoms
	4182	non-hydrogen atoms

Amino acids in asymmetric unit:	125	G1C
	375	α-actin
	500	

Amino acids not located in electron density: 16
Amino acids truncated to alanine: 46

Average B-factors:	41.1Å^2	all protein atoms
	40.1Å^2	all main chain atoms
	42.1Å^2	all side chain atoms
	32.6Å^2	gelsolin segment 1
	44.2Å^2	a-actin
	30.4Å^2	ATP
	41.3Å^2	latA
	45.8Å^2	calcium ions
	44.3Å^2	water oxygens

RMS deviation from mean B-factor:	18.7Å^2	for main chain atoms
	19.1Å^2	for side chain atoms

RMS deviations from small molecule data:
Bonds (1-2 neighbours): 0.19 Å
Angles (1-3 neighbours): 2.36°
RMS deviation from planarity:
4.9° for Torsion angle of peptide bonds
0.0016 Å for planar side chains

R_{cryst}: 0.228 for all data to 2.0Å

Table 5.2

In order to refine the model with the atomic co-ordinates of latA geometric restraints had to be defined. For ease of convenience SHELX was chosen to further refine the model including latA manually fitted into the binding site. Water oxygens whose B-factor refined to more than 63.2 Å^2 were set to half occupancy and if their B-factor again refined to more than 63.2 Å^2 they were deleted. The R_{cryst} converged at 0.224 and the R_{free} dropped to 0.282. Results of the refinement are presented in Table 5.2, Table 5.3, and Figure 5.5.

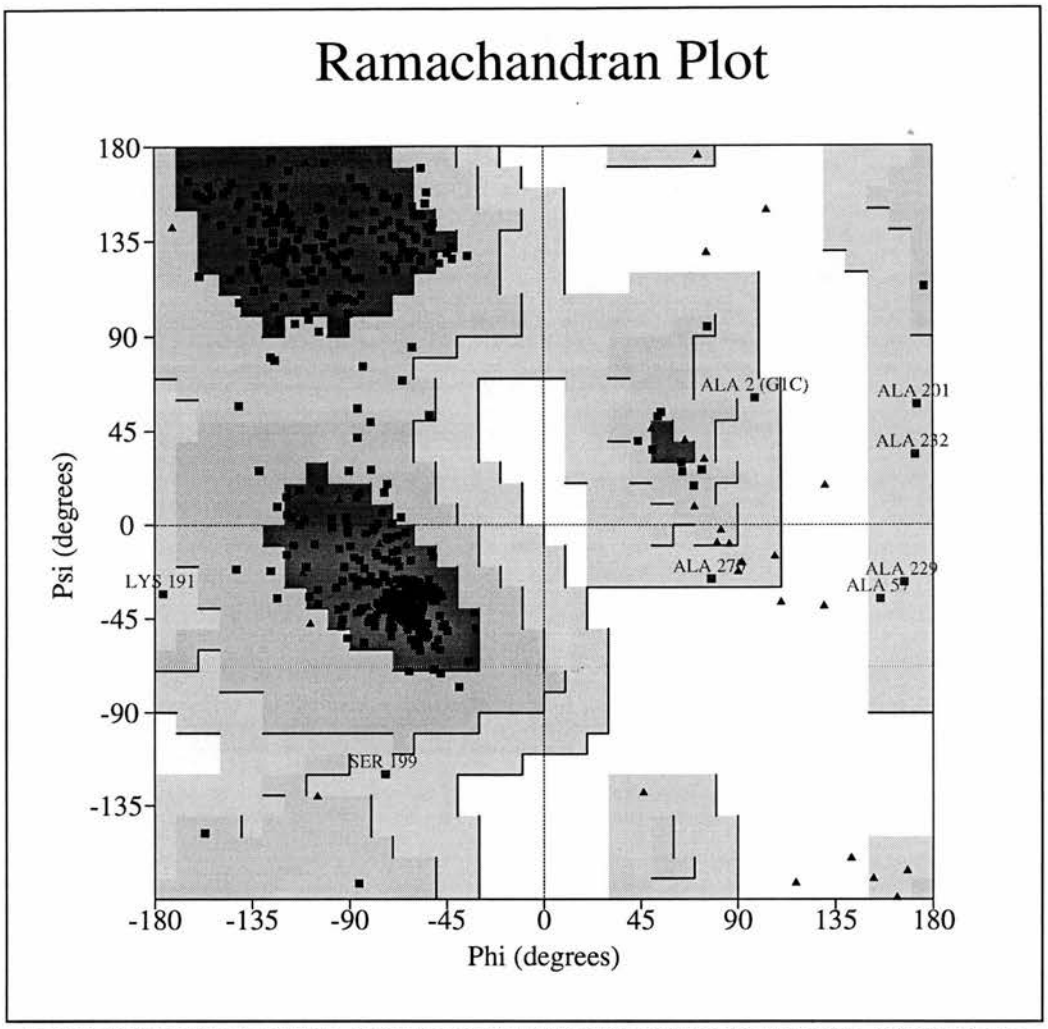

Figure 5.5: Ramachandran plot of α-actin:G1C with latA bound to actin. Glycines are represented with black triangles, all other residues with squares. Highlighted residues are of actin apart from Ala2(G1C). They are in generously allowed regions of the Ramachandran plot and are located in regions of the structure with high B-factors.

The relatively high R_{cryst} and B-factors of the refined model complies with the weak electron density around the previously mentioned regions in subdomain 2 and 4. SigmaA-weighted 2Fo-Fc electron density maps improved only slightly in those regions. Electron density maps definitely improved in the binding site and the model of latA was well covered by a sigmaA-weighted simulated-annealing (SA) OMIT Fo-Fc electron difference map (Figure 5.6).

Ramachandran plot statistics:		
Residues in most favoured regions	362	87.0%
Residues in additional allowed regions	46	11.1%
Residues in generously allowed regions	8	1.9%
Residues in disallowed regions	0	0.0%
Number of non-glycine and non-proline residues	416	100.0%
Number of end-residues (excl. Gly and Pro)	6	
Number of glycine residues	39	
Number of proline residues	23	
Total number of residues	484	

Table 5.3

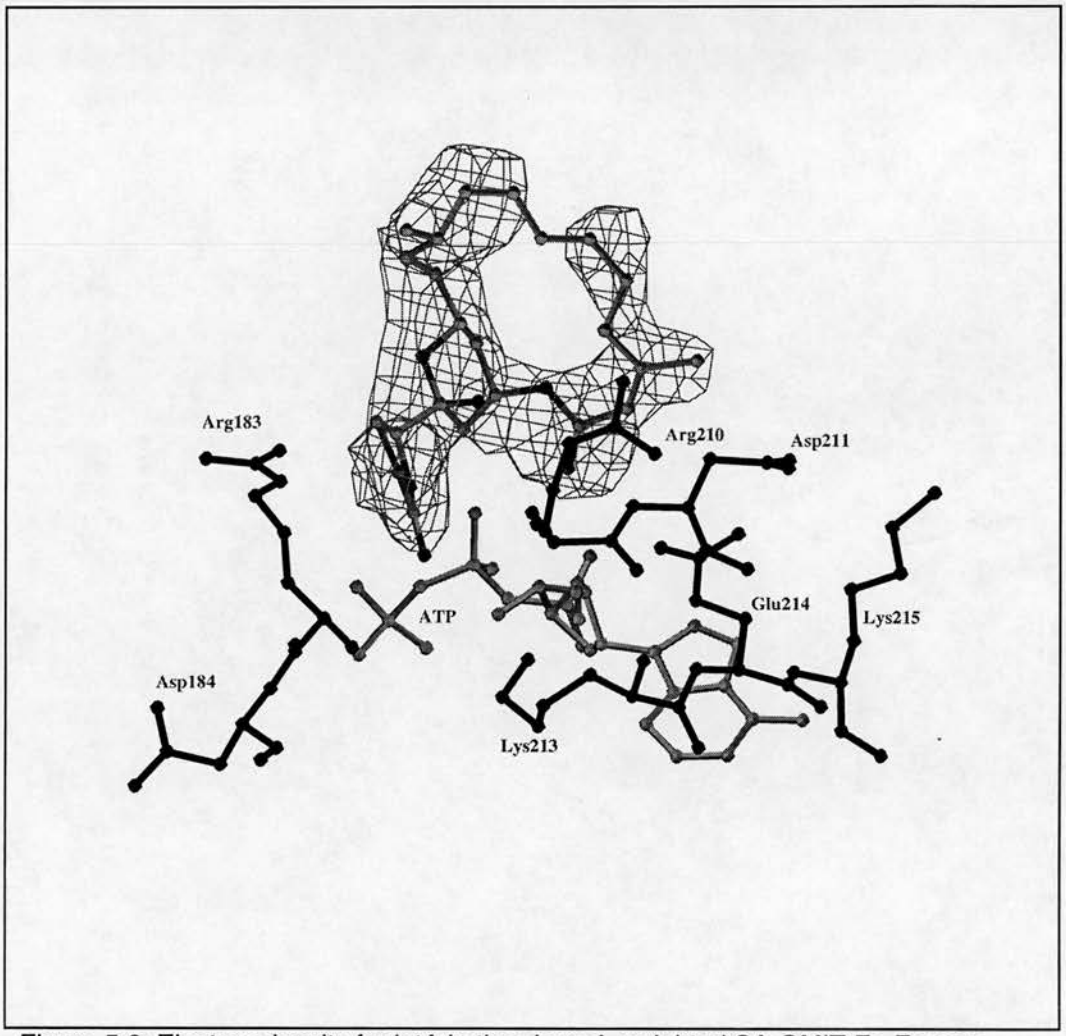

Figure 5.6: Electron density for latA in the sigmaA-weighted SA-OMIT Fo-Fc map. The picture shows the difference electron density contoured at 1.6 x σ enveloping the refined model of latA. The ATP is shown in grey and the amino acids involved in latA binding (Ayscough et al. 1997) in black. The picture was created using O/Oplot.

5.3 Discussion of latrunculin A binding to actin

5.3.1 The binding site of latrunculin A on actin

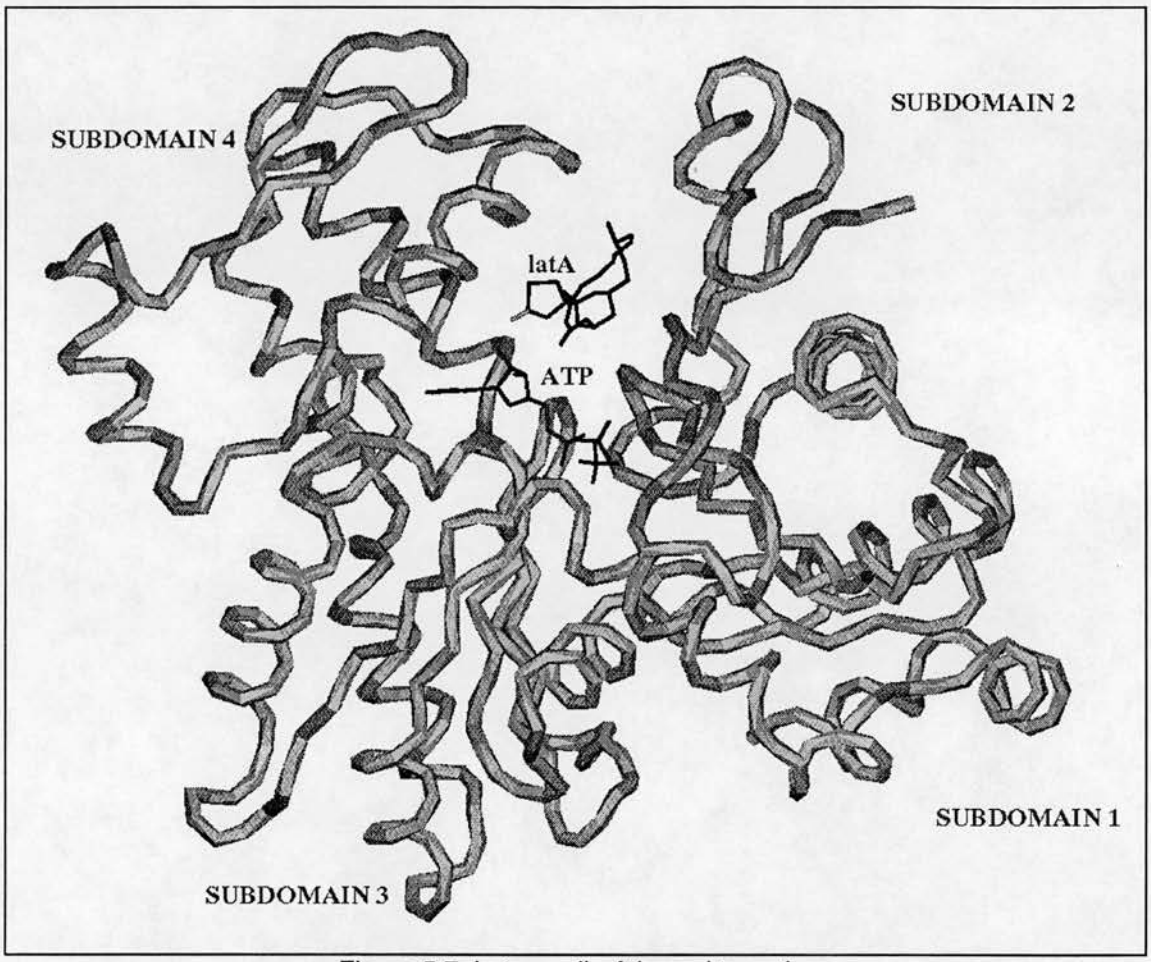

Figure 5.7: Latrunculin A bound to actin.

Latrunculin A binds to actin in the cleft between subdomains 2 and 4 (Figure 5.7). It is located just above the ATP which resides at the bottom of the cleft. Access to the binding site is quite unrestricted when entering from above, past the top ends of subdomain 2 and 4, and straight from the viewer's side into the plane of the picture shown as Figure 5.7. Access from the back of the picture plane is restricted by the side chains of Tyr69 and Arg183.

5.3.2 Changes in thermal displacement and disorder:

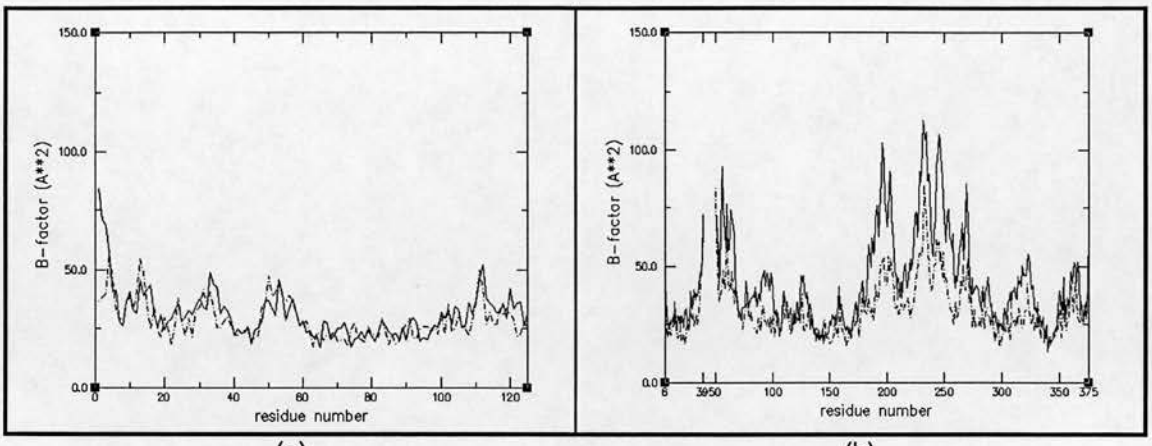

(a) (b)

Figure 5.8: Plot of main-chain B-factor averaged for each residue against residue number. The solid line represents B-factor values of the α-actin:G1C with latA, the dashed line represents values from the native structure. The picture was created using XMgr, SNAPSHOT, and XV. (a) Residues of G1C. (b) Residues of α-actin.

The binding of latA does not affect the structure of gelsolin segment 1 but appears to cause destabilising changes in the structure of the actin monomer, mostly in subdomains 2 and 4. Average B-factor values for the main-chain atoms of each amino acid of the latA containing structure and α-actin:G1C without latrunculin X-rayed at 100K (see chapter 3) were calculated using the CCP4 program BAVERAGE and the results compared (Figure 5.8). On average the B-factors of the whole main chain increased by 18.3 $Å^2$. The structure without latA shall be referred to as the "native" structure in the remainder of the text.

Apart from the first three amino acids, B-factors of G1C appear to be basically unaffected by latA binding. In the structure of actin the more disordered regions are even less localised after binding of latA. These regions are located at the top of the monomer in subdomain 2 and 4 (Figure 5.3) and coincide with the regions in weak electron density. The largest differences in B-factors between the native and the latA containing actin structure can be found with actin residues 55-66 in subdomain 2, and 183-204 and 216-274 in subdomain 4.

Residues 55-66 form a short helix followed by a surface exposed loop. In the latA containing actin structure the short helix is in a more strained or "bent" conformation than in the native structure. Residues 51-54 appear remarkably localised considering that these 4 amino acids separate a very weak density region (40-50) from a weak density region (55-66). The stabilising influence probably comes from forming an anti-parallel β-sheet with residues 34-36. Residues 183-208 and residues 220-250 constitute the majority of subdomain 4, emphasising that changes due to latA binding affect mostly the top half of the actin monomer.

5.3.3 Changes to the main chain:

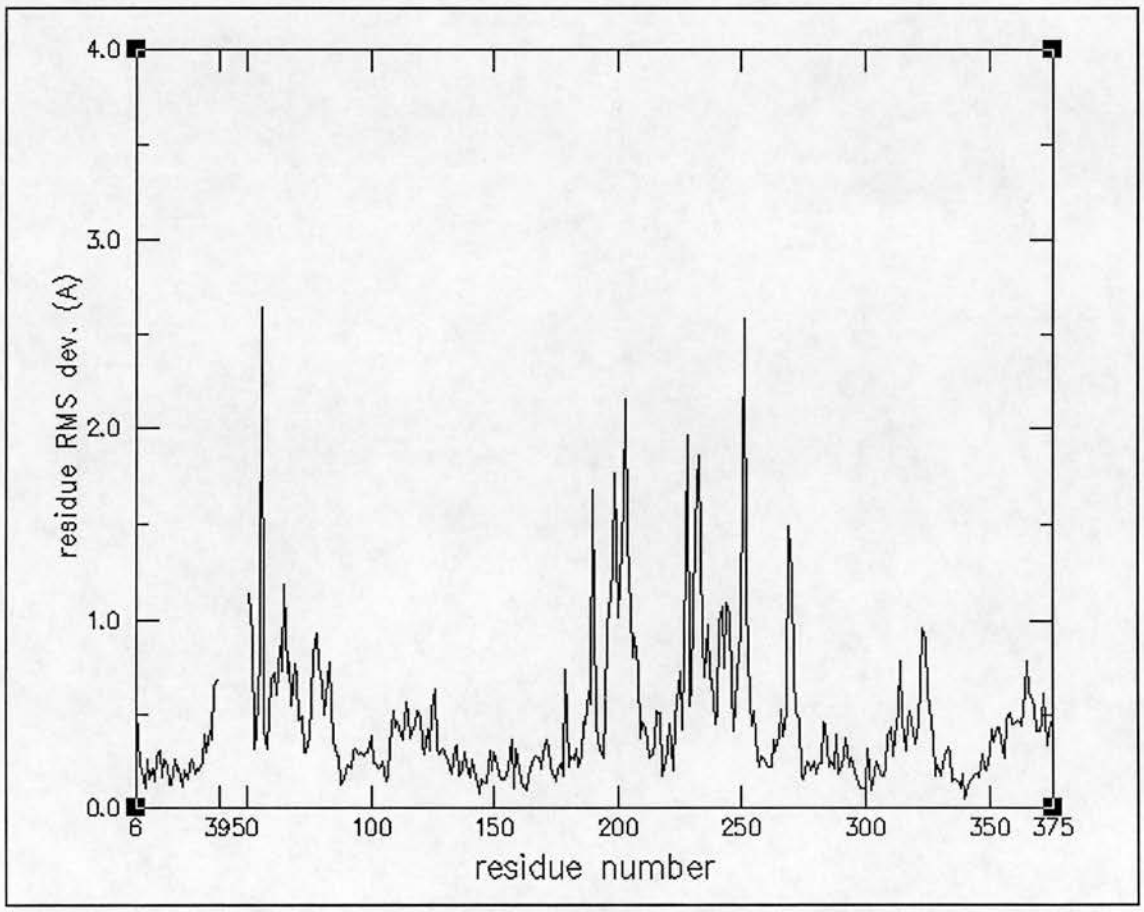

Figure 5.9: Plot of main-chain atom RMS distances between the refined α-actin model and the LSQ fitted native model. The largest distances lie within the areas of weak density and high B-factors: residues 51-52, 190-207, 227-252, and 269-270.

To determine changes of the main chain of actin due to binding of latA the structure of α-actin determined at 100K (see chapter 3) was fitted over the model of the latA containing α-actin using the program LSQMAN (see chapter 2) and least-squares fitting over main-chain atoms. The amino acids with the largest RMS deviation of their main-chain atoms (Figure 5.9) also lie in the regions of high B-factors and weak electron density (Figure 5.8).

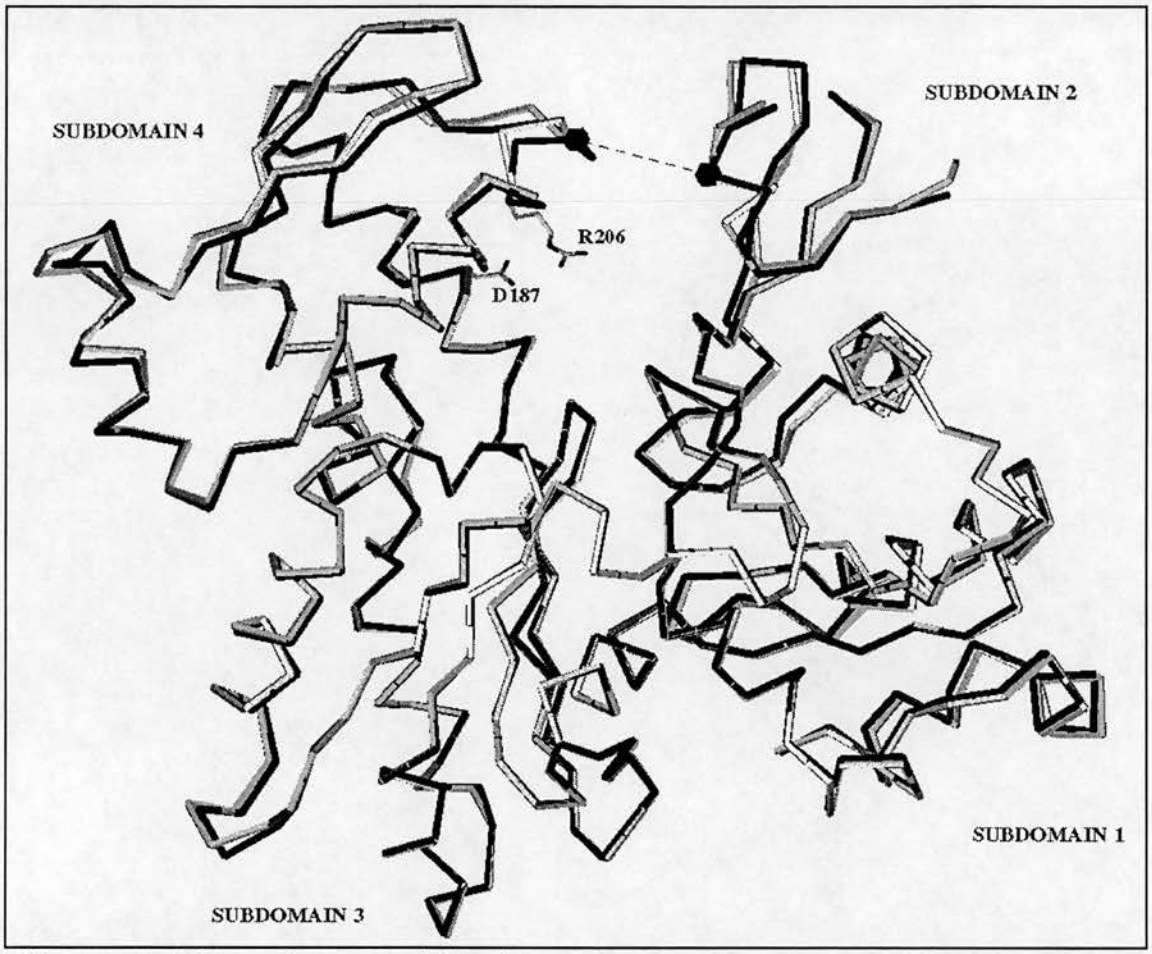

Figure 5.10: Distance between subdomain 2 and 4. The picture shows LSQ fitted Cα traces of native α-actin (light grey), α-actin from the latA containing complex (black), and tight-state β-actin from the complex with profilin (Schutt et al. 1993) (dashed line). Only the β-actin model displays the full DNaseI binding loop in subdomain 2. The shortest distance between Cα atoms of subdomain 2 and 4 of the refined model is marked with a dashed line. The left sphere marks the Cα position of residue 204 and the right sphere marks the Cα position of residue 59. Amino acids D187 and R206 are labelled because they form a new salt bridge in the latA containing structure. The picture was generated with Oplot, SNAPSHOT, and XV.

Examining the Cα traces of the two LSQ fitted actin structures in O (Figure 5.10) gives the impression that the cleft between subdomain 2 and 4 of the latA containing structure is slightly narrower than in the native structure. The shortest distance between subdomain 2 and 4 at the top of the actin structure is from the C-terminal end of helix 55-63 in subdomain 2 to the N-terminal end of helix 202-216 in subdomain 4. When examining the two closest Cα atom pairs (Table 5.4) it appears that in the latA containing α-actin structure subdomains 2 and 4 have moved closer than in the native structure.

structure	*residue number of Cα in subdomain 2*	*residue number of Cα in subdomain 4*	*distance*	*RMS main chain deviation to the refined actin model after LSQ fit*
refined model	59	204	8.8Å	
	59	203	9.5Å	
native	59	204	10.0Å	0.5Å
	62	203	10.1Å	
tight β-actin (profilin)	63	203	5.8Å	1.1Å
	63	204	6.8Å	

Table 5.4: Closest Cα atom distances from subdomain 2 to 4 at the top of the actin structure

Yet this cleft closure is not as extensive as in the tight structure of β-actin complexed to profilin (Schutt et al. 1993). The fact that the latA-containing α-actin structure is more similar to the native structure than to tight β-actin is also reflected in the overall RMS deviations of main-chain atoms fitted over each other. The RMS distance between the refined model and the native structure is only 0.5Å as opposed to 1.1Å between refined model and tight β-actin (Schutt et al. 1993).

5.3.4 Changes to individual residues:

None of the residues involved in conferring resistance (Ayscough et al. 1997) changed significantly in conformation due to the binding of latA. The major changes

occur with Ile34 and Gln59 in subdomain 2, and Arg206 in subdomain 4.

Cδ of Ile34 in its native position would be only 2.8 Å away from the macrolide ring of latA. This appears to be unfavourable since in the refined structure its side chain is rotated by about 180° to move the longer branch of the side chain out of latrunculin's way.

The amide group of Gln59's side chain in its native position would clash with latA's macrolide ring. Unsurprisingly the side chain is rotated away by approximately 180° in the refined structure, pointing into open solvent area.

Nε of Arg206 in the native structure is at a hydrogen bonding distance of 3.1 Å to a carboxyl oxygen (Oδ) of Asp187 and the guanidino group is approximately at right angles to the carboxyl group of Asp187. Both residues are located in subdomain 4 (Figure 5.10). In the refined latA complex the guanidino group of Arg206 is rotated by about 90° to lie in the same plane as the carboxyl group of Asp187. This reduces the distance between Nε(Arg206) and Oδ(Asp187) to 3.0 Å and brings the terminal trans nitrogen (NH2) of Arg206 3.4 Å close to the carboxyl oxygen of Asp187. A strong salt bridge is thus formed which is reflected in strong electron density covering the guanidino and the carboxyl group (Figure 5.11). In the the other four actin structures (Kabsch, McLaughlin, Schutt, Chik) the functional groups of Asp187 and Arg206 are also further apart than in the latA containing structure (Table 5.5) and the flat functional groups do not lie in one plane.

α-actin (Kabsch)	3.4Å
α-actin (McLaughlin)	5.2Å
β-actin (Schutt)	3.1Å
β-actin (Chik)	3.7Å

Table 5.5: Closest distance between the functional groups of Asp187 and Arg206.

In its refined position latA displaces four water molecules from the native structure. These waters would clash with O1, O5, C14, and C21 of latA respectively. Despite

its hydrophobicity Latrunculin A is capable of forming 4 hydrogen bonds to residues of actin (Table 5.6).

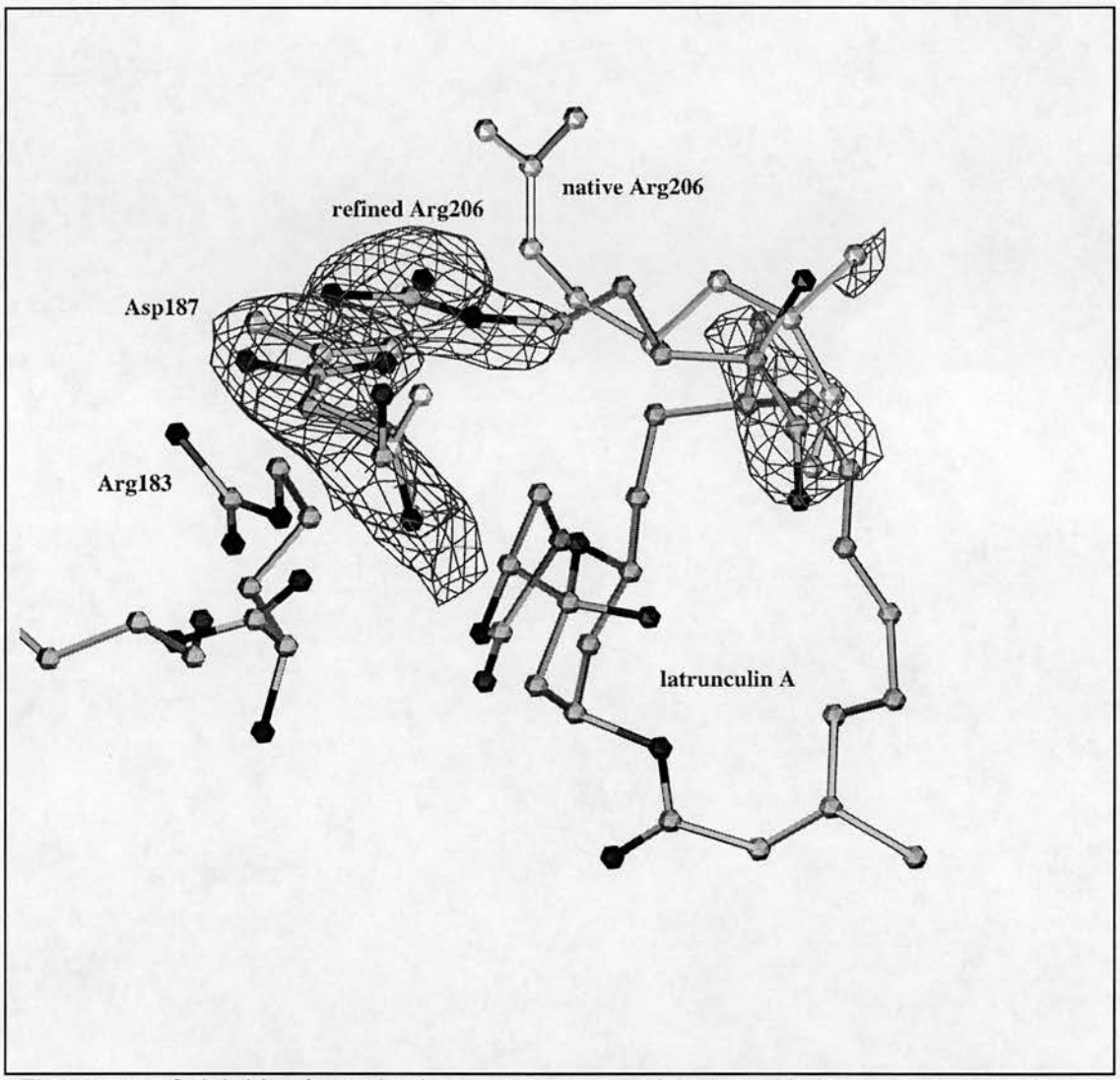

Figure 5.11: Salt bridge formation between Arg206 and Asp187. Native Arg206 and Asp187 are shown in plain grey, whereas residues from the refined structure and refined latA have oxygen, nitrogen and sulphur coloured dark. The electron density drawn around Asp187 and Arg206 is from a sigmaA-weighted 2Fo-Fc map at a contour level of 1.6 x σ. At this level the main-chain and the salt bridge feature strong electron density but not the flexible part of the Arg206 side-chain. The picture was generated with Oplot.

O4(latA)	NE(Arg210)	3.2Å
O4(latA)	O(water)	2.9Å
O3(latA)	OH(Tyr69)	2.9Å
O5(latA)	OG1(Thr186)	2.7Å
N1(latA)	OD1(Asp157)	2.8Å
O1(latA)	O(water)	3.2Å

Table 5.6: Possible hydrogen bonds involving latA

The ester carbonyl oxygen O1 of latA, situated on the macrolide ring, is not close enough to any hydrogen donor atom to form a hydrogen bond with an actin residue. At 3.3Å distance to the ATP ribose ring it is the closest point of latA to the nucleotide. No hydrogen bonds can be formed with ribose oxygens since they lie on the opposite side of the ribose ring. O1 is however in hydrogen bonding position to a water oxygen which in turn is in position to from a hydrogen bond to the carboxyl group of Glu214. This possibly exerts a small additional stabilising effect on latA's position counteracting the rejecting forces between the ribose carbon atoms and latA's O1.

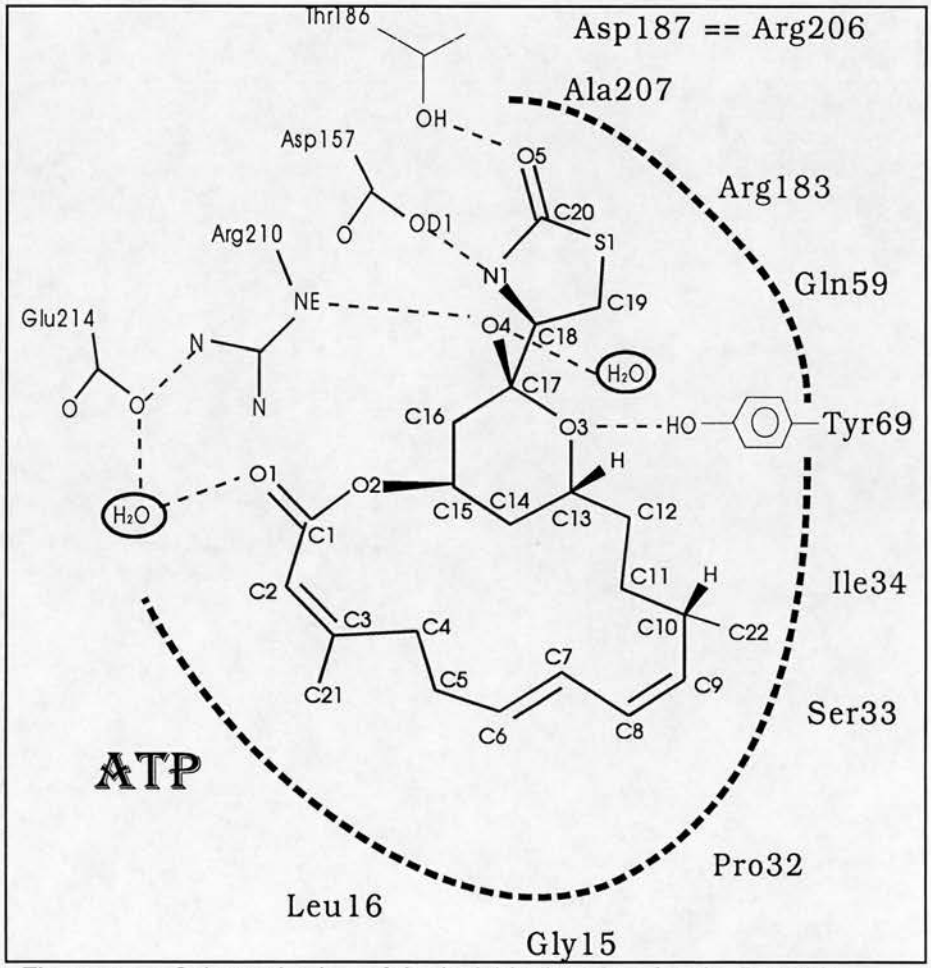

Figure 5.12: Schematic view of the latA binding site of actin. Possible hydrogen bonds are drawn with dashed lines. The thick dashed line partially surrounding latA marks the more hydrophobic part of the binding pocket. Residues involved in hydrophobic interaction are labelled in large print.

With latA bound to actin the solvent accessible area of ATP, calculated with the CCP4 program SURFACE, is only 35Å^2 as opposed to 53Å^2 in the native structure. Latrunculin A is responsible for the loss of only 10Å^2, which is the buried surface area only between ATP and latA. The loss of further 8Å^2 is due to conformational changes of actin residues around the ATP. These could be concerted conformational changes accompanying the closure of the cleft.

Other residues close to latA are Gly15, Leu16, Pro32, Ile34, Ala207 and, with their hydrophilic groups turned away, Ser33, Gln59, Arg183, including the salt bridge forming Asp187 and Arg206. These residues create a hydrophobic pocket and should make binding of the hydrophobic latA thermodynamically favourable. These extensive hydrophobic interactions together with the 4 actin-latA hydrogen bonds and the indirect interaction of O1 with Glu214 via a water molecule (Figure 5.12) may explain the low dissociation constant of 0.2μM (Spector et al. 1989).

5.3.5 Residues involved in conferring resistance to latrunculin A:

In the course of their experiments Ayscough et al. (1997) needed to ascertain the specificity of latA, which was used to disrupt the actin cytoskeleton in budding yeast cells (*Saccharomyces cerevisiae*). Using a charged-to-alanine scan of the ACT1, the single yeast conventional actin gene (Wertman et al. 1992), they discovered three latA resistant cell lines, varying in increased salt and heat sensitivity. The mutations found in the three cell lines are listed in Table 5.7. All residues involved cluster at the inside of the nucleotide binding cleft in subdomain 4 of actin (Figure 5.13) and are conserved in both the mammalian α-actin and the yeast ACT1 sequence. As mentioned before none of these residues changed conformation significantly on binding of latA.

Cell line	Mutation
act1-117	R183A, D184A
act1-113	R210A, D211A
act1-112	K213A, E214A, K215A

Table 5.7: Residues involved in conferring latA resistance to actin.

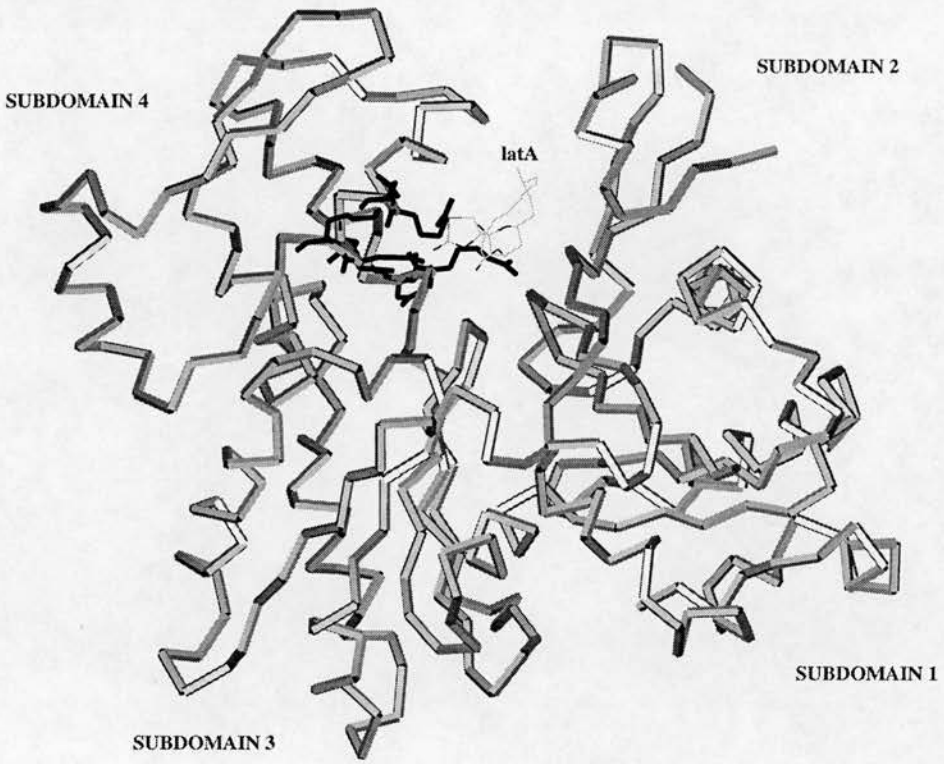

Figure 5.13: Residues involved in conferring resistance to latA. The Cα trace of the refined actin model is shown in grey and Arg183, Asp184, Arg210, Asp211, Lys213, Glu214, and Lys215 are shown in black. Latrunculin A is labelled and drawn in its final refined position. The picture was generated with Oplot.

Including the residues mentioned above the sequence of yeast ACT1 actin and mammalian α-actin is 87% identical (Table 5.8). Due to this high identity it was thought important to analyse the residues involved in conferring latA resistance to yeast in the context of the α-actin structure. Any indication as to why the alanine mutations of these residues might lead to decreased latA affinity could be valid for both proteins and would allow the assumption that the same mutations introduced into the α-actin sequence would also lead to decreased latA sensitivity.

```
ACT1        2 DSEVAALVIDNGSGMCKAGFAGDDAPRAVFPSIVGRPRHQGIMVGMGQKDSYVGDEAQSK 61
              :.|.:||| |||||: |||||||||||||||||||||||:||||||||||||||||||
α-actin     2 EDETTALVCDNGSGLVKAGFAGDDAPRAVFPSIVGRPRHQGVMVGMGQKDSYVGDEAQSK 61

ACT1       62 RGILTLRYPIEHGIVTNWDDMEKIWHHTFYNELRVAPEEHPVLLTEAPMNPKSNREKMTQ 121
              ||||||:|||||||:|||||||||||||||||||||||||.|||||||:|||:|||||||
α-actin    62 RGILTLKYPIEHGIITNWDDMEKIWHHTFYNELRVAPEEHPTLLTEAPLNPKANREKMTQ 121

ACT1      122 IMFETFNVPAFYVSIQAVLSLYSSGRTTGIVLDSGDGVTHVVPIYAGFSLPHAILRIDLA 181
              ||||||||||.||:||||||||:|||||||||||||||| ||||.|::|||||:|:|||
α-actin   122 IMFETFNVPAMYVAIQAVLSLYASGRTTGIVLDSGDGVTHNVPIYEGYALPHAIMRLDLA 181

ACT1      182 GRDLTDYLMKILSERGYSFSTTAEREIVRDIKEKLCYVALDFEQEMQTAAQSSSIEKSYE 241
              |||||||||||:|||||| ||||||||||||||||||||:|| ||| |||:|||||
α-actin   182 GRDLTDYLMKILTERGYSFVTTAEREIVRDIKEKLCYVALDFENEMATAASSSSLEKSYE 241

ACT1      242 LPDGQVITIGNERFRAPEALFHPSVLGLESAGIDQTTYNSIMKCDVDVRKELYGNIVMSG 301
              |||||||||||||| ||:||:|| :|:|||||.:||||||||||:|:||:||:| ||||
α-actin   242 LPDGQVITIGNERFRCPETLFQPSFIGMESAGIHETTYNSIMKCDIDIRKDLYANNVMSG 301

ACT1      302 GTTMFPGIAERMQKEITALAPSSMKVKIIAPPERKYSVWIGGSILASLTTFQQMWISKQE 361
              ||||:||||:||||||||||||:||:|||||||||||||||||||||:||||||||:|||
α-actin   302 GTTMYPGIADRMQKEITALAPSTMKIKIIAPPERKYSVWIGGSILASLSTFQQMWITKQE 361

ACT1      362 YDESGPSIVHHKCF 375
              |||:||||||:|||
α-actin   362 YDEAGPSIVHRKCF 375
```

Table 5.8: Sequence comparison of α-actin and yeast ACT1 actin.
Sequence identity: 86.90%, sequence conservation: 95.99%, 325 matches (|), 34 conservative changes (:), 15 mismatches (<space> and ". ")

The flexible side chain of Arg183 is involved in hydrophobic interaction with the thiazolidinone group of latA, its guanidino group pointing away. Asp184 is 6.7 Å away from latA and its side chain is oriented away into the solvent area. Mutation of these two residues to alanine will cause little change in respect to residue 184, but it will reduce the contact made by residue 183 with latA, weakening the hydrophobic interaction. In both the native and the refined structure the NH2 of Arg183 (guanidino group, trans) is in hydrogen bonding position to the main chain oxygen of residue 14 and the carboxyl group of Asp157. Loss of these interactions due to

R183A mutation might contribute to destabilising latA binding.

Asp211 is 7.4 Å away from latA and has no interaction within the binding site. On the other hand the side chain of Arg210 stretches into the concave side of latA between the thiazolidinone group and the macrolide ring and a hydrogen bond can be formed with latA's hydroxyl group. The R210A mutation will obviously result in changes in the binding site reducing the affinity for latA.

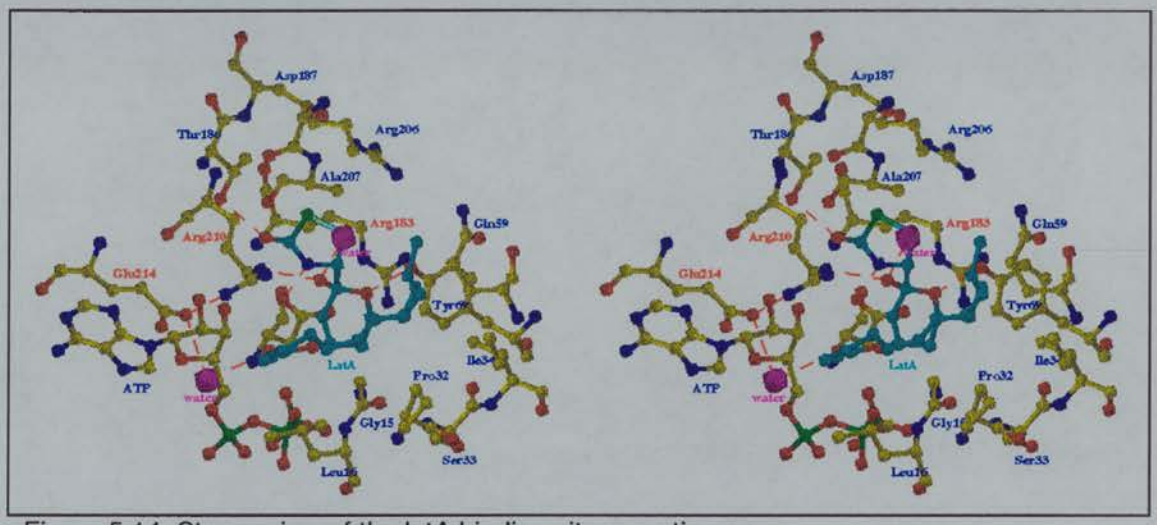

Figure 5.14: Stereo-view of the latA binding site on actin.
Colour code: blue ..... nitrogen atoms,
labels of amino acids and ATP.
purple ..... water oxygen atoms and their labels.
red..... dashed lines depicting the possible hydrogen bonds with latA,
labels of residues involved in confering latA resistance,
oxygen atoms except those of water.
green ..... sulfur and phosphorus atoms.
yellow ..... carbon atoms of amino acids and ATP.
cyan..... carbon atoms of latA and label of latA.
The picture was generated with Oplot, SNAPSHOT, and XV.

The terminal side-chain nitrogen of Lys215 is 8.8Å away from latA and its side chain points into the solvent area. Being that far away from the binding site the K215A mutation will probably have very little influence on latA binding. But Glu214 is at a hydrogen bonding distance of 2.7Å to an ATP-ribose hydroxyl group and, probably more significantly, at a distance of 2.9Å to NH2 of the Arg210 guanidino group. This probably helps in pulling the Arg210's side chain into the right position to interact

with latA. Lys213 is relatively far from the binding site but its side chain stretches towards it, so that the terminal amino group is in hydrogen bonding distance to the hydroxyl groups of the ATP-ribose ring (2.9Å and 3.8Å), to OG1 of Thr186 (2.9Å), and to the main chain oxygen of Gly182 (3.6Å). Also the amino group is 4.0Å away from O5 of latA, which admittedly is at the uppermost distance limits for hydrogen bond interaction. The most important mutation of these residues is probably E214A, although the loss of Lys213's amino group close to the binding site will also have its implications for latA binding.

This analysis shows that particularly the mutations R183A, R210A, K213A, and E214A (Figure 5.14) should be the main contributors to decreased latA affinity, when applied to mammalian α-actin. Considering that the residue range 182-225 only contains two sequence differences between α-actin and ACT1 actin, T195S and V202S respectively, it can be suggested that the observations should also hold in the case of yeast actin.

5.4 Cytochalasin D

5.4.1 Attempt to soak cytochalasin D into the α-actin:G1C complex

Cytochalasin D, like latA, is a very hydrophobic compound. The basic soaking problem again was to balance cytochalasin D solubility with actin crystal stability in buffers containing organic solvent.

Cytochalasin D at a concentration of 0.1mM was just about completely solubilised in a buffer containing 0.15% (v/v) DMF, 19.85% (v/v) ethanol, 25% (v/v) glycerol, 10% (w/v) polyethylene glycol 6000, 0.1mM ATP, 10mM DTT, 1.0mM NaN_3, 0.1mM $MgCl_2$, 150mM NaCl, and 50mM MES pH6.6.

One crystal soaked in this buffer over night was X-rayed at the SRS Daresbury on beamline PX9.6 at 100K with $\lambda = 0.87$Å. A 92% complete data set to 2.5Å was collected and scaled with an Rmerge of 0.094. The following refinement of the α-actin:G1C model against the data and calculation of sigmaA-weighted difference maps did not indicate the presence of cytochalasin D. Co-crystallisation of α-actin:G1C and cytochalasin D was also tried but yielded no crystals. Meanwhile cytochalasin D crystallised in form of clear needles, about 0.1-1.0mm long and 40-100μm in diameter (Figure 5.15) in some soaking buffers.

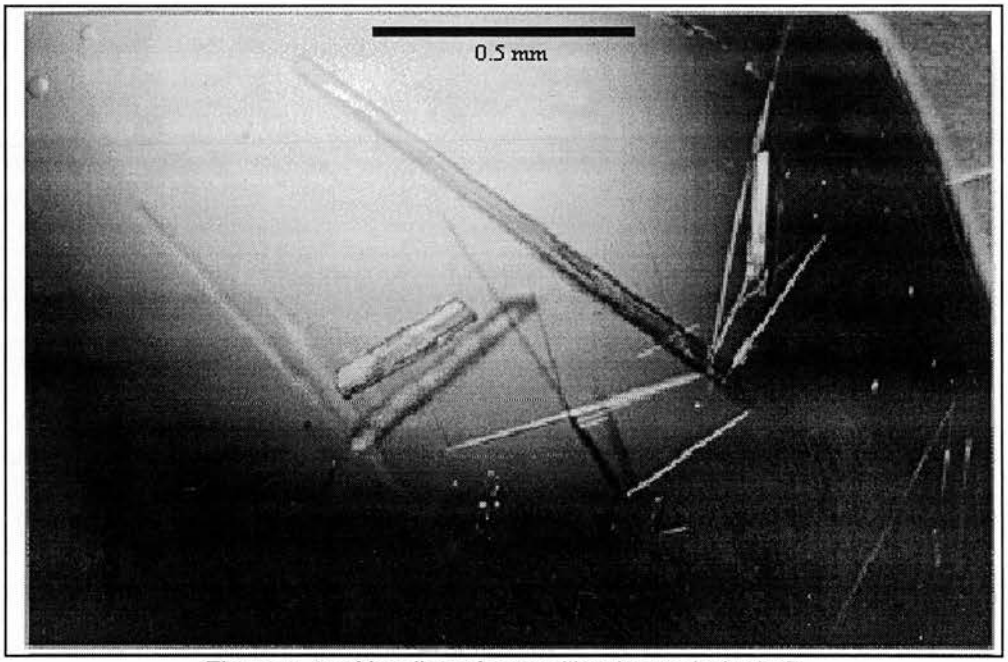

Figure 5.15: Needles of crystallised cytochalasin D

5.4.2 The crystal structure of cytochalasin D

The structure of cytochalasin D (formerly also known as Zygosporin A, Aldridge and Turner in J. Antibiotics 1969) had been solved using chemical methods, mass spectroscopy, NMR (Aldridge and Turner in J. Chem. Soc. 1969, Minato and Matsumoto 1970, Macotta et al. 1993) and X-ray diffraction analysis of the analogue

isozygosporin A p-bromobenzoate (Tsukuda et al. 1972), but not verified by X-ray diffraction analysis of native cytochalasin D crystals.

Crystallographic data of cytochalasin D	
Cell symmetry	Monoclinic
Spacegroup	$P2_1$
a = 7.57Å	
b = 30.26Å	
c = 12.12Å	
$\alpha = \gamma = 90.00°$	
$\beta = 96.45°$	
Atoms in asymmetric unit	$C_{60}\ H_{76}\ N_2\ O_{13}$
Molecules in the unit cell	4 cytochalasin D 2 water molecules
Temperature	220K
Radiation wavelength	1.542Å
Radiation type	CuKα
total number of reflections	4469
Average σI/<I>	0.20
θ_{min}	2.92°
θ_{max}	59.89°
range of H	-7 to 8
range of K	-28 to 27
range of L	-8 to 13
R_{cryst}	0.074

Table 5.9

The cytochalasin D needles, which had grown in some of the soaking buffers, were taken to the X-ray source of the Department of Chemistry, the University of Edinburgh, where Dr. Simon Parsons collected the diffraction data and Dr. Robert Gould solved the structure using the co-ordinates from the isozygosporin A p-bromobenzoate crystal structure (Cambridge Structural Database entry ZYGSBB10) as a search model. Crystallographic data are compiled in Table 5.9 and the contents of the asymmetric unit are shown in Figure 5.16. Unfortunately the data were not good enough to reveal the positions of hydrogen atoms.

The results confirm the structure of cytochalasin D. Despite the hydrophobic nature of cytochalasin D the asymmetric unit contains two NCS related cytochalasin D molecules and a water molecule hydrogen bonded to them. The water oxygen atom is also in hydrogen bonding distance to a cytochalasin molecule of the neighbouring (1-

x,y,z) asymmetric unit.

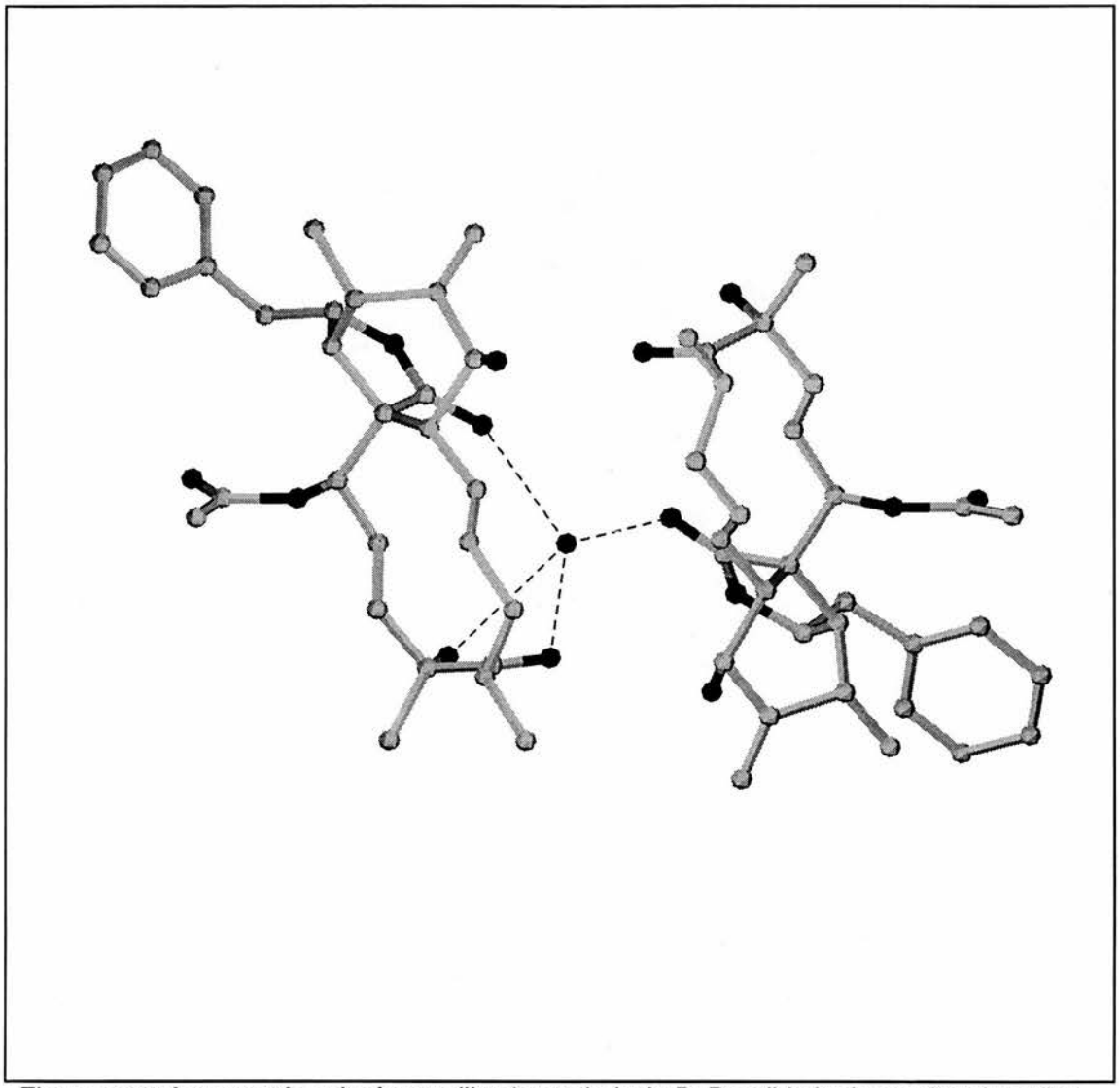

Figure 5.16: Asymmetric unit of crystallised cytochalasin D. Possible hydrogen bonds to the central water oxygen are drawn as dashed lines.

5.5 Conclusion

The binding of latA to actin induces a slight closure of the cleft between subdomain 2 and 4. In addition parts of both subdomains at the top of the actin monomer are more disordered in the crystal structure than in the native structure without latA. Several amino acids at the binding site rearrange on binding of latA. The most striking change is the roughly 90° twist of the side chain of Arg206 to form a strong salt bridge with Asp187. Both residues are located in subdomain 4 and point into the nucleotide binding cleft between the two major actin domains. As can be seen in Figure 5.10, it is mainly due to movements in subdomain 4 that subdomain 2 and 4 are slightly closer to each other than in the native structure. This is probably due to the salt bridge formation causing a slight contraction of subdomain 4.

These changes in conformation at the top of the actin monomer might be the reason why latA prevents actin monomers from polymerising. Subdomain 4 may be hindered in adopting the most favourable conformation for binding to the barbed end of F-actin due to the salt bridge formed between Asp187 and Arg206. Thus latA can be regarded as an actin sequestering agent, preventing actin monomers from participating in F-actin formation.

Latrunculin A was found to impede actin nucleotide exchange (Ayscough et al. 1997). This concurs with the closure of the actin domain cleft discussed above. The 34.5% smaller solvent accessible area around the ATP due to binding of latA might lead to the suggestion that nucleotide hydrolysis in the binding site could be restricted too.

When gelsolin segment 1 binds a free actin monomer, it forces the monomer into the same overall conformation (see chapter 3) irrespective of the actin isoform, provided that any influence of the crystallisation buffer is ruled out. This work has shown that the control gelsolin segment 1 exerts on actin is not stringent enough to prevent conformational changes induced by the binding of latA. Gelsolin can nucleate and

stably cap actin filaments (Yin H.L. et al. 1988), which implies that the two monomers bound are in a conformation compatible with the barbed end of actin monomers. This hypothesis might not apply to the overall conformation of actin since G1 binds to parts of actin subdomain 1 and 3. Any restrictive influence G1 exerts will be largest in respect to these two "barbed-ended" subdomains. Obviously the generally more flexible subdomains 2 and 4 have to be able to adopt the same conformation as in polymerised actin, otherwise the ternary actin:gelsolin complex would not cap barbed ends of F-actin. Gelsolin segment 1 also prevents actin nucleotide exchange (Tellam R. 1986) and keeps actin in a "tighter" state than observed in the complex of open-state β-actin with profilin (Chik et al. 1996). The full extent of latA's influence on subdomains 2 and 4 might not be visible in the structure determined as is indicated by the higher degree of disorder in the crystal structure in comparison to native α-actin:G1C.

Even so, all actin structures solved with gelsolin segment 1 bound have an extremely mobile loop at the pointed end of subdomain 2 and the binding of latA to the α-actin:G1C complex can induce conformational changes both in subdomain 2 and 4 at the "pointed" end of the monomer. This suggests that if the conformation of subdomains 2 and 4 in the complex with G1C is not identical to the conformation in a filament subunit, they are sufficiently mobile to potentially adopt the conformation in polymerised actin.

The structural studies on the α-actin:G1C complex containing latA show that actin in this complex might be in the same conformation as a subunit in a filament. Latrunculin A does not bind at a subunit:subunit interface. If we had seen no conformational change, we would have had to conclude that latA merely stabilised the monomeric G conformation of actin. However we cannot prove that the conformation in the latrunculin-free structure is that of a filament subunit due to the mobility of the subdomains 2 and 4. This mobility is demonstrated in the latA containing α-actin:G1C complex since latA can elicit a different conformation at the pointed end of the monomer despite the tightly bound G1C. Therefore it is possible

that, when gelsolin bound actin associates with other actin molecules via subdomains 2 and 4 of gelsolin bound actin, a different conformation of subdomains 2 and 4 could potentially be stabilised allowing the tight association of actin molecules in a filament.

To determine the full extent of the changes caused by the binding of latA to actin, co-crystallisation with latA could be attempted. This could be done without any other actin binding protein since latA would prevent any polymerisation of actin under crystallisation conditions. This would provide further insights into the extent of G1C's influence on actin in the crystal structure.

6. Discussion

6.1 Previous considerations of the flexibility of actin

α-actin :DNaseI	Kabsch et al. 1990
α-actin : gelsolin segment 1	McLaughlin et al. 1993
β-actin (tight state) : profilin	Schutt et al. 1993
β-actin (open state) : profilin	Chik et al. 1996

Table 6.1

Actin, like many large proteins, consists of multiple domains which are distinct structural units connected by flexible structural elements (Page et al. 1998). Rotations of such protein domains with respect to one another are often important in many biological processes such as enzyme catalysis, ligand binding, and oligomerisation (Huber and Bennet 1983). Normally these events occur on a timescale of milliseconds to microseconds and are not usually hindered by high energy barriers. Multiple conformations of proteins are therefore accessible in solution under biological ionic and temperature conditions. Although the number of conformations of a protein in crystallised form is greatly restricted, information on the flexibility of the protein and its biological relevance can be obtained by comparing crystal structures under different conditions.

The four previously published crystal structures (Table 6.1) of actin demonstrated that the actin structure has scope for flexibility, and could adopt different conformations when bound to different proteins and crystallised under different conditions. A detailed summary and analysis of conformational changes between those actin complexes was published by Page et al. (1998).

The conformation of actin has only been determined for its monomeric form in complex with various actin binding proteins. Its conformation in the filament has been modelled (Holmes et al. 1990, Lorentz et al. 1993, Tirion et al. 1995) but no high resolution data are available to confirm postulated models of the conformation of F-actin.

Gelsolin can stably cap actin filaments, yet the tight binding of G1 to the barbed end (between subdomains 1 and 3) of the actin monomer suggests a certain degree of control exerted by G1 on the actin conformation, particularly for subdomains 1 and 3. It remains unclear whether the structure of actin in complex with G1 has sufficient flexibility at its pointed end (subdomains 2 and 4) alone to adopt F-conformation or whether actin bound to G1 is already in the proper conformation to add to the barbed end of a filament.

6.2 The conformations of α- and β-actin complexed to G1

Compared to all previously published actin crystal structures the model for α–actin complexed to G1C and X-rayed at 100K was most similar to the structure of β-actin in complex with G1C, also X-rayed at 100K (Table 6.2). The major conformational differences to the previously published β-actins (Schutt et al. 1993, Chik et al. 1996) are located at the solvent exposed parts of actin subdomain 2 and 4.

LSQ fitted structure	RMS deviation of main chain (Å)
α-actin (100K, chapter 3)	0.3
α-actin (Kabsch et al. 1990)	0.9
α-actin (McLaughlin et al. 1993)	0.6
β-actin (Schutt et al. 1993)	1.0
β-actin (Chik et al. 1996)	1.6

Table 6.2: Mean main chain RMS deviations to the refined β-actin model from the complex with G1C. Actin structures were LSQ fitted over the refined model for β-actin in complex with G1C at 100K. Mean RMS deviations (in Å) were calculated for actin residues 11-39 and 52-370.

Also the orientation of the large and the small actin domain to each other differs from the orientation in tight-state β–actin (Schutt et al.,1993) by about 5°, which is very similar to what Schutt et al. found when comparing their structure to α-actin from the complex with DNaseI. It appears that either the binding of G1C to β-actin and/or the

chosen crystallisation conditions forced β-actin to adopt a similar conformation as α-actin.

This allows the conclusion that the conformation of actin isoforms mainly depends on the type of ligand bound, if crystallised under the same conditions.

6.3 Structures of gelsolin segment 1

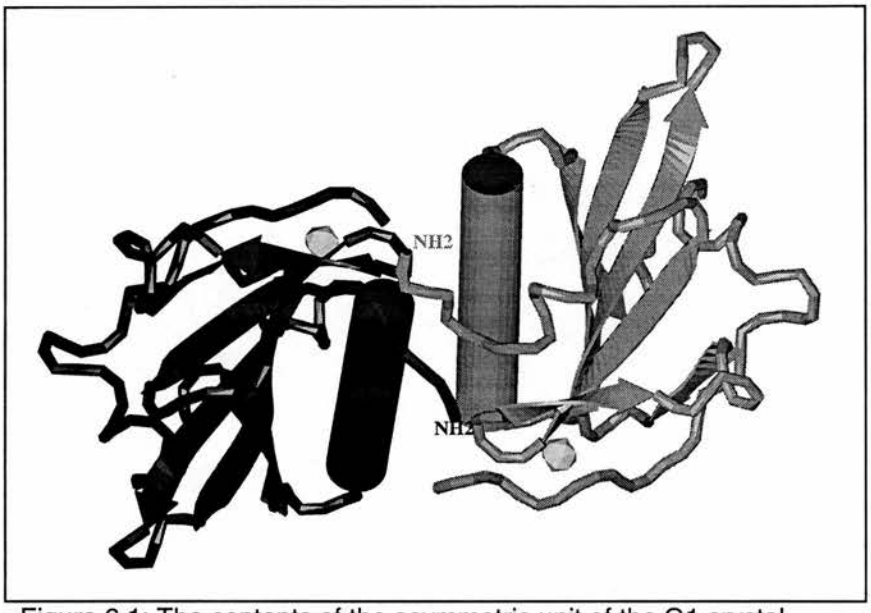

Figure 6.1: The contents of the asymmetric unit of the G1 crystal structure excluding water oxygens. G1B is shown in black on the left, G1A in grey on the right. The calcium ions are represented by grey spheres. The N-termini of the proteins are labelled and the main α-helix is drawn as a full cylinder.

Gelsolin segment 1 can bind tightly to an actin monomer enabling whole gelsolin to not only cap but also sever actin filaments. Comparison of the crystal structures of G1 (Figure 6.1), G1C from its complex with actin, and equine G1 from the structure of horse gelsolin (Burtnick et al. 1997) shows that apart from conformational changes at the N- and C-terminus gelsolin segment 1 retains its fold regardless of quarternary structure and crystallisation conditions (Table 6.3).

Its interaction with actin is via a hydrophobic patch centred on G1's main α-helix surrounded by a ring of hydrogen bonds (McLaughlin et al. 1993). But not only binding to actin involves hydrophobic interaction of the main α-helix with an α-helix of the binding partner. The association in the G1 crystal structure with the NCS related G1 molecule in the asymmetric unit and contacts of equine G1 with a gelsolin segment 4 of an adjacent gelsolin molecule (Figure 4.14) are mainly via crossed helix association with the closest point of the helices at the glycine-valine rich region of the G1 main α-helix or the equivalent site on the G4 main α-helix. Although the angles, at which the helices cross vary, particularly the association in the G1 asymmetric unit is reminiscent of how G1C binds to actin.

	G1A	*G1B*	*G1C*
G1B	0.5		
G1C	0.7	0.6	
eG1	0.6	0.4	0.6

Table 6.3: RMS distances (Å) between superimposed co-ordinate sets LSQ-fitted over the main chain atoms (excl. carbonyl O) of G1A residues 29-144. G1C is the N57C mutant of G1 and eG1 is segment 1 of equine gelsolin.

When taken out of its context in the gelsolin structure and expressed individually, it is conceivable that G1 should try to reduce its hydrophobic surface presented to the surrounding water. Its overall conformation is stable enough not to denature under these circumstances. It might be possible that the observed association of the G1 molecules in the asymmetric unit is the way G1 overcomes this problem in solution. This could give an explanation for the leading peak observed during the purification of G1 by gel-filtration (Figure 4.1 and Figure 4.2).

The crystal structure of G1 determined in this work shows that under crystallisation conditions G1 binds one Ca^{2+} ion. The binding site is at the G1C intramolecular site found in the α-actin:G1C complex (McLaughlin et al. 1993). This confirms the conclusion Weeds et al. (1995) arrived at from the results of their biochemical experiments. They suggested that of the two calcium ions in the actin:G1C complex

at pH6.6 only the one in the position described above (the G1 intramolecular site) can be found in the actin:G1C complex at pH8.

The high similarity between the structure of Ca^{2+}-containing G1 and G1C in complex with actin in presence of Ca^{2+} demonstrates that G1 naturally adopts the ideal conformation to bind tightly to actin, provided Ca^{2+} ions are available. In the absence of calcium ions the G1 fold, found in whole gelsolin, does not change except at V145, whose peptide bond is rotated 180° moving the main chain oxygen away from the potential binding site of Ca^{2+} (Burtnick et al. 1997). This might tie in with the lower occupancy of the Ca^{2+} and the weaker electron density for the C-terminus of the second G1 molecule in the asymmetric unit (G1B). One could imagine that the interaction between the two molecules in the asymmetric unit is an attempt to mimic the interaction between G1 and actin. In this respect, G1B would function as the G1 binding site of actin, allowing an association with G1A, whose Ca^{2+} is at full occupancy and whose C-terminal Phe149 is in the same position as in G1C in complex with actin.

6.4 Probing the α-actin:G1 structure with latrunculin A

Gelsolin segment 1 is known to prevent actin nucleotide exchange (Tellam 1986) and to keep actin in a "tighter" state than observed in the complex of open-state β-actin with profilin (Chik et al. 1996). The determination of the latrunculin A containing α-actin:G1C structure (Figure 6.2) has shown that the control gelsolin segment 1 exerts on actin is not stringent enough to prevent conformational changes in subdomain 2 and 4 induced by the binding of latA. Still, the full extent of latA's influence might not be visible in the structure determined as is indicated by the higher degree of disorder in the crystal structure in comparison to native α-actin:G1C.

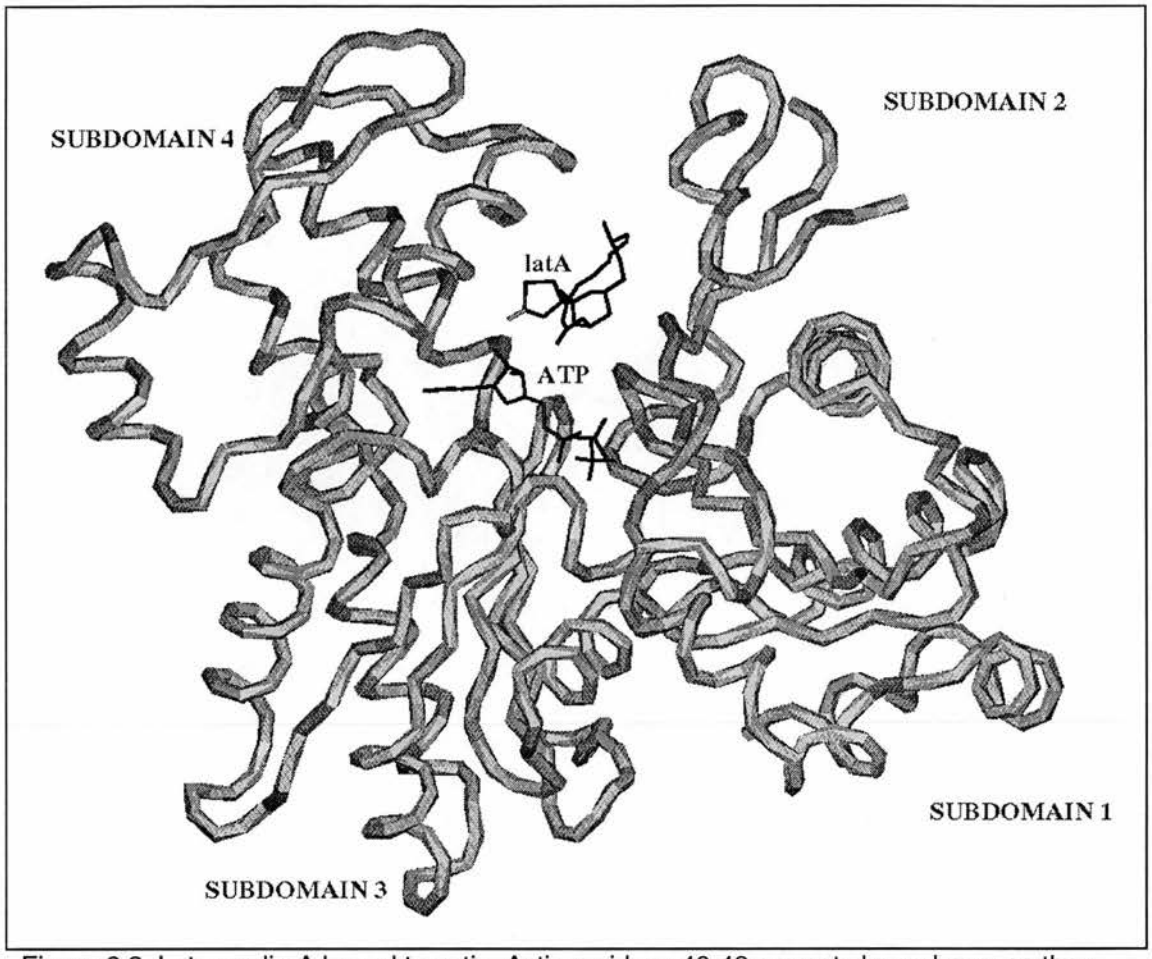

Figure 6.2: Latrunculin A bound to actin. Actin residues 40-49 are not shown because they could not be located in electron density.

The most striking changes induced by the binding of latA are a slight closure of the cleft between subdomain 2 and 4 and the roughly 90° twist of the side chain of Arg206 to form a strong salt bridge with Asp187 (Figure 5.11). These two residues are located in subdomain 4 at the nucleotide binding cleft between the two major actin domains. As can be seen in Figure 5.10 subdomain 4 is pulled together by a fraction in comparison to the native model. This is probably due to the salt bridge formation and induces the slight closure of the cleft. These changes in conformation at the top of the actin monomer might be the reason why latA prevents actin monomers from polymerising.

Latrunculin A was found to impede the exchange of the actin-bound ATP (Ayscough et al. 1997). This concurs with the above discussed closure of the actin domain cleft and the 34.5% smaller solvent accessible area around the ATP due to binding of latA. This explains the role of latA as an actin sequestering agent, preventing actin monomers from participating in F-actin formation.

6.5 Actin flexibility and its interfaces with G1 and other actin molecules

A recent survey (Lo Conte et al. 1999) has shown that most protein-protein interfaces of previously determined structures of complexes can be classified according to the total solvent accessible area excluded by the protein-protein interaction. Most complexes fall into the category with "standard" size interfaces. The mean value for the total solvent excluded area of standard interfaces is around 1600Å^2. When comparing the protein conformations in complex with available structures of the free protein, it was found that the proteins involved in this category undergo, no or only small conformational change, when forming the complexes.

Protein-protein interactions via "large" interfaces, with a mean solvent accessible area excluded of 3300Å^2, conversely involve large conformational changes in respect to the pre-bound state of the proteins. Apart from large movements of main chain loops and changes in the relative position of domains, disorder-to-order transitions of the protein chain can be observed when the proteins associate.

According to this classification, the binding of G1 to the barbed end of actin can be described as the interaction of two protein areas undergoing little change when contacting each other by excluding a "standard" area (1986Å^2) from access to the solvent. Our observations agree with this as there seems to be little conformational change between actin-bound G1 and free G1. Interestingly, the same domain in the context of whole gelsolin differs in its conformation.

The interaction of the pointed end with the barbed end of another actin molecule in the actin filament represents the interaction of two protein areas accompanied by extensive postulated conformational changes and conformational stabilisation (Holmes et al. 1990, Lorentz et al. 1993, Tirion et al. 1995, Page et al. 1997) and the exclusion of a larger area from access to solvent (between 2000 and 3000Å^2, McLaughlin and Weeds 1995).

Perhaps the regions, that were observed in this work to be highly flexible, may become more ordered in an actin molecule that is part of an actin filament. It may be that this altered conformation ultimately stabilises the filament and leads to the hydrolysis of bound ATP.

6.6 Conclusions drawn in this thesis

G1 has proven its stability and retained its fold even when crystallised on its own. The hydrophobic actin binding domain causes an almost symmetric association of two G1 molecules via this binding site in the crystal structure, reminiscent of the associations between actin and G1 and between G1 and G4 in the gelsolin crystal structure. This is probably due to the thermodynamically more stable arrangement of matching two hydrophobic patches together to form a unit displaying the remaining more hydrophilic surface to the aqueous environment. During the purification of G1, gel-filtration gave an indication that this association of two G1 molecules might also occur in solution.

When crystallised in complex with G1 under the same conditions, both the α- and β-isoform of actin are forced into the same conformation despite the sequence differences between the isoforms. The flexibility of the actin monomer bound to G1 is demonstrated by the continued inability of locating the DNaseI binding loop even

in the structure at 100K. Areas with higher B-factors in the room temperature structure also display higher than average B-factors in the 100K structure, despite the 24.0% decrease of the overall B-factor for the structure at lower temperature (Figure 3.10).

Additionally, latrunculin A was able to induce conformational changes in the actin structure in complex with G1. These changes are especially pronounced in subdomains 2 and 4 and lead to a slight narrowing of the gap between these two subdomains. The effect of latA on subdomains 1 and 3 is far less pronounced and can be considered insignificant. If we had not seen any conformational change, even in subdomain 2, we would have had to conclude that latA merely stabilised a monomeric G conformation of actin, thereby preventing polymerisation, since it does not bind at an actin subunit:subunit interface. This would have meant, that the actin conformation seen in its complex with G1 is not likely to be similar to the conformation of F-actin.

On the other hand, we cannot conclude that the conformation in the latrunculin-free structure is that of a filament subunit due to the mobility of subdomains 2 and 4, especially the DNaseI binding loop. This mobility is demonstrated by the conformational changes that latA can illicit at the pointed end of the monomer despite the tightly bound G1. Based on these latA induced conformational changes, we can presume that actin bound to gelsolin is sufficiently flexible at the pointed end to adopt a conformation different from those known, which is necessary to bind to the barbed end of a filament.

6.7 Future studies

To determine the full extent of the changes caused by the binding of latA to actin, co-crystallisation of actin and latA could be attempted. This could be done without any other actin binding protein since latA would prevent any polymerisation of actin under crystallisation conditions. This would provide further insights into the extent of G1C's influence on actin in the crystal structure.

A more ambitious project would be to try to obtain the crystal structure of gelsolin bound to two actin monomers. Not only the mechanism of action of gelsolin could be studied but this complex would give detailed structural information on the actin monomers at the barbed end of a filament.

The results from this work allow the assumption that α-actin complexed to profilin will assume a similar conformation as was observed for β-actin (Schutt et al. 1993, Chik et al. 1996). The open-state conformation (Chik et al. 1996) was obtained by varying the precipitant concentration and the pH. Since crystals of β-actin:G1C were obtained at pH6.0, it might prove interesting to determine the structure to compare it with the structure solved during this work at pH6.6.

Insights might also be obtained from the crystal structure of segment 1 of CapG, which is also a member of the gelsolin family of actin binding proteins but whose first segment binds actin less tightly than G1 and in a calcium dependent manner. During this work a crystal form was found to diffract X-rays to 2.7Å at room temperature, forming the basis for further crystallographic studies.

7. References

Albrecht-Buehler G., Lancaster R.M., 1976. A quantitative description of the extension and retraction of surface protrusions in spreading 3T3 mouse fibroblasts. J. Cell Biol. 71: 370-82.

Aldridge D.C., Turner W.B., 1969. Structures of cytochalasin C and D. J. Chem. Soc. (C): 923-8.

Aldridge D.C., Turner W.B., 1969. The identity of zygosporin A and cytochalasin D. J. Antibiotics 22: 170.

Ayscough K.R., Stryker J., Pokala N., Sanders M., Crews P., Drubin D.G., 1997 . High rates of actin filament turnover in budding yeast and roles for actin in establishment and maintenance of cell polarity revealed using the actin inhibitor latrunculin A. J. Cell Biol. 137: 399-416.

Barkalow K., Witke W., Kwiatkowski D.J., Harwig J.H., 1996. Coordinated regulation of platelet actin filament barbed ends by gelsolin and capping protein. J. Cell Biol. 134: 389-99.

Bragg W.H., 1913. The diffraction of short electromagnetic waves by a crystal. Proc. Camb. Phil. Soc. 17: 43-57.

Bragg W.H., von Laue M., Hermann C. (Eds.). 1935. International tables for the determination of crystal structures. First volume. Tables on the theory of groups., Borntraeger, Berlin, Germany.

Brenner S.L., Korn E.D., 1979. Substoichiometric concentrations of cytochalasin D inhibit actin polymerisation. J. Biol. Chem. 254: 9982-5.

Brenner SL., Korn ED., 1980. The effects of cytochalasins on actin polymerization and actin ATPase provide insights into the mechanism of polymerization., J. Biol. Chem. 255: 841-4.

Brenner S.L., Korn E.D., 1983. On the mechanism of actin monomer-polymer subunit exchange at steady state. J. Biol. Chem. 258: 5013-20.

Brigogne G., Irwin J., 1996. Maximum-likelihood refinement of incomplete models with BUSTER + TNT. Proceedings of the CCP4 study weekend January 1996: 85-92.

Brünger A.T., 1992. Free R value - a novel statistical quantity for assessing the accuracy of crystal-structures. Nature 355: 472-5.

Brünger A. T., Krukowski A., Erickson J., 1990. Slow-cooling protocols for crystallographic refinement by simulated annealing. Acta Cryst. A46: 585-93.

Brünger A.T., Kuriyan J., Karplus M., 1987. Crystallographic R factor refinement by molecular dynamics. Science 235: 458-60.

Bryan J., Kurth M.C., 1984. Actin-gelsolin interactions: evidence for two actin-binding sites. J. Biol. Chem. 259: 7480-7.

Bryan J., 1988. Gelsolin has three actin-binding sites. J. Cell Biol. 106: 1553-62.

Burtnick L.D., Koepf E.K., Grimes J., Jones E.Y., Stuart D.I., McLaughlin P.J., Robinson R.C., 1997. The crystal structure of plasma gelsolin: implications for actin severing, capping, and nucleation. Cell 90: 661-70.

Carlier M.F., 1990. Actin polymerization and ATP hydrolysis. Adv. Biophys. 26: 51-73.

Carlier M.F., 1991. Actin: protein structure and filament dynamics. J. Biol. Chem. 266: 1-4.

Carlier M.F., Criquet P., Pantaloni D., Korn E.D., 1986. Interaction of cytochalasin D with actin filaments in the presence of ADP and ATP. J. Biol. Chem. 261: 2041-50.

Chik J.K., Schutt C.E., 1996. The structure of an open state of β-actin at 2.65Å resolution. J. Mol. Biol. 263: 607-23.

Clarke M., Schatten G., Mazia D., Spudich J.A.,. 1975. Visualization of actin fibers associated with the cell membrane in amoebae of *Dictyostelium discoideum*. Proc. Natl. Acad. Sci.U.S.A. 72: 1758-62.

Collaborative Computational Project, Number 4., 1994. The CCP4 suite: programs for protein crystallography. Acta Cryst. D50: 760-3.

Cooke R., 1975. The role of the bound nucleotide in the polymerization of actin. Biochemistry 14: 3250-6.

Coue M., Brenner S.L., Spector I., Korn E.D., 1987. Inhibition of actin polymerisation by latrunculin A. FEBS Letters 213: 316-318.

Coue M., Korn E.D., 1986. Interaction of plasma gelsolin with ADP-actin. J. Biol. Chem. 261: 3628-31.

Cribbs D.H., Glenney JR Jr., Kaulfus P., Weber K., Lin S.,. 1982. Interaction of cytochalasin B with actin filaments nucleated or fragmented by villin. J. Biol. Chem. 257: 395-9.

Dabiri G.A., Young C.L., Rosenbloom J., Southwick F.S., 1992. Molecular cloning of human macrophage capping protein cDNA. J. Biol. Chem. 267: 16545-52.

Dabrowska R., Hinssen H., Galazkiewicz B., Nowak E., 1996. Modulation of gelsolin induced actin filament severing by caldesmon and tropomyosin and the effect of these proteins on the actin activation of myosin Mg^{2+}-ATPase activity. Biochem. J. 315: 753-9.

De La Cruz E.M., Pollard T.D., 1995. Nucleotide-free actin: stabilisation by sucrose and nucleotide binding kinetics. Biochemistry 34: 5452-61.

DeLucas L.J., Bugg C.E., et al., 1986. Preliminary investigations of protein crystal growth using the space shuttle. J. Crystal Growth 76: 681-93.

Ewald P.P., 1921. Das'reziproke' Gitter in der Strukturtheorie. Teil I: Das reziproke eines einfachen Gitters. Z. Krist. 56: 129-56.

Elzinga M., Collins J.H., Kuehl W.M., Adelstein R.S., 1973. Complete amino-acid sequence of actin of rabbit skeletal muscle. Proc. Natl. Acad. Sci. U.S.A. 70: 2687-91.

Elzinga M., Maron B.J., Adelstein R.S., 1976. Human heart and platelet actins are products of different genes. Science 191: 94-5.

Feher G., Kam Z., 1985. Nucleation and growth of protein crystals: general principles and assays. Methods in Enzymology 114: 77-112.

Friedel G., 1913. Concerning symmetries of crystals that can be revealed by X-ray diffraction. Comptes Rendus, Acad. Sci. (Paris) 157: 1533-6.

Frieden C., Patane K., 1985. Differences in G-actin containing bound ATP or ADP: the Mg^{2+}-induced conformational change requires ATP. Biochemistry 24: 4192-6.

Friederich E., Kreis T.E., Louvard D., 1993. Villin induced growth of microvilli is reversibly inhibited by cytochalasin D. J. Cell Sci. 105: 765-75.

Friedrich W., Knippig P., Laue M., 1912. Interferenz-Erscheinungen bei Röntgenstrahlen. Sitzungsbericht der mathematisch-physikalischen Klasse der Königlichen Bayrischen Akademie der Wissenschaften zu München: pp.303-12.

Gilman J.J., 1963. The art and science of growing crystals. Wiley: New York.

Goddette D.W., Frieden C., 1985. The binding of cytochalasin D to monomeric actin. Biochem. Biophys. Red. Commun. 128: 1087-92.

Goddette D.W., Frieden C., 1986. Actin polymerisation: the mechanism of action of cytochalasin D. J. Biol. Chem. 261: 15974-80.

Goldschmidt-Clermont P.J., Machesky L.M., Doberstein S.K., Pollard T.D., 1991. Mechanism of the interaction of human platelet profilin with actin. J. Cell Biol. 113: 1081-9.

Grazi E., Magri E., Cuneo P., Cataldi A., 1991. The control of cellular motility and the role of gelsolin. FEBS 295: 163-6.

Griffith L.M., Pollard T.D., 1982. The interaction of actin-filaments with microtubules and microtubule-associated proteins. J. Biol. Chem. 257: 9143-51.

Hartwig J.H., Chambers K.A., Stossel T.P., 1989. Association of gelsolin with actin filaments and cell membranes of macrophages and platelets. J. Biol. Chem. 108: 467-79.

Hayden S.M., Miller P.S., Brauweiler A., Bamburg J.R., 1993. Analysis of the interactions of actin depolymerising factor with G- and F-actin. Biochemistry 32: 9994-10004.

Hendrickson W.A., Konnert J.H., 1980. Computing in Crystallography. I.U.Cr. and Indian Acad.Sci., Banglore, India.

Hesketh J., 1991. Association of ribosomes with myofibrils and microfilaments - a role in the spatial-organization of protein-synthesis. Biochem. Soc. Trans. 19:. 1103-7

Hessel J.F.C. 1830. Krystallometrie oder Krystallonomie und Krystallographie. reprinted 1897 in Ostwalds Klassiker der exakten Wissenschaften 89, 41-124, Leipzig, Germany :.

Hiyoshi M., Taesung I.M., Sasaki A., Hashimoto K., Tatsumi N., 1989. Involvement of calcium ion in the interaction between the actin-gelsolin complex and

phosphatidylinositol-4-monophosphate or 4,5-bisphosphate. Biochem. Int. 18: 1009-15.

Hodel A., Kim S.H. Brünger A.T., 1992. Model bias in macromolecular crystal structures. Acta Cryst. A48: 851-8.

Holden A., Singer P., 1960. Crystals and crystal growing. Anchor Books, Doubleday:Garden City, NY, U.S.,

Holmes K.C., Popp D., Gebhard W., Kabsch W., 1990. Atomic model of the actin filament. Nature 347: 44-49.

Hope H., 1990. Crystallography of biological macromolecules at ultra-low temperature. Annu. Rev. Biophys. Biophys. Chem.19: 107-26.

Houk T.W. Jr., Ue K., 1974. The measurement of actin concentration in solution: a comparison of methods. Anal. Biochem. 62: 66-74.

Huber R., Bennet W.S., 1983. Functional significance of flexibility in proteins. Biopolymers 22: 261-79.

International Union of Crystallography. 1987. International Tables of Crystallography. Volume A, Space group symmetry, edited by Hahn T., D. Reidel Publishing Company, NL.

Janin J., Chothia C., 1990. The structure of protein-protein recognition sites. J. Biol. Chem. 265: 16027-30.

Janmey P., 1993. A slice of actin. Nature 364: 675-6.

Janmey P.A., Matsudaira P.T., 1992. Phosphoinositide-binding peptides derived from the sequences of gelsolin and vilin. J. Biol. Chem. 267: 11818-23.

Janmey P.A., Stossel T.P., 1987. Modulation of gelsolin function by phosphatidylinositol-4,5-bisphosphate. Nature 325: 362-4.

Janmey P.A., Stossel T.P., 1989. Gelsolin-polyphosphoinositide interaction. J. Biol. Chem. 264: 4825-31.

Jefford C.W., Bernardinelli G., Tanaka J., Higa T., 1996. Structures and absolute configurations of the marine toxins latrunculin A and laulimalide. Tetrahedron Lett. 37: 159-62.

Jones T.A., Zou J.Y., Cowan S.W., Kjeldgaard M., 1991. Improved methods for building protein models in electron density maps and the location of errors in these models. Acta Cryst A47: 110-9.

Kabsch W., Mannherz H.G., Suck D., Pai E.F., Holmes K.C., 1990. Atomic structure of the actin:DNase I complex. Nature 347: 37-44.

Kashman Y., Groweiss A., Shmueli U., 1980. Latrunculin, a new 2-thiazolidinone macrolide from the marine sponge *Latrunculia magnifica*. Tetrahedron Lett. 21: 3629-32.

Kinosian H.J., Selden LA., Estes J.E., Gershman L.C., 1993. Nucleotide binding to actin. J. Biol. Chem. 268: 8683-91.

Kirschner M.W., 1980. Implications of treadmilling for the stability and polarity of actin and tubulin polymers *in vivo*. J. Cell Biol. 86: 330-4.

Kleywegt G.J., 1996. Use of non-crystallographic symmetry in protein structure refinement. Acta Cryst D52: 842-57.

Kleywegt G.J., Jones T.A., 1996. xdlMAPMAN and xdlDATAMAN - programs for reformatting, analysis and manipulation of biomacromolecular electron-density maps and reflection data sets. Acta Cryst D52: 826-8.,

Kondo H., Ishiwata S., 1976. Uni-directional growth of F-actin. J. Biochem. 79: 159-71.

Korenbaum E., Nordberg P., Bjorkegren-Sjogren C., Schutt C.E., Lindberg U., Karlsson R., 1998. The role of profilin in actin polymerisation and nucleotide exchange. Biochemistry 37: 9274-83.

Korn E.D., Carlier M.F., Pantaloni D., 1987. Actin polymerization and ATP hydrolysis. Science 238: 638-44.

Kuznetsov S.A., Langford G.M., Weiss D.G., 1992. Actin-dependent organelle movement in squid axoplasm. Nature 356: 722-5.

Kwiatkowski D.J., Stossel T.P., Orkin S.H., Mole J.E., Colten H.R., Yin H.L., 1986. Plasma and cytoplasmic gelsolins are encoded by a single gene and contain a duplicated actin-binding domain. Nature 323: 455-8.

Kwiatkowski D.J., Janmey P.A., Yin H.L., 1989. Identification of critical functional and regulatory domains in gelsolin. J. Cell Biol. 108: 1717-26.

Laham L.E., Lamb J.A., Allen P.G., Janmey P.A., 1993. Selective binding of gelsolin to actin monomers containing ADP. J. Biol. Chem. 268: 14202-7.

Lal A.A., Brenner S.L., Korn E.D., 1984. Preparation and polymerisation of skeletal muscle ADP-actin. J. Biol. Chem. 259: 13061-5.,

Lauweryns J.M., Baert J., De Loecker W., 1975. Intracytoplasmic filaments in pulmonary lymphatic endothelial cells. Fine structure and reaction after heavy meromyosin incubation., Cell & Tissue Research. 163: 111-24.

Lees A., Haddad J.G., Lin S., 1984. Brevin and vitamin D binding protein: comparison of the effects of two serum proteins on actin assembly and disassembly. Biochemistry 23: 3038-47.

Leslie A.G.W., 1990. Crystallographic Computing. Oxford University Press., U.K.,

Lin K.M., Wenegieme E., Lu P.J., Chen C.S., Yin H. L., 1997. Gelsolin binding to phosphatidylinositol-4,5-bisphosphate is modulated by calcium and pH. J. Biol. Chem. 272: 20443-50.

Lo Conte L., Chothia C., Janin J., 1999. The atomic structure of protein-protein recognition sites. J. Mol. Biol. 285: 2177-98.

Lorentz M, Popp D., Holmes K.C., 1993. Refinement of the F-actin model against X-ray fibre diffraction data by the use of a directed mutation algorithm. J. Mol. Biol. 234: 826-36.

Macotta A., Valensin G., Vivi A., Gaggelli E., 1993. The conformation of cytochalasin D in DMSO solution from ^{1}H and ^{13}C NMR relaxation rates. J. Chem. Soc. Perkin Trans. 2: 729-32.

Matsudaira P., Janmey P., 1988. Pieces in the actin-severing protein puzzle. Cell 54: 139-40.

Matthews. 1968. Solvent content of protein crystals. J.Mol.Biol. 33: 491-7.

Maury C.P.J., Nurmiaho-Lassila E.L., 1992. Creation of amyloid fibrils from mutant Asn187 gelsolin peptides. Biochem. Biophys. Res. Commun. 183: 227-31.

Maury C.P.J., Nurmiaholassila E.L., Rossi H., 1994. Amyloid fibril formation in gelsolin-derived amyloidosis. Lab Invest. 70: 558-64.

Maury C.P.J., 1991. Gelsolin-related amyloidosis. J. Clin. Invest. 87: 1195-9.

McLaughlin P.J., Gooch J., 1992. Crystallisation of human gelsolin. FEBS 302: 253-5.

McLaughlin P.J., Weeds A. G., 1995. Actin-binding protein complexes at atomic resolution. Annu. Rev. Biophys. Biomol. Struct. 24: 643-75.

McLaughlin P.J., Gooch J.T., Mannherz H.G., Weeds A.G., 1993. Structure of gelsolin segment 1-actin complex and the mechanism of filament severing. Nature 364: 685-92.

McLeod J.F., Kowalski M.A., Haddad JG Jr., 1989. Interactions among serum vitamin D binding protein, monomeric actin, profilin, and profilactin. J. Biol. Chem. 264: 1260-7.

McPherson A., 1985. Crystallisation of macromolecules: general principles. Methods in Enzymology 114: 112-120.

McPherson A. 1976. The growth and preliminary investigation of protein and nucleic acid crystals for X-ray diffraction analysis. Methods of Biochemical Analysis. 23: 249-345.

McPherson A., Koszelak S., Axelrod H., Day J., Williams R., Robinson L., McGrath M., Cascio D., 1986. An experiment regarding crystallisation of soluble proteins in the presence of β-octyl glucoside. J. Biol. Chem. 261: 1969-75.

McRee D.E., 1993. Practical protein crystallography. Academic Press Inc., USA:.

Minato H., Matsumoto M., 1970. Studies on the metabolites of of *Zygosporium masonii*. Part I. Structure of zygosporin A. J. Chem. Soc. (C): 38-45.

Minato H., Takeuchi M., et al.,1973. Structure activity relationships among zygosporin derivatives. Chem. Phrm. Bull. 21: 2268-77.

Mishra V.S., Henske E.P., Kwiatkowski D.J., Southwick F.S., 1994. The human actin-regulatory protein cap G: gene structure and chromosome location. Genomics 23: 560-5.

Moldovan N.I., Milliken E.E., Irani K., Chen J., Sohn R.H., Finkel T., Goldschmidt-Clermont P.J., 1997. Regulation of endothelial cell adhesion by profilin. Curr. Biol. 7: 24-30.

Murshudov G.N., Vagin A.A., Dodson E.J., 1997. Refinement of macromolecular structures by the maximum-likelyhood method. Acta Cryst. D53: 240-55.

Nakajima-Iijima S., Hamada H., Reddy P., Kakunaga T., 1985. Molecular structure of the human cytoplasmic β-actin gene: interspecies homology of sequences in the introns. Proc. Natl. Acad. Sci. USA 82: 6133-7.

Neeman I., Fishelson L., Kashman Y., 1975. Isolation of a new toxin from the sponge *Latrunculina magnifica* in the Gulf of Aquaba (Red Sea). Mar. Biol. 30: 293-6.

Ohmori H., Toyama S., Toyama S., 1992. Direct proof that the primary site of action of cytochalasin on cell motility processes is actin. J. Cell Biol. 116: 933-41.

Okabe S., Hirokawa N., 1989. Incorporation and turnover of biotin-labeled actin microinjected into fibroblastic cells: an immunoelectron microscopic study. J. Cell Biol. 109: 1581-95.

Onoda K., Yu F.X., Yin H.L., 1993. gCap39 is a nuclear and cytoplasmic protein. Cell Motil. Cytoskeleton 26: 227-38.

Orlova A., Egelman E.H., 1992. Structural basis for the destabilisation of F-actin by phosphate release following ATP hydrolysis. J. Mol. Biol. 227: 1043-53.

Otey C.A., Bulinski J.C., Kalnoski M.H., 1987. Identification and quantification of actin isoforms in vertebrate cells and tissue. J. Cell Biochem. 34: 113-24.

Page R., Lindberg U., Schutt C.E., 1998. Domain motions in actin. J. Mol. Biol. 280: 463-74.

Pannu N.S., Read R.J., 1996. Improved structure refinement through maximum likelihood. Proceedings of the CCP4 study weekend January 1996: 75-84.

Perry S.V., 1955. Myosin adenosinetriphosphatase. Methods in Enzymology 2: 582-8.

Pinder J.C., Gratzer W.B., 1995. Concentrated Tris solutions for the preparation, depolymerisation, and assay of actin: application to erythroid actin. Anal. Biochem. 225: 291-5.

Pollard T.D., 1984. Polymerization of ADP-actin. J. Cell Biol. 99: 769-77.

Pollard T.D., 1986 (a). Assembly and dynamics of the actin filament system in non-muscle cells. J. Cell Biochem. 31: 87-95.

Pollard T.D., 1986 (b). Rate Constants of the Reaction of ATP- and ADP-Actin with the Ends of Actin Filaments. J. Cell Biol. 103: 2747-54.

Pollard T.D., Almo S., Quirk S., Vinson V., Lattman E.E., 1994. Structure of actin binding proteins: insights about function at atomic resolution. Annu. Rev. Cell Biol. 10: 207-49.

Pollard T.D., Schwarz W.H., 1992. Nucleotide exchange, structure, and mechanical properties of filaments assembled from ATP-actin and ADP-actin. J. Biol. Chem. 267: 20339-45.

Pollard T.D., Weeds A.G., 1984. The rate constant for ATP hydrolysis by polymerized actin. FEBS Lett. 170: 94-8.

Pope B., Maciver S., Weeds A., 1995. Localization of the calcium-sensitive actin monomer binding site in gelsolin to segment 4 and identification of calcium binding sites. Biochemistry 34: 1583-8.

Pope B., Way M., Weeds A.G., 1991. Two of the three actin-binding domains of gelsolin bind to the same subdomain of actin. FEBS Lett. 280: 70-4.

Porter A.B., 1906. On the diffraction theory of microscopic vision. Phil. Mag. 11: 154-66.

Powell M.J.D., 1977. Restart procedures for the conjugate gradient method. Mathematical Programming 12: 241-54.

Prendergast G.C., Ziff E.G., 1991. Mbh1: a novel gelsolin/severin-related protein which binds actin in vitro and exhibits nuclear localization in vivo. EMBO J. 10: 757-66.

Pring M., Weber A., Bubb M.R., 1992. Profilin-actin complexes directly elongate actin filaments at the barbed end. Biochemistry 31: 1827-36.

Quiñoà E., Kakou Y., Crews P., 1988. Fijianolides, polyketide heterocycles from a marine sponge. J. Org. Chem. 53: 3642-4.

Read R., 1986. Improved Fourier coefficients for maps using phases from partial structures with errors. Acta Cryst. A42: 140-9.

Rivero F., Koppel B., Peracino B., Bozzaro S., Siegert F., Weijer C.J., Schleicher M., Albrecht R., Noegel A.A., 1996. The role of the cortical cytoskeleton: F-actin crosslinking proteins protect against osmotic stress, ensure cell size, cell shape and motility, and contribute to phagocytosis and development. J. Cell Sci. 109: 2679-91.

Rodgers D.W., 1997. Practical cryocrystallography. Methods in Enzymology 276: 183-203.

Rosenberg-Schaier S., 1992. Purification and characterisation of platelet actin, actin-binding protein, and α-actinin. Methods in Enzymology 215: 58-77.

Rosenblatt J., Peluso P., Mitchison T.J., 1995. The bulk of unpolymerised actin in xenopus egg extracts is ATP-bound. Mol Biol Cell 6: 227-36.

Rybakova I.N., Amann K.J., Ervasti J.M., 1996. A new model for the interaction of dystrophin with F-actin. J. Cell Biol. 135: 661-72.

Sambrook J., Maniatis T. et al., 1989. Molecular cloning: a laboratory manual. Cold Spring Harbor Laboratory Press, USA.

Sanger J.M., Sanger J.W., 1980. Banding and polarity of actin filaments in interphase and cleaving cells. J. Cell Biol. 86: 568-75.

Schafer D.A., Cooper J.A., 1995. Control of actin assembly at filament ends. Annu. Rev. Cell Dev. Biol. 11: 497-518.

Schoepper B., Wegner A., 1991. Rate constants and equilibrum constants for binding actin to the 1:1 gelsolin-actin complex. Eur. J. Biochem. 202: 1127-31.

Schutt C.E., Lindberg U., 1992. Actin as the generator of tension during muscle contraction. Proc. Natl. Acad. Sci. U.S.A. 89: 319-23.

Schutt C.E., Myslik J.C., Rozycki M.D., Goonesekere N.C.W., Lindberg U., 1993. The structure of crystalline profilin-β-actin. Nature 365: 810-6.

Selden L.A., Gershman L.C., Kinosian H.J., Estes J.E., 1987. Conversion of ATP-actin to ADP-actin reverses the affinity of monomeric actin for Ca^{2+} vs. Mg^{2+}. FEBS Letters 217: 89-93.

Sheldrick G.M., Schneider T.R., 1997. SHELXL: High-resolution refinement. Methods in Enzymology 277: 319-43.

Sheterline P., Sparrow J.C., 1994. Actin. Protein Profile Vol.1: Academic Press.

Shu W.P., Wang D., Stracher A., 1992. Chemical evidence for the existence of activated G-actin. Biochem. J. 283: 567-73.

Spector I., Shochet N.R., Blasberger D., Kashman Y., 1989. Latrunculins - novel marine macrolides that disrupt microfilament organisation and affect cell growth: I. Comparison with cytochalasin D. Cell Mot. Cytoskel. 13: 127-44.

Spector I., Shochett N.R., 1983. Latrunculins: Novel marine toxins that disrupt microfilament organization in cultured cells. Science 219: 493-5.

Spudich J.A., Watt S., 1971. The regulation of rabbit skeletal muscle contraction. J. Biol. Chem. 246: 4866-71.

Stossel T.P., 1993. On the crawling of animal cells. Science 260: 1086-94.

Stossel T.P., Hartwig J.H., 1976. Interaction of actin, myosin, and a new actin-binding protein of rabbit pulmonary macrophages: role in cytoplasmic movement and phagocytosis. J. Cell Biol. 68: 602-19.

Straub F.B., Feuer G., 1950. Adenosinetriphosphate functional group of actin. Biochim. Biophys. Acta 4: 455-70.

Strickland-Constable R.F., 1968. Kinetics and mechanism of crystallization. Academic Press: London, New York.

Studier FW., Moffatt BA., 1986. Use of bacteriophage T7 RNA polymerase to direct selective high-level expression of cloned genes., J. Mol. Biol. 189: 113-30.

Sturrock S.S., 1997. Improved tools for protein structure prediction. Ph.D. thesis, The University of Edinburgh.

Sun H.Q., Wooten D.C., Janmey P.A., Yin H.L., 1994. The actin side-binding domain of gelsolin also caps actin filaments. J. Biol. Chem. 269: 9473-9.

Suzuki N., Mihashi K., 1991. Binding mode of cytochalasin B to F-actin is altered by lateral binding of regulatory proteins. J. Biochem. Tokyo 109: 19-23.

Tabb J.S., Molyneaux B.J., Cohen D.L., Kuznetsov S.A., Langford G.M., 1998. Transport of ER vesicles on actin filaments in neurons by myosin V. J. Cell Sci. 111: 3221-34.

Tellam R., Frieden C., 1982. Cytochalasin D and platelet gelsolin accelerate actin polymer formation. A model for regulation of the extent of actin polymer formation in vivo. Biochemistry 21: 3207-14.

Tellam R., 1986. Gelsolin inhibits nucleotide exchange from actin. Biochemistry 25: 5799-804.

Tirion M.M., Benavraham D., Lorenz M., Holmes K.C., 1995. Normal modes as refinement parameters for the F-actin model. Biophys. J. 68: 5-12.

Trotter J.A., Foerder B.A., Keller J.M., 1978. Intracellular fibres in cultured cells: analysis by scanning and transmission electron microscopy and by SDS-polyacrylamide gel electrophoresis. J. Cell Sci. 31: 369-92.

Tsukuda Y., Koyama H., 1972. Crystal structure of isozygosporin A p-bromobenzoate. J.C.S. Perkin II: 739-44.

Vandekerckhove J., 1990. Actin-binding proteins. Curr. Opin. Cell Biol. 2: 41-50.

Vandekerckhove J., 1993. Actin and actin binding proteins. in Guidebook to the Cytoskeletal and Motor Proteins, Oxford University Press Inc., New York, U.S.A.,

Vandekerckhove J., Weber K., 1979. The complete amino acid sequence of actins from bovine aorta, bovine heart, bovine fast skeletal muscle, and rabbit slow skeletal muscle. A protein chemical analysis of muscle actin differentiation., Differentiation 14: 123-33.

Wang K., 1977. Filamin, a new high-molecular weight protein found in smooth muscle and non-muscle cells. Purification and properties of chicken gizzard filamin., Biochemistry 16: 1857-65.

Wanger M., Wegner A., 1983. Similar affinities of ADP and ATP for G-actin at physiological salt concentrations. FEBS 162: 112-6.

Way M., Weeds A., 1988. Nucleotide sequence of pig plasma gelsolin. Comparison of protein sequence with human gelsolin and other actin-severing proteins shows strong homologies and evidence for large internal repeats., J. Mol. Biol 203: 1127-33.

Way M., Gooch J., Pope B., Weeds A.G., 1989. Expression of human plasma gelsolin in *Escherichia coli* and dissection of actin binding sites by segmental deletion mutagenesis. J. Cell Biol. 109: 593-605.

Way M., Pope B., Gooch J., Hawkins M., Weeds A.G., 1990. Identification of a region in segment 1 of gelsolin critical for actin binding. EMBO J. 9: 4103-9.

Weeds A., Maciver S., 1993. F-actin capping proteins. Curr. Opin. Cell Biol. 5: 63-9.

Weeds A.G., Gooch J., McLaughlin P., Pope B., Bengtsdotter M., Karlsson R., 1995. Identification of the trapped calcium in the gelsolin segment 1:actin complex:

implications for the role of calcium in the control of gelsolin activity. FEBS 360: 227-30.

Weeds A.G., Gooch J., McLaughlin P., Maury C.P.J., 1993. Variant plasma gelsolin responsible for familial amyloidosis (finnish type) has defective actin severing activity. FEBS Lett. 335: 119-23.

Wegner A., Engel J., 1975. Kinetics of the cooperative association of actin to actin filaments. Biophys.Chem. 3: 215-25.

Welch M.D., Iwamatsu A., Mitchison T.J., 1997. Actin polymerisation is induced by arp2/3 protein complex at the surface of *Listeria monocytogenes*. Nature 385: 265-9.

Wertman K.F., Drubin D.G., Botstein D., 1992. Systematic mutational analysis of the yeast ACT1 gene. Genetics 132: 337-50.

Westrin H., Backman L., 1983. Association of rabbit muscle glycolytic-enzymes with filamentous actin - a countercurrent distribution study at high ionic-strength. Eur. J. Biochem. 136: 407-11.

Whalen RG., Butler-Browne GS., Gros F., 1976. Protein synthesis and actin heterogeneity in calf muscle cells in culture. Proc. Natl. Acad. Sci. U.S.A. 73: 2018-22.

Winder S.J., Hemmings L., Maciver S.K., Bolton S.J., Tinsley J.M., Davies K.E., Critchley D.R., Kendrick-Jones J., 1995. Utrophin actin binding domain: analysis of actin binding and cellular targeting. J. Cell Sci. 108: 63-71.

Woodrum D.T., Rich S.A., Pollard T.D., 1975. Evidence for biased bidirectional polymerization of actin filaments using heavy meromyosin prepared by an improved method. J. Cell Biol. 255: 9494-500.

Xian W., Vegners R., Janmey P.A., Braunlin W.H., 1995. Spectroscopic studies of a phosphoinositide-binding peptide from gelsolin: behaviour in solutions of mixed solvent and anionic micelles. Biophysical J. 69: 2695-702.

Yang Y., Dowling J., Yu Q.C., Kouklis P., Cleveland D.W., Fuchs E., 1996. An essential cytoskeletal linker protein connecting actin microfilaments to intermediate filaments. Cell 86: 655-65.

Yin H.L., Iida K., Janmey P.A., 1988. Identification of a polyphosphoinositide-modulated domain in gelsolin which binds to the sides of actin filaments. J. Cell Biol. 106: 805-12.

Yin H.L., Stossel T.P., 1979. Control of cytoplasmic actin gel-sol transformation by gelsolin - a calcium-dependent regulatory protein. Nature 281: 583-86.

Yin H.L., Stossel T.P., 1980. Purification and structural properties of gelsolin, a Ca^{2+}-activated regulatory protein of macrophages. J. Biol. Chem. 255: 9490-3.

Yin H.L., 1988. Gelsolin: calcium and polyphosphoinositide-regulated actin modulating protein. Bioessays 7: 176-9.

Young C.L., Feierstein A., Southwick F.S., 1994. Calcium regulation of actin filament capping and monomer binding by macrophage capping protein. J. Biol. Chem. 269: 13997-4002.

Young C.L., Southwick F.S. Weber A., 1990. Kinetics of the interaction of a 41-kilodalton macrophage capping protein with actin: promotion of nucleation during prolongation of the lag period. Biochemistry 29: 2232-40.

Yu F.X., Zhou D.M. Yin H.L., 1991. Chimeric and truncated gCap39 elucidate the requirements for actin filament severing and end capping by the gelsolin family of proteins. J. Biol. Chem. 266: 19269-75.

Yu F.X., Lin S.C., Morrisonbogorad M., Atkinson M.A.L., Yin H.L., 1993. Thymosin beta 10 and thymosin beta 4 are both actin monomer sequestering proteins. J. Biol. Chem. 268: 502-9.

Yu F.X., Yin H.L., 1992. Identification of a polyphosphoinositide-binding sequence in an actin monomer-binding domain of gelsolin. J. Biol. Chem. 267: 14616-21.